Vol 12 • No. 1 • April 2018

ISSN: 0976 - 1330

Journal of GEOMATICS

INDIAN SOCIETY OF GEOMATICS

Journal of Geomatics

(A publication of the Indian Society of Geomatics)

Editorial Board

Advisory Board

Indian Society of Geomatics
Executive Council 2017 – 2020

Secretary: (address for correspondence)
6202, SAC Bopal Campus, Ahmedabad – 380058, India
Email: secretary@isgindia.org; sasharma@sac.isro.gov.in

Journal of Geomatics
(A Publication of the Indian Society of Geomatics)

Vol. 12. No. 1 Research articles April 2018

Journal of Geomatics Vol 12 No. 1 April 2018

Performance enhancement of Rational Function Model (RFM) for improved geo-position accuracy of IKONOS stereo satellite imagery

Tamer M. Saleh, Mohamed I. Zahran, Ayman R. El-Sheaby, and Mahmoud S. Gomaa
Department of Surveying Engineering, University of Benha, 108 Shoubra Street, Cairo, Egypt
Email: tamer.mohamed@feng.bu.edu.eg, mohamed.zahran01@feng.bu.edu.eg, ayman.alshehaby@feng.bu.edu.eg, mahmoud.goma@feng.bu.edu.eg

(Received: Oct 20, 2017; in final form: Apr 08, 2018)

Abstract: The RFM has been considered as a generic sensor model. Compared to the widely used polynomial models, RFM is essentially a more generic and expressive form. Utilizing the RFM to replace physical sensor models in photogrammetric mapping is becoming a standard way for economical and fast mapping from high-resolution imagery. This model uses the Rational Polynomial Coefficients (RPCs) supplied with the images, since IKONOS precise sensor and orbit parameters are not released by the satellite company. This paper presents three mathematical models for performance enhancement of RFM using IKONOS stereo satellite images, namely: 1) Bias-corrected image space; 2) Bias-corrected RPCs; and 3) Bias-corrected ground space. The three models were tested and compared with the well-known 3D-Affine and Direct Linear Transformation (DLT) models. The Least Squares Method (LSM) was applied to implement the different mathematical setups for estimating the correction parameters. Attained results show that the accuracies of the five models are slightly variant. With five GCPs, an accuracy of 0.8 m in X, 1.2 m in Y, and 1.3 m in height is achieved using the bias corrected image space and an accuracy of 0.9 m in X, 1 m in Y, and 1.6 m in height is reached using the bias corrected RPCs. On the other hand, the results indicate the effectiveness of 3D-Affine and DLT models especially when the RPCs and/or commercial software packages are not available for users.

Keywords: RFM, RPCs, Bias correction, 3D-Affine, DLT and Matlab.

1. Introduction

With the current growth in demand for high resolution satellite imagery (HRSI), great efforts have been made in natural hazards monitoring, resource management, change detection, planning, 3D shoreline extraction, DTM (Digital Terrain Model) and DSM (Digital Surface Model) generation (Poon et al., 2005; Xu et al., 2005; Di et al., 2003). A critical issue is the choice of a sensor model for HRSI to acquire high-accuracy 3D-reconstruction. In general, sensor models can be grouped into two classes, physical sensor models and generic sensor models. Physical sensor models are more rigorous and normally provide better accuracies since the model parameters employed represent the physical imaging process of sensors. However, building such physical sensor models requires information of the physical sensor and its imaging model. This information includes focal length, principal point location, pixel size, lens distortions and orientation parameters of the image. Collinear equations are rigorous models available for frame and push-broom sensors (Vincent and Yong, 2000). It is realized that this information is not always available, especially for images from commercial satellites. The generic sensor models are independent on sensor platforms as well as sensor types. Such properties have made generic sensor models very popular in the remote sensing community. The typical generic sensor models are polynomial-based ones (Vincent and Yong, 2000; Vincent and Yong, 2002). In terms of accuracy and computational stability, the bias compensation method (Fraser and Hanley, 2003) so far appears to be the best method and has been widely used (Fraser and Hanley, 2003, 2005; Hu et al., 2004). However, this method is effective only when the camera field of view (FOV) is narrow and the position and attitude errors are small (Grodecki and Dial, 2003).

Fraser and Hanley (2003) developed a method for the removal of exterior orientation biases in RPCs of IKONOS imagery. They found that only bias corrected RPCs of IKONOS is capable of generating accurate results with just one ground control point. Fraser and Hanley (2005) recognized the notable positioning accuracy attained with the RPC bundle adjustment with bias compensation. Furthermore, Fraser et al. (2006) gave an overview of the RPC model for high resolution satellite imagery, and highlighted the accuracy potential of RPC block adjustment. It has been demonstrated that bias compensated RPC block adjustment can yield sub-pixel positioning accuracy and highly accurate Ortho-images and digital surface models. Similar results were reported in Tong et al. (2010), which presented the two schemes: RPCs modification; and RPCs regeneration for orientation bias correction based on Quick-Bird stereo images in Shanghai. Four cases of bias correction were tested including: shift bias correction, shift and drift bias correction, affine model bias correction, and second-order polynomial bias correction. A least squares adjustment method is adopted for correction parameter estimation. The modified RPCs improve the accuracy from 23 m to 3 m in planimetry and from 17 m to 4 m in height. With the shift and drift bias correction method, the regenerated RPCs achieved a further improved positioning accuracy of 0.6 m in planimetry and 1 m in height with minimal two GCPs. The Rational Function Model (RFM) based on Rational Polynomial Coefficients (RPCs) is one of the generic models in use in place of rigorous models (Volpe and Rossi, 2003). After a rigorous sensor bundle adjustment is performed, multiple evenly distributed image/object grid points can be generated and used as ground control points (GCPs). Then, the RPCs are

calculated by these GCPs (Di et al., 2003). A least-squares method is used to estimate the RFM coefficients (RPCs) from a three-dimensional pseudo grid of points and orientation parameters. The RPCs are usually provided by imagery vendors of IKONOS, Quick-Bird, CARTOSAT – 1 etc. and were utilized for transformation from image to object space coordinates in a geographic reference system. Since sensor orientation is directly observed, there would be some systematic error in orientation parameters. Thus the refinement of RFM is required (Wu et al., 2008). In most studies mentioned above, biases in the image space or in the object space were modelled and corrected to refine RPCs-derived ground coordinates, while the original RPCs remained unchanged. Few studies were conducted to take the original set of coefficients from the RPC model and add new adjustable functions for both line and sample to the normal equations based on the known GCPs (Singh et al., 2008). For IKONOS stereo images, the sensor physical parameters are derived from the satellite ephemeris and attitude data without using GCPs. The satellite ephemeris data are determined using on-board Global Positioning System (GPS) receivers and sophisticated ground processing of the GPS data. The satellite attitude is determined by optimally combining star tracker data with measurements taken by the on-board gyros. Since the IKONOS satellite imagery vendor, Space Imaging Company, has not released the satellite ephemeris data, no physical mathematical model can be established. This causes a major problem in the process of geo-positioning from KONOS stereo imagery with high precision. Therefore, some generalized generic mathematical models are needed to substitute the physical models for IKONOS imagery restitution (Hu et al., 2004).

This paper deals with the biases in the RPC mapping due to the errors in sensor orientation. The performance of bias-corrected image space, bias-corrected RPCs and bias-corrected object space will be further investigated with IKONOS stereo-pair imagery. The main objective is to find the best set of parameters with least number of GCPs for RFM refinement. The models described in this paper were implemented through a prototype software developed by the authors in a Matlab environment. In addition, 3D Affine and DLT models are also applied and their accuracies are investigated for 3D positioning, compared with traditional and modified RFM.

The steps for RFM refinement using IKONOS stereo-pair imagery are similar to that using other types of stereo satellite images, which consist of, shown in figure 1.

- Affixing a set of distinct ground control and check points in the overlap area of the test image pair. The coordinates of those points are determined precisely by using static GPS positioning technique.
- Measuring the image coordinates of affixed control points in each of the two images of the test pair.
- Extracting the RPCs provided with the metadata files associated with the test image pair.
- Performing least-squares adjustment involving the provided RPCs and measured image coordinates of control points based on RFM as a mathematical model to get estimated coordinates of the control points.
- Assessing the accuracy of provided RPCs by computing the differences among measured and estimated coordinates of control points.
- Modelling biases are provided in RPCs by adding parameters to the traditional RFM , using different setups and different control configurations.
- Resolving the modified versions of RFM using least-squares method to get estimates for the added parameters associated with each version.
- Assessing the accuracy of modified RFM associated with each version by computing the differences among measured values of check points and their corresponding values estimated by the modified RFM.

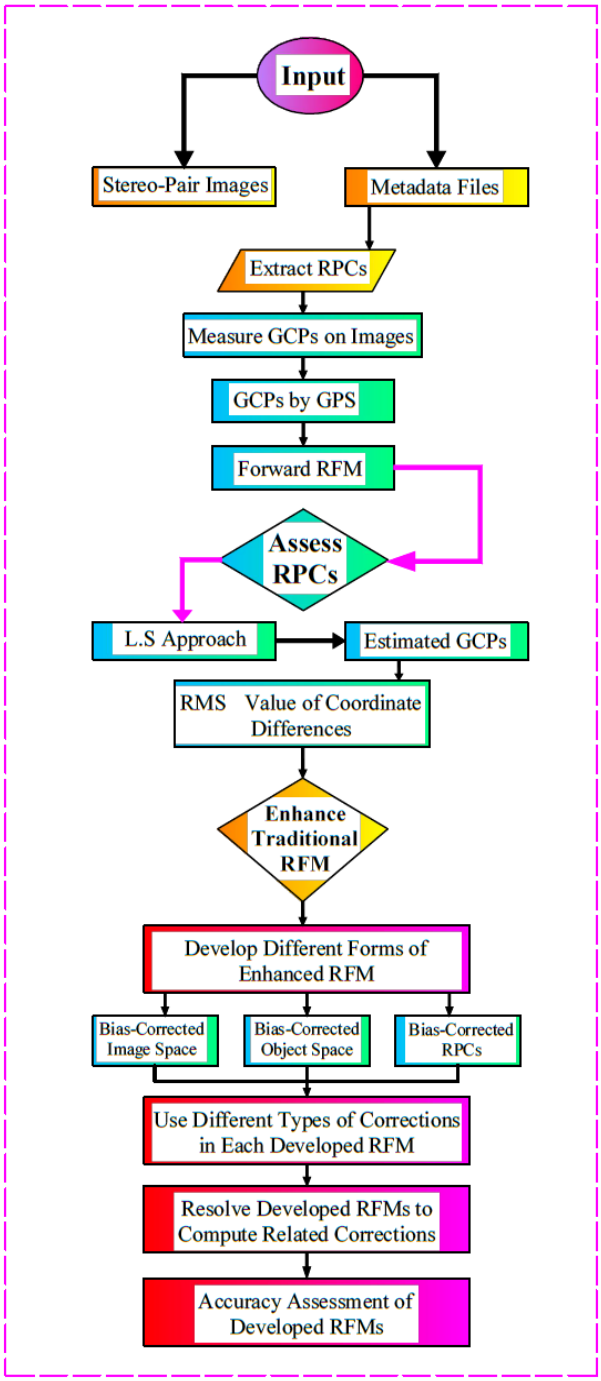

Figure 1: The strategy of developing the RF model

2. Mathematical models

2.1 Rational Function Model (RFM)

The RFM is one of the generic models that uses a ratio of two polynomial functions to compute the x and y coordinate in the image. The validation of this model has been tested in several researches with aerial photography data and satellite imageries (Tao et al., 2000). It takes the following general form (OGC, 1999):

$$l_n = \frac{\mathrm{P}_1\left(\mathrm{X_n}, \mathrm{Y_n}, \mathrm{Z_n}\right)}{\mathrm{P}_2\left(\mathrm{X_n}, \mathrm{Y_n}, \mathrm{Z_n}\right)} = \frac{\sum_{i=0}^{m_1}\sum_{j=0}^{m_2}\sum_{k=0}^{m_3} a_{\mathrm{ijk}} \mathrm{X}_n^i \mathrm{Y}_n^j \mathrm{Z}_n^k}{\sum_{i=0}^{n_1}\sum_{j=0}^{n_2}\sum_{k=0}^{n_3} b_{\mathrm{ijk}} \mathrm{X}_n^i \mathrm{Y}_n^j \mathrm{Z}_n^k}$$

$$s_n = \frac{\mathrm{P}_3\left(\mathrm{X_n}, \mathrm{Y_n}, \mathrm{Z_n}\right)}{\mathrm{P}_4\left(\mathrm{X_n}, \mathrm{Y_n}, \mathrm{Z_n}\right)} = \frac{\sum_{i=0}^{m_1}\sum_{j=0}^{m_2}\sum_{k=0}^{m_3} c_{\mathrm{ijk}} \mathrm{X}_n^i \mathrm{Y}_n^j \mathrm{Z}_n^k}{\sum_{i=0}^{n_1}\sum_{j=0}^{n_2}\sum_{k=0}^{n_3} d_{\mathrm{ijk}} \mathrm{X}_n^i \mathrm{Y}_n^j \mathrm{Z}_n^k} \quad (1)$$

Polynomial functions included in the model can be expressed as:

$$\begin{aligned}
\mathrm{P}_1\left(\mathrm{X_n}, \mathrm{Y_n}, \mathrm{Z_n}\right) &= a_0 + a_1 X_n + a_2 Y_n + a_3 Z_n + \ldots + a_{19} Z_n^3 \\
\mathrm{P}_2\left(\mathrm{X_n}, \mathrm{Y_n}, \mathrm{Z_n}\right) &= b_0 + \mathrm{b}_1 X_n + \mathrm{b}_2 Y_n + \mathrm{b}_3 Z_n + \ldots + \mathrm{b}_{19} Z_n^3 \\
\mathrm{P}_3\left(\mathrm{X_n}, \mathrm{Y_n}, \mathrm{Z_n}\right) &= c_0 + \mathrm{c}_1 X_n + \mathrm{c}_2 Y_n + \mathrm{c}_3 Z_n + \ldots + \mathrm{c}_{19} Z_n^3 \\
\mathrm{P}_4\left(\mathrm{X_n}, \mathrm{Y_n}, \mathrm{Z_n}\right) &= d_0 + \mathrm{d}_1 X_n + \mathrm{d}_2 Y_n + \mathrm{d}_3 Z_n + \ldots + \mathrm{d}_{19} Z_n^3
\end{aligned} \quad (2)$$

Where:

l_n, *and* s_n are the normalized line and sample coordinates in the image space. X_n,, Y_n, and Z_n are the normalized geodetic longitude, latitude and height in the object space. a_i, b_i, c_i *and* d_i are the polynomial coefficients RPCs (Total of 80). i, j and k are the increment values. m_1, m_2, m_3, n_1, n_2, n_3: are the order of the polynomial model (0-3), where $\mathrm{i} + \mathrm{j} + \mathrm{k} \leq 3$. The normalization of the coordinates is computed by (OGC, 1999):

$$l_n = \frac{\mathrm{Line} - \mathrm{Line\_OFF}}{\mathrm{Line\_Scale}} \; ; \; s_n = \frac{\mathrm{Sample} - \mathrm{Sample\_OFF}}{\mathrm{Sample\_Scale}} \quad (3)$$

$$\mathrm{X_n} = \frac{\lambda - \mathrm{Long\_OFF}}{\mathrm{Long\_Scale}} \; ; Y_n = \frac{\varphi - \mathrm{Lat\_OFF}}{\mathrm{Lat\_Scale}} \; ; \; \mathrm{Z_n} = \frac{h - \mathrm{Height\_OFF}}{\mathrm{Height\_Scale}}$$

Where Line and Sample are the image coordinates. Line_OFF and Sample_OFF are the offset values for the two image coordinates. Line_Scale and Sample_Scale are the scale factors for the two image coordinates. Similarly, $\boldsymbol{\varphi}$, $\boldsymbol{\lambda}$, and h are the geodetic latitude, longitude, and height in the object space. Lat_OFF, Long_OFF, and Height_OFF are the offset values for the three ground coordinates. Lat_Scale, Long_Scale, and Height_Scale are the corresponding scale factors.

2.1.1 3D-reconstruction using RFM

3D-reconstruction using various sensor models is one of the most important steps in accuracy assessment and enhancement of RPCs from IKONOS stereo-pair imagery. 3D-reconstruction could be achieved using the vendor-supplied RPCs. To assess the accuracy and bias distribution of the results using the raw RPCs, all the ground points (GPs) were used as check points (ChkPs). From the coordinates (l_n, s_n) in Equation (1), the following four equations can be derived for left (L) and right image (R):

$$\begin{aligned}
F_1 &= P_{1L}\left(\mathrm{X}_n, \mathrm{Y}_n, \mathrm{Z}_n\right) - l_{nL} P_{2L}\left(\mathrm{X}_n, \mathrm{Y}_n, \mathrm{Z}_n\right) = 0 \\
F_2 &= P_{3L}\left(\mathrm{X}_n, \mathrm{Y}_n, \mathrm{Z}_n\right) - s_{nL} P_{4L}\left(\mathrm{X}_n, \mathrm{Y}_n, \mathrm{Z}_n\right) = 0 \\
F_3 &= P_{1R}\left(\mathrm{X}_n, \mathrm{Y}_n, \mathrm{Z}_n\right) - l_{nR} P_{2R}\left(\mathrm{X}_n, \mathrm{Y}_n, \mathrm{Z}_n\right) = 0 \\
F_4 &= P_{3R}\left(\mathrm{X}_n, \mathrm{Y}_n, \mathrm{Z}_n\right) - s_{nR} P_{4R}\left(\mathrm{X}_n, \mathrm{Y}_n, \mathrm{Z}_n\right) = 0
\end{aligned} \quad (4)$$

Because of non-linearity of the equation and by applying the Taylor series expansion, the following equations are obtained (Grodecki et al., 2003):

$$\begin{aligned}
&\frac{\partial F_1}{\partial X_n}\Big|_0 dX_n + \frac{\partial F_1}{\partial Y_n}\Big|_0 dY_n + \frac{\partial F_1}{\partial Z_n}\Big|_0 dZ_n + \frac{\partial F_1}{\partial l_{nL}} V_{lnL} + \frac{\partial F_1}{\partial s_{nL}} V_{snL} = -F_1^0 \\
&\frac{\partial F_2}{\partial X_n}\Big|_0 dX_n + \frac{\partial F_2}{\partial Y_n}\Big|_0 dY_n + \frac{\partial F_2}{\partial Z_n}\Big|_0 dZ_n + \frac{\partial F_2}{\partial l_{nL}} V_{lnL} + \frac{\partial F_2}{\partial s_{nL}} V_{snL} = -F_2^0 \\
&\frac{\partial F_3}{\partial X_n}\Big|_0 dX_n + \frac{\partial F_3}{\partial Y_n}\Big|_0 dY_n + \frac{\partial F_3}{\partial Z_n}\Big|_0 dZ_n + \frac{\partial F_3}{\partial l_{nR}} V_{\mathrm{lnR}} + \frac{\partial F_3}{\partial s_{nR}} V_{snR} = -F_3^0 \\
&\frac{\partial F_4}{\partial X_n}\Big|_0 dX_n + \frac{\partial F_4}{\partial Y_n}\Big|_0 dY_n + \frac{\partial F_4}{\partial Z_n}\Big|_0 dZ_n + \frac{\partial F_4}{\partial l_{nR}} V_{\mathrm{lnR}} + \frac{\partial F_4}{\partial s_{nR}} V_{snR} = -F_4^0
\end{aligned} \quad (5)$$

The equations can be described in a matrix form as follow (Ghilani and Wolf, 2006).

$$AX + BV = K \quad (6)$$

$$\begin{bmatrix}
\frac{\partial F_{11}}{\partial X_n^1} & \frac{\partial F_{11}}{\partial Y_n^1} & \frac{\partial F_{11}}{\partial Z_n^1} & \ldots & 0 & 0 & 0 \\
\frac{\partial F_{21}}{\partial X_n^1} & \frac{\partial F_{21}}{\partial Y_n^1} & \frac{\partial F_{21}}{\partial Z_n^1} & \ldots & 0 & 0 & 0 \\
\frac{\partial F_{31}}{\partial X_n^1} & \frac{\partial F_{31}}{\partial Y_n^1} & \frac{\partial F_{31}}{\partial Z_n^1} & \ldots & 0 & 0 & 0 \\
\frac{\partial F_{41}}{\partial X_n^1} & \frac{\partial F_{41}}{\partial Y_n^1} & \frac{\partial F_{41}}{\partial Z_n^1} & \ldots & 0 & 0 & 0 \\
\ldots & & & \ldots & & & \\
\ldots & & & \ldots & & & \\
\ldots & & & \ldots & & & \\
\ldots & & & \ldots & & & \\
0 & 0 & 0 & \ldots & \frac{\partial F_{1N}}{\partial X_n^N} & \frac{\partial F_{1N}}{\partial Y_n^N} & \frac{\partial F_{1N}}{\partial Z_n^N} \\
0 & 0 & 0 & \ldots & \frac{\partial F_{2N}}{\partial X_n^N} & \frac{\partial F_{2N}}{\partial Y_n^N} & \frac{\partial F_{2N}}{\partial Z_n^N} \\
0 & 0 & 0 & \ldots & \frac{\partial F_{3N}}{\partial X_n^N} & \frac{\partial F_{3N}}{\partial Y_n^N} & \frac{\partial F_{3N}}{\partial Z_n^N} \\
0 & 0 & 0 & \ldots & \frac{\partial F_{4N}}{\partial X_n^N} & \frac{\partial F_{4N}}{\partial Y_n^N} & \frac{\partial F_{4N}}{\partial Z_n^N}
\end{bmatrix}
\begin{bmatrix} dX_n^1 \\ dY_n^1 \\ dZ_n^1 \\ \vdots \\ dX_n^N \\ dY_n^N \\ dZ_n^N \end{bmatrix} +
\begin{bmatrix}
\frac{\partial F_{11}}{\partial l_{nL}^1} & \frac{\partial F_{11}}{\partial s_{nL}^1} & 0 & 0 & \ldots \\
\frac{\partial F_{21}}{\partial l_{nL}^1} & \frac{\partial F_{21}}{\partial s_{nL}^1} & 0 & 0 & \ldots \\
0 & 0 & \frac{\partial F_{31}}{\partial l_{nR}^1} & \frac{\partial F_{31}}{\partial s_{nR}^1} & \ldots \\
0 & 0 & \frac{\partial F_{41}}{\partial l_{nR}^1} & \frac{\partial F_{41}}{\partial s_{nR}^1} & \ldots \\
 & & \ldots & & \\
 & & \ldots & & \\
 & & \ldots & & \\
 & & \ldots & & \\
\ldots & \frac{\partial F_{1N}}{\partial l_{nL}^N} & \frac{\partial F_{1N}}{\partial s_{nL}^N} & 0 & 0 \\
\ldots & \frac{\partial F_{2N}}{\partial l_{nL}^N} & \frac{\partial F_{2N}}{\partial s_{nL}^N} & 0 & 0 \\
\ldots & 0 & 0 & \frac{\partial F_{3N}}{\partial l_{nR}^N} & \frac{\partial F_{3N}}{\partial s_{nR}^N} \\
\ldots & 0 & 0 & \frac{\partial F_{4N}}{\partial l_{nR}^N} & \frac{\partial F_{4N}}{\partial s_{nR}^N}
\end{bmatrix}
\begin{bmatrix} V_{\mathrm{ln}L}^1 \\ V_{snL}^1 \\ V_{\mathrm{ln}R}^1 \\ V_{snR}^1 \\ \vdots \\ V_{\mathrm{ln}L}^N \\ V_{snL}^N \\ V_{\mathrm{ln}R}^N \\ V_{snR}^N \end{bmatrix} =
\begin{bmatrix} -F_{11}^0 \\ -F_{21}^0 \\ -F_{31}^0 \\ -F_{41}^0 \\ \vdots \\ -F_{1N}^0 \\ -F_{2N}^0 \\ -F_{3N}^0 \\ -F_{4N}^0 \end{bmatrix} \quad (7)$$

The partial derivatives can be calculated similar to what follows (Xu et al., 2005):

$$\frac{\partial F_1}{\partial X_n}\Big|_0 = (a_{1L} - l_{nL}b_{1L}) + (a_{4L} - l_{nL}b_{4L})Y_n + (a_{5L} - l_{nL}b_{5L})Z_n + 2(a_{7L} - l_{nL}b_{7L})X_n + (a_{10L} - l_{nL}b_{10L})Y_nZ_n + 3(a_{11L} - l_{nL}b_{11L})X_n^2 + (a_{12L} - l_{nL}b_{12L})Y_n^2 + (a_{13L} - l_{nL}b_{13L})Z_n^2 + 2(a_{14L} - l_{nL}b_{14L})X_nY_n + 2(a_{17L} - l_{nL}b_{17L})X_nZ_n \quad (8)$$

The full set of unknowns in Equation (7) can be resolved by using the least squares adjustment method as follow:

$$X = \left(A^T\left(BB^T\right)^{-1}A\right)^{-1}\left(A^T\left(BB^T\right)^{-1}K\right) \quad (9)$$

$$V = \left(B^T\left(BB^T\right)^{-1}\right)(K - AX) \quad (10)$$

Where A is a (4*No. of GPs) * (3*No. of GPs) matrix. X is a (3*No. of GPs)* (1) unknown vector. B is a matrix of observations (4*No. of GPs) * (4*No. of GPs). V is the vector of residual errors (4*No. of GPs)* (1). K is an (4*No. of GPs) * (1) Absolute vector. (No. of GPs) is the number of ground control points selected by the user. The unknown object space coordinates are solved for iteratively. At the first iteration, initial values for coordinates are needed, which could be determined through linear equations such as 3D-Affine or DLT model.

2.2 RPCs refinement methods

The RPCs may be refined directly or indirectly. Direct refining methods calculate the RPCs and thus requires a large number (more than 39) of GCPs for the 3rd order RFM, while indirect refining methods introduce complementary transformations in image or object space, and do not change the original RPCs directly (Hu et al., 2004). In this research, indirect method is adopted using three different approaches, as described in the following subsections.

2.2.1 Bias-corrected image space

This bias correction method proposes a polynomial model defined in image space, in which Δl and Δs are added to the rational functions to capture the differences between the nominal and the measured image space coordinates (Fraser and Hanley, 2003; Grodecki and Dial, 2003). The following equations provide the form of the refined RFM using first order polynomials transformation (Hanley and Fraser, 2004):

$$l + \Delta l = \frac{P_1(X_n, Y_n, Z_n)}{P_2(X_n, Y_n, Z_n)} * \text{Line\_Scale} + \text{Line\_OFF}$$

$$s + \Delta s = \frac{P_3(X_n, Y_n, Z_n)}{P_4(X_n, Y_n, Z_n)} * \text{Sample\_Scale} + \text{Sample\_OFF} \quad (11)$$

Where l and s are line and sample coordinates; Δl and Δs represent the differences between the measured and the calculated line and sample coordinates, which can be generally described as polynomials of the image line and sample coordinates as follows (Grodecki and Dial, 2003; Gong and Fritsch, 2016):

$$\Delta l = A_0 + A_1 l + A_2 s + A_3 l^2 + A_4 l.s + A_5 s^2 + \ldots$$

$$\Delta s = B_0 + B_1 l + B_2 s + B_3 l^2 + B_4 l.s + B_5 s^2 + \ldots \quad (12)$$

Where A_i and B_i (i = 1, 2, 3, …) are the correction parameters. By using affine transformation, sub-pixel accuracy can be obtained (Fraser and Hanley, 2003. However, the method is effective only when the camera FOV is narrow and the position and attitude errors are small (Grodecki and Dial, 2003).

In view of the high-order dynamic characteristic of the IKONOS sensor, three comparative choices of correction parameters are tested in this research: 1) A_0, A_1, B_0, B_1 which models the shift and scale; 2) A_0, A_1, A_2, B_0, B_1, B_2 which models the bias using the entire transformation model; 3) $A_0 \approx A_5$, $B_0 \approx B_5$ which models the bias using second-order polynomials. This model is used to check whether distinct high order errors exist in IKONOS imaging orientation.

With an adequate provision of GCPs, the correction parameters are estimated by using the LSM. First, using the original vendor provided RPCs and measured object coordinates of control points based on RFM as a mathematical model to get the calculated image space (l_c, s_c) potentially containing inherent biases. The calculated image coordinates are compared with the measured image coordinates (l_m, s_m) to obtain the residuals (Δl, Δs). After that, the correction parameters are further computed based on the discrepancies on all the image control points using the LSM. For clarity, assume that 4 GCPs exist for the affine parameter estimation. The observation equations (AX + BV = K) can be described in a matrix form as follow;

$$\begin{bmatrix} \frac{\partial F_{11}}{\partial A_{0L}} & \frac{\partial F_{11}}{\partial A_{1L}} & \frac{\partial F_{11}}{\partial A_{2L}} & 0\ 0\ 0 \\ 0\ 0\ 0 & \frac{\partial F_{21}}{\partial B_{0L}} & \frac{\partial F_{21}}{\partial B_{1L}} & \frac{\partial F_{21}}{\partial B_{2L}} \\ \frac{\partial F_{12}}{\partial A_{0L}} & \frac{\partial F_{12}}{\partial A_{1L}} & \frac{\partial F_{12}}{\partial A_{2L}} & 0\ 0\ 0 \\ 0\ 0\ 0 & \frac{\partial F_{22}}{\partial B_{0L}} & \frac{\partial F_{22}}{\partial B_{1L}} & \frac{\partial F_{22}}{\partial B_{2L}} \\ \frac{\partial F_{13}}{\partial A_{0L}} & \frac{\partial F_{13}}{\partial A_{1L}} & \frac{\partial F_{13}}{\partial A_{2L}} & 0\ 0\ 0 \\ 0\ 0\ 0 & \frac{\partial F_{23}}{\partial B_{0L}} & \frac{\partial F_{23}}{\partial B_{1L}} & \frac{\partial F_{23}}{\partial B_{2L}} \end{bmatrix} \begin{bmatrix} A_{0L} \\ A_{1L} \\ A_{2L} \\ B_{0L} \\ B_{1L} \\ B_{2L} \end{bmatrix} + \begin{bmatrix} \frac{\partial F_{11}}{\partial l_{nL}^1} & 0 & 0 & 0 & 0 & 0 \\ 0 & \frac{\partial F_{21}}{\partial s_{nL}^1} & 0 & 0 & 0 & 0 \\ 0 & 0 & \frac{\partial F_{12}}{\partial l_{nL}^2} & 0 & 0 & 0 \\ 0 & 0 & 0 & \frac{\partial F_{22}}{\partial s_{nL}^2} & 0 & 0 \\ 0 & 0 & 0 & 0 & \frac{\partial F_{13}}{\partial l_{nL}^3} & 0 \\ 0 & 0 & 0 & 0 & 0 & \frac{\partial F_{23}}{\partial s_{nL}^3} \end{bmatrix} \begin{bmatrix} V_{\ln L}^1 \\ V_{\text{sn}L}^1 \\ V_{\ln L}^2 \\ V_{\text{sn}L}^2 \\ V_{\ln L}^3 \\ V_{\text{sn}L}^3 \end{bmatrix} = \begin{bmatrix} -F_{11}^0 \\ -F_{21}^0 \\ -F_{12}^0 \\ -F_{22}^0 \\ -F_{13}^0 \\ -F_{23}^0 \end{bmatrix} \quad (13)$$

The six affine parameters in Equation (12) can be resolved by using the LSM, described in Equation (9). If the shift and scale bias [A_0, A_1, B_0, *and* $B1$] are the only factors taken into account, the correction can be made by improving the original RPCs. As detailed in Fraser and Hanley (2003 and 2005), only the parameters in numerator need to be updated, and the refined RPC model becomes:

$$l_n = \frac{(a_0 - b_0\Delta l_n) + (a_1 - b_1\Delta l_n)X_n + \ldots + (a_{19} - b_{19}\Delta l_n)Z_n^3}{P_2(X_n, Y_n, Z_n)}$$

$$s_n = \frac{(c_0 - d_0\Delta s_n) + (c_1 - d_1\Delta s_n)X_n + \ldots + (c_{19} - d_{19}\Delta s_n)Z_n^3}{P_4(X_n, Y_n, Z_n)} \quad (14)$$

Where a_i, b_i, c_i, and d_i are the original vendor-provided RPCs, Δl_n and Δs_n are the normalized values of the image shift and scale bias parameters Δl and Δs.

Effectively, all original terms in the numerator of each expression in Equation (11) are modified; each coefficient a_i is replaced by $(a_i - b_i\ \Delta l_n)$. In this way, the vendor-supplied RPCs can be replaced using the method mentioned above. The bias inside the initial RPCs could be corrected. This would be much more convenient for some digital photogrammetric software packages such as IMAGINE Photogrammetry, which only support the use of RPCs to do the 3D-reconstruction of IKONOS imagery (Xu et al., 2005). Figure 2 shows the 3D-reconstruction steps when using updated RPCs:

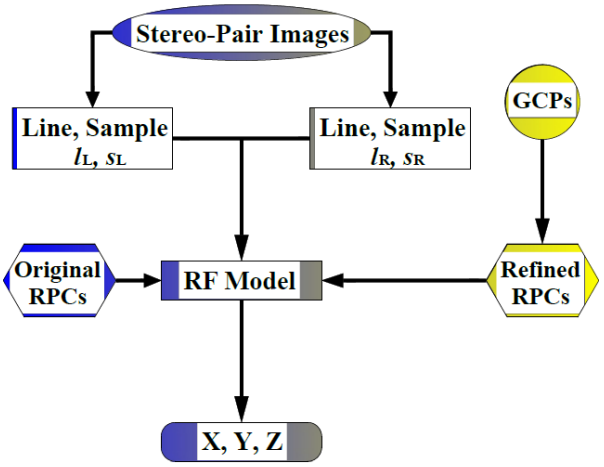

Figure 2: Steps of 3D-reconstruction using updated RPCs

2.2.2 Bias-corrected RPCs

This approach is implemented by adding a set of new adjustable functions ΔN (numerator coefficient) and ΔD (denominator coefficient) for both line and sample equations based on the known GCPs to correct the RPCs (Singh et al., 2008). The new adjustable functions can be defined as follows:

$$l_n = \frac{P_1(X_n, Y_n, Z_n) + \Delta P_1}{P_2(X_n, Y_n, Z_n) + \Delta P_2}$$

$$s_n = \frac{P_3(X_n, Y_n, Z_n) + \Delta P_3}{P_4(X_n, Y_n, Z_n) + \Delta P_4} \quad (15)$$

ΔP_1, ΔP_2, ΔP_3, and ΔP_4 are the differences between the original and the adjustable, which can be generally described as (Singh et al., 2008):

$$\begin{aligned}
\Delta P_1 &= A_0 + A_1 X_n + A_2 Y_n + A_3 Z_n + \ldots + A_{19} Z_n^3 \\
\Delta P_2 &= B_0 + B_1 X_n + B_2 Y_n + B_3 Z_n + \ldots + B_{19} Z_n^3 \\
\Delta P_3 &= C_0 + C_1 X_n + C_2 Y_n + C_3 Z_n + \ldots + C_{19} Z_n^3 \\
\Delta P_4 &= D_0 + D_1 X_n + D_2 Y_n + D_3 Z_n + \ldots + D_{19} Z_n^3
\end{aligned} \quad (16)$$

A_i, B_i, C_i and D_i are the correction parameters in the correction model. The resulted estimates of correction parameters are added to the original coefficients to get refined RPCs. The correction parameters are further computed based on the control points using the LSM. For clarity, assume that 3 GCPs are used for estimation of the shift parameters (A_0, B_0, C_0, and D_0) for both left and right images. As a result, 12 observation equations in 8 unknowns are yielded. They can be described as in Equation (17). The unknown shift parameters can be resolved by using the LSM, utilizing Equation (9).

$$\begin{bmatrix}
\frac{\partial F_{11}}{\partial A_{0L}} & \frac{\partial F_{11}}{\partial B_{0L}} & 0 & 0 & 0 & 0 & 0 & 0 \\
0 & 0 & \frac{\partial F_{21}}{\partial C_{0L}} & \frac{\partial F_{21}}{\partial D_{0L}} & 0 & 0 & 0 & 0 \\
0 & 0 & 0 & 0 & \frac{\partial F_{31}}{\partial A_{0R}} & \frac{\partial F_{31}}{\partial B_{0R}} & 0 & 0 \\
0 & 0 & 0 & 0 & 0 & 0 & \frac{\partial F_{41}}{\partial C_{0R}} & \frac{\partial F_{41}}{\partial D_{0R}} \\
\frac{\partial F_{12}}{\partial A_{0L}} & \frac{\partial F_{12}}{\partial B_{0L}} & 0 & 0 & 0 & 0 & 0 & 0 \\
0 & 0 & \frac{\partial F_{22}}{\partial C_{0L}} & \frac{\partial F_{22}}{\partial D_{0L}} & 0 & 0 & 0 & 0 \\
0 & 0 & 0 & 0 & \frac{\partial F_{32}}{\partial A_{0R}} & \frac{\partial F_{32}}{\partial B_{0R}} & 0 & 0 \\
0 & 0 & 0 & 0 & 0 & 0 & \frac{\partial F_{42}}{\partial C_{0R}} & \frac{\partial F_{42}}{\partial D_{0R}} \\
\frac{\partial F_{13}}{\partial A_{0L}} & \frac{\partial F_{13}}{\partial B_{0L}} & 0 & 0 & 0 & 0 & 0 & 0 \\
0 & 0 & \frac{\partial F_{23}}{\partial C_{0L}} & \frac{\partial F_{23}}{\partial D_{0L}} & 0 & 0 & 0 & 0 \\
0 & 0 & 0 & 0 & \frac{\partial F_{33}}{\partial A_{0R}} & \frac{\partial F_{33}}{\partial B_{0R}} & 0 & 0 \\
0 & 0 & 0 & 0 & 0 & 0 & \frac{\partial F_{43}}{\partial C_{0R}} & \frac{\partial F_{43}}{\partial D_{0R}}
\end{bmatrix}
\begin{bmatrix} A_{0L} \\ B_{0L} \\ C_{0L} \\ D_{0L} \\ A_{0R} \\ B_{0R} \\ C_{0R} \\ D_{0R} \end{bmatrix}
+
\begin{bmatrix}
\frac{\partial F_{11}}{\partial l_{nL}^1} & 0 & 0 & 0 & 0 & 0 & 0 & 0 & 0 & 0 \\
0 & \frac{\partial F_{21}}{\partial s_{nL}^1} & 0 & 0 & 0 & 0 & 0 & 0 & 0 & 0 \\
0 & 0 & \frac{\partial F_{31}}{\partial l_{nR}^1} & 0 & 0 & 0 & 0 & 0 & 0 & 0 \\
0 & 0 & 0 & \frac{\partial F_{41}}{\partial s_{nR}^1} & 0 & 0 & 0 & 0 & 0 & 0 \\
0 & 0 & 0 & 0 & \frac{\partial F_{12}}{\partial l_{nL}^2} & 0 & 0 & 0 & 0 & 0 \\
0 & 0 & 0 & 0 & 0 & \frac{\partial F_{22}}{\partial s_{nL}^2} & 0 & 0 & 0 & 0 \\
0 & 0 & 0 & 0 & 0 & 0 & \frac{\partial F_{32}}{\partial l_{nR}^2} & 0 & 0 & 0 \\
0 & 0 & 0 & 0 & 0 & 0 & 0 & \frac{\partial F_{42}}{\partial s_{nR}^2} & 0 & 0 \\
0 & 0 & 0 & 0 & 0 & 0 & 0 & 0 & \frac{\partial F_{13}}{\partial l_{nL}^3} & 0 \\
0 & 0 & 0 & 0 & 0 & 0 & 0 & 0 & 0 & \frac{\partial F_{23}}{\partial s_{nL}^3} \\
0 & 0 & 0 & 0 & 0 & 0 & 0 & 0 & \frac{\partial F_{33}}{\partial l_{nR}^3} & 0 \\
0 & 0 & 0 & 0 & 0 & 0 & 0 & 0 & 0 & \frac{\partial F_{43}}{\partial s_{nR}^3}
\end{bmatrix}
\begin{bmatrix}
V_{lnL}^1 \\ V_{snL}^1 \\ V_{lnR}^1 \\ V_{snR}^1 \\ V_{lnL}^2 \\ V_{snL}^2 \\ V_{lnR}^2 \\ V_{snR}^2 \\ V_{lnL}^3 \\ V_{snL}^3 \\ V_{lnR}^3 \\ V_{snR}^3
\end{bmatrix}
=
\begin{bmatrix}
-F_{11}^0 \\ -F_{21}^0 \\ -F_{31}^0 \\ -F_{41}^0 \\ -F_{12}^0 \\ -F_{22}^0 \\ -F_{32}^0 \\ -F_{42}^0 \\ -F_{13}^0 \\ -F_{23}^0 \\ -F_{33}^0 \\ -F_{43}^0
\end{bmatrix}^a \quad (17)$$

Where 1, 2, and 3 in a matrix form are the number of control points.

2.2.3 Bias-corrected ground space

A polynomial model defined in the domain of object space to correct the ground coordinates derived from the vendor-provided RPCs as in Equation (18) (Di et al., 2003; Zhen Xiong and Yun Zhang, 2009). In this method, the polynomial correction parameters are determined by the GCPs as follows:

$$\begin{aligned}
X^{GPS} &= a_0 + a_1 X^{RF} + a_2 Y^{RF} + a_3 Z^{RF} \\
Y^{GPS} &= b_0 + b_1 X^{RF} + b_2 Y^{RF} + b_3 Z^{RF} \\
Z^{GPS} &= c_0 + c_1 X^{RF} + c_2 Y^{RF} + c_3 Z^{RF}
\end{aligned} \quad (18)$$

Where X^{GPS}, Y^{GPS}, Z^{GPS} are the observed ground coordinates; X^{RF}, Y^{RF}, Z^{RF} are the ground coordinates derived from the RPC; and a_i, b_i, c_i are the correction parameters.

2.3 Affine model

Since 2D Polynomial models do not take into account the heights of the GCPs, these models can be efficiently used when the image is not influenced by the topographic effects. In this case, low order polynomials can provide accurate results. The model can be represented as follow:

$$x = a_0 + a_1X + a_2Y$$
$$y = b_0 + b_1X + b_2Y \quad (19)$$

Where x, y are the image coordinates; X, Y are the 2D ground coordinates; and a_0, a_1, a_2, b_0, b_1, b_2 are polynomial coefficients. Some studies have shown that the use of low-order polynomial 3D models for images of hilly and mountainous areas can reach the accuracy level that is close to the rigorous models (Fraser et al., 1999). A typical formula can be expressed as follow:

$$x = a_0 + a_1X + a_2Y + a_3Z + a_4XY + a_5YZ + a_6XZ$$
$$y = b_0 + b_1X + b_2Y + b_3Z + b_4XY + b_5YZ + b_6XZ \quad (20)$$

Where X, Y, Z are the 3D ground coordinates.

2.4 Direct Linear Transformation (DLT) model

The DLT model was developed by Abdel Aziz and Karara (1971) for close range photogrammetry applications and can also be used for image rectification (Vincent and Yong, 2000). The DLT represents a special case of the RF Model, with first degree polynomials and common denominators:

$$x = \frac{L_1X + L_2Y + L_3Z + L_4}{L_9X + L_{10}Y + L_{11}Z + 1}$$
$$y = \frac{L_5X + L_6Y + L_7Z + L_8}{L_9X + L_{10}Y + L_{11}Z + 1} \quad (21)$$

Where x, y are the image coordinates; X, Y, Z are the ground coordinates; and L_1, L_2, L_3, L_4, L_5, L_6, L_7, L_8, L_9, L_{10} and L_{11} are polynomial coefficients.

3. Study area and dataset

A Pan-sharpened stereo pair of IKONOS imagery, for an area in the *north of Khartoum in Sudan* about 16 km north of *Omdurman city* is obtained by the Edge Pro Company. The study area covers almost 5.8 km x 5.3 km. It includes various topographic features, urban area, hilly terrain and a part of *Wadi Sayidna Air Base* as shown in figure 3. It was the first stereo pair of IKONOS images acquired over Sudan in December 27, 2003. The data are delivered in Geo-Tiff format with text files containing the rational polynomial coefficients (RPCs) for each image. Table 1 shows the main parameters of the stereo-pairs.

A set of 21 well-identified and well distributed points on the images were selected. Mostly corners of buildings and fences/walls as well as road intersections were selected and surveyed using GPS in a static mode with about 5 mm accuracy. Leica Geo-office software was used to process the data with survey positions being referenced to the UTM/WGS84 zone 36N. Corresponding image coordinates on both the left and right image of the stereo-pair were measured in the IMAGINE photogrammetry software. Figure 4 shows the distribution of the GPS points; GCP environment in red and ChkPs in green.

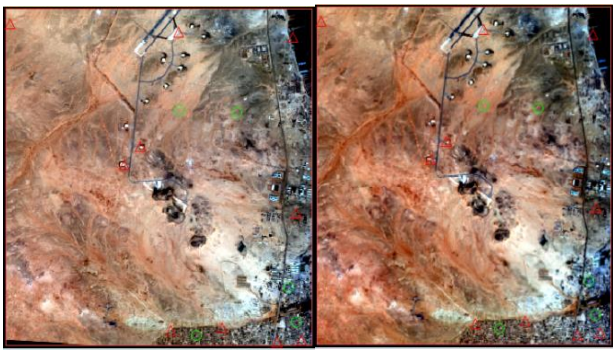

Figure 3: Stereo IKONOS image for the study area

Table 1: Main parameters of the available IKONOS HRSI 1 m stereo-pair

Acquisition Date / Time	08:41 GMT 27-12-2003 and 08:42 GMT 27-12-2003
Sun Angle Azimuth	156.1241 and156.3809 degrees
Sun Angle Elevation	63.50707 and 47.50945 degrees
Overlap	99%
Rows	5893 and 6004 pixels
Columns	5351 and 5357 pixels
Pixel Size	1.000 meters
Percent Component Cloud Cover	0

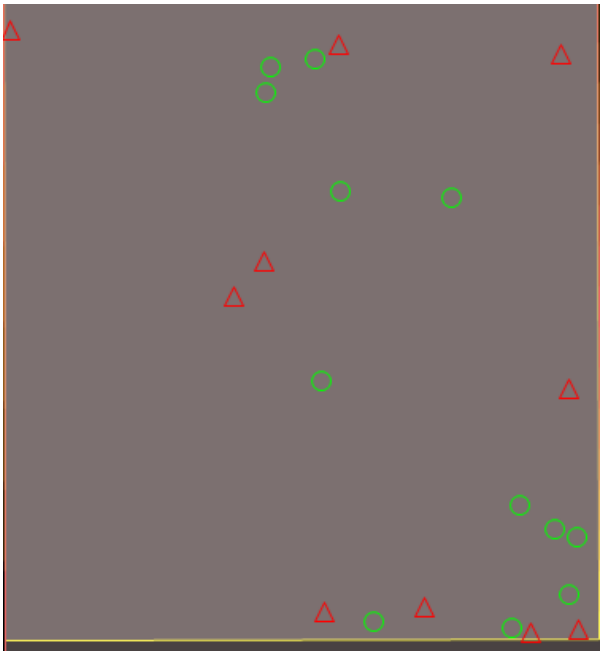

Figure 4: GCPs and ChkPs distribution

4. Results and analysis

Several experiments were performed to apply the described mathematical models. Before testing and evaluating those models, the accuracy of the acquired IKONOS images was checked by locating the twenty one GCPs on the images, estimating their ground coordinates using RFM and comparing estimated coordinates to known coordinates. The results show that the RMS value of differences in X, Y and Z were 7.2 m, 3.1 m, and 16.7 m respectively.

4.1 Performance evaluation of RFM

In the first experiment, the 3D-reconstruction has been achieved using the vendor-supplied RPCs. To assess the accuracy and bias distribution of the results using the raw RPCs, all the 21 ground points were used as ChkPs. The RMS value of differences between known and estimated coordinates were calculated and listed in table 2 which significantly indicate the existence of large shift bias. Figure 5 shows the planimetric and vertical accuracies at ChkPs based on vendor-supplied RPCs and figure 6 shows bias vectors of left and right image at the same points.

Table 2: RMS value for ChkPs using RPCs without GCPs

Statistic	RMS of check points coordinate differences (meters)		
	ΔX	ΔY	ΔZ
RMS	7.2	3.1	16.7

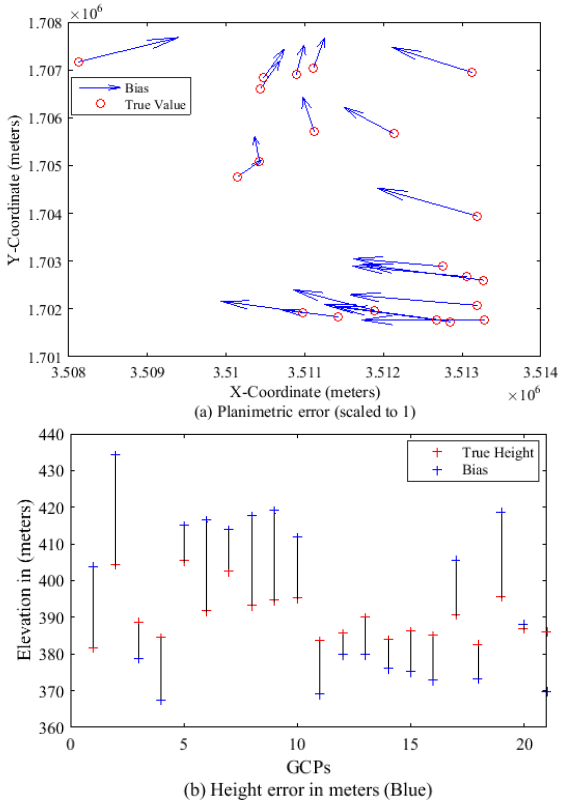

Figure 5: Bias vectors of (a) planimetry and (b) elevation at ChkPs based on vendor-supplied RPCs

4.2 Bias-corrected image space

The refined RFM in image space was applied using the IKONOS stereo images. Tables 3, 4 and 5 list the RMS value for the 18 ChkPs in the object space, which implement the refined model with polynomial transformation and different numbers of GCPs. Compared with the case without any GCPs, the results are significantly improved. It is clear that increasing the GCPs from 3 to 17 points does not improve much the accuracy. Therefore, five control points were sufficient to compensate for the shift and scale bias correction. Detailed discussions on the result of each correction model are given below:

4.2.1 Modelling with shift and scale

In shift and scale bias correction with all GCPs being employed (A_0, A_1, B_0, B_1), the biases in the object space are listed in table 3. To be more circumspect, the 1st order and 2nd order polynomials for the bias correction were further examined.

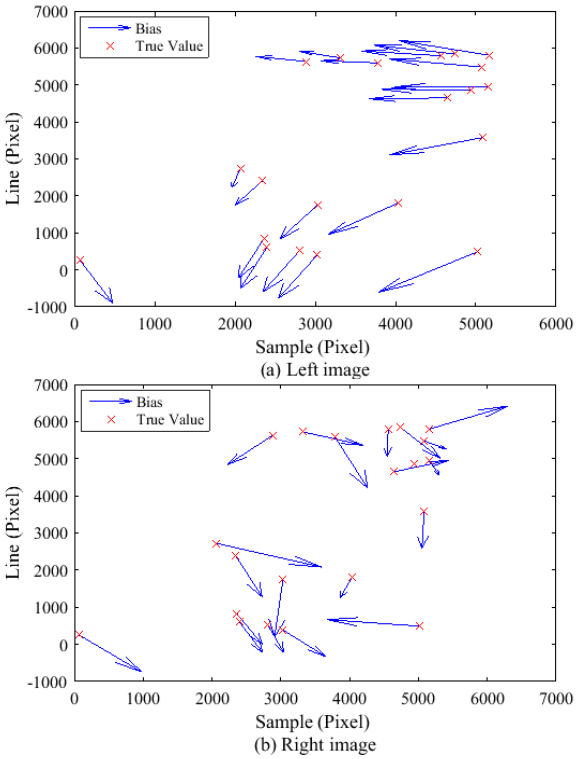

Figure 6: Bias vectors of (a) left and (b) right image at ChkPs, calculated using vendor-supplied RPCs

Table 3: RMS value of ChkPs using different selection of GCPs with shift and scale bias correction model

No. of GCPs/ChkPs	RMS of check points coordinate differences (meters)		
	X	Y	Z
3/18	2.4	1.0	1.2
5/16	0.9	1.0	1.6
7/14	0.9	0.9	1.7
9/12	1.0	1.0	1.8
13/8	0.3	1.0	1.5
15/6	0.3	0.6	1.5
17/4	0.3	0.6	1.2

4.2.2 Modelling with 1st order polynomial

In this experiment, with A_0, A_1, A_2, B_0, B_1, and B_2 unknown parameters, the regenerated RPCs were found to be of slightly higher quality which indicates that there was a little additional distortion error absorbed by scale parameters. With a minimum of five GCPs, an accuracy of 0.8 m in X, 1.2 m in Y and 1.3 m in height has been achieved. The biases in the ground space are listed in table 4.

Table 4: RMS value of ChkPs using different selection of GCPs with 1st order bias correction model

No. of GCPs/ChkPs	RMS of check points coordinate differences (meters)		
	X	Y	Z
5/16	0.8	1.2	1.3
7/14	0.8	1.1	1.5
9/12	0.8	1.2	1.6
13/8	0.2	1.2	1.2
15/6	0.2	1.0	1.2
17/4	0.2	0.9	0.9

4.2.3 Modelling with 2nd order polynomial

To further test the effect of the GCPs distribution and parameters selection ($A_0 \approx A_5$, $B_0 \approx B_5$), seven GCPs were used to calculate the bias coefficients. In this case, one redundant point is available, which will make the calculation more reliable. From table 5, the results generated under the control of seven GCPs show some differences from their counter parts in tables 3 and 4. Results in this test are of slightly lower quality than the former two tests. Consequently, only few GCPs are needed in the bias correction in the image space.

Table 5: RMS value of ChkPs using different selection of GCPs with 2nd order bias correction model

No. of GCPs/ChkPs	RMS of check points coordinate differences (meters)		
	X	Y	Z
7/14	1.2	1.3	2.1
9/12	1.2	1.5	2.2
13/8	0.4	1.3	1.5
15/6	0.3	1.1	1.3
17/4	0.2	1.2	1.0

4.3 Bias-corrected RPCs

The third experiment was to improve the geo-location accuracy of IKONOS stereo-pair in the object space based on the bias corrected RPCs with different bias correction models and different control configurations. In this regard, the bias correction parameters were first estimated by using the LSM with the GCPs, and the bias-corrected RPCs were subsequently obtained through the RPC modification. Afterwards, the geo-location accuracies with the refined RPCs were estimated by calculating the ChkPs biases on the ground through space intersection. Detailed discussions on the result of each correction model are given below.

4.3.1 Modelling with one parameter

The assessment for orientation using one parameter (A_0, B_0, C_0, and D_0) offers a simple way to improve the geo-location accuracy. The results in table 6 indicate that when the shift-bias was removed through RPCs modification with only three GCPs, the accuracy of ground point determination was greatly improved from the 7.2 m to 2.3 m in X, 3.1 m to 1.0 in Y and from 16.7 m to 1.2 m in height. However, additional GCPs contributed to the improvement of the planimetric accuracy. When the 17 GCPs were employed, the overall metric potential was 0.7 m in planimetry and about 1.2 m in height. Figure 7 is a typical example shows both the planimetric and height error based on 3 GCPs. As well, figure 9 indicates that the planimetric and vertical accuracies of the refined RPCs with a single parameter are accurate and stable. Under such an observation, the planimetric accuracy of the refined RPC is around one meter when using 13 to 17 GCPs. On the other hand, the vertical accuracy with 3 GCPs was 1.2 meter with IKONOS data and it remains the same when 17 GCPs were used.

Table 6: RMS value of ChkPs using different selection of GCPs with one parameter bias correction model

No. of GCPs/ChkPs	RMS of check points coordinate differences (meters)		
	X	Y	Z
3/18	2.3	1.0	1.2
5/16	0.9	1.0	1.6
7/14	0.8	0.9	1.7
9/12	0.9	1.0	1.8
13/8	0.3	1.0	1.5
15/6	0.3	0.6	1.5
17/4	0.3	0.6	1.2

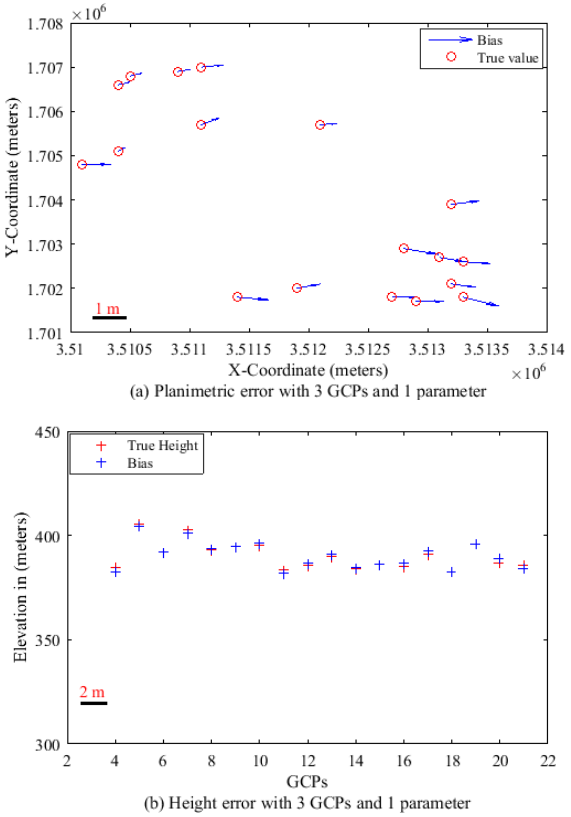

Figure 7: Bias errors of (a) planimetry and (b) height at ChkPs using 3 GCPs and 1 parameter

4.3.2 Modelling with two parameters

To further test the effect of the GCP configuration, five GCPs were used to calculate the eight coefficients, A_0, A_1, B_0, B_1, C_0, C_1, D_0, and D_1. By using these five GCPs, one redundant point is available. From figure 8 and the RMS value on the ChkPs listed in table 7, it is clear that the use of five GCPs could also achieve very good results in bias removing. The RMS values are of the same order of magnitude as in the case of using three GCPs. Figure 9

shows the planimetric and vertical accuracies of the refined RPCs with only two parameters. In essence, 1.4 meter was the observed vertical accuracy when using five GCPs and 0.9 meter was achieved with 17 GCPs, which is not quite significant when compared with the results of the initial case. On the other hand, the planimetric accuracy yields 1.8 meter with 5 GCPs and 1.1 meter with 17 GCPs.

Table 7: RMS value of ChkPs using different selection of GCPs with two parameters bias correction model

No. of GCPs/ChkPs	RMS of check points coordinate differences (meters)		
	X	Y	Z
5/16	1.2	1.4	1.4
7/14	0.6	1.3	1.6
9/12	0.7	1.4	1.7
13/8	0.2	1.3	1.3
15/6	0.2	1.1	1.2
17/4	0.2	1.1	0.9

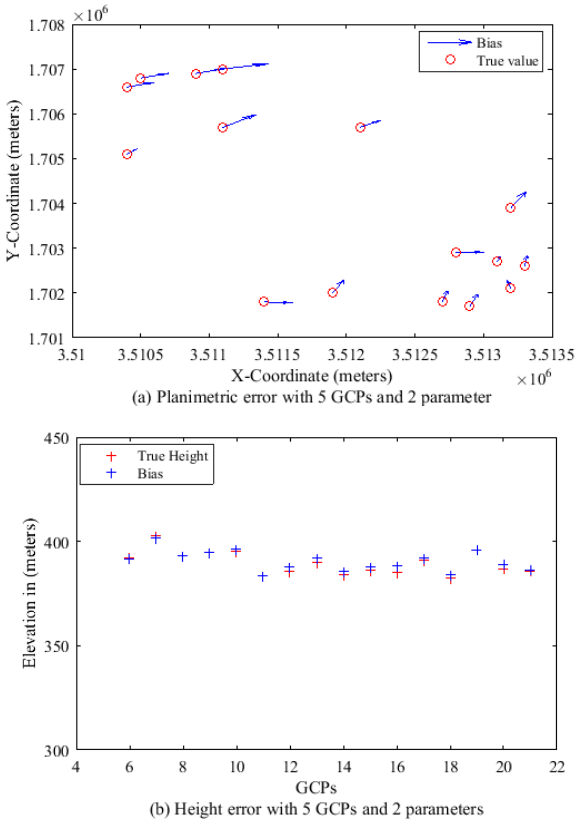

Figure 8: Error vectors in (a) planimetry and (b) height of ChkPs using 5 GCPs and 2 parameters

In the bias corrected RPCs, it was found that the results are getting worse with more parameters (modelling with three and four parameters).

4.4 Bias-corrected object space

The objective is to find out in which domain the bias compensation could achieve a better result with different bias correction models and different control information. For each model in object space, RFM based triangulation (Di et al., 2003; X. Niu et al., 2004) is applied to calculate the ground coordinates (X^{RF}, Y^{RF}, Z^{RF}). Since the GPS coordinates (X^{GPS}, Y^{GPS}, Z^{GPS}) are known, three equations can be established in accordance with the model equations in subsection (2.2.3). Using all available GCPs, over-determined equation systems can be setup to compute the optimal estimates of the transformation parameters by a LSM. The transformation parameters can be used to compute the improved coordinates of other points. ChkPs are used to assess the appropriateness of the models. RMS value of each model is calculated based on differences between RFM derived and known coordinates of the ChkPs.

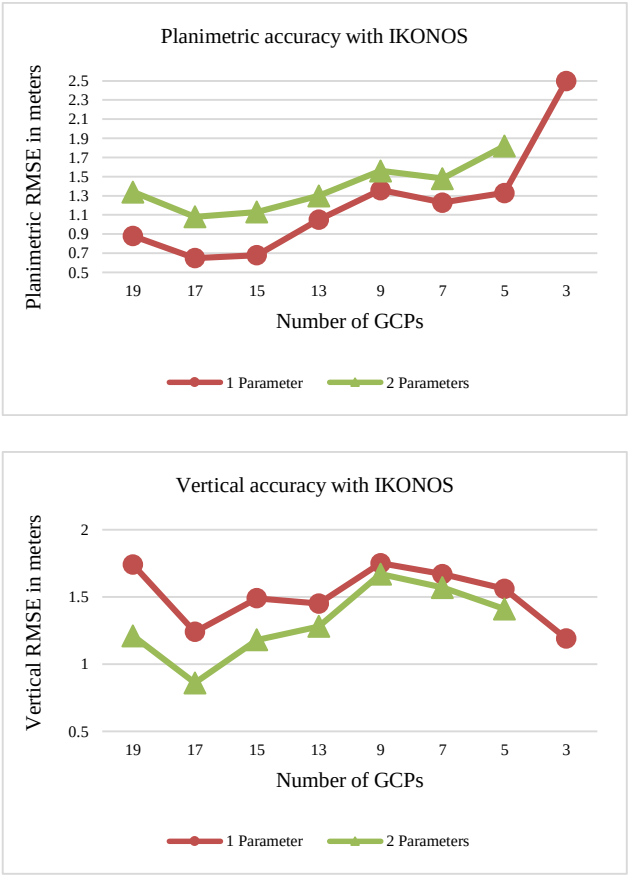

Figure 9: Planimetric and vertical accuracy of object coordinates

The shift parameters (a_0, b_0, c_0) and three additional scale factors (a_1, b_1, c_1) have been applied to correct for non-homogeneous scale distortions. Minimum of two GCPs are required. An affine and a 2nd order polynomial transformation are applied to the second and third models, respectively.

Additional GCPs are then added to improve accuracy. Different combinations of the number and configuration of GCPs are also tested to determine the effectiveness of different distributions. Tables 8, 9 and 10 show improvements in accuracy achieved by the three different models performed in the object space for IKONOS stereo-pair imagery. A discussion of the results of each model is given below.

4.4.1 Modelling with shift and scale

The scale and shift model has additional scaling factors in the coordinate axis directions (a_0, b_0, c_0, a_1, b_1, c_1). The experiment starts with three GCPs and in order to increase redundancy, more GCPs should be used. With nine evenly distributed GCPs, the result is improved. The RMS value is 1.7 m in X, 1.2 m in Y and 1.9 m in height. With 17 GCPs, more consistent and better results were obtained. A RMS value of 1.2 m in X, 0.9 m in Y and 2 m in height were achieved. The RMS values are listed in table 8.

Table 8: RMS value of ChkPs using different selection of GCPs with shift and scale bias correction model

No. of GCPs/ChkPs	RMS of check points coordinate differences (meters)		
	X	Y	Z
3/18	1.9	1.0	4.3
5/16	1.8	1.2	3.3
7/14	1.6	1.1	2.7
9/12	1.7	1.2	1.9
11/10	1.5	1.0	2.1
13/8	1.5	1.2	2.0
15/6	1.4	0.9	2.1
17/4	1.2	0.9	2.0

4.4.2 Modelling with 1st order polynomials

The affine model, 1st order polynomials, offers the capability of considering affinity. However, the additional affine parameters and GCPs can generate an improvement over the result from the scale and shift model. From the RMS values listed in table 9, one can observe that the same accuracy level was achieved with modelling in the bias corrected image space with first order polynomial, see table 4.

Table 9: RMS value of ChkPs using different selection of GCPs with 1st order bias correction model

No. of GCPs/ChkPs	RMS of check points coordinate differences (meters)		
	X	Y	Z
5/16	0.9	1.3	1.5
7/14	0.7	1.1	1.5
9/12	0.8	1.2	1.7
11/10	0.8	1.0	1.8
13/8	0.5	1.2	1.2
15/6	0.4	1.0	1.2
17/4	0.2	0.9	0.9

4.4.3 Modelling with 2nd order polynomials

The addition of the 2nd order parameters requires the use of a larger number of GCPs, at least 10 control points. With 11 GCPs, no significant improvements are found in comparison to the other two models. In general, high-order polynomials are very sensitive and require a large number of GCPs. The 2nd order polynomial model does not exhibit convincing advantages over other models, see table 10.

Table 10: RMS value of ChkPs using different selection of GCPs with 2nd order bias correction model

No. of GCPs/ChkPs	RMS of check points coordinate differences (meters)		
	X	Y	Z
11/10	4.6	2.2	2.9
13/8	2.0	2.2	0.9
15/6	1.3	3.2	0.9
17/4	0.5	1.4	1.1

4.5 3D-Affine model

The 3D affine model transforms the 3D object space to 2D image space for scanners with a narrow AFOV. When modelling with the 3D 1st order polynomial model, 8 coefficient values change for one image (A_0, A_1, A_2, A_3, B_0, B_1, B_2, and B_3), which requires a minimum of 4 points for the space resection. Four equations are derived for each GCP with just three unknowns X, Y and Z. Table 11 summarizes the performances of the first order 3D-Affine model under different evenly distributed GCP and ChkPs combinations. When 5 GCPs are used, the 3D-Affine model produced an overall RMS value of 1.7 m in planimetry and 1.5 m in height. The RMS value reached the lowest RMS value when 17 GCPs were used, RMS values of 1.0 m in planimetry and 1.2 in height.

Table 11: RMS value for ChkPs Using 3D-Affine Model for Stereo Images with 1st order polynomials

No. of GCPs/ChkPs	RMS of check points coordinate differences (meters)		
	X	Y	Z
5/16	1.0	1.4	1.5
7/14	0.8	1.2	1.5
9/12	0.8	1.2	1.6
11/10	0.8	1.0	1.8
13/8	0.5	1.2	1.3
15/6	0.4	1.0	1.4
17/4	0.2	0.9	1.2

When modelling with the 3D 2nd order polynomial model, 14 coefficient values change for one image which requires a minimum of 7 points for the space resection. Table 12 lists the results for different number of GCPs. One can observe that the results are improved as the number of GCPs is increased.

Table 12: RMS value for ChkPs Using 3D-Affine Model for Stereo Images with 2nd order polynomials

No. of GCPs/ChkPs	RMS of check points coordinate differences (meters)		
	X	Y	Z
7/14	3.8	1.7	2.2
9/12	2.7	1.6	2.3
11/10	1.3	1.1	1.9
13/8	1.8	1.4	2.0
15/6	1.1	1.6	1.6
17/4	1.0	1.2	1.1

4.6 DLT model

As new sensors become operational with the new high resolution satellite imagery, their sensor modelling may still not be available immediately. For this reason, during this investigation the capabilities of the existing systems were tested using the DLT model. First, the image space and the ground space coordinates are used to calculate the respective DLT model parameter; L_1, L_2, L_3, L_4, L_5, L_6, L_7, L_8, L_9, L_{10}, and L_{11}. This requires a minimum of 6 GCPs for the space resection. After that, check points were measured on each image for assessing the accuracy of the derived DLT parameters.

Table 13 listed the RMS value of the ChkPs for the IKONOS stereo-pair imagery. The RMS values of the ground residuals were 1.8 m in X, 1.5 m in Y, and 2.1 m in height when 7 GCPs were used. On the other hand, RMS values of 1.2 m in X, 1.0 m in Y, and 1.1 in height were achieved with 17 GCPs. The results can be further improved if the image pixels are corrected for systematic errors.

Table 13: RMS value for ChkPs Using DLT Model for Stereo Images

No. of GCPs/ChkPs	RMS of check points coordinate differences (meters)		
	X	Y	Z
7/14	1.8	1.5	2.1
9/12	1.7	1.7	2.2
11/10	1.6	1.8	2.4
13/8	1.6	1.4	1.5
15/6	1.8	1.4	1.4
17/4	1.2	1.0	1.1

5. Conclusions

Based on the experimental results with IKONOS stereo-pair images, several conclusions were made. The accuracy figures of the 3D-reconstruction using the vendor-supplied RPCs was 7 m in X, 3 m in Y, and 17 m in the Z direction. By applying five bias reduction models with a few number of GCPs, this bias can be compensated to around one meter level of accuracy. The experimentation results show that the accuracies of the used five models are slightly variant. With five GCPs, planimetric and vertical accuracies of better than 1.3 m and 1.6 m respectively, can be obtained using the bias-corrected RPCs and the bias corrected image space approaches. The bias corrected ground space is feasible for RPC refinement in the cases of using shift and scale model and the affine model. Among the simple geometric models, the 1st order 3D polynomial gives accuracies within 1 m in planimetry and 1.5 m in height. On the other hand, the 2nd order 3D polynomial model gives less accuracy figures. Regarding the DLT model, obtained accuracy numbers in X, Y, and Z direction are nearly one meter when using large number of control points.

References

Abdel-Aziz, Y.I. and H. M Karara (1971). Direct linear Transformation from Comparator coordinates into Object space coordinates in close-range Photogrammetry. Proceedings of the Symposium on Close-Range Photogrammetry. Falls Church, VA: American Society of Photogrammetry, pp. 1-18.

Di, K., R. Ma. and R. Li (2003). Rational functions and potential for rigorous sensor model recovery, Photogrammetric Engineering & Remote Sensing, 69(1), 33-41.

Fraser et al., (2006). Sensor orientation via RPCs. ISPRS Journal of Photogrammetry and Remote Sensing, 60(3), 182-194.

Fraser, C., A., T. Ono., S. Akamatsu., S. Hattori. and H. Hasegawa (1999). Geometric characteristics of alternative triangulation models for satellite imagery. Proceedings of 1999 ASPRS Annual Conference, From Image to Information, Oregon, May 17-21.

Fraser, C.S. and H. B. Hanley (2003). Bias compensation in rational functions for IKONOS satellite imagery. Photogrammetric Engineering & Remote Sensing, 69(1), 53-58.

Fraser, C.S. and H. B. Hanley, (2005). Bias compensated RPCs for sensor orientation of high-resolution satellite imagery. Photogrammetric Engineering & Remote Sensing, 71(8), 909-915.

Ghilani, C. D. and P. R. Wolf, (2006). Adjustment Computations: Spatial Data Analysis, Fourth Edition John Wiley & Sons, Inc. ISBN: 978-0-471- 69728-2.

Gong, K. and D. Fritsch (2016). A detailed study about Digital Surface Model generation using high resolution satellite stereo imagery. ISPRS Annals of the Photogrammetry, Remote Sensing and Spatial Information Sciences, Volume III-1.

Grodecki, J. and G. Dial (2003). IKONOS stereo accuracy without ground control, ASPRS Annual Conference Proceedings, Anchorage, Alaska.

Grodecki, J. and G. Dial, (2003). Block adjustment of high-resolution satellite images described by rational polynomials. Photogrammetric Engineering & Remote Sensing, 69(1), 59-68.

Hanley, H.B, and C. S. Fraser (2004). Sensor orientation for high resolution satellite imagery: Further insights into bias compensated RPCs. The International Archives of the Photogrammetry, Remote Sensing and Spatial Information Sciences, 35 Part B1, Istanbul, Turkey.

Hu, Y., V. Tao. and A. Croitor (2004). Understanding the Rational Function Model: Methods and Applications. The International Archives of the Photogrammetry, Remote Sensing and Spatial Information Sciences.

Niu X, et al., (2004). Geometric modelling and photogrammetric processing of high resolution satellite imagery. Mapping and GIS Laboratory, CEEGS, the Ohio State University. Commission IV, WG IV/7

OGC (Open GIS Consortium) (1999). The Open GIS Abstract Specification-Topic 7: The earth imagery Case. http://portal.opengeospatial.org/files/?artifact_id=7467.

Poon, J., C. Fraser., C. Zhang., L. Zhang. and A. Gruen (2005). Quality assessment of Digital Surface Models generated from IKONOS imagery. Photogrammetric Record, 20(110), 162-171.

Singh, G., M. Michel, G., Markus, and A., Shefali, (2008). Improved geometric modelling of space borne push-broom imagery using modified rational polynomial coefficients and the impact on DSM generation. MSc. Thesis, International Institute for Geo-information Science and Earth Observation.

Tao, C., Y. Hu., J. Mercer., S. Schnick. And Y. Zhang (2000). Image rectification using a generic sensor model-rational function model. The International Archives of Photogrammetry and Remote Sensing, 33(B3), 874-881.

Tong X., L. Shijie. and W. Qihao (2010). Bias corrected rational polynomial coefficients for high accuracy geo-positioning of Quick-Bird stereo imagery. ISPRS Journal of Photogrammetry and Remote Sensing 65, 218-226.

Vincent, T. and H. Yong (2000). Image rectification using a generic sensor model – Rational Function Model. International Archives of Photogrammetry and Remote Sensing. XXXIII, Part B3.

Vincent, T. and H. Yong (2002). 3D reconstruction methods based on the Rational Function Model. Photogrammetric Engineering & Remote Sensing, 68(7), 705-714.

Xu Sun., L. Jonathan. and A. Michael (2005). Automatic extraction of Digital Elevation Models from IKONOS in-track stereo images. Department of Civil Engineering, Ryerson University.

Zhen Xiong and Yun Zhang (2009). A generic method for RPC refinement using ground control information. Journal of the American Society for Photogrammetry and Remote Sensing. 75(9), 1083–109.

Journal of Geomatics Vol 12 No. 1 April 2018

Adjustment of DGPS data using artificial intelligence and classical least square techniques

I. Yakubu[1], Y.Y. Ziggah[1] and M. S. Peprah[2]
[1]Department of Geomatic Engineering, University of Mines and Technology, Tarkwa, Ghana
[2]Covenant Institute of Professional Studies, Tarkwa, Ghana
Email: yissaka@umat.edu.gh

(Received: Jan 27, 2018; in final form: Apr 12, 2018)

Abstract: To improve on the accuracy of survey works, there is the need for proper adjustment of survey data. Adjustments and computations of survey field data has played a vital role in mathematical geodesy, it has been applied for the study of magnitude of errors and the determination of tolerance levels. Several studies have been carried out over the years in adjusting survey field data through the application of classical least squares techniques and other methods. With current increase in usage of GPS for most ground truth survey works, the need to adjust field data after post processing have not been taken seriously resulting in suspicion in the accuracy of final output of GPS surveyed data. This study evaluates and test alternative techniques in adjusting Differential Global Positioning System (DGPS) survey field data. Hence, the objective of this study was to explore the efficiency and performance of two artificial intelligence techniques namely, Back propagation Artificial Neural Network (BPANN), and Multivariate Adaptive Regression Spline (MARS) as a realistic alternative technique in adjusting DGPS survey field data. The study also compares the performance of BPANN and MARS models to two classical techniques namely: Ordinary Least Square (OLS) and Total Least Square (TLS). The statistical findings revealed that, BPANN, OLS, and TLS offered satisfactory results in adjusting the DGPS field data. Also, the MARS model compares to BPANN model showed better stability and more accurate results in adjusting the DGPS field data. In terms of their two-dimensional mean horizontal error, the BPANN model attained 0.0654 m while MARS model achieved 0.0296 m as compared to OLS and TLS model which archived 3.3975E -06 m and 1.0027E-09 m respectively. This present study, can conclude that BPANN and MARS provides a promising alternative in the adjustment of DGPS survey field data for Cadastral and Topographic surveys.

Keywords: Adjustment, DGPS, MARS, BPANN, Classical Least Squares

1 Introduction

Survey field measurements since generation are usually compromised with errors in field observations and needs to be adjusted using mathematical models (Okwuashi, 2014). There are two types of survey measurements techniques namely, the direct technique and the indirect technique. The direct techniques are the actual collection of field data. Errors may be incorporated due to personal, the type of instrument used, and the type of survey techniques applied. Indirect techniques are the alternate techniques of achieving field data. In this technique, errors involve in the direct method may propagate into the indirect techniques (Ghilani and Wolf, 2014). Hence, the field data needs to be adjusted to minimize the errors using both survey techniques.

Adjustments and computations studies have become obligatory in the field of mathematical geodesy, to study the magnitude of the errors whether these errors are acceptable and within tolerance limits (Ghilani and Wolf, 2012). In the past centuries, the least squares mathematical regression models (LS) (Gauss, 1823) adjustment techniques was developed and have been applied in many fields. LS is the classical technique for adjusting surveying measurements (Okwuashi and Asuquo, 2012). The LS technique minimizes the sum of the squares of differences between the observation and the estimate (Bezrucka, 2011). Various techniques utilized in the recent and past decades include, Kalman Filter (KF) (Kalman, 1960), Least Squares Collocation (LSC) (Moritz, 1978), and Total Least Square (TLS) (Golub and Van Loan, 1980; Akyilmaz, 2007; Annan *et al*., 2016a, 2016b). In this study, two classical techniques namely the ordinary least square (OLS) and total least square were adopted to assess the performance of two artificial intelligence techniques namely Multivariate Adaptive Regression Splines (MARS) and Backpropagation Neural Networks (BPANN) as an alternative technique in adjusting field data due to some defects with the classical methods.

The Ordinary Least Square (OLS) have been the conventional techniques for adjusting surveying networks (Okwuashi and Eyoh, 2012). OLS only considers the observations equations to be stochastic (Acar *et al*., 2006) and adjust only the errors in the observation matrix to make the square of the sum of residuals minimum. Several researchers (Annan *et al*., 2016a; Ziggah *et al*., 2013) in the field of geoscientific studies have applied OLS to solve many scientific problems. The Total Least Square TLS) is a data modelling technique which can be used for many types of statistical analysis such as regression or classification. In the regression technique, both dependent and independent variables are measured with errors. Thereby, the TLS approach in statistics is sometimes called an errors-in-variables (EIV) modelling. Moreover, this type of regression is usually known as an orthogonal regression (Golub and Van Loan, 1989). The total least squares (TLS) was invented to resolve the working efficiency of the OLS (Annan *et al*., 2016a). The TLS can adjust the errors in both the observation matrix and design matrix (Acar *et al.*, 2006) to yield a better estimate. Researchers such as (Acar *et al*., 2006; Annan *et al*., 2016a, 2016b; Okwuashi and Eyoh, 2012) have applied TLS to solve many scientific problems and they concluded that, the TLS working efficiency is encouraging. For large sample properties of the TLS estimator, that is a strong and weak consistency, and an asymptote distribution. The

standard procedure for solving TLS problem involves the singular value decomposition (SVD) of the extended data matrix (Lemmerling *et al*., 1996). However, the SVD does not preserve the structure of the extended data matrix. This implies that the TLS approach will not yield the statistically optimal parameter vector in the frequently occurring case where the extended data matrix is structured (Golub and Van Loan, 1989). In view of this, MARS and BPANN were adopted to evaluate its efficiency and performance as an alternative adjustment technique for adjusting DGPS field measurement data.
In the recent times, artificial neural network (ANN) has been widely adopted and applied to different areas of mathematical geodesy. Its suitability as an alternative technique to the classical methods of solving most geodetic problems has been duly investigated (Ziggah *et al*., 2016a). Some of the problems solved in mathematical geodesy include GPS height conversion (Fu and Liu, 2014; Liu *et al*., 2011), geodetic deformation modelling (Bao *et al*., 2011; Du *et al*., 2014), earth orientation parameter determination (Liao *et al*., 2012). ANN are being criticized for its long training process in achieving the optimal network's topology, and it is not easy to identify the relative importance of potential input variables, and certain interpretive difficulties (Lee and Chen, 2005; Samui, 2013). For this reason, the MARS model was also adopted. BPANN and MARS are both machine learning techniques.

Multivariate Adaptive Regression Splines (MARS) is an adaptive modelling process invented by Friedman (1991) used for non-linear relationships. In addition, MARS divides the predictor variables into piece-wise linear segments to describe non-linear relationships between the predictor and the dependent variable (Leathwick *et al*., 2005; Samui, 2013). There is limited availability of literature of MARS in survey field adjustment studies, but many studies have successfully applied MARS for solving different problems in engineering. Some of the areas of applications include estimating energy demand (Alreja et. al. 2015), slope stability analysis (Samui, 2013; Lall *et al*., 1996).

The existing knowledge and publications have not fully addressed the issue of applying alternative techniques in the adjustment of DGPS field data. In addition, upon careful review of existing studies, the authors realized that the utilization of the BPANN and MARS techniques have not been applied as a practical alternative technology to the existing approaches. This present study for the first time explored the utilization of the BPANN and MARS in the adjustment of DGPS data. To achieve the aim of this present study, the ANN and MARS methods were applied. This study also highlights the comparison between BPANN and MARS to two classical techniques namely the ordinary least square (OLS) and total least square (TLS). Each model was assesses based on statistical performance indicators such
as mean horizontal error (MHE), mean square error (MSE), and standard deviation (SD). The statistical findings of these two models (BPANN and MARS) will reveal the working efficiency and performance of the models for adjustment of the DGPS data. Hence this study will serve as an added contribution to existing knowledge of ANN and MARS in mathematical geodesy.

2 Resources and methods used

The study area (Figure 1) is in the Southwest of Ghana with geographical coordinates between longitudes: 2 º 05 ´ 00 ″ W, and 2 º 45 ´ 00 ″ W; and latitude 4 º 55 ´ 00 ″ N, and 5 º 30 ´ 00 ″ N. The type of coordinate system used in the study area is the Ghana projected grid derived from the Transverse Mercator 1 º NW and the (WGS84) (UTM Zone 30N).

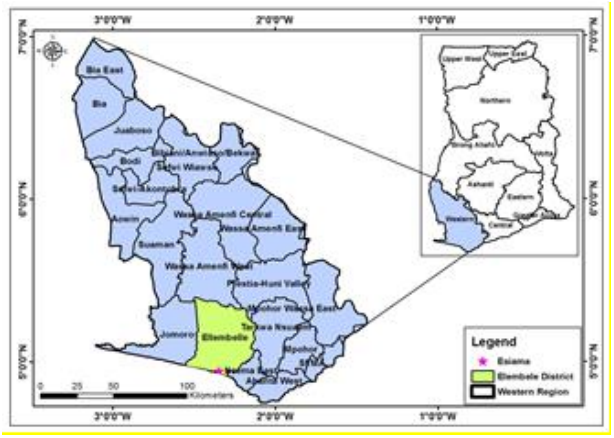

Figure 1: Map of the Study Area

In this study, a total of 53 DGPS data collected by field measurements around Esiama in the Elembelle District of the Western Region, Ghana-West Africa, were used in the model's formulation. It is well acknowledged that, one of the contributing factors affecting the estimation accuracy of models is related to the quality of datasets used in model-building (Dreiseitl and Ohno-Machado, 2002; Ismail *et al*., 2012). Therefore, to ensure that the obtained field data from the GPS receivers are reliable, several factors such as checking of overhead obstruction, observation period, observation principles and techniques as suggested by many researchers (Yakubu and Kumi-Boateng, 2011; Ziggah *et al*., 2016b) were performed on the field. In addition, all potential issues relating to DGPS survey work were also considered. Table 1 shows a sample of the data used to embark on this study. The differential (relative) was adopted in the collection of data due to its ability to adjust and compensate for errors in the baselines measurements.

2.1 Methods

2.1.1 Backpropagation Artificial Neural Network (BPANN)

BPANN consist of three layers namely, the input layer, hidden layer and output layer. In BPANN model formulation, the dataset must be normalized. Before using the dataset for training, it was ensured that the dataset are free from systematic and gross errors, random errors are the only error in the data which follows a normal distribution. The data to be used for the BPANN training and its model formulation are expressed in different units with different physical meanings. Therefore, to ensure constant variation in the BPANN model, datasets are frequently normalized to a certain interval such as [-1, 1],

[0, 1] or other scaled criteria (Ziggah *et al*., 2016b). The selected input and output variables were normalized between the intervals [−1, 1] according to Equation 1 denoted as (Muller and Hemond, 2013):

$$y_i = y_{\min} + \frac{(y_{\max} - y_{\min}) \times (x_i - x_{\min})}{(x_{\max} - x_{\min})} \quad (1)$$

where y_i represents the normalized data, x_i is the measured coordinates, while $x_{\min}$ and $x_{\max}$ represent the minimum and maximum values of the measured coordinates with $y_{\max}$ and $y_{\min}$ values set at 1 and -1, respectively.

Table 1: Sample of data used for the study (Units in meters)

Northings (m)	Eastings (m)
29516.8527	125559.5038
29612.3465	125168.1490
29695.5483	124868.5474
29766.1450	124750.3910
29774.2700	124741.4477
29813.5507	124768.5206
29786.7162	124619.4892
29847.7689	124426.1192
30133.1594	123937.8123
30174.3410	123719.6955

To find the optimum weight combination, the network was trained up using Bayesian Regularization learning algorithm. The datasets were divided into training (70 %) and testing (30 %). The input variables were the eastings and northings denoted as (E_{input}, N_{input}) and the output were the eastings and northings denoted as (E_{output}) and (N_{output}) respectively. The objective of training is to find the set of weights between the neurons that determine the global minimum of error function. The main function of the testing set is to evaluate the generalization ability of a trained network. Training is stopped when the error of the testing set starts to increase (Chakraborty and Goswani, 2017). The coefficient of correlation (R) and the mean square error (MSE) are the main performance criteria indices that are often used to evaluate the prediction performance of ANN models. The MSE is represented by Equation (2) and R is represented by Equation (3) respectively as:

$$MSE = \frac{1}{n}\sum_{i=1}^{n}(\alpha_i - \beta)_i^2 \quad (2)$$

where α_i and β are the measured and predicted plane displacements from the BPNN model.

$$R = \frac{\sum_{i=1}^{N}(Z_{jai} - \bar{Z}_{ja})(Z_{jpi} - \bar{Z}_{jp})}{\sqrt{\sum_{i=1}^{N}(Z_{jai} - \bar{Z}_{ja})}\sqrt{\left(\sum_{i=1}^{N} Z_{jpi} - \bar{Z}_{jp}\right)}} \quad (3)$$

where Z_{jai} and Z_{jpi} are the actual and predicted Z_j values, respectively. $\bar{Z}_{ja}$ and $\bar{Z}_{jp}$ are the mean of actual and predicted Z_j values corresponding to N patterns. For a good model, the value of R should be close to one (Samui, 2013).

2.2.2 Multivariate Adaptive Regression Splines (MARS)

The MARS model is nonparametric (Friedman, 1991) and it works by dividing the variables into regions, producing each region a linear regression equation (Leathwick *et al*., 2005). The general formula for the MARS model adopted in this study is given by Equation 4 as denoted by (Samui and Kurup, 2012):

$$y(i) = f(x) = a_0 + \sum_{n=1}^{N}\alpha_n\beta_n(x) \quad (4)$$

Where, $y(i)$ is the dependent variable (measured data) predicted by the function $f(x)$, a_0 is a constant, and N is the number of terms, each of them formed by a coefficient α_n and $\beta_n(x)$ is an individual basis functions or a product of two or more basis functions. The MARS model was developed in two steps. In the first step (the forward algorithm), basis functions are presented to define Equation 4. Many basis functions are added in Equation 4 to get a better estimate of the dependent value (Samui and Kim, 2012). The developed MARS may experience overfitting due to the large number of basis functions used (Friedman, 1991). To mitigate this problem, the second step that is the backward algorithm prevents overfitting by removing redundant basis functions from Equation 4. The MARS model adopts Generalized Cross-Validation (GCV) to delete the redundant basis functions (Samui and Kothari, 2012). The expression of GCV is given by Equation 5 written as (Craven and Wahba, 1979):

$$GCV = \frac{\frac{1}{N}\sum_{i=1}^{N}\left[y_i - \dot{f}(x_i)\right]^2}{\left[1 - \frac{C(H)}{N}\right]^2} \quad (5)$$

Where N is the number of data and $C(H)$ is a complexity penalty that increases with the number of basis function (BFs) in the model and which is defined as denoted by Equation 6:

$$C(H) = (h+1) + dH \quad (6)$$

Where d is a penalty for each BFs included into the model and H is the number of basis functions in Equation 4 (Friedman, 1991; Samui and Kothari, 2012). In this present study, the salford predictive model software (SPM) was adopted to train the MARS model. This is because, the SPM software is designed to be highly accurate, ultra-fast analytics, and data mining platform for creating predictive, descriptive and analytical models from databases of any size (Anon., 2018).

2.1.3 Ordinary Least Square (OLS) and Total Least Square (TLS)

OLS is used to solve a system of over determined equations as given by Equation 7 as (Miller, 2006):

$$AX = L + V_L \quad (7)$$

The solution by OLS is given by Equation 8:

$$X = inv(A' * PA) * (A' * PL) \quad (8)$$

The error vector V_L associated with the OLS is given by Equation 9 as (Schaffrin, 2006):

$$V_L = AX - L \quad (9)$$

TLS is a method of treating an over determined system of linear equations by solving for the unknown parameters, $\hat{X}$ in Equation (10) (Golub and Van Loan, 1980) through the form:

$$L + V_L = (A + V_A)\hat{X}, \quad rank(A) = m < n, \quad (10)$$

Where V_L and V_A is the vector of errors in the observation and the data matrix. Both V_L and V_A are assumed to have independent and identical distributed rows with zero mean and equal variance (Felus and Schaffrin, 2005; Akyilmaz; 2007). The TLS method is an iterative algorithm that minimizes the errors through a minimizing matrix $[\hat{A}, \hat{L}]$. The iteration continues until any $\hat{X}$ that satisfies $\hat{A}\hat{X} = \hat{L}$ becomes the TLS solution (Golub and Van Loan; 1980; Yanmin *et al*., 2011). The singular value decomposition (SVD) of the matrix $[A, L]$ was used in solving the TLS problem. SVD is used to present $[A, L]$ through Equation (11) as denoted by:

$$[A, L] = USV^T \quad (11)$$

Where $U = [U_1, U_2], U_1 = [U_1, \cdots, U_m]$, $U_2 = [U_{m+1}, \cdots, U_n]$, $U^T U = In$ and $U_i \in R^n$. $V = [V_1, \cdots, V_m, V_{m+1}]$, $V^T V = I_{m+1}$ and $V_i \in R^{m+1}$.

$S = diag(\delta_1, \cdots, \delta_m, \delta_{m+1})$, $S \in R^{n(m+1)}$. Through the SVD, the solution for the TLS problem is finally given by Equation 12 as:

$$[\hat{X}^T, -1]^T = \frac{-1}{V_{m+1}, m+1} * V_{m+1} \quad (12)$$

If $V_{m+1}, m+1 \neq 0$, then

$$\hat{L} = \hat{A}\hat{X} = -1/(V_{m+1}, m+1)\hat{A}[V_1, m+1, \cdots, V_m, m+1]^T$$

which belongs to the column space of $\hat{A}$, so $\hat{X}$ solves the basic TLS problem. The corresponding TLS correction is expressed by Equation (13) by:

$$[\Delta\hat{A}, \Delta\hat{L}] = [A, L] - [\hat{A} - \hat{L}] \quad (13)$$

2.2 Models Performance Assessment

To compare the results obtained from the BPANN, MARS, OLS and TLS model, the residuals computed between the measured coordinates and the adjusted coordinates were used. The statistic indicators used include the Mean Squared Error (MSE), Root Mean Square Error (RMSE), Horizontal Position Error (HE), Mean Horizontal Position Error (MHE) and Standard Deviation (SD). The mathematical expression for the various performance indices are given by Equations 14 to 17 respectively.

$$MSE = \frac{1}{n}\sum_{i=1}^{n}(O_i - P_i)^2 \quad (14)$$

$$HE = \sqrt{(E_2 - E_1)^2 + (N_2 - N_1)^2} \quad (15)$$

$$MHE = \frac{1}{n}\sum_{i=1}^{n} HE_i \quad (16)$$

$$SD = \sqrt{\frac{1}{n-1}\sum_{i=1}^{n}(e - \bar{e})^2} \quad (17)$$

With reference to Equations (14) to (17), n is the total number of points, O and P are the measured coordinates and adjusted coordinates produced by the various methods applied. *e* represents the residuals between the existing and transformed projected grid coordinates and $\bar{e}$ is the mean value of the residuals.

3 Results and discussions

The Tansig and Purelin functions were used for both the hidden and output layer respectively. The optimal model in adjusting the DGPS data by the BPANN model was [2, 1, 1] for the eastings and [2, 1, 1] for the northings. Thus, two inputs variables, one hidden neuron and one output variable respectively. In the MARS model formulations, 20 basis functions were in the training and testing for adjusting the DGPS data. In terms of the eastings, 6 basis functions were used in the final model formulation. This implies that, 14 basis functions were removed during the backward training due to overfitting. For the northings, 4 basis functions were used in the final model formulation. Table 2 shows the model performance for BPANN and MARS model and figure 2 represent the horizontal displacement graph by the BPANN and MARS model. It can be observed that the MARS model outperforms the BPANN model in adjusting the DGPS field data with better accuracy. The capabilities of MARS in achieving a

better result in this study as compare to BPANN may be due to its less time in training the dataset. The correlation coefficient (R) which shows how close the estimated values are to the measured values were approximately one. This implies there is a stronger correlation between the independent variables (input data) and dependent variables (output data). Hence, both models can be successfully used to adjust the DGPS field data.

The basis functions used for the final model formulations by the MARS model is tabulated in table 3. Equation 18 and Equation 19 is the optimal model equation in adjusting the eastings and northings by the MARS model respectively.

Table 2: BPANN and MARS Model (Units in meters)

MODEL	BPANN		MARS	
PCI	MSE	R	MSE	R
Training Easting	0.00290	0.99999	0.00023	0.99999
Testing Easting	0.00590	0.99998	0.00886	0.99990
Training Northing	0.00380	0.99999	4.4169 x 10^{-6}	0.99999
Testing Northing	1.12620	0.99999	5.87177 x 10^{-6}	0.99999

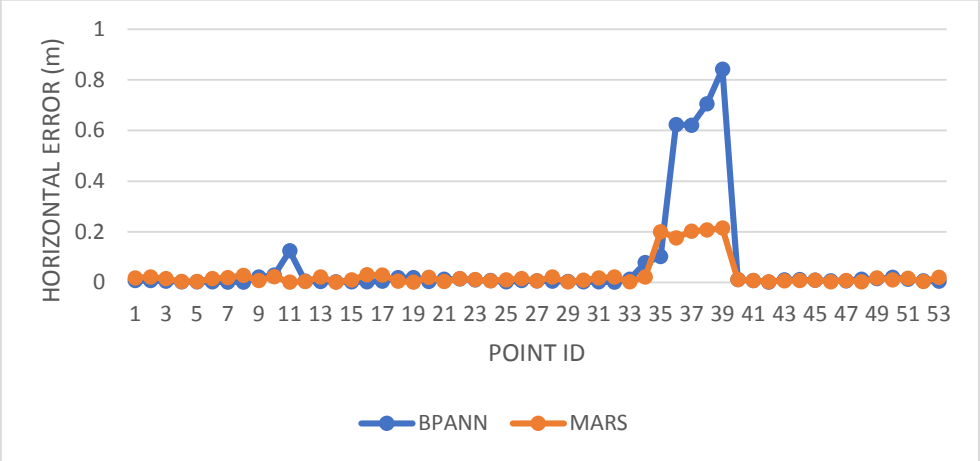

Figure 2: Horizontal Shift Graph of MARS and BPANN Models

Table 3: Basis Functions used by the MARS Model

Eastings	Northings
$BF1 = \max(0, E - 403194);$	$BF1 = \max(0, N - 97656.9);$
$BF6 = \max(0, E - 417262);$	$BF2 = \max(0, 97656.9 - N);$
$BF8 = \max(0, E - 419430);$	$BF3 = \max(0, N - 92505.5);$
$BF10 = \max(0, N - 89823.3);$	$BF6 = \max(0, E - 410677) * BF3;$
$BF11 = \max(0, N - 92505.5);$	
$BF15 = \max(0, N - 97226.4);$	

$$E(i) = 403194 + 0.999992 \times BF1 + 4.39746e-006 \times BF6 + 3.59577e-006 \times BF8 + 2.01793e-006 \times BF10 - 1.56173e-005 \times BF11 - 1.78743e-006 \times BF15 \quad (18)$$

$$N(i) = 97656.9 + 1 \times BF1 - 1 \times BF2 + 4.1672e-012 \times BF3 - 1.00e-004 \times BF6 \quad (19)$$

The horizontal displacement graphs of the two classical techniques is represented by figure 3. From figure 3, it can be observed that the TLS outperforms the OLS technique due to its capabilities to model out both errors in the observation and design matrix. The OLS model only considers errors in the observation matrix and the remaining ones in the design matrix are considered as uncertainties. Table 4 shows the horizontal displacement

results by all the models. From table 4, it can be observed that the results achieved by TLS model was very encouraging as compared to the MARS, BPANN and OLS model which perform better but with less accuracy. Upon carefully analyzing the results, it was realized that the MARS model can be used as a realistic alternative technique to the classical least squares (OLS and TLS) in adjusting some survey field data due to its performance in achieving satisfactory result in this present study. The BPANN which is also a machine learning technique achieved a better result but with lesser accuracy. This implies that, the BPANN may not be an alternative adjustment technique to the classical techniques for the study area. The developed MARS equations given by Equation 15 and Equation 16 can be used for adjusting DGPS data for the study as an alternative technique to the classical methods

.

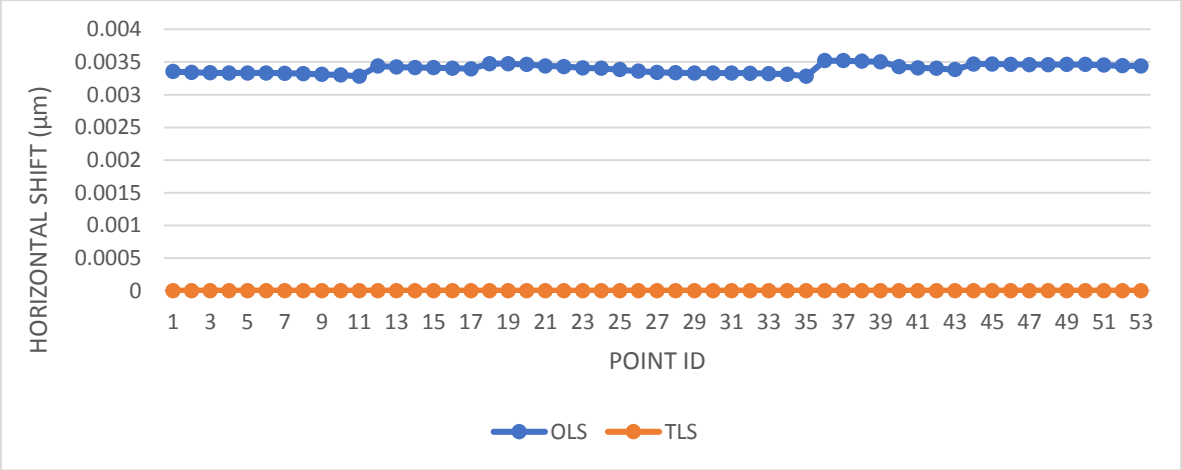

Figure 3: Horizontal displacement graph by the OLS and TLS model

Table 4: Horizontal displacement results by the models (Units in metres)

PCI	MHE	MSE	SD
MARS	0.0296	0.0562	0.0039
ANN	0.0654	0.0380	0.0344
OLS	3.3975E-06	1.1547E-11	4.4329E-15
TLS	1.0027E-09	1.0060E-18	6.0484E-22

The mean horizontal error (MHE) graph by all the models is represented by figure 4 below. From the graph below, TLS, OLS, and MARS can use as an adjustment technique for the study area due to their minimum horizontal shift achieved in this study.

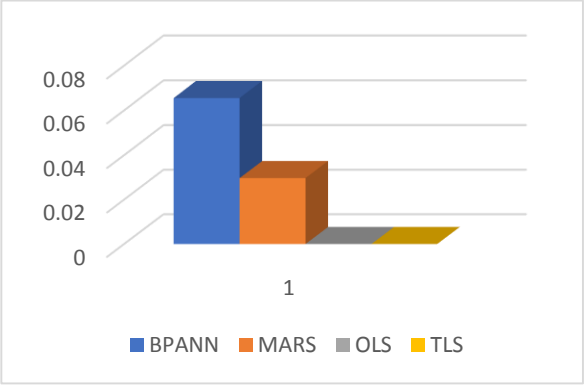

Figure 4: Mean Square Error Graph of the Models

4 Conclusions and recommendations

Adjustments and computations studies of survey field data have become obligatory and common practice in mathematical geodesy to assess the magnitude of errors and to evaluate whether the errors are within acceptable tolerance. However, the existing knowledge has focus more on classical techniques in adjustment of survey data. In the area of DGPS data collection, little knowledge exist in terms of the use of artificial intelligence in adjusting field data post processed.

Artificial intelligence has been applied in this study to adjust DGPS survey field data after the use of the classical least squares techniques. This study is the first time of utilizing artificial intelligence (BPANN and MARS) theoretically and practically on DGPS field data post processed. Machine learning techniques of BPANN and MARS have been presented in this study.

The statistical findings revealed that the BPANN, MARS, OLS and TLS offered satisfactory results in the adjustment of DGPS post processed data. However, MARS model showed superior stability and more accurate adjustment of the DGPS data compared to BPANN model. It can be therefore be proposed that the MARS model can be used as a realistic alternative technique considering certain degree of accuracies to the classical OLS and TLS models within the study area in adjusting DGPS post processed data. Based on the analysis of results achieved, the Eastings and Northings of the DGPS data can be incorporated into the MARS models to give a better estimate as the actual positioning of the ground control point. Therefore, this study does not only have a localized significance but will also open more scientific discourse into the applications of MARS techniques in solving some of the problems in mathematical geodesy within the geoscientific community.

References

Acar, M., M. T. Ozuledemir., O. Akyilmaz., R. Celik., and T Ayan. (2006). Deformation analysis with Total Least Squares, Natural Hazards and Earth System Sciences, 6, 663-669.

Akyilmaz, O. (2007). Total Least Squares Solution of Coordinate Transformation, Survey Review, 39(303), 68-80.

Alreja, J., S. Parab., S. Mathur., and P. Samui (2015). Estimating Hysteretic Energy Demand in Steel Moment Resisting Frames using Multivariate Adaptive Regression Spline and Least Square Support Vector Machine, Ains Shans Engineering Journal, doi: http://dx.doi.org//10.1016/j.as.ej.2014.12.006, 1-7, Accessed: February 10, 2017.

Annan, R. F., Y.Y Ziggah., J. Ayer., and C. A. Odutola (2016a). Accuracy Assessment of heights obtained from Total station and level instrument using Total Least Squares and Ordinary Least Squares Methods, Journal of Geomatics and Planning, 3(2), 87-92.

Annan, R. F., Y.Y Ziggah., J. Ayer., and C. A. Odutola (2016b). A Hybridized Centroid Technique for 3D Molodensky-Badekas Coordinate Transformation in the Ghana Reference Network using Total Least Squares Approach, South African Journal of Geomatics, 5(3), 269-284.

Anon., (2018). Salford Predictive Model, https://www.scientificcomputing.com/product-release/2015/04/salford-predictive-modeler-data-mining-software-suite.

Bao, H., D. Zhao., Z. Fu., J. Zhu. and Z. Gao. (2011). Application of genetic algorithm improved BP neural network in automated deformation monitoring, Seventh International Conference on Natural Computation, Shanghai-China, IEEE, doi: 10.1109/ICNC.2011.6022149, 1-5.

Bezrucka, J. (2011). The Use of a Kalman filter in geodesy and navigation, Slovak Journal of Civil Engineering, 2, 8-15.

Chakraborty, A. and D. Goswami. (2017). Slope Stability Prediction using Artificial Neural Network (ANN), International Journal of Engineering and Computer Science, 6(6), 21845-21848, doi: 10.18535/ijecs/v616.49.

Craven, P. and Wahba, G. (1979), Smoothing noisy data with spline function: estimating the correct degree of smoothing by the method of generalized cross-validation, Numer Math, 31, 317-403.

Dreiseitl, S., and L. Ohno-Machado. (2002). Logistic Regression and Artificial Neural Network Classification Models: A Methodology Review, J Biomed Int,, 35(5-6), 352-359.

Du, S., J. Zhang., Z. Deng. and J. Li. (2014). A new approach of geological disasters forecasting using meteorological factors based on genetic algorithm optimized BP neural network, Elektronika IR Elektro Technika, 20(4), 57-62.

Felus, Y. A. and B. Schaffrin. (2005). Performing Similarity Transformations using the Error-In-Variable Model", In ASPRS 2005Annual Conference, Geospatial Goes Global: From Your Neighborhood to the Whole Plant, Baltimore, Maryland, 1-5.

Friedman, J. H. (1991). Multivariate adaptive regression splines", Annals Statistics, 19, 1-67.

Fu, B., and Liu, X. (2014). Application of artificial neural network in GPS height transformation, Appl Mech Mater, 501(504), 2162-2165.

Gauss, C. F. (1823). Theoria Combinationis observationum erroribusminimis obnoxiae, Werke, 4, Gottingen, Germany, 1-5.

Ghilani, D. C., and P. R. Wolf. (2012). Elementary Surveying, An Introduction to Geomatics. Thirteen Edition", Pearson Education Inc., Upper Saddle River, New Jersey 07458, USA, 983 p.

Ghilani, D. C., and P. R. Wolf. (2014). Elementary Surveying (13th ed.). Palgrave Macmillan, New York, 983 p.

Golub, G. H., and C. F. Van Loan. (1980). An analysis of the Total Least Squares problem, SIAM Journal on Numerical Analysis, 17(6), 883-893.

Golub, G. H., and C. F. Van Loan. (1989). Matrix Computations, 2nd Ed., Baltimore, MD: Johns Hopkins University Press, 200p.

Ismail, S., A. Shabri. and R. Samsudin. (2012). A Hybrid Model of Self-Organizing Maps and Least Square Support Vector Machine for River Flow Forecasting, Hydrol Earth Syst Sci, 16, 4417-4433.

Kalman, R. E. (1960). A New Approach to Linear Filtering and Prediction Problems, Transactions of the ASME-Journal of Basic Engineering, (Series D), 82, 35-45.

Lall, U., T. Sangoyomi., H. D. I. Abarbanel. (1996). Nonlinear dynamics of the Great Salt Lake: nonparametric short-term forecasting, Water Resour Res, 32, 975-985.

Leathwick, J. R., D. Rowe., J. Richardson., J. Elith. and T. Hastie. (2005). Using multivariate adaptive regression splines to predict the distributions of New Zealand's freshwater diadromous fish, Freshw Biol, 50, 2034–2051.

Lee, T. S., and I. F. Chen. (2005). A two-stage hybrid credit scoring model using artificial neural networks and multivariate adaptive regression splines, Expert Syst Appl, 28, 743-752.

Lemmerling, P., N. Mastronardi. and S. Van Huffel. (1996). Efficient implementation of a structured total least squares based speech compression method, Linear Algebra and its Application, Elsevier, 366, 295-315.

Liao, D. C., Q. J. Wang., Y. H. Zhou., X. H. Liao. and C. L. Huang. (2012). Long-term prediction of the earth orientation parameters by the artificial neural network technique, J Geodyn, 62, 87-92.

Liu, S., J. Li. and S. Wang. (2011). A hybrid GPS height conversion approach considering of neural network and topographic correction, International Conference on Computer Science and Network Technology, China, IEEE, 1-5, doi: 10.1109/ICCSNT.2011.6182386.

Miller, S. J. (2006). Methods of Least Squares, Statistics Theory, Cornell University, USA, 3, 1-2.

Moritz, H. (1978). Least squares collocation, Reviews of Geophysics and Space Physics, 16(3), 421-430.

Muller, V. A. and F. H. Hemond. (2013). Extended artificial neural networks: in-corporation of a priori chemical knowledge enables use of ion selective electrodes for in-situ measurement of ions at environmental relevant levels, Talenta, 117, 112-118.

Okwuashi, O. (2014). Adjustment Computation and Statistical Methods in Surveying, Unpublished Report, A Manual in the Department of Geoinformatics & Surveying, Faculty of Environmental Studies, University of Eyoh, Nigeria, 1-10.

Okwuashi, O., and A. Eyoh. (2012). Application of total least squares to a linear surveying network, Journal of science and Arts, 4(21),401-404.

Okwuashi, O., and I. Asuquo. (2012). Basics of Least Squares Adjustment Computations in Surveying, International Journal of Science and Research (IJSR), 3(8), 1988-1993.

Samui, P. (2013). Multivariate Adaptive Regression Spline (MARS) for prediction of Elastic Modulus of jointed Rock Mass, Geotech Geol Eng, 31, 249-253.

Samui, P. and D. P. Kothari. (2012). A Multivariate Adaptive Regression Spline Approach for Prediction of Maximum Shear Modulus (Gmax) and Minimum Damping Ratio (£min), Engineering Journal, 16(5), 1-10.

Samui, P., and Kim, D. (2012), Modelling of Reservoir-induced Earthquakes: A Multivariate Adaptive Regression Spline", Journal of Geophysics and Engineering, 9, 494-497.

Samui, P., and P. Kurup. (2012). Multivariate Adaptive Regression Spline (MARS) and Least Squares Support Vector Machine (LSSVM) for OCR Prediction, Soft Comput, 16, 1347-1351.

Schaffrin, B. (2006). A note on Constrained Total Least Square estimation, Linear Algebra and Its Application, 417, 245-258.

Yakubu, I., and B. Kumi-Boateng (2011). Control Position Fix using Single Frequency Global Positioning System Receiver Techniques – A Case Study, Res J Environ Earth Sci, 3(1), 32-37.

Yanmin, J., T. Xiaohua. and L. Lingyun. (2011). Total Least Squares with Application in Geospatial Data Processing, In Proceedings of Nineteenth International Conference on Geoinformatics, Shanghai, China, 1-3.

Ziggah, Y. Y., H. Youjian, A. Tierra., A. A. Konate. and Z. Hui. (2016a). Performance Evaluation of Artificial Neural Networks for Planimetric Coordinate Transformation-A Case Study, Ghana, Arab J Geosci, 9, 698-714, doi: 10.1007/s12517-016-2729-7.

Ziggah, Y. Y., H. Youjian. and C. A. Odutola. (2013). Determination of GPS Coordinate Transformation Parameters of Geodetic Data between reference datums, A Case Study of Ghana Geodetic Reference Network, International Journal of Engineering Sciences and Research Technology, 2(4), 2277-9655.

Ziggah, Y. Y., H. Youjian., X. Yu. and L. P. Basommi. (2016b). Capability of Artificial Neural Network for forward Conversion of Geodetic Coordinates (Φ, λ, h) to Cartesian Coordinates (X, Y, Z). Math Geosci, 48, 687-721, doi: 10.1007/s11004-016-9638-x.

Journal of Geomatics Vol 12 No. 1 April 2018

A comparative analysis of the performance of GNSS permanent receivers at the Centre for Geodesy and Geodynamics, Nigeria

Olalekan Adekunle Isioye[1], Mefe Moses[1], Farouk Musa Isa[1] and Mohammed Bojude[2],
[1]Department of Geomatics, Ahmadu Bello University, Zaria-Kaduna State, Nigeria
[2]Centre for Geodesy and Geodynamics, National Space Research Agency, Toro- Bauchi state, Nigeria
Email: lekkyside4u@yahoo.com, oaisioye@abu.edu.ng

(Received: Feb 14, 2018; in final form: Apr 13, 2018)

Abstract: This study compares the performance of two continuously operating Global Navigation Satellite System (GNSS) receivers at the Toro observatory in Nigeria. The observatory is a proposed site for part of the global geodetic core network for collocation of GNSS and other space geodetic techniques. The pair of GNSS receivers (Ashtech UZ-12 and Trimble NetR8) are connected via a GNSS splitter to a single antenna (Trimble GNSS Choke Ring TRM59800.00). Observation files, precise orbit and clock files, and satellite differential code bias files with respect to the two receivers were collected for a period of 30 days. The WaSoft software (WaPPP module) was employed to estimate the receivers' position, zenith tropospheric delay (ZTD) and tropospheric gradients. Also, the Gopi software was used to estimate the receivers' bias and total electron content (TEC). The resulting parameters from the estimation software were subjected to hypothetical testing using the Student t-test based on the Bland Altman method of analysis for comparison tests. The results of the statistical tests show that the choice of GNSS receiver does affect the estimation of Z-component of the coordinate, ZTD, receiver bias and TEC at 95% confidence level. However, the results show that the X and Y-components of the receivers' position and tropospheric gradients were not influenced by the choice receiver. The results obtained from this study pinpoint the need to ascertain the accuracy of parameters estimated from geodetic grade receivers and ensure that the parameters do not differ significantly from each other, particularly when these are required for very precise scientific applications.

Keywords: Global Navigation Satellite System (GNSS), receiver bias, tropospheric gradients, total electron content (TEC), zenith tropospheric delay (ZTD), performance and analysis of receivers

1.0 Introduction

Global Navigation Satellite System (GNSS) ground infrastructure is on the increase globally; the ground infrastructure comprises many hundreds (if not thousands) of continuously operating reference stations (CORSs). As the name suggests, this GNSS infrastructure typically comprises GNSS receivers, antennas and computer systems (identical to surveying user equipment). The highest CORS tier is the network of stations that contributes to the international GNSS service (IGS), and in effect makes up part of the physical infrastructure of the global geodetic observing system. Such CORS stations have well-established, very stable monuments, and operate continuously for many years. The IGS supports the realisation of the international terrestrial reference frame and the determination of highly accurate satellite orbit and clock products to facilitate techniques such as precise point positioning (PPP) (Kouba, 2009).

GNSS-CORS data consist of carrier phase and code range measurements in support of three-dimensional positioning, agriculture, construction, meteorology, space weather, seismology and other geophysical applications across the globe (Rizos, 2007; Dow et al., 2009). GNSS-CORS are typically operated by scientific agencies, government departments (federal, state and local), private companies and academia, but even individuals. Furthermore, these CORS have the task to store data, in some circumstances process the data, and then transmit these data to roving receivers. These CORS help users by economising on one GNSS receiver, as the operation of the reference station is performed by the service provider of the CORS network.

Every CORS network consists of several GNSS stations interconnected by reliable communications to enable real-time computations and control. Each station has a minimum requirement of a receiver, an antenna, communications and a power supply. In most cases, a computer is installed additionally for data transmission and control. The precision of results differs for the different users or applications of CORS. The precision of results for the different applications also depends on the type of ground infrastructure (receiver, antenna, and cabling options) and computer accessories, which include software.

The CORS antenna tracks signals emitted by a satellite in space and these signals follow a path from the satellite mounted in space, propagating through the atmosphere and down to the receiver located on the surface of the earth. In the process of transmission, the signal undergoes a lot of delay along its path, which reduces its strength, and in some cases diverts or breaks the signal path, causing error in signal transmission. However, satellite signal propagation and antenna error can be mitigated with appropriate correction schemes

(Chuang and Gupta, 2013). More so, several studies have evolved to develop and validate multi-antenna GNSS receiver systems that can perform excellently even under jamming attacks or resilient navigation (Vagle et al., 2016; Gupta et al., 2016; Cuntz et al., 2016).

The influence of the choice of permanent GNSS receivers, receiver architecture, settings and stability of estimated parameters from satellite signals for the different users and applications have received attention from different researchers. Zhang et al. (2010) performed a series of tests using highly sensitive (HS) receivers and a number of geodetic and navigation grade antennas in order to examine the variation in their performance. The study reveals clear advantages of using HS receivers instead of conventional receivers in applications requiring meter level accuracies with moderate antenna dynamics.

Odolinski and Teunissen (2016) compared the performance of a low-cost ublox single-frequency dual system (SF-DS) to that of a dual-frequency single system (DF-SS), based on much more expensive survey-grade receivers. The experiment revealed that SF-DS has the potential to achieve comparable ambiguity resolution performance to that of a DF-SS (L1, L2 GPS), based on the survey-grade receivers. High-sensitivity low-cost receivers have thousands of correlators to reduce the search space of each correlator and are able to acquire signals with low decibel watt (Schwieger, 2007).

The performance of low-cost single-frequency receivers can be improved by using a geodetic grade antenna instead of the low-cost single-frequency antenna (Takasu and Yasuda, 2008). In addition, Sousa and Nunes (2014) studied the influence of receiver architecture on the estimated parameter (ionospheric scintillation, multipath and high dynamics motion) from satellite signals. The study analysed the gains and drawbacks of a vector delay/frequency-locked loop architecture regarding the conventional scalar and the vector delay-locked loop architectures for GNSS receivers in harsh scenarios that include ionospheric scintillation, multipath and high dynamics motion.

From the foregoing, it is evident that since low-cost single-frequency receivers became available, several attempts have been made to reduce the cost and increase the accuracy of such receivers compared with geodetic grade receivers. Very little attention is paid to the accuracy of estimated parameters from geodetic grade GNSS receivers themselves. Many permanent GNSS installations have unique cabling requirements. Depending on the available infrastructure, the antenna may need to be mounted at a substantial distance from the receiver. The degree of loss in a coaxial cable depends on the frequency of the signal passing through it. There are no universal conventions in terms of the type of receivers or cabling options for varying applications. Thus it is imperative to ascertain if the choice of GNSS receiver does affect the parameters estimated for the satellite signals.

In this study, we compared the accuracies of the two geodetic receivers at the Centre for Geodesy and Geodynamics (CGG) in Toro, Nigeria. The two receivers operated by different agencies (Jet Propulsion Laboratory (JPL) and the office of the Surveyor General of the Federation (OSGOF, the Nigerian mapping agency)) both receive signals from the same antenna (single antenna) via a connection from a GNSS splitter. The result of the present study would be a great contribution to user knowledge in relation to GNSS-CORS in Nigeria and the world at large. The strategic relevance of CGG Toro as the only geodetic observatory in Nigeria and the host of the only IGS station in Nigeria further highlights the significance of the study. The datasets, hypothesis and analysis method used in this study are described in section 2. Results and discussions on the estimated parameter from the two receivers is presented in Section 3. Concluding remarks are presented in the final section.

2.0 Materials and methods

The scope of this research work covers comparative analysis of the positional accuracy, receiver biases, ionosphere and tropospheric parameter estimates in Toro observatory of the National Space Research Agency from permanent geodetic grade GNSS receivers, both connected to a single geodetic grade antenna via a GNSS splitter.

The stages of this study involve four tasks with reference to the schematic diagram, figure 1. The first is to acquire experimental data, the second to process the data for the experiment, the third to compare the results obtained from the processing and the last to analyse and draw conclusions, as well as present the data.

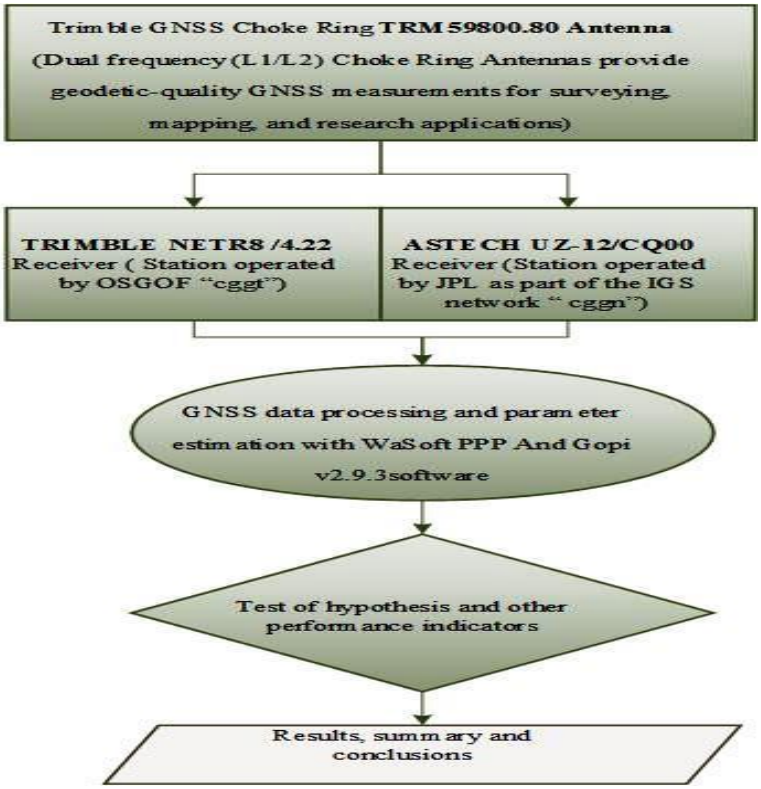

Figure 1: Schematic diagram of methodology

2.1 GNSS station location and instrumentation

The CGG located at Toro LGA in Bauchi State in North Central Nigeria is one of the seven centres of NASRDA. The Toro Observatory is situated on a part of the Basement Complex of Nigeria. It is composed of older granites and magmatites. These geological features that occur in these areas necessitated the choice of the Geodetic and Geodynamics Observatory site. In addition, the site has surface expressions of the West African Craton – an ancient, stable core of the African continent that has not been deformed over geological time. This large igneous unit is representative of the most stable region of Africa (corresponding to the Canadian Shield in North America). The CGG is central to geodetic activities in Nigeria; the observatory is the host to the only IGS station in Nigeria (Figure 2). OSGOF also has one of its numerous GNSS stations across the country located in the observatory of CGG. The centre streams GNSS raw data from CGGN to the JPL. The CGGN is archived at the Crustal Dynamics Data Information Centre (CDDIS). Similarly, GNSS data from CGGT are streamed to OSGOF's office located in Abuja, the federal capital city. The OSGOF receiver (CGGT) is the Trimble NET R8 receiver version 4.22 and the receiver for CGGN is an ASTECH UZ-12 receiver version CQ00 (Figure 3). The NetR8 GNSS reference receiver is a multiple-frequency GNSS receiver. It can track all GPS signals (L1/L2/L5) as well as GLONASS (L1/L2). The Trimble NetR8 receiver is designed to serve in all common geodetic reference receiver roles. This receiver also has specialised capabilities that make it an excellent reference receiver for scientific applications. The NetR8 receiver provides a TNC-type female connector for connecting to an antenna. The receiver is intended for use with a Zephyr™ Geodetic Model 2 antenna or a Trimble GNSS Choke Ring antenna. The Ashtech UZ-12 processes signals from the GPS satellite constellation, deriving real-time position, velocity and time measurements. The Ashtech UZ-12 receives satellite signals via an L-band antenna and low-noise amplifier (LNA). The receiver operates as a stand-alone reference station providing raw measurements, and as a real-time differential base station broadcasting (DGPS) corrections based on code-phase, and real-time kinematic mode. The receiver features 12-parallel channel/12-space vehicle (SV) all-in-view operation; each of up to 12 visible SVs can be assigned to a channel and then continuously tracked. Each SV broadcasts almanac and ephemeris information every 30 seconds, and the unit automatically records this information in its non-volatile memory. The unit has an L1/L2-band radio frequency port and four RS-232 serial input/output ports. Ports A, B, C, and D are capable of two-way communication with external equipment. Ports A and B have expanded support for more advanced communication strategies. The receiver permits uninterrupted use even when anti-spoofing (AS) is turned on. When AS is on, the receiver automatically activates our patented Z-tracking mode that mitigates the effects of AS. A GNSS splitter connects the two receivers (CGGT and CGGN) to a Trimble choke ring TRM59800.80 antenna (Figure 3).

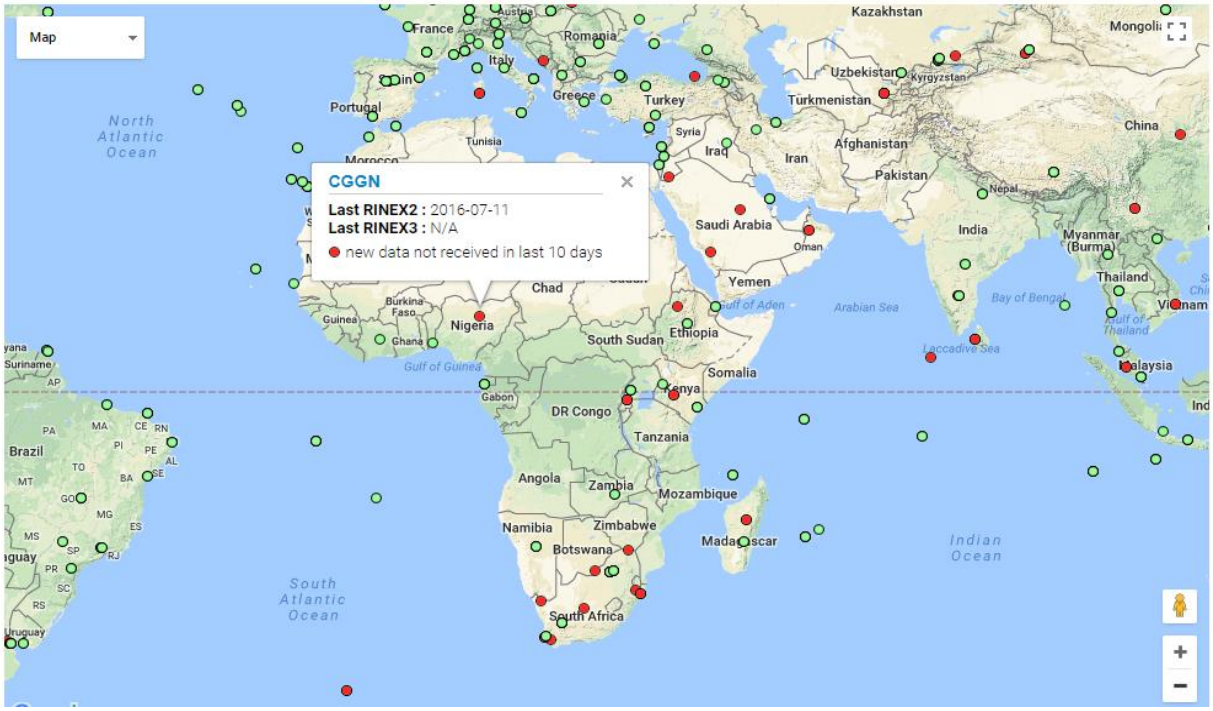

Figure 2: IGS network showing location of IGS station (CGGN) in Nigeria (after www.igs.org)

Figure 3: GNSS CORS antenna and receivers in Toro: A) Antenna (TRM59800.00), B) CGGT Trimble NET R8 Receiver, C) CGGN Ashtech UZ-12

Trimble GNSS Choke Ring TRM59800.00 (Dual frequency (L1/L2) Choke Ring) antennas provide geodetic-quality GNSS measurements for surveying, mapping, and research applications. Typical dual-frequency choke ring antennas maintain a stable phase centre that has less than 1 mm of drift. The choke ring antenna is based on the geodetic research standard and features aluminium choke rings and a Dorne Margolin antenna element. This antenna is very durable and has low power consumption and excellent multipath rejection characteristics. The Trimble GNSS Choke Ring TRM59800.00 is a TRM29659.00 reworked with a wide-band LNA for GNSS.

2.2 GNSS Data Download and Processing

Observation and navigation data for CGGT were obtained from the Nigerian GNSS Network (NIGNET) download site. The NIGNET comprises 14 other stations aside from the CGGT; it is the primary network for the new Nigerian geocentric datum (Jatau et al., 2010; Dodo et al., 2011; Naibbi and Ibrahim, 2014). The capability of the NIGNET in varying scientific applications (i.e., meteorological and space weather studies) has been demonstrated (Isioye et al., 2017a & b; Moses et al., 2017). Similarly, observation and navigation data for the CGGN were downloaded from the Scripps Orbit and Permanent Array Center (SOPAC) website via the CDDIS website; both sets of data were obtained in RINEX2.X format.

In additional, broadcast ephemerides for GLONASS channel numbers in RINEX format, a satellite and antenna phase correction file in ANTEX format, precise satellite orbit files in SP3 format, precise clock correction files in RINEX-CLK format, and satellite differential code bias (DCB) files were obtained. Table 1 is a summary of the different data types and their download sources. Thirty-day data were downloaded for the month of January 2012; the days were common to both stations and the network (CGGT and CGGN). The RINEX data were compressed files and so the files were unzipped using the Win-rar unzipper. The files were extracted and converted from D files to O files (observation files) by using the CRX2RNX and unpack applications. To achieve the objective of this study, we employed Wasoft software and GPS-TEC analysis v2.2 software in processing of all downloaded GNSS data and products.

The Wasoft software is modular GNSS processing software with the capability of PPP processing for GNSS observation of single stations. The PPP engine or "WaPPP" is capable of automatic processing without user interaction and suitable for batch processing. WaPPP computes coordinates based on GNSS observations in RINEX format; it also provides the option for the estimation of tropospheric delay and tropospheric gradients. It is useful for obtaining sub-metre, decimetre, or centimetre level accuracies. The highest accuracies require long-term (a few to many hours) of continuous dual-frequency carrier-phase observations in addition to precise satellite orbits and clock corrections, satellite antennas and user antenna corrections. WaPPP weights the different observations types (code and carrier phase, various GNSS) according to a variance component estimation. It uses a robust estimation algorithm in the estimation of position results and other estimated parameters.

Table 1: Station data and sources

Sr. No.	Data description	Data Source
1	Daily observation and navigation data in compacted RINEX format from the NIGNET for 'CGGT'	www. nignet.net
2	Daily observation and navigation data in compacted RINEX format from the NIGNET for 'CGGN'	ftp//cddis.gsfc.nasa.gov/pub/~ gps/products
3	Ephemerides data GLONASS(.g file)	ftp//cddis.gsfc.nasa.gov/pub/~ glonass/products/
4	Precise satellite correction data from IGS (.sp3 file)	ftp//cddis.gsfc.nasa.gov/pub/~ gps/products
5	Final IGS clock product (.clk file)	ftp//cddis.gsfc.nasa.gov/pub/~ gps/products
6	Antenna correction file from IGS (igs08.atx)	ftp//cddis.gsfc.nasa.gov/pub/~ station/general/igs08.atx
7	Satellite differential code bias	(ftp://ftp.unibe.ch/~ aiub/CODE

The WaPPP engine processes GNSS data for the CGGN and CGGT with the option of outputting the 3D station coordinates, zenith tropospheric delay and tropospheric gradient components. The GPS-TEC analysis v2.2 software (http://seemala.blogspot.com) is free software for the estimation of total electron content (TEC) from GPS observations developed by Gopi Seemata at Boston College, USA. The features of this software application include the ability to batch process the input files (RINEX and others). It also has the ability to download the navigation file automatically were necessary. Using the available GNSS data, satellite navigation data and the DCB files, the TEC was processed from the GPS-TEC analysis software for the two receivers. In addition, the software estimates DCBs (along with the inter-channel biases for different satellites in the receiver) for the ground GNSS station.

2.3 Statistical analysis and hypothesis testing

Based on comprehensive evaluation of the different parameters (station coordinates, ZTD, tropospheric gradients, TEC, and receiver bias) estimated from the two receivers, we use the Bland Altman method validation/method comparison test. The Bland Altman analysis in XLSTAT software estimates bias, using the chosen criterion (difference, difference in percentage, or ratio), the standard error, Pearson correlation coefficient, and difference and Bland Altman plots. The bias is the mean of the differences between the two methods, in this case Trimble NET R8 receiver version 4.22 (CGGT) and ASTECH UZ-12 receiver version CQ00 (CGGN). The standard error is computed, as well as a confidence interval. Ideally, the confidence interval should contain zero. The Bland Altman plot displays the difference between the two methods (receivers) for visualisation. XLSTAT software displays the correlation between the abscissa and the ordinates. One would expect it to be non-significantly different from zero, which means the confidence interval around the correlation should include zero. Next, one has the results of the Student t-test, performed on the means for each receiver. This test computes the difference between the two for each receiver, and checks whether it is different from zero or not. This test requires the assumption that the differences are normally distributed. Thus, the t-test helps to test the hypothesis on the influence of the choice of GNSS receiver on the estimated parameters from GNSS satellite signals. The null hypothesis (H_0) and alternative hypothesis (H_1) are as follows:

i. Null hypothesis H_0 states that mean ($\mu1-\mu2=0$): the choice of GNSS receivers does not affect the estimated parameters from GNSS satellites in the study area.
ii. Alternative hypothesis H_1 states that mean ($\mu1-\mu2\neq0$): the choice of GNSS receiver affects the estimated parameters from GNSS satellites in the study area.

3.0 Results and discussion

This section presents the results of the various tests for the performance comparison for the two receivers. The discussions cover the different parameters estimated from the receivers, which include the 3D position estimates, tropospheric parameters (ZTD and tropospheric gradients), TEC and receiver differential biases.

3.1 3D position information

The computed geographic coordinates from the Wasoft software were converted to the Universal Traverse Mercator (UTM) system for easy comparison. The daily series plot of the 3D coordinate values is shown in figure 4.

Table 2: Summary of the descriptive statistics for information on the receivers' position

Stn	Min	Max	Mean	Std Dev
Easting (X-component)				
CGGT	512961.537	512961.552	512961.548	0.003
CGGN	512961.546	512961.552	512961.549	0.002
Northing (Y-component)				
CGGT	1119024.705	1119024.709	1119024.707	0.001
CGGN	1119024.704	1119024.709	1119024.706	0.001
Height (Z-component)				
CGGT	916.443	916.454	916.448	0.003
CGGN	916.442	916.453	916.447	0.003

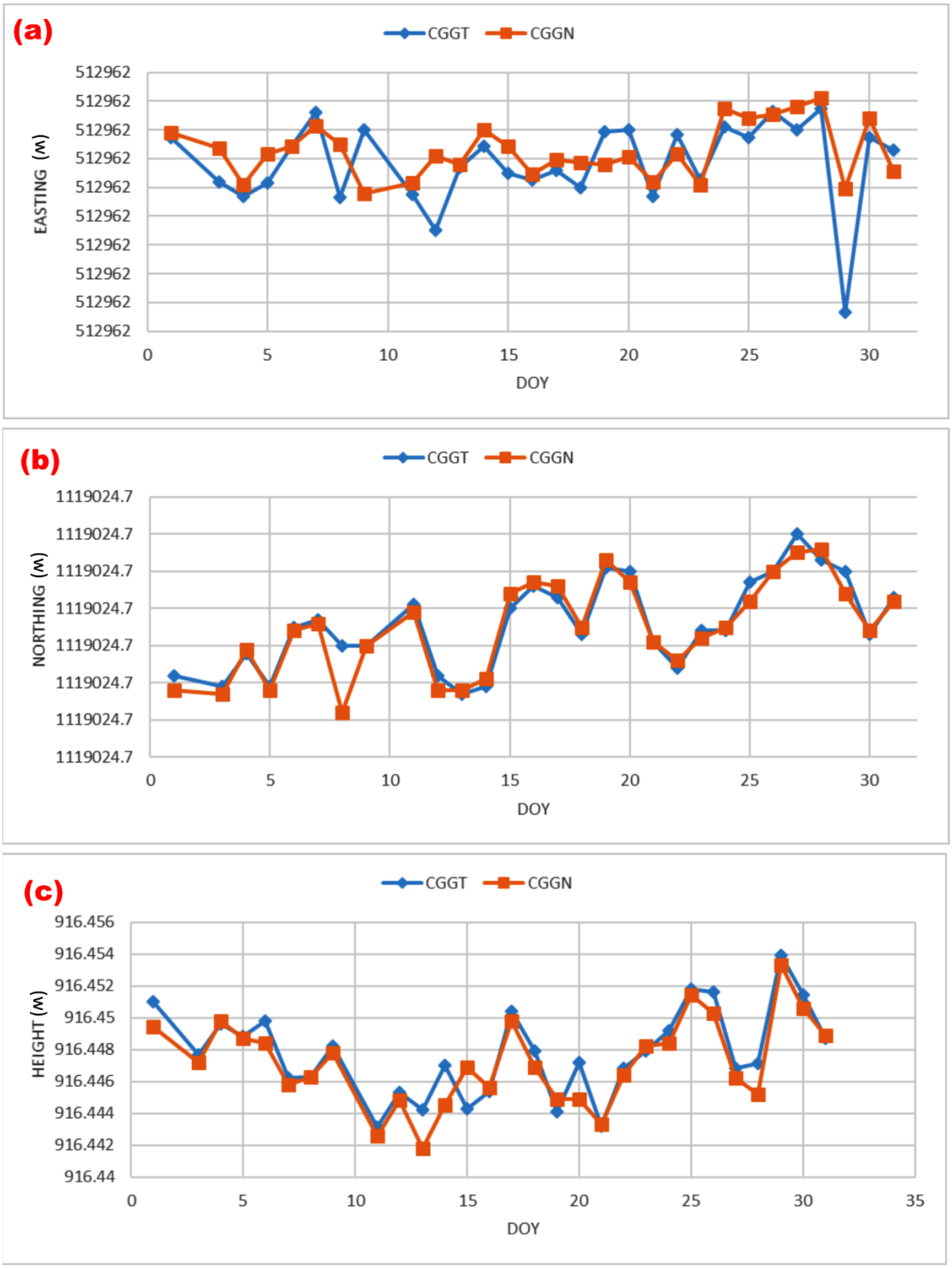

Figure 4: Time series plot of estimated coordinates from the two receivers: a) is the northing or y-component in metres b) is the easting or x-component in metres and c) is the height or z-component in metres

The summary of the statistics of the estimated position of the two receivers is presented in Table 2. The positional estimates do not show much variation. The Pearson correlation coefficient from scatter plots comparing CGGT and CGGN (Figure 5) reveals a strong relation of 0.604, 0.944, and 0.928 for the X, Y, and Z components of the position for the receivers, respectively.

The Bland and Altman estimate of bias is 8.28E-04, -1.103E-04, and -5.724E-04, for the X, Y, and Z component, respectively. The difference (Bland and Altman) plot displays the difference between the estimated coordinates from CGGN and CGGT against their average value, as shown in Figure 6. There was good agreement between the two receivers, since most of the data fall within the 95% confidence interval of the bias and standard error. The estimated p-value from the Student t-test is 0.070, 0.165, and 0.006, for the X, Y, and Z components, respectively. Thus, the computed p-value is greater than the significance level alpha = 0.05 for the X and Y components. The null hypothesis H_0 cannot be rejected for the X and Y component and the risk of rejecting the null hypothesis H_0 is 6.98% and 16.51%, respectively. Conversely, the t-test results for the height component show that the computed p-value is lower than the significance level alpha = 0.05. The null hypothesis H_0 was rejected; the risk of rejecting the null hypothesis H_0 while it is true is lower than 0.59%.

3.2 Tropospheric parameters

The descriptive statistics for the estimated tropospheric parameters (ZTD, tropospheric gradient E-N components) from CGGN and CGGT receivers are contained in Table 3. The Pearson correlation coefficient from the scatter plot comparing ZTD at CGGT and CGGN (Figure 7) reveals a very strong relation of 0.970. A time series plot of the different tropospheric parameters is presented in Figure 8.

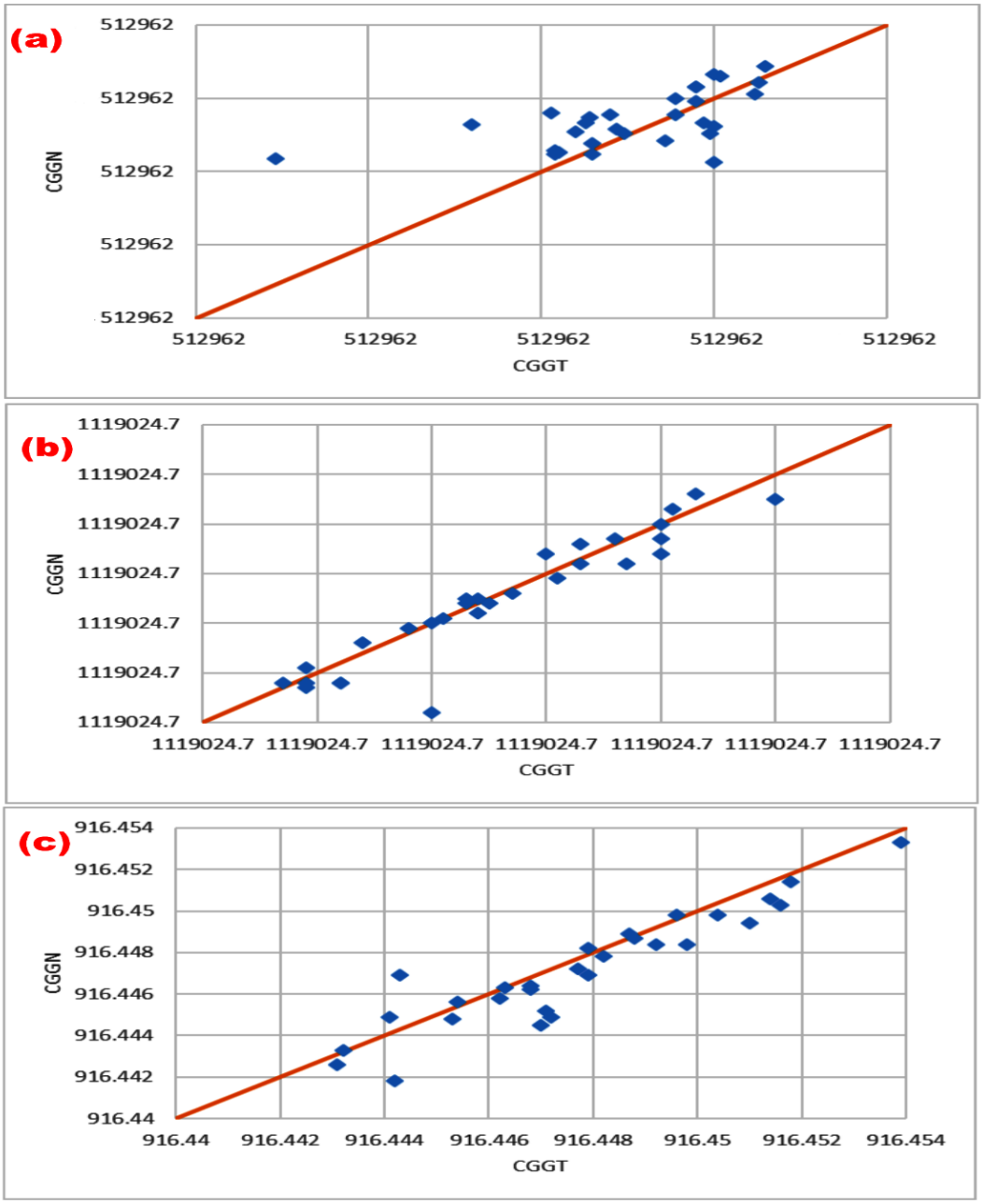

Figure 5: Scatter plots of estimated coordinates from the two receivers: a) is the northing or y-component b) is the easting or x-component and c) is the height or z-component

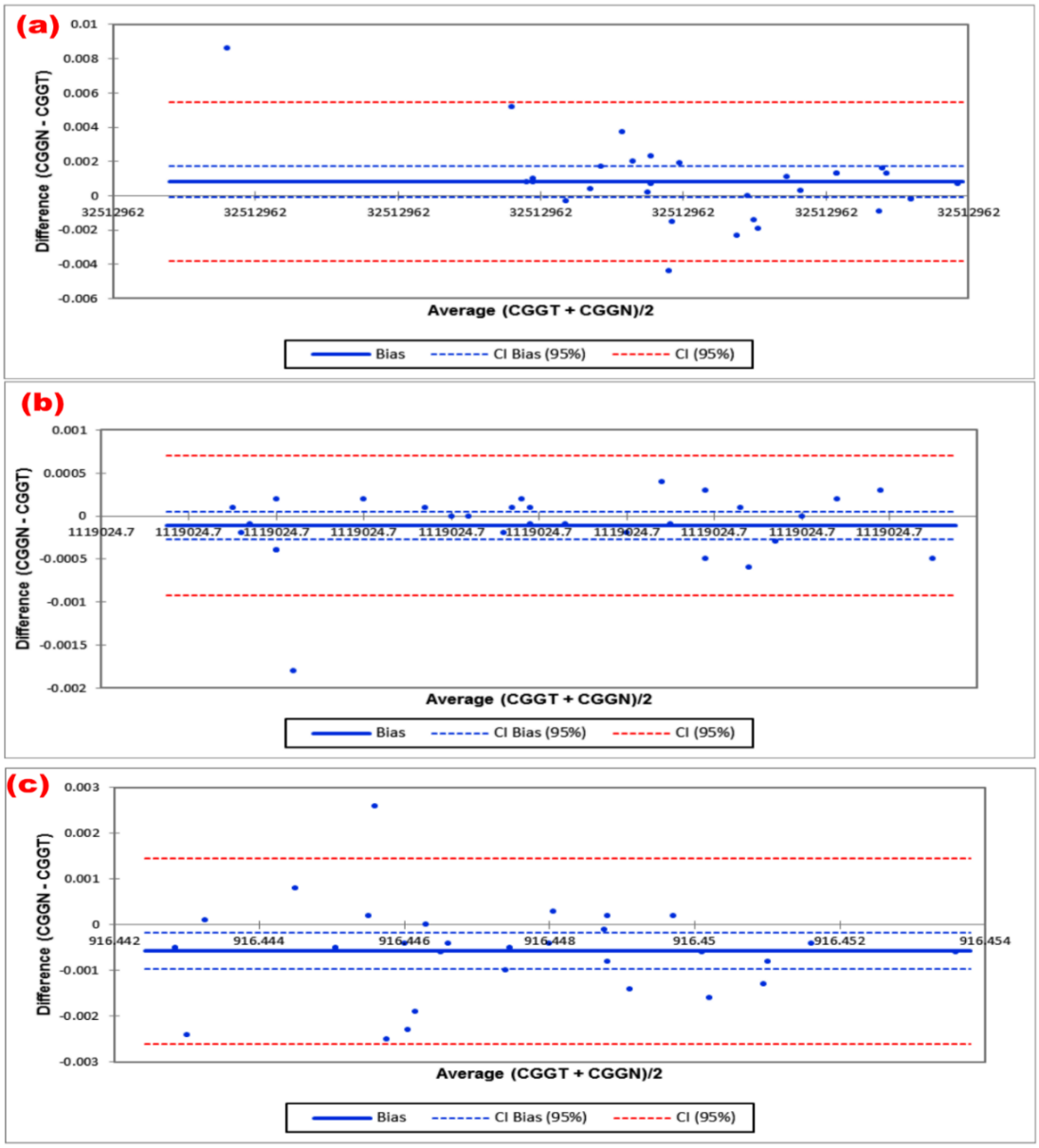

Figure 6: Bland and Altman (difference) plot of estimated coordinates from the two receivers: a) is the northing or y-component in metres b) is the easting or x-component in metres and c) is the height or z-component in metres

Table 3: Summary of the descriptive statistics for estimated tropospheric parameters

Station	Min	Max	Mean	Std Dev
ZTD (m)				
CGGT	2.125	2.181	1.151	0.011
CGGN	2.122	2.186	1.150	0.011
Tropospheric Gradient (E-component (m))				
CGGT	-0.006	0.002	-0.002	0.002
CGGN	-0.006	0.003	-0.002	0.002
Tropospheric Gradient (N-component (m))				
CGGT	-0.004	0.000	-0.002	0.001
CGGN	-0.005	0.000	-0.002	0.001

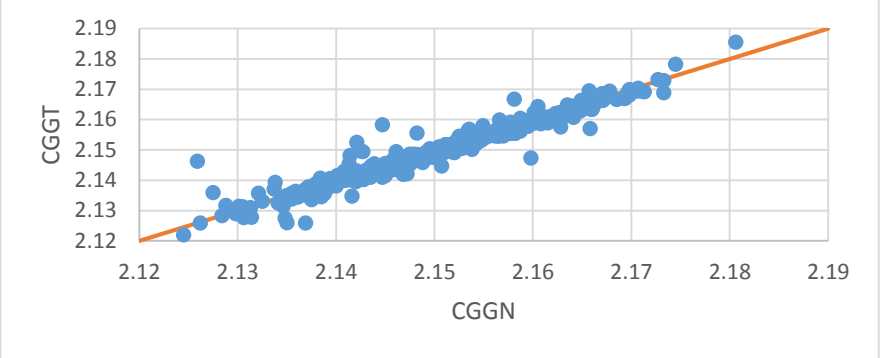

Figure 7: Scatter plot of estimated ZTD from the two receivers

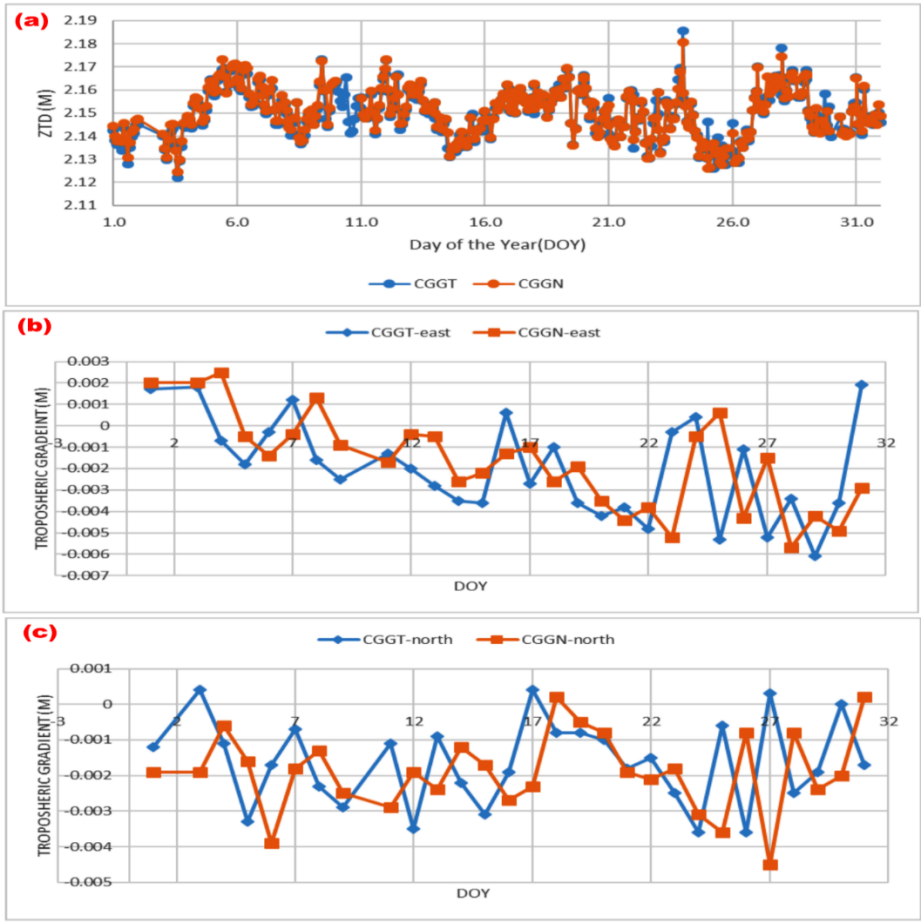

Figure 8: Time series plot of estimated tropospheric parameters from the two receivers; a) is the ZTD in metres b) is the tropospheric gradient (east component) in metres and c) is the tropospheric gradient (north component) in metres

The Bland and Altman estimate of bias is 4.876E-04, 2.655E-04, and -5.552E-04, for the ZTD, east component, and the north component of the tropospheric gradients, respectively. The difference (Bland and Altman) plot displays the difference between the estimated coordinates from CGGN and CGGT against their average value as shown in figure 9. There are was good agreement in ZTD estimates between the two receivers, since most of the data fall within the 95% confidence interval of the bias. The estimated p-value from the Student t-test is 0.000, 0.562, and 0.440, for the ZTD, east component, and the north component of the tropospheric gradients, respectively. Thus, the computed p-value is greater than the significance level alpha = 0.05 for the east component, and the north component of the tropospheric gradients. The null hypothesis H_0 cannot be rejected for the east component, and the north component of the tropospheric gradients and the risk of rejecting the null hypothesis H_0 is 56.24% and 43.97%, respectively. Conversely, the t-test results for the ZTD show that the computed p-value is lower than the significance level alpha = 0.05, and the null hypothesis H_0 is rejected; the risk of rejecting the null hypothesis H_0 while it is true is lower than 0.03%.

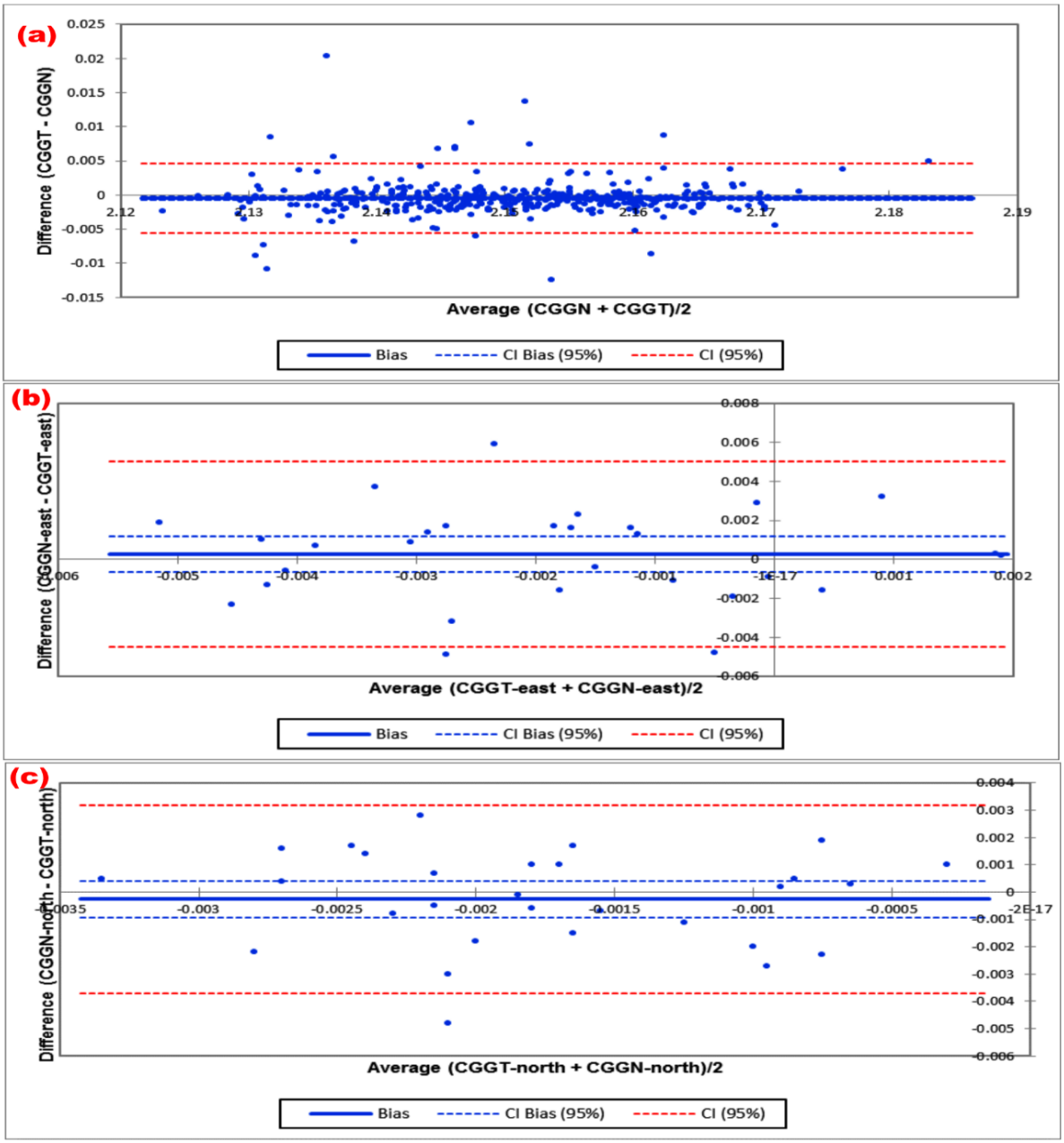

Figure 9: The Bland and Altman (difference) plot of estimated tropospheric parameters from the two receivers: a) is the ZTD in metres b) is the tropospheric gradient (east component) in metres and c) is the tropospheric gradient (north component) in metres

3.3 Receiver bias and TEC

From the box plot of the differences (Figure 10), the Bland and Altman estimate of bias is -54.4, and 0.541 for the receiver bias and TEC respectively. The confidence interval of the bias is between -55.235 and -53.565, with a standard error of 0.426; the receiver bias for CGGN was positive all through and out of the confidence level of the bias. In addition, from the time series plot (Figure 11), the maximum and minimum receiver bias stood at 14.600 and 1.100 for CGGT, and 39.000 and 53.000 for CGGN. The difference plot displays the difference between the estimated receiver bias from CGGN and CGGT against their average value, as shown in figure 11b. The estimated p-value from the Student t-test is < 0.000. Thus, the computed p-value is less than the significance level alpha = 0.05. The null hypothesis H_0 is rejected and the risk of rejecting the null hypothesis H_0 while it is true is lower than 0.01%. Scatter plot of estimated TEC from the dual receivers is shown in figure 12.

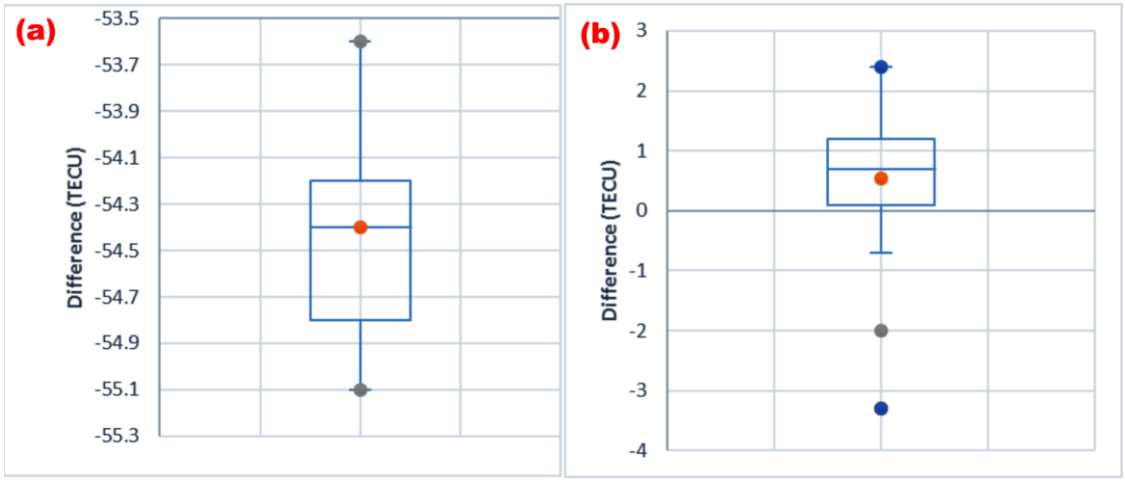

Figure 10: Box plot of differences in receiver bias and TEC estimations from the CGGN and CGGT

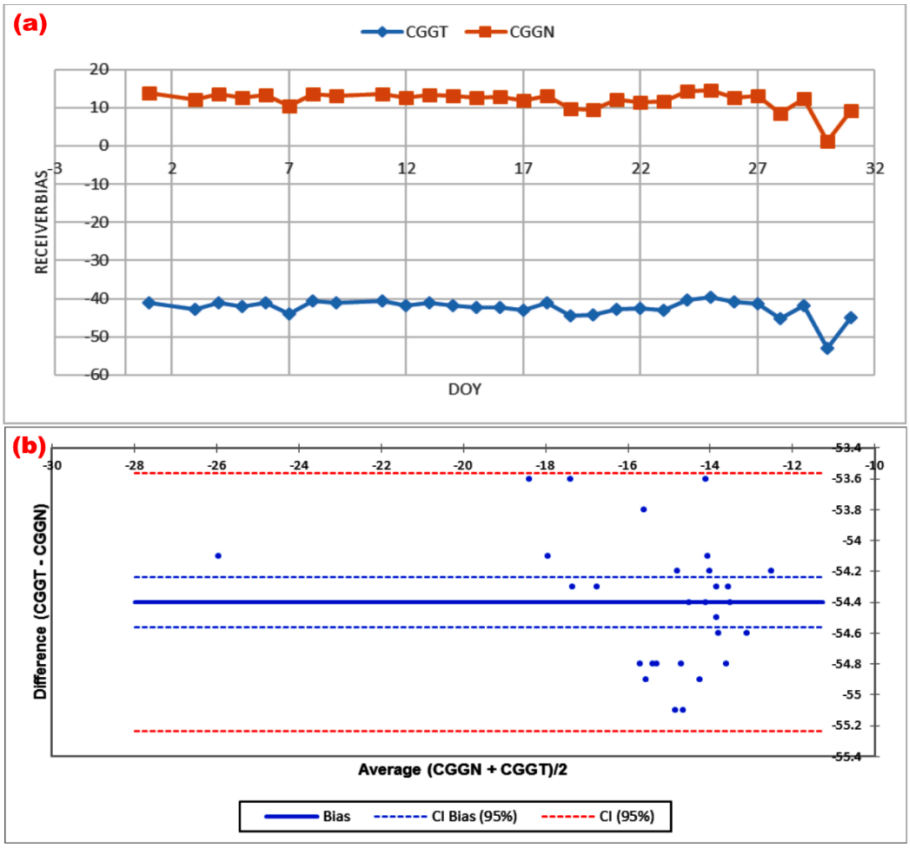

Figure 11: Receiver code bias estimated from the two receivers: a) Time series plot of estimated biases from the dual receivers b) Bland and Altman (difference) plot of estimated biases from the dual receivers

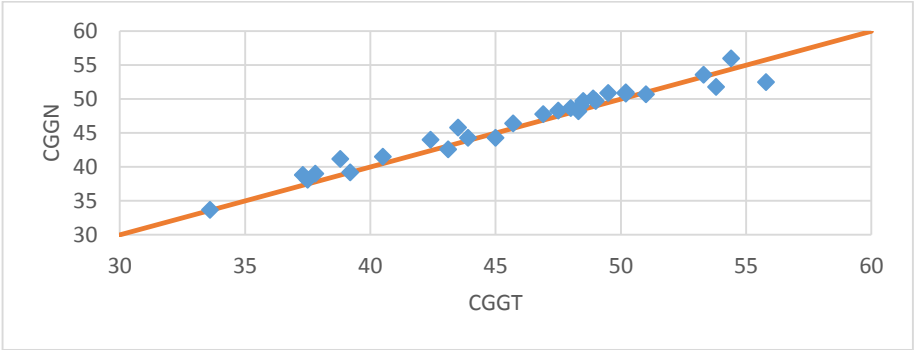

Figure 12: Scatter plot of estimated TEC from the dual receivers

The difference plot for the estimated TEC from CGGT and CGGN is shown in figure 13. The t-test result shows that if the computed p-value is lower than the significance level alpha = 0.05, one should reject the null hypothesis H_0, and accept the alternative hypothesis H_1. The risk of rejecting the null hypothesis H_0 while it is true is lower than 1.82%.

4.0 Concluding remarks

In this paper, a performance comparison test was carried out between two geodetic grade GNSS receivers at the CGG, Nigeria. The observatory at CGG remains the only geodetic observatory in Nigeria. The fact that CGG hosts an IGS site in Nigeria and that it is a proposed site for the global geodetic core network for collocation of GNSS and other space techniques underpinned this study. The results of the various comparison tests from this study are affirmative of the fact that the choice of GNSS receiver could significantly influence parameters estimated from data logged by them, as summarised in Table 4. Thus, we recommend further study of the performance of geodetic grade receivers over a longer period to study the possible effects of GNSS receiver clock stability adequately and it consequential effects on parameters estimated from them. The results of our study are preliminary in the sense that more complex statistical tests and a longer period are required to further validate how the differences observed in estimated parameters from receivers can influence scientific applications.

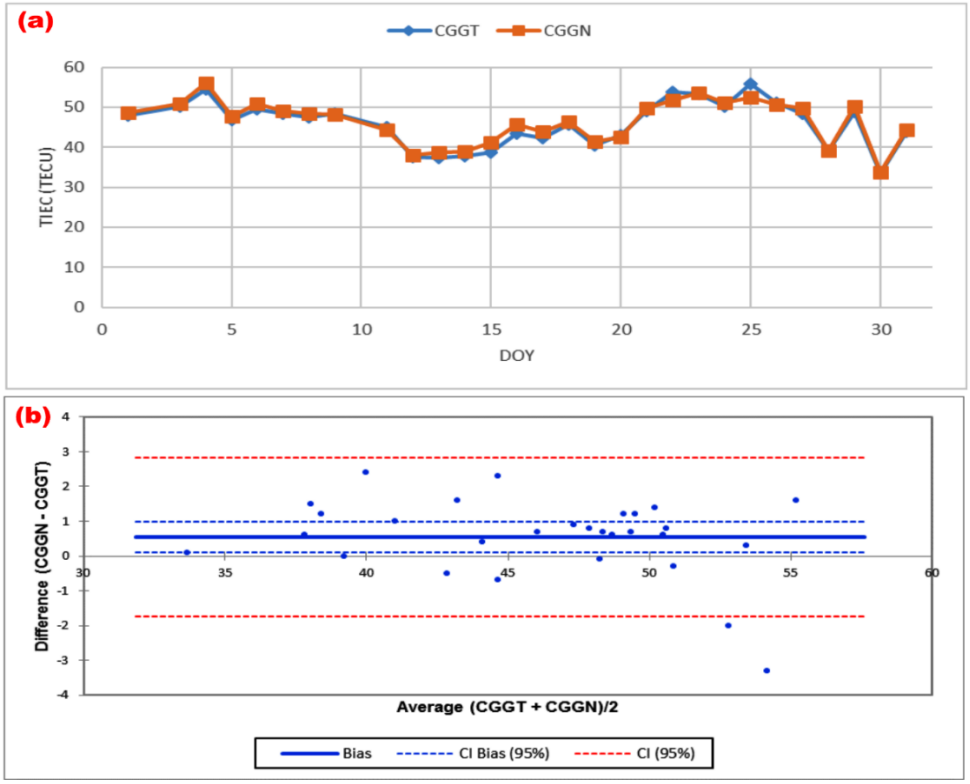

Figure 13: TEC estimated from the duo receiver: a) Time series plot of estimated TEC from the dual receivers b) Bland and Altman (difference) plot of estimated TEC from the dual receivers

Table 4: Summary of hypothesis test of estimated parameters

Estimate Parameters	Hypothesis Test	Risk
UTM Coordinate (Easting)	H_0 is not rejected	6.98%
UTM Coordinate (Northing)	H_0 is not rejected	16.51%
UTM Coordinate (Height)	H_0 is rejected and H_1 hypothesis accepted	0.59%
Tropospheric Zenith Delay	H_0 is rejected and H_1 hypothesis accepted	0.03%
Tropospheric Gradient (North Component)	H_0 is not rejected	43.97%
Tropospheric Gradient (East Component)	H_0 is not rejected	56.24%
Receiver Code Bias	H_0 is rejected and H_1 hypothesis accepted	0.01%
Total Electron Content	H_0 is rejected and H_1 hypothesis accepted	1.82%

Acknowledgement
The authors wish to express their profound gratitude to the numerous reviewers for their productive observations that helped to improve the manuscript. The authors thank CODE for making the DCBs files used in this study publicly available. We wish to thank the office of the Surveyor General of the Federal Republic of Nigeria and CDDIS for the GNSS data. Finally, thanks also go to Gopi Seemata for providing the GPS TEC analysis software and Prof Lambert Wanninger for the Wasoft software license.

References

Chuang, Y.C. and I. J. Gupta (2013). Antenna Induced Biases in GNSS Receiver Measurements. Proceedings of the International Technical Meeting of the Institute of Navigation. San Diego, CA, USA. (28–30): 164–171.

Cuntz, M., A. Konovaltsev, and M. Meurer (2016). Concepts, Development, and Validation of Multiantenna GNSS Receivers for Resilient Navigation. Proc. IEEE. (104):1288–1301. doi: 10.1109/JPROC.2016.2525764.

Dodo, J.D., T.A Yakubu, E.S. Usifoh, and A.M. Bojude (2011). ITRF 2008 Realization of the Nigerian Geocentric Datum (GDN2012): Preliminary Results. Journal of Emerging Trends in Engineering and Applied Sciences (JETEAS). 2(6):978-986.

Dow, J. M., R. E. Neilan, and C. Rizos (2009). The International GNSS Service in a Changing Landscape of Global Navigation Satellite Systems. *J Geod*, 83:191-198.

Gupta, I.J., I.M. Weiss, and A.W. Morrison (2016). Desired Features of Adaptive Antenna Arrays for GNSS Receivers. Proceedings of IEEE. (104):1195–1206. doi: 10.1109/JPROC.2016.2524416.

Isioye, O. A., L. Combrinck, and O. J. Botai (2017). Evaluation of Spatial and Temporal Characteristics of GNSS-derived ZTD Estimates in Nigeria. Theoretical and Applied Climatology, A publication of Springer-Verlag Wien, 1-18.

Isioye, O. A., L. Combrinck, and O. J. Botai (2017). Retrieval and Analysis of Precipitable Water Vapour Based on GNSS, AIRS, and Reanalysis Models over Nigeria. International Journal of Remote Sensing, 38(20): 5710-5735.

Jatau, B., M., Rui, A. Adeyemi, and G. Nuno (2010). NIGNET: The New Permanent GNSS Network of Nigeria. FIG Congress 2010: Facing the Challenges – Building the Capacity, Sydney: Australia. http://fig.net/pub/fig2010/papers/fs02h%5Cfs02h_jatau_fernandes_et_al_4549.pdf.

Kouba, J. (2009). A Guide to Using International GNSS Service (IGS) Products. Retrieved online from: http://igs.org/igscb/resource/pubs/UsingIGSProductsVer21.pdf

Moses, M., J. D., Dodo, and L. M. Ojigi (2017). Spatio-temporal and Solar Activity Variation of Ionospheric Total Electron Content over the Nigerian GNSS CORS. Conference of the Nigerian Association of Geodesy (NAG), Rivers State University, Port Harcourt, Rivers State, Nigeria, from 24th-27th October, 2017.

Naibbi, A. I. and S. S. Ibrahim (2014). An Assessment of the existing Continuously Operating Reference Stations (CORS) in Nigeria: An Exploration using Geographical Information System (GIS). American Journal of Geographic Information Systems, 3(4):147–157.

Odolinski, R. and P. Teunissen (2016). Single-frequency, Dual-GNSS versus Dual-frequency, Single-GNSS: a Low-cost and High-grade Receivers GPS-BDS RTK Analysis. Journal of Geodesy. 90(11): 1255-1278.

Schwieger, V. (2007). High-Sensitivity GPS – The Low Cost Future of GNSS. FIG Working Week, Hong Kong, 13-17 May, 2007. pp. 1-16.

Sousa, F. and F. Nunes (2014). Performance Comparison of a VDFLL versus VDLL and Scalar GNSS Receiver Architectures in Harsh Scenarios, ESA Workshop on Satellite Navigation User Equipment Technologies (NAVITEC), Noordwijk, Netherlands, Vol. 1, pp. 1 - 8

Takasu, T. and A. Yasuda (2008). Evaluation of RTK-GPS Performance with Low-Cost Single-Frequency GPS Receivers. Proceedings of International Symposium on GPS/GNSS, Tokyo. pp. 852-861.

Vagle, N., A., Broumandan, and G. Lachapelle (2016). Analysis of Multi-Antenna GNSS Receiver Performance under Jamming Attacks. Sensors (Basel, Switzerland). 16(11): 1937.

Journal of Geomatics Vol 12 No. 1 April 2018

Evaluation of the performance of the fused product of Hyperion and RapidEye red edge bands in the context of classification accuracy

Ritu Anilkumar, Dibyajyoti Chutia, Jonali Goswami, Vikas Sharma and PLN Raju
North Eastern Space Applications Centre, Department of Space, Government of India
Umiam, Shillong, Meghalaya, India- 793103
Email: ritu.anilkumar@nesac.gov.in, d.chutia@nesac.gov.in,
jonali.goswami@gmail.com, vikashsharmamy@gmail.com, raju@nesac.gov.in

(Received: Feb 07, 2018; final form: Apr 16, 2018)

Abstract: Satellite images are characterized by a large number of features in spectral and spatial domain. However, due to SNR constraints, development of a high spatial resolution and spectral resolution sensor is challenging. Hence, fusion techniques were developed for incorporating the spatial characteristics from a high spatial resolution multispectral or panchromatic sensor and the spectral information from the hyperspectral sensor of low spatial resolution. Here, the fusion was achieved by utilizing the Gram-Schmidt orthogonalization procedure and classification was performed on the obtained high spatial and spectral resolution image and a case study over the Dhemaji and Lakhimpur districts of Assam, India was performed. Investigations were carried out utilizing the Hyperion image, RapidEye image, fused image and the Red Edge subsets of the Hyperion and fused data sets where a number of vegetation, water and land cover classes have been selected for three test sites. All comparisons were performed using standard supervised classifiers such as maximum likelihood classifier, spectral angle mapper and support vector machines with the polynomial and radial basis function kernel. RapidEye data classifies the scene best with the MLC classifier. SVM classifiers with RBF or polynomial kernels perform consistently better with Hyperion and fused data sets. Red Edge subsets of the Hyperion and fused images are observed to perform well with both MLC and SVM classifiers.

Keywords: Hyperspectral remote sensing, Hyperion, Fusion, Classification, Red Edge, Spectral sharpening

1. Introduction

The economy of India is primarily agrarian with 56.3% of its population dependent upon agriculture as a source of income and 17.32% contribution to the GDP (Ministry of Statistics and Programme Implementation). Modern agriculture has seen rapid improvements starting with mechanization during the industrial revolution to manipulation of the genetic structure of the crop. Technological advancements in the form of accurate navigation systems and sophisticated satellite and airborne sensors have permitted large scale monitoring of agricultural structures. Over the last decade, space based instruments such as RapidEye, QuickBird, LandSat, CartoSat, Hyperion, Compact High Resolution Imaging Spectrometer/Proba (CHRIS/Proba) etc have gained much importance in precision agriculture. This is particularly reflected in the introduction of the Red Edge band in the sensors. Red Edge refers to the sharp increase in reflectance as observed in the vegetation spectrum beyond the red wavelengths, generally from 680-750 nm (Vogelmann, 1993, Penuelas et. al., 1995, Cho et. al., 2008). Horler et. al. 1983, Dawson and Curran, 1998 and Schulster et. al., 2012 document two reasons for this prominent Red Edge in vegetation: (1) strong chlorophyll absorption in the red region of the electromagnetic spectrum and (2) high internal leaf scattering causing a strong reflectance of the near infrared region of the electromagnetic spectrum.

1.1 Classical techniques and challenges

Early studies in crop stage discrimination, plant health monitoring or even species identification using the Red Edge region were established (Gupta et. al. 2003, Smith et. al. 2004). However, the large weight of the instruments and costs associated with such techniques led to the necessity of using broad band, multispectral sensors for the same. Plenty of studies have performed classification of multispectral images utilizing spectral indices generated out of manipulating the features of the spectrum (Jackson and Huete, 1991, Schuster et. al., 2012, Ustuner et. al. 2015). However, these methods face a significant drawback as a result of the broad band nature of multispectral imaging being unable to map the finer aspects of the spectrum (Ferrato and Forsythe, 2012). To cater to this specific advantage, hyperspectral imaging sensors for space borne and airborne applications were developed and improved significantly over the last two decades (Pignatti et. al., 2009; Purkis and Klemas, 2011; Heiden et. al., 2012). Through hyperspectral imagery, we are now able to monitor crop health utilizing the chlorophyll and photosynthesis related absorptions at 437 (chlorophyll a), 460 (chlorophyll b), 642 (chlorophyll a) and 659 nm (chlorophyll b) (Porra et. al., 1989, Penuelas et. al., 1995, Wu et. al., 2008), 705 nm (chlorophyll absorption Wu et. al., 2008), 530, 735 nm (indicating photosynthesis Lang et. al., 1991). Soil moisture studies can be performed to optimize growth parameters possible in VNIR as well as SWIR due to soil-water interactions from 350 nm to 2500 nm (Gao, 1996, Ceccato et. al., 2001, Champagne et. al., 2003, Stimson et. al., 2005). Vegetation parameters such as Leaf Area Index, biomass are estimated using the Red Edge specifically from 680 to 750 nm (Vogelmann, 1993, Penuelas et. al., 1995, Cho et. al., 2008). Plant physiological parameters including nitrogen content using 1510, 1680 nm bands (Penuelas et. al. 1995, Serrano et. al., 2002), lignin using 1680 and 1754 nm bands and cellulose quantification using bands from 2000

to 2200 nm (Serrano et. al., 2002, Daughtry et. al. 2006) can be achieved. Moisture related plant stress can also be studied due to the water absorptions at 1400 and 1900 nm (Gao 1996, Ceccato et. al. 2001).

1.2 Motivation and contributions

Hyperspectral imagery permits a precise measurement of the radiant flux (Jensen and Im, 2007) and the differentiation of a variety of agricultural species and crop health stages. They however fail spatially due to the trade-off between spectral resolution, spatial resolution and Signal to Noise Ratio (SNR) (Yokoya et. al., 2017). This inherent trade-off between spatial resolution, spectral resolution and SNR prompted the necessity to use image processing techniques to use the spatial information of high resolution panchromatic imagery and spectral information from hyperspectral imagery thereby metaphorically being able live in the best of both worlds. This process is called fusion. The fused data sets along with hyperspectral and multispectral data sets were compared for their classification accuracy using standard classifiers such as support vector machines (SVM), spectral angle mapper (SAM) and maximum likelihood classifier (MLC). The major contributions of this study are summarized as follows:

1. Performing fusion of Hyperion data set with the Red Edge band of the RapidEye data set via the technique of Gram Schmidt spectral sharpening to yield a high spatial and spectral resolution image.

2. Classification of the multispectral image, hyperspectral image and fused image using SVM (using radial basis function (RBF) kernel and polynomial kernel of order 3), SAM and MLC to evaluate the utility of the fused product.

2. Data used and study area

This study attempts to characterize vegetation by emphasising on the Red Edge bands of Hyperion data and compare classification results of hyperspectral imagery from Hyperion, multispectral imagery from RapidEye and a fused product of the same. Characteristics of the Hyperion and RapidEye sensors are tabulated in table 1.

2.1 Satellite imagery used

Earth Observer-1 Hyperion: Hyperion (Pearlmann, et al., 2003) is a hyperspectral sensor on board the NASA (National Aeronautics and Space Administration) Earth Observer 1 (EO-1) which functioned from November, 2001 to April, 2016. With a 242 channels ranging from the VNIR (Visible and Near Infrared) to SWIR (Short Wave Infrared), 400 to 2500 nm, Hyperion images at a spatial resolution of 30m and a radiometric resolution of 12bits. Hyperion data is available as level 1, radiometrically calibrated product (Level 1R) as well as geometrically corrected and georeferenced data (Level1 GST and IT) at the USGS (United States Geological Survey) website Earth Explorer: https://earthexlorer.usgs.gov. Each of these datasets need to be further corrected before they can be used to develop products of our interest. Of the 242 bands, some are highly noisy and a redundancy exists due to the overlap of detecting regions by the VNIR and SWIR detector. Hence we ignore these bands and the total usable bands comes down to 196 (1-7, 58-78 and 225-242 are removed). This is followed by correction due to effects of the atmosphere. The corrections often reduce the SNR. To correct for this, attempts to separate the noise from the data are performed using the Minimum Noise Fraction (MNF) denoising technique (Green et. al., 1998).

RapidEye: The RapidEye constellation is a set of 5 satellites designed and developed by Surrey Satellite Technology Ltd in 2008 and later acquired by Planet in 2015. It provides imagery of 5m/pixel spatial resolution in 5 bands (red, green, blue, red-edge and near infrared) available at the Planet Server webpage. With an elevation of 630km and a 77km swath, RapidEye has a revisit time of 5.5 days at nadir. All five satellite sensors are calibrated similarly leaving no distinction between satellite imagery from any sensor. The mosaic of 5 level 3 ortho-corrected imagery was used for this study. Atmospheric correction was performed using the Quick Atmospheric Correction (QuAC) technique. (Bernstein et al., 2005).

2.2 Study area

The study area is the Dhemaji and Lakhimpur region of Assam which is abundant in rice crop cultivation. Hence, the Red Edge region is specifically used for further discrimination within the vegetation class. Dhemaji district of Assam is bounded by Arunachal Pradesh in the North and the river Brahmaputra in the South. It is a plain area with an average elevation of 104 m above sea level. Numerous drainage systems originating from the hills of Arunachal Pradesh flow through Dhemaji to drain into the Brahmaputra. Physiographically, Dhemaji is in the form of three main sub districts: the piedmont zone where Dhemaji borders the Arunachal Himalayas, the active flood plains near the river Brahmaputra and its tributaries, and the low lying alluvial belt.

Table 1: Sensor information for the Hyperion and RapidEye instruments

Instrument/ Parameter	Wavelength Range nm	No of spectral channels	Spectral Resolution	Spatial Resolution	Quantization
EO-1/Hyperion	400-2500	242	10nm (detector dependant)	30m	12 bits
RapidEye	440-850	5	non-uniform	5m	12 bits

With a total geographic area of 323,700 ha. Dhemaji covers a variety of socio-geographic features including build up (208 ha), horticultural lands (2534 ha), forest cover (53,225 ha) and grasslands (97,167 ha), making it a perfect study area for the classification techniques aimed towards vegetation. Three Test Sites were selected across Dhemaji and Lakhimpur and data of Hyperion and RapidEye taken on October, 2012 were analysed and regions of interest were selected based on the existing Land Use Land Cover (LULC) map for 2011-2012. Each region and the subsequent classes we have classified into are summarized below. The Test Sites used for the study are depicted in figure 1. Details of training and test samples are available in table 2-4.

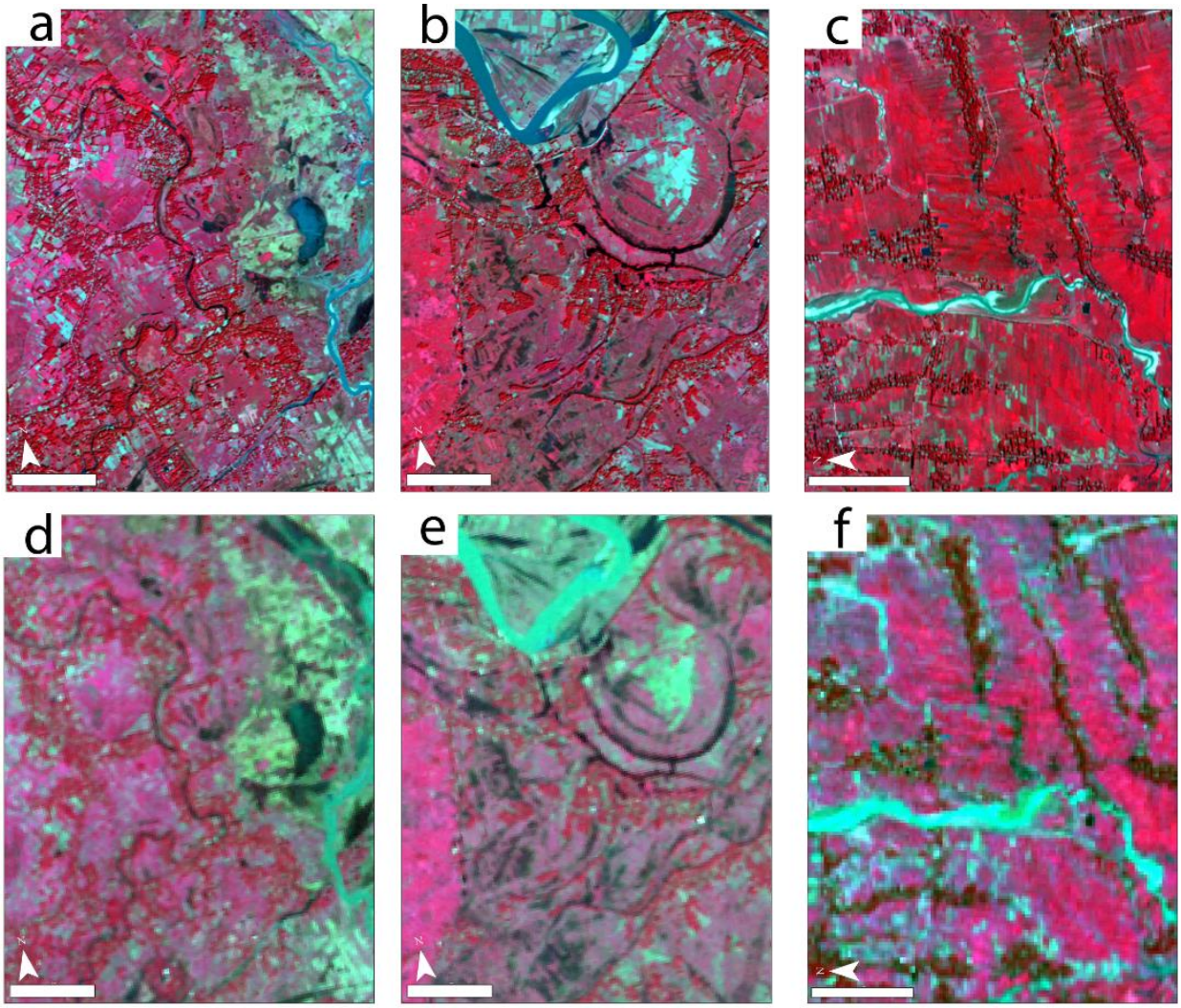

Figure 1: False colour composite (NIR, Red, Green) for Test Site 1, 2 and 3 respectively obtained using RapidEye (fig: 1a-1c, band combination: 5, 3 and 2) and Hyperion data sets (fig: 1d-1f, band combination: 44, 23 and 13)

Table 2: Information on the testing and training samples for each class of Test Site 1

S.No	Class name	Hyperion		RapidEye	
		Train Size	Test size	Train Size	Test size
1	Kharif crop	696	176	6162	4933
2	Open forest	358	156	12642	5455
3	Fallow	362	176	3322	3382
4	Water Body	293	154	4571	1576

Table 3: Information on the testing and training samples for each class of Test Site 2

S.No	Class name	Hyperion		RapidEye	
		Train Size	Test size	Train Size	Test size
1	Kharif crop	180	628	5094	5563
2	Perennial River	149	323	2704	2580
3	Inland Wetland	140	240	1742	2115
4	Fallow	162	227	2846	2407
5	Open forest	168	261	3711	3064

Table 4: Information on the testing and training samples for each class of Test Site 3

S.No	Class name	Hyperion		RapidEye	
		Train Size	Test size	Train Size	Test size
1	Open forest	223	260	1276	1330
2	Perennial River	172	190	761	1860
3	Fallow/Sandy	128	108	732	1207
4	Kharif Crop	190	262	6862	2283
5	Double Crop	119	119	4305	1516

Test Site 1: This Test Site depicts mainly the following features in the LULC map. A perennial and non-perennial drainage system, agricultural lands, fallow lands and open forests surrounding the rural build up near the water bodies. As the rural build up was evident only in the form of a few pixels in the RapidEye image, we have selected four classes for this site: (1) water body, (2) vegetation type 1 for agricultural lands of the kharif crop, (3) vegetation type 2 for dense open forest regions intermingled with rural build up and (4) fallow lands.
Test Site 2: This site is geographically similar to site one. There exists a perennial water body as well as waterlogged regions, agricultural lands, fallow lands and open forest around rural build up. Five classes were selected: (1) water body (perennial), (2) vegetation type 1 for agricultural lands (kharif), (3) vegetation type 2 for open forests, (4) fallow lands and (5) water logged inland wetlands. The similarity with site 1 was maintained so that accuracies could be checked in varying the number of classes.

Test Site 3: Five classes were selected for this site. However, a larger variety of vegetation types were selected to check if the Red Edge bands could accurately assess the class type. The classes selected are as follows: (1) water body, (2) vegetation type 1 for agricultural lands, (3) vegetation type 2 for agricultural lands, (4) open forests and (5) barren/fallow lands.

3 Methodology

A Hyperion strip over the Dhemaji and Lakhimpur districts of Assam taken on October, 2012 was used. RapidEye images over the same site for October, 2012 at similar local times were mosaicked and subsetted to the same areal extent as the Hyperion data. This was followed by georeferencing the Hyperion data set to the RapidEye data set using control points. Once both datasets were prepared, the processing in the form of bad band removal was performed for Hyperion and atmospheric corrections were performed on both Hyperion and RapidEye images. The corrected and georeferenced images were fused using the Gram-Schmidt hyperspectral sharpening method. The original Rapid Eye image, Hyperion image and fused image is displayed in figure 2 a, b and c respectively. The spectral characteristic of the region is as observed in figure 3 a, b and c. Hyperspectral datasets require significant denoising for enhanced spectral understanding. Hence, the MNF transformation as implemented by Green et. al., 1998 was used. A spectral subset of the fused image and the Hyperion image in the Red Edge region was also considered to understand if a Red Edge based classification depicts superior results in the case of vegetation classification.

3.1 Fusion

Multiple previous studies (Chutia et al, 2010, Pohl, 2013, Akhtar et. al., 2015, Yokoya et. al., 2017) have been performed using fusion of hyperspectral or multispectral images and panchromatic high resolution images. Yokoya et. al., 2017 has further performed a comparison of results for the different fusion methods for a variety of datasets including AVIRIS, HyDICE etc. Many fusion algorithms exist which vary in the accuracy either resulting in spatial or spectral distortions (Zhang et. al., 2007; Yakoya et. al., 2012; Qian and Chen, 2012). Recent years have seen more sophisticated attempts at the hyperspectral fusion challenge. Chen et.al.., 2014 performed fusion by dividing the multispectral image into individual bands and hyperspectral image into segments of bands centred around a corresponding multispectral band and performed pan sharpening on each segment. In this study, we use the Gram Schmidt spectral sharpening method (Laben and Brower, 2000; Maurer, 2013).

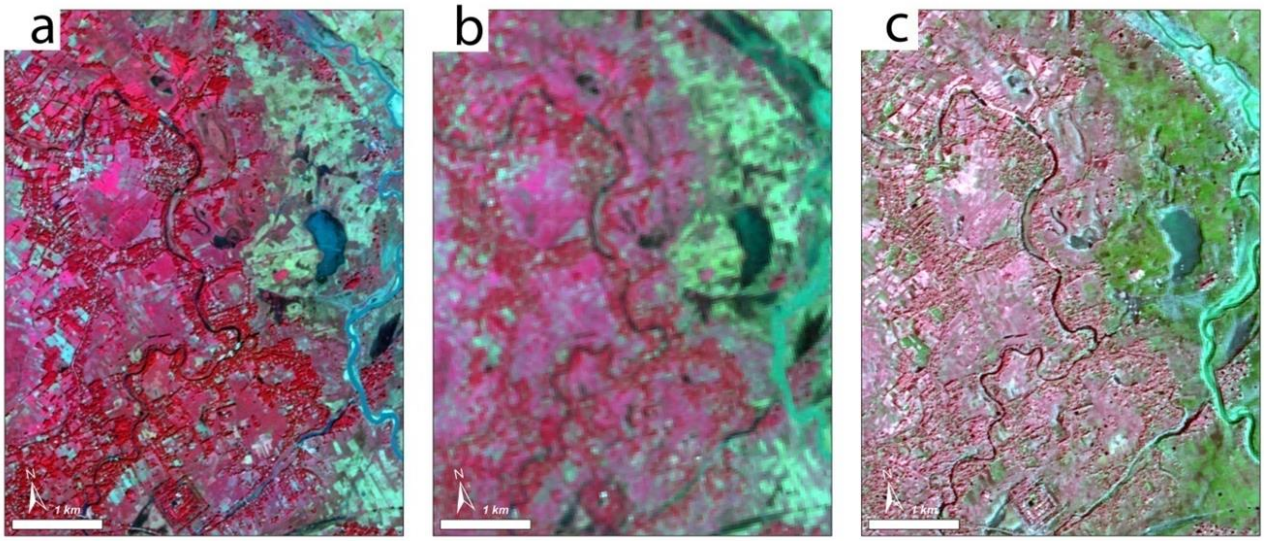

Figure 2: Spatial characteristics of the (a) RapidEye image, (b) Hyperion image and (c) Fused image as observed over Test Site 1

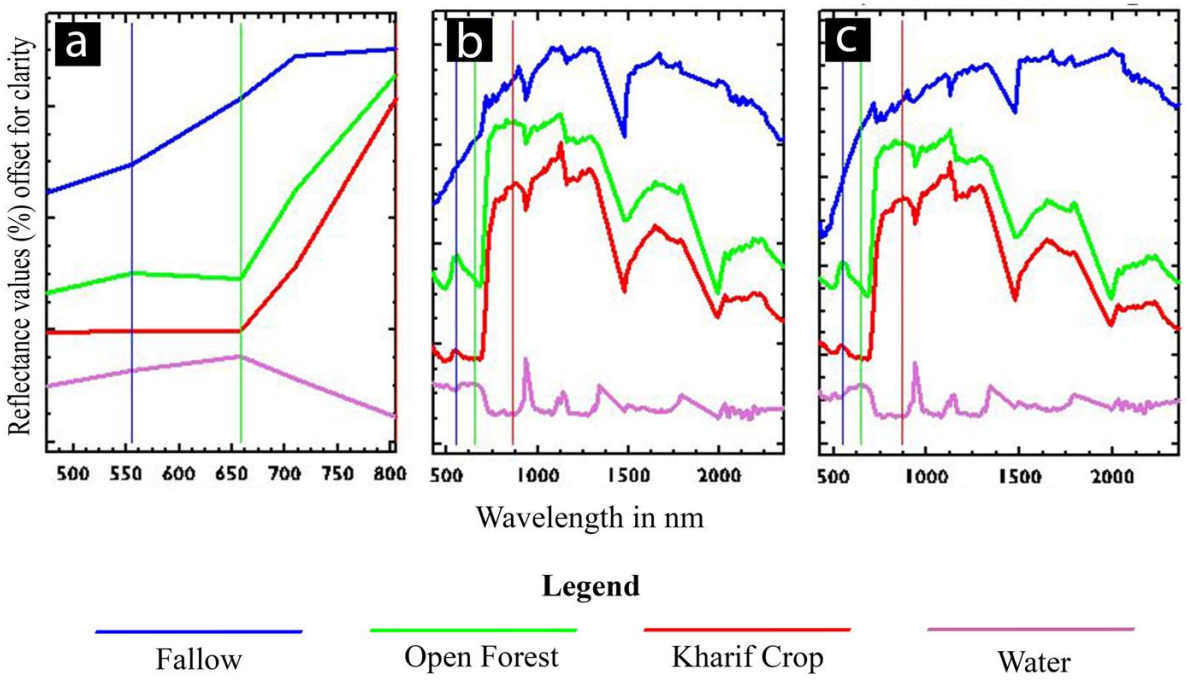

Figure 3: Spectral characteristics of the (a) RapidEye image, (b) Hyperion image and (c) Fused image as observed over Test Site 1

This involves the hyperspectral image combined via a linear combination by using weights to represent it as a panchromatic image.

$$PAN_{sim} = \sum_{i=1}^{N} w_i H_i \quad \text{... (1)}$$

This is followed by the Gram Schmidt orthonormalization of the vectors in the N dimensional space where each band represents an N dimensional vector where N is the number of pixels. This procedure decorrelates the bands. The orthonormalization procedure involves the pan band taken as the first vector (v_1). It follows the general formula as follows where u_i is the orthonormal vector and v_i is the original vector:

$$u_1 = v_1 \quad \text{... (2)}$$

$$u_i = v_i - \sum_{j=1}^{i-1} \left(\frac{u_j^T v_i}{u_j^T u_j} \right) v_i \quad \text{... (3)}$$

This is followed by replacing the averaged panchromatic image with the high spatial resolution panchromatic image and performing an inverse Gram Schmidt transform (similar to the forward transform). This gives us the fused product.

In order to check for the validity of the fused product, point to point spectral correlation was investigated between the fused data and the Hyperion data and the correlation coefficient and regression coefficient were calculated.

3.2 Classification

Three Test Sites within the Dhemaji-Lakhimpur region was considered. Classification was performed using ROIs derived from the LULC map and visual examination of the images. Hyperspectral classification techniques are adversely affected by the Houghes effect due to which the required number of training samples for larger number of bands increases to maintain the accuracy (Chutia et. al., 2015). Breunig et. al., 2011 suggest that the SVM and SAM classifiers do not demonstrate a reduction in accuracy. Hence, these two classifiers were used for the purpose. Classification was performed on the three test sites using RapidEye, Hyperion and the fused result of RapidEye and Hyperion with classes defined in accordance to the existing LULC map and the results were assessed by comparing the kappa coefficient and accuracy assessment. For a comprehensive list of hyperspectral classification techniques, refer to Chutia et. al., 2015.

3.2.1 Spectral Angle Mapper (SAM) Classifier

SAM is a classifier that compares the similarity between the test and training samples by considering the spectrum to be a D dimensional vector where D is given by the number of bands (Yuhas et. al., 1992). The training samples are either the laboratory spectra in the form of spectral libraries that have been resampled to the dimensionality of the test samples. Alternately, they are obtained from known regions within the satellite imagery that is being classified. This study uses ROIs as obtained from a ground survey performed in the Dhemaji and Lakhimpur district in 2012. Spectral similarity is estimated by calculating the angle between the test and training spectrum vectors.

$$\alpha = \cos^{-1}\left[\frac{\sum_{i=1}^{D} T_i R_i}{\left(\sum_{i=1}^{D} T_i^2\right)^{\frac{1}{2}}\left(\left(\sum_{i=1}^{D} R_i^2\right)^{\frac{1}{2}}\right)}\right] \text{---- (4)}$$

Larger angles suggest dissimilarity. An advantage SAM has over other traditional classifiers is the independence from intensity values permitting regions of shadow to also be classified accurately.

3.2.2 Support Vector machine (SVM) Classifier

SVM based classification is a well-recognized classification technique (Chutia et. al., 2014) where an N-1 dimensional hyperplane is used to separate the data by maximizing the margin between them. The hyperplane is called the optimal hyperplane and the data points closest to the hyperplane are the constraining factors and are called the support vectors (Suykens and Vandewalle, 1999). This suggests that SVM is a linear classifier. However, to account for non-linear classification, SVM can be used alongside kernels such as polynomial, RBF, sigmoid etc. (Sharma et. al., 2016). This study utilizes two commonly used kernels which have demonstrated significant success in the past (Gordon, 2004). The mathematical form of the polynomial kernel is given as below:

$$K(x, xi) = 1 + \sum_i (x * xi)^d \quad \text{... (5)}$$

Here, x is the input, xi is the support vector and d is the degree of the polynomial to be used. The RBF kernel expression is as follows:

$$K(x, xi) = e^{\left(-\Upsilon * (\sum_i (x - xi)^2)\right)} \quad \text{... (6)}$$

There are two parameters of concern that can be tweaked: the gamma parameter and the penalty parameter (Sharma et. al., 2016). The gamma parameter depicts the influence of the training sample with smaller values causing far reaching influence. The penalty parameter or the misclassification trade off parameter affects the smoothness of the decision boundary. Larger values cause over fitting.

3.2.3 Maximum Likelihood Classifier (MLC)

MLC is based on the Bayes law following posterior=prior*likelihood/evidence given by:

$$\mathrm{Lx} = \mathrm{P}\left(\frac{\omega}{\mathrm{x}}\right) = \frac{\mathrm{P}(\omega) * \mathrm{P}\left(\frac{\mathrm{x}}{\omega}\right)}{\mathrm{P}(\mathrm{x})} \quad \text{... (7)}$$

Generally, the prior probability of the for a class ω is assumed to be a constant or expected to be equal to each other and the evidence, P(x), is usually common to all classes, therefore L_x is dependent on P(x/ω). Classification is performed such that the likelihood of x belonging to a class ω is maximized (Strahler, 1980). Sampling should be such that the estimation of the mean and covariance is reflective of that of the population. The maximum likelihood method is not useful when the distribution of the population does not follow the normal distribution.

4. Results and discussion

For very small regions, we obtain better results using the higher spatial resolution images as expected. MLC consistently displayed best results with the RapidEye data due to the inferior performance of the classifier with higher number of bands (Houghes Phenomenon). For high inter class similarity, as is the case is for the water and vegetation classes in Test Site 2, we observe that the classification was performed best using the hyperspectral data of Hyperion and the Red Edge subset from the Hyperion data. Fused data is also observed to perform well in this case. For low interclass similarity in a small Test Site, however, we observe that fused data provides good results. However, the separability between the vegetated and non-vegetated classes is brought out better using the Red Edge subsets of the fused dataset and the Hyperion dataset. Thus the utility of the Red Edge subsetting for optimum feature extraction for classification is established. Details on the denoising, assessment of fusion and classification results are as documented in the following subsections.

4.1 Denoising Using the MNF Transform

The Eigen values and Eigen vectors of the image obtained are ordered (Figure 4). The image was then projected onto the Eigen space to decorrelate the bands and noise whitening was performed. The noise related Eigen values (normalized to 1) were discarded and the signal rich Eigen-images were employed for the inverse that generated us the denoised image that is used for classification.

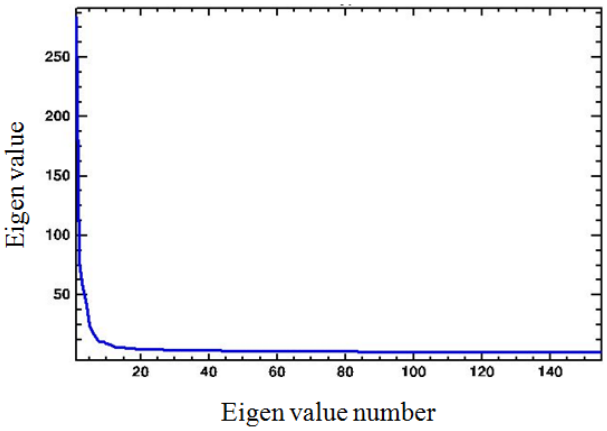

Figure 4: Eigen value graph based on which we select the Eigen values that can be used to maximize the SNR

4.2 Spectral characteristics of the fused product

From figure 5, we observe that the Gram Schmidt spectral sharpening leads to an offset in the intensity values of the fused product. In order to study if any distortion occurs or if the difference lies solely in the offset, we have performed a correlation test on the data set. Ten random regions were selected from both the Hyperion image and the fused image. The average spectrum of each region was computed and a scatter plot was used to check for the correlation. Very high correlation was observed with an average Pearson coefficient of correlation as 0.998 (Figure 6).

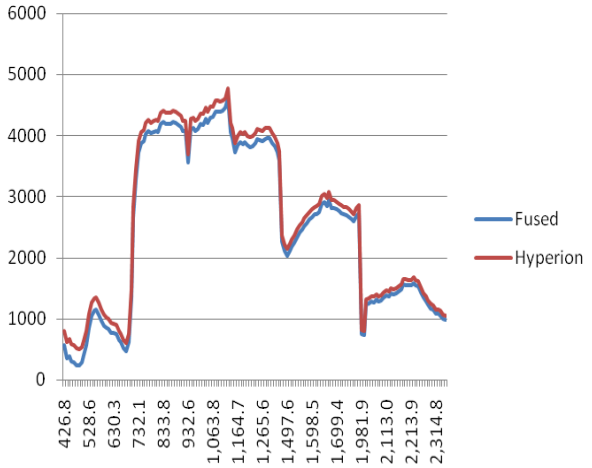

Figure 2: Spectrum of a vegetated region as displayed by the fused image and the Hyperion image after all corrections have been performed. X axis is wavelength in nm and y axis is reflectance.

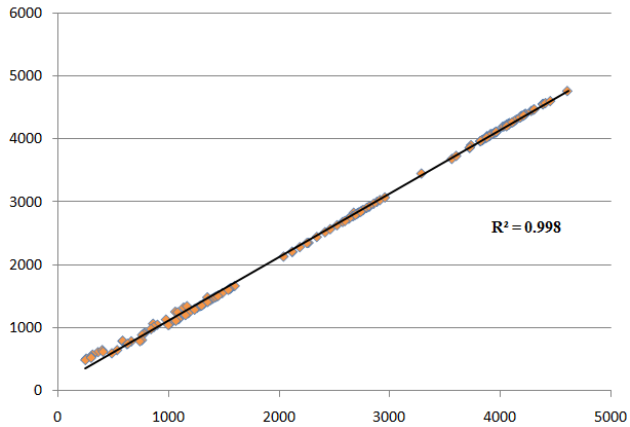

Figure 3: Scatter plot between fused spectra and Hyperion spectra

4.2 Classification results

The results of classification accuracy in the form of overall accuracy and kappa coefficients are documented in the tables 5-7.

Test site 1 classification yields a maximum accuracy by the Red Edge bands subset of the Hyperion image. However, the fused image and the Red Edge subset also depict similar high accuracy. The RapidEye image yields a maximum accuracy with the ML classifier, the fused image with the SVM classifier and the Hyperion image with the SVM classifier. The Red Edge spectral subsets of the fused and Hyperion image presented highest accuracies for the ML and the SVM classifiers respectively. The SVM classification results for each dataset for the test site is given in figure 6.

Test site two portrays a maximum accuracy for the RapidEye image with the ML classifier and the Hyperion image with the SVM classifier. The Red Edge spectral subset of the Hyperion also presents a comparable accuracy followed by the fused data set and the spectral subset of the same. The RapidEye image accuracies follow the order of ML, SVM and finally SAM classifiers. The Red Edge subset of Hyperion also follows the same order as expected. The Red Edge subset of the fused subset depicts a deviation from the expected results with SVM performing better than MLC in spite of the reduced number of bands. However, the Hyperion image and the fused image follow the expected trend of SVM accuracies greater than the SAM accuracies and finally the ML accuracies. This arises due to the Houghes phenomenon. The SVM classification results for each dataset for the test site is given in figure 7.

Test site 3 depicts maximum accuracies for the Hyperion image followed by the Red Edge subset of the Hyperion image. The RapidEye image and fused image classification results are also competitive. However, the Red Edge subset of the fused image displays a significantly deteriorated accuracy level. The performance of SVM is better in images with larger bands such as Hyperion and the fused product. SVM and ML classifiers perform comparably for the Red Edge subsets. However, the RapidEye image due to its minimum spectral bands and

high spatial resolution demonstrate a high accuracy with the ML classifier. ML classified output for Hyperion is not available due to lack of training samples. The SVM classification results for each dataset for the test site is given in figure 8.

Table 5: Table depicting overall accuracy and kappa coefficient for the RapidEye, Fused, Red Edge of Hyperion, Red Edge of Fused image and Hyperion images classified using the SAM, MLC, SVM with Polynomial order 3 and RBF kernel classifiers for Test Site 1

	SVM		SAM		MLC		SVM Poly	
	Kappa	Accuracy in %	Kappa	Accuracy in %	Kappa	Accuracy in %	Kappa	Accuracy in %
RapidEye	0.91	93.35	0.76	83.06	0.92	94.48	0.90	93.24
Fused	0.96	97.13	0.64	74.03	0.64	73.43	0.96	97.03
Red Edge Fused	0.93	95.16	0.70	78.28	0.95	96.57	0.93	95.02
Red Edge Hyperion	0.96	97.28	0.71	78.55	0.94	95.47	0.95	96.53
Hyperion	0.93	94.71	0.83	87.61	0.61	70.09	0.94	95.47

Table 6: Table depicting overall accuracy and kappa coefficient for the RapidEye, Fused, Red Edge of Hyperion, Red Edge of Fused image and Hyperion images classified using the SAM, MLC, SVM with Polynomial order 3 and RBF kernel classifiers for Test Site 2

	SVM		SAM		MLC		SVM Poly	
	Kappa	Accuracy in %	Kappa	Accuracy in %	Kappa	Accuracy in %	Kappa	Accuracy in %
RapidEye	0.84	87.51	0.76	81.21	0.87	89.86	0.84	87.48
Fused	0.79	83.30	0.54	64.19	0.53	61.43	0.78	82.99
Red Edge Fused	0.76	81.61	0.64	72.31	0.74	79.52	0.76	81.55
Red Edge Hyperion	0.85	88.24	0.60	68.34	0.87	89.61	0.85	87.99
Hyperion	0.87	89.23	0.81	84.61	0.41	51.56	0.86	88.99

Table 7: Table depicting overall accuracy and kappa coefficient for the RapidEye, Fused, Red Edge of Hyperion, Red Edge of Fused image and Hyperion images classified using the SAM, MLC, SVM with Polynomial order 3 and RBF kernel classifiers for Test Site 3

	SVM		SAM		MLC		SVM Poly	
	Kappa	Accuracy in %	Kappa	Accuracy in %	Kappa	Accuracy in %	Kappa	Accuracy in %
RapidEye	0.69	74.91	0.57	65.41	0.70	75.79	0.51	59.81
Fused	0.52	61.14	0.46	56.37	0.32	42.68	0.69	75.01
Red Edge Fused	0.51	60.37	0.45	56.33	0.51	60.05	0.51	60.10
Red Edge Hyperion	0.72	77.53	0.48	59.32	0.72	77.85	0.72	78.06
Hyperion	0.73	78.38	0.65	73.16	N/A	N/A	0.74	79.45

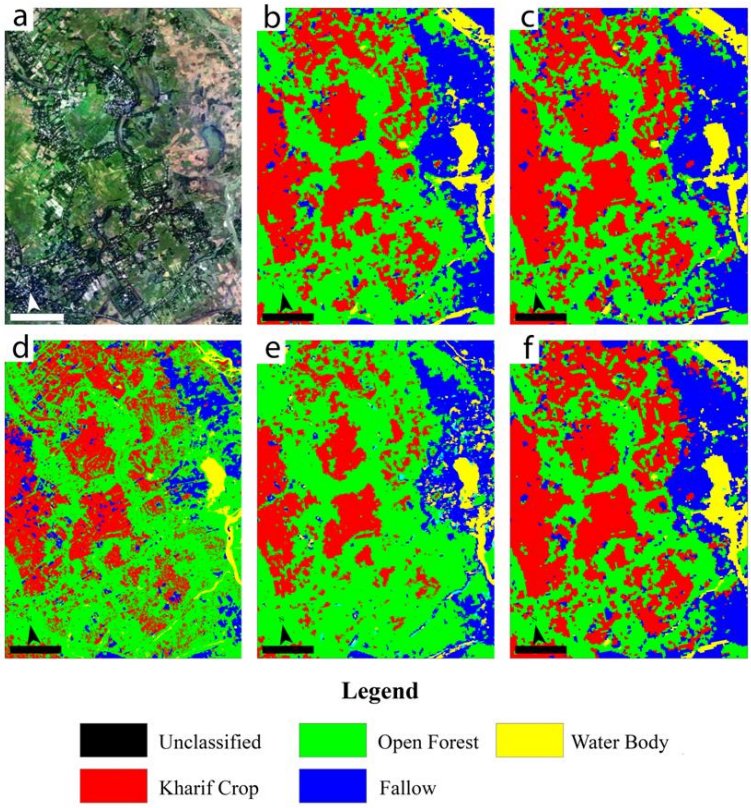

Figure 4: (a) RapidEye image as a reference, (b) the fused image classification results, (c) Hyperion image classification results, (d) RapidEye image classification results, (e) Red Edge subset of the fused image classification result and the (f) Red Edge subset of the Hyperion image classification result for Test Site 1

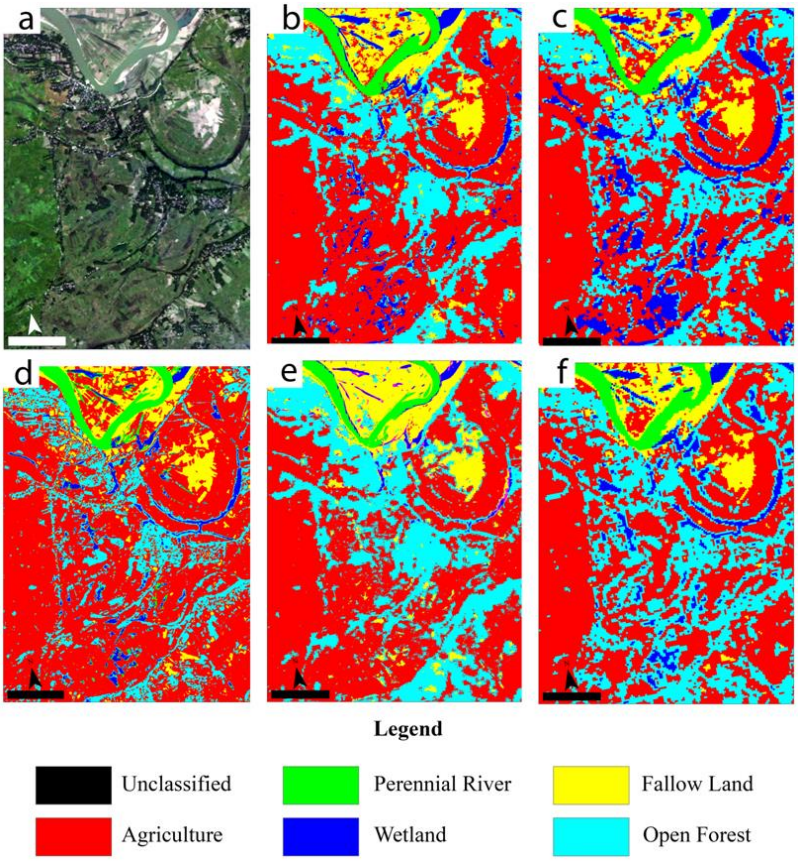

Figure 5: (a) RapidEye image as a reference, (b) the fused image classification results, (c) Hyperion image classification results, (d) RapidEye image classification results, (e) Red Edge subset of the fused image classification result and the (f) Red Edge subset of the Hyperion image classification result for Test Site 2

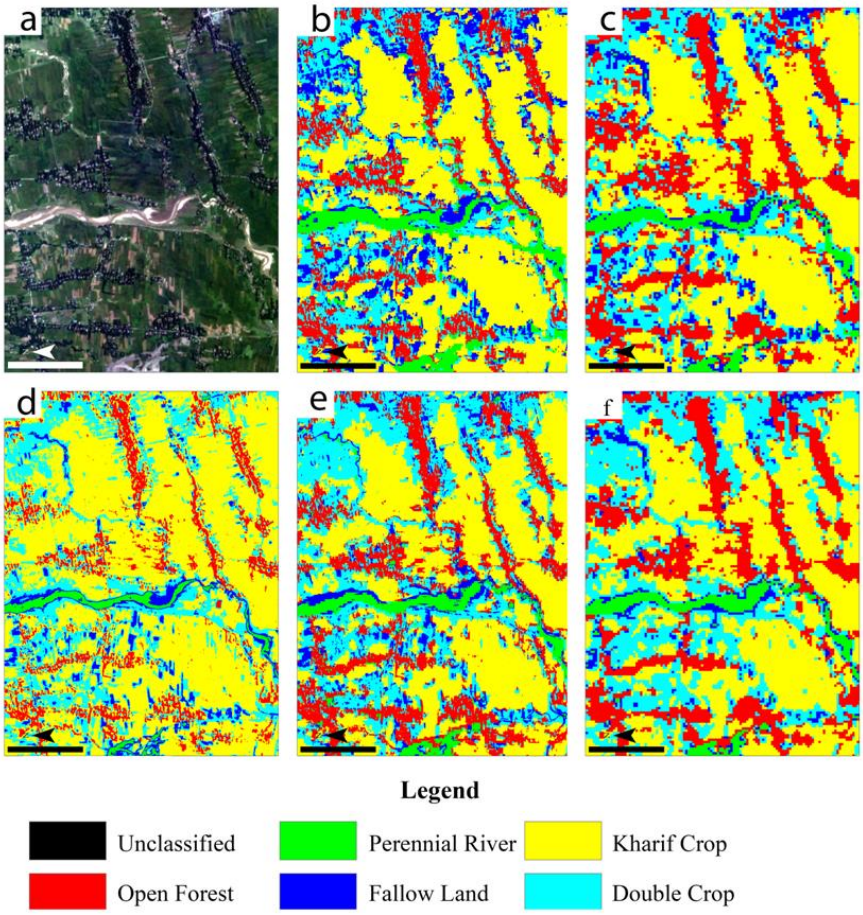

Figure 6: (a) RapidEye image as a reference, (b) the fused image classification results, (c) Hyperion image classification results, (d) RapidEye image classification results, (e) Red Edge subset of the fused image classification result and the (f) Red Edge subset of the Hyperion image classification result for Test Site 3

5. Conclusion

Satellite images permit accurate mapping of the land cover via high spatial resolution multispectral images such as those of RapidEye, CartoSat, SkySat, PlanetScope, WorldView series etc. However, to distinguish within the more similar land use features, spectral identification is required. The use of hyperspectral imagery thus provides additional spectral features for use in the various classification techniques. However, due to the low spatial resolution of hyperspectral imagery, the fused products were generated and their utilities tested with established classification techniques. Our results suggest optimal classifiers to be used with the types of data are independent of the test site and depend only upon the sensor and number of bands. RapidEye data classifies the scene best with the MLC classifier. However, as the number of bands increases as is the case with the fused or Hyperion images, MLC responds in a sub-optimal manner. SVM classifiers with RBF or polynomial kernels perform consistently better. Red Edge subsets of the Hyperion and fused images are observed to perform well with both MLC and SVM classifiers. With regard to the Test Sites, RapidEye images can be directly used for classification in case of diverse and less number of classes. Hyperion data can be used where there exists similarity within the data such as multiple vegetation classes where minute differences in the spectra come into consideration. However, best results are observed with the red edge subsets of the fused and Hyperion data sets. In case of small regions approaching the fused red edge subset performs better. However, if the spatial resolution of the Hyperion data is not limiting, it presents comparable results.

The fusion technique in this study exhibited good results in smaller regions where resolution of land cover classes at proximity are required. However, on larger scales, the results are obsolete when compared to hyperspectral image classification. This however can be improved by usage of other fusion techniques (Yokoya et. al., 2017, Akhtar et. al., 2015). An aspect to be considered for future applications include the utilization of high spatial resolution multispectral data via Unmanned Aerial Vehicles (UAV) or aircrafts with low resolution satellite based hyperspectral data for accurate cm level mapping and classification of the land use.

Acknowledgements

The authors would like to thank the facilities provided by North Eastern Space Applications Centre (NESAC), Department of Space, Government of India, Shillong, Meghalaya, India for providing the satellite datasets and the necessary scientific tools and environment to accomplished this work.

References

Akhtar, N., F. Shafait and A. Mian (2015). Bayesian sparse representation for hyperspectral image super resolution, In Proceedings of the IEEE Conference on Computer Vision and Pattern Recognition, 3631-3640.

Bernstein, L. S., Adler-Golden S. M., Sundberg R. L., Levine R.Y, Perkins T.C., Berk A., Ratkowski A.J., Felde G., Hoke M.L.., (2005). Validation of the QUick Atmospheric Correction (QUAC) algorithm for VNIR-SWIR multi- and hyperspectral imagery. SPIE Proceedings, Algorithms and Technologies for Multispectral, Hyperspectral, and Ultraspectral Imagery XI, 5806, 668-678.

Breunig, F.M., L.S. Galvao, A.R. Formaggio and J.C. Epiphanio (2011). Classification of soybean varieties using different techniques: case study with Hyperion and sensor spectral resolution simulations, Journal of Applied Remote Sensing, 5(1), 053533-053533.

Ceccato, P, Flasse S, Tarantola S, Jacquemond S, Gregoire J.M. (2001). Detecting vegetation leaf water content using reflectance in the optical domain. Remote Sensing of Environment, 77(1), 22-33

Champagne, C. M., Staenz K, Bannari A, McNairn H, DeGuise J.C. (2003). Validation of a hyperspectral curve-fitting model for the estimation of plant water content of agricultural canopies. Remote Sensing of Environment 87(2-3) , 148-160.

Cho, M. A., Sobhan, I., Skidmore, A. K., & De Leeuw, J. (2008). Discriminating species using hyperspectral indices at leaf and canopy scales. The International Archives of the Photogrammetry, Remote Sensing and Spatial Information Sciences, 37(B7), 369-376.

Chutia, D. and D.K. Bhattacharyya (2010). An efficient approach for extraction of linear features from high resolution Indian satellite imageries, PAN, 12000, 1223-1227.

Chutia, D., D.K. Bhattacharyya, K.K. Sarma, R. Kalita, and S. Sudhakar (2015). Hyperspectral remote sensing classifications: a perspective survey. Transactions in GIS, 20(4), 463-490.

Chutia, D., D.K. Bhattacharyya, R. Kalita and S. Sudhakar (2014). OBCsvmFS: Object-based classification supported by support vector machine feature selection approach for hyperspectral data Journal of Geomatics, 8(1), 12-19.

Daughtry, C. S., Doraiswamy, P. C., Hunt Jr, E. R., Stern, A. J., McMurtrey Iii, J. E., & Prueger, J. H. (2006). Remote sensing of crop residue cover and soil tillage intensity. Soil and Tillage Research, 91(1-2), 101-108.

Ferrato, L.J. and K.W. Forsythe (2012). Comparing hyperspectral and multispectral imagery for land classification of the lower Don river. Toronto, Journal of Geography and Geology, 5(1), 92-107.

Gao, B.C. (1996). NDWIA normalized difference water index for remote sensing of vegetation liquid water from space, Remote Sensing of Environment, 58.3, 257-266

Green, A.A., M.D. Craig, and C. Shi (1988). The application of the minimum noise fraction transform to the compression and cleaning of hyper-spectral remote sensing data, Geoscience and Remote Sensing Symposium, IGARSS'88, Remote Sensing: Moving Toward the 21st Century, International, 3, 1807-1807

Gupta, R.K., D. Vijayan and T.S. Prasad (2003). Comparative analysis of red-edge hyperspectral indices. Advances in Space Research, 32(11), 2217-2222.

Heiden, U., W. Heldens, S. Roessner, K. Segl,T. Esch, and A. Mueller (2012). Urban structure type characterization using hyperspectral remote sensing and height information, Landscape and urban Planning, 105(4), 361-375.

Jackson, R.D. and A.R. Huete (1991). Interpreting vegetation indices. Preventive veterinary medicine, 11(3-4), 185-200.

Jensen, J.R. and J. Im, (2007). Remote sensing change detection in urban environments, Geo-spatial technologies in urban environments, Springer Berlin Heidelberg, 7-31.

Laben, C.A. and B.V. Brower (2000) Eastman Kodak Company, Process for enhancing the spatial resolution of multispectral imagery using pan-sharpening, U.S. Patent 6,011,875.

Lang, M. F. Stober and H.K. Lichtenthaler (1991) Fluorescence emission spectra of plant leaves and plant constituents, Radiat Environ Biophys 30(4), 333-347.

Maurer, T. (2013). How to pan-sharpen images using the Gram-Schmidt pan-sharpen method-a recipe. International Archives of the Photogrammetry, Remote Sensing and Spatial Information Sciences, 1, 239-244.

Pearlman, J., P. Barry, C. Segal, J. Shepanski, D. Beiso, S. Carman (2003). Hyperion, a Space Based Imaging Spectrometer, IEEE Transactions on Geoscience and Remote Sensing, 41(6), 1160-1173.

Penuelas, J., F. Baret, and I. Filella. (1995) Semi-empirical indices to assess carotenoids chlorophyll a ratio from leaf spectral reflectance, Photosynthetica 31.2, 221-230.

Pignatti, S., R.M. Cavalli, V. Cuomo, L. Fusilli, S. Pascucci, M. Poscolieri, and F. Santini (2009). Evaluating Hyperion capability for land cover mapping in a fragmented ecosystem: Pollino National Park, Italy, Remote Sensing of Environment, 113(3), 622-634.

Pohl, C (2013). Challenges of Remote Sensing Image Fusion to Optimize Earth Observation Data Exploitation, European Scientific Journal, 4, 355-365

Porra R.J, Thomson W.A, Kriedemann P.E, (1989). Determination of accurate extinction coefficients and simultaneous equations for assaying chlorophylls a and b

extracted with four different solvents: verification of the concentration of chlorophyll standards by atomic absorption spectroscopy, Biochimica et Biophysica Acta (BBA) - Bioenergetics, 975(3), 384-394,

Purkis, S. J., and V.V. Klemas (2011). Remote Sensing and Global Environmental Change, Wiley-Blackwell ltd., 1-367

Schuster, C., M. Förster and B. Kleinschmit (2012). Testing the Red Edge channel for improving land-use classifications based on high-resolution multi-spectral satellite data, International Journal of Remote Sensing, 33(17), 5583-5599.

Serrano, L., J. Penuelas J, and Ustin S.L. (2002). Remote sensing of nitrogen and lignin in Mediterranean vegetation from AVIRIS data: Decomposing biochemical from structural signals, Remote Sensing of Environment, 81(2-3), 255-264

Sharma, V., D. Baruah, D. Chutia, P.L.N. Raju and D.K. Bhattacharya (2016). An assessment of support vector machine kernel parameters using remotely sensed satellite data, In Recent Trends in Electronics, Information & Communication Technology (RTEICT), 1567-1570.

Smith, K.L., M.D. Steven, and J.J. Colls (2004). Use of hyperspectral derivative ratios in the red-edge region to identify plant stress responses to gas leaks, Remote sensing of environment, 92(2), 207-217.

Stimson, H. C., Breshears, D. D., Ustin, S. L., & Kefauver, S. C. (2005). Spectral sensing of foliar water conditions in two co-occurring conifer species: Pinus edulis and Juniperus monosperma. Remote Sensing of Environment, 96(1), 108-118.

Strahler, A. H. (1980). The use of prior probabilities in maximum likelihood classification of remotely sensed data, Remote Sensing of Environment, 10(2), 135-163.

Suykens, J. A., & J. Vandewalle (1999). LEast squares support vector machine classifiers. Neural processing letters, 9(3), 293-300.

Ustuner, M., F.B. Sanli and B. Dixon (2015). Application of support vector machines for landuse classification using high-resolution RapidEye images: a sensitivity analysis, European Journal of Remote Sensing, 48(1), 403-422.

Vogelmann, T.C. (1993). Plant tissue optics, Annual review of plant biology, 44(1), 231-251

Wu, C., Niu, Z., Tang, Q., & Huang, W. (2008). Estimating chlorophyll content from hyperspectral vegetation indices: Modeling and validation. Agricultural and forest meteorology, 148(8-9), 1230-1241.

Yokoya, N., C Grohnfeldt and J Chanussot (2017). Hyperspectral and Multispectral Data Fusion: A Comparative Review, IEEE Geoscience and Remote Sensing Magazine, 1-25

Yuhas, R. H., A.F. Goetz and J.W. Boardman (1992). Discrimination among semi-arid landscape endmembers using the spectral angle mapper (SAM) algorithm. JPL, Summaries of the Third Annual JPL Airborne Geoscience Workshop. Volume 1: AVIRIS Workshop,147-149.

Journal of Geomatics Vol 12 No. 1 April 2018

Quantification of agricultural landuse during Kharif and Rabi season of Datia district, Madhya Pradesh, India

Pushpendra Singh Rajpoot[1], Ajay Kumar[1] and Sandeep Goyal[2]
[1]Department of Physical Sciences, Mahatma Gandhi Chitrakoot Gramodaya Vishwavidyalaya, Chitrakoot, M.P. - 485334
[2]Madhya Pradesh Council of Science & Tech. Bhopal MP - 462003
Email: prajpoot179@gmail.com

(Received: Dec 15, 2017; in final form: Apr 17, 2018)

Abstract: Land is an incredible resource of nature and optimum use of this resource should be in proper planned manner. In India major part of agricultural land remains fallow during different cropping practices due to various reasons. Datia is one of the district which is facing the problem of fallow land. In Datia district agricultural land covers 75.54 % and its utilization during seasons of Rabi and Kharif varies as mapped by Landsat ETM+ images (September 2016 and February 2017) with the help of geospatial technology. Agricultural land used during Kharif season is 39 % and during Rabi season is 84 % of total agricultural land. Thus a large area of agricultural land, a reusable resource is non-utilized which leads to loss of crop production. Lack of soil conservation facility & sowing of non-selected crops in western part, insufficient drain network & water logging in eastern part are the main reasons of this huge amount of fallow land. For maximum utilization of agricultural land and to increase the production during Kharif season, proper water management and modern agricultural technique plan should be prepared and implemented.

Keywords: Rabi Season, Kharif Season, Land use/ land cover, Fallow land

1. Introduction

Agriculture land is one of the most important land resources for food and fodder security of living beings. It is limited and cannot be exploited infinitely. Formation of agricultural land takes a very long time. As such its optimum use is must. Agricultural land resources well supported in association with water (naturally/ irrigation) leads to high production. In India at present, a small area of agricultural land is under irrigation facility and remaining is rainfed. Increase in water management system for agriculture use shows that in future production will increase (Seckler et al., 1999).

In Datia district agriculture is done during Kharif season (rain based) and Rabi (irrigation based), twice a year. Total agricultural land is 220965.5 ha out of total 293000 ha land of the district and there is a big gap in agricultural land utilization during Rabi & Kharif seasons. Main objective of this paper is to quantify the available land resources utilization during Rabi and Kharif seasons using remote sensing & GIS techniques to understand the lack of optimum utilization of agricultural land and its cause.

In this regards, recent studies have shown production forecasting of certain crops, crop yield modeling and crop stress detection using remotely sensed data. Historical aspects of agricultural growth, disparity and impact on farmers' income and employment have been studied by several scholars. Some recent studies include those of Sawant and Achuthan (1995), Bhalla and Singh (2001), Radhakrishna (2002) and Vaidyanathan (2010). Some studies also looked at the effect of agricultural technology (irrigation pattern) on growth of crop output and its instability (Cummings and Ray, 1969; Hazell, 1982; Mahendradev, 1987; Deshpande, 1988; Vaidyanathan, 1992; Chand and Raju, 2009). Datia district is situated in northern part of Madhya Pradesh and is located between 78°12'36"E to 78°53'29"E longitude and 26°17'39"N to 25°24'51"N latitude and covers about 293000 ha area (Figure 1). Whole district is divided into four tahsils ie. Datia, Bhander, Indergarh & Seondh and are the main cities of Datia district. There are about 445 villages and total population is 786,375 (Census, 2011). The major crops of Rabi season are wheat, gram, pea & mustard and major Kharif crops are Groundnut, Jwar, Bazara, Maize & Sesame as per data from Agriculture Contingency Plan for District: Datia.

Yearly calendar is divided into three seasons (Summer, Monsoon and Winter) and the average rainfall is 793 mm. Rainfall is very erratic and irregular. The climate in these regions is characterized by complex climatic deficiencies as water scarcity for rainfed crops. The climate is semi-arid and dry sub-humid with a short (occasionally intense) wet season followed by long dry season. Rainfall is highly unreliable, both in time and space, with strong risks of dryspells at critical growth stages even during good rainfall years (Seraj 2009, Kumar & Rajpoot, 2013). Maximum temperature of this area reaches up to 48 ^{0}C in May and minimum temperature goes to 2 ^{0}C in January. The main occupation for livelihood of this area is agriculture.

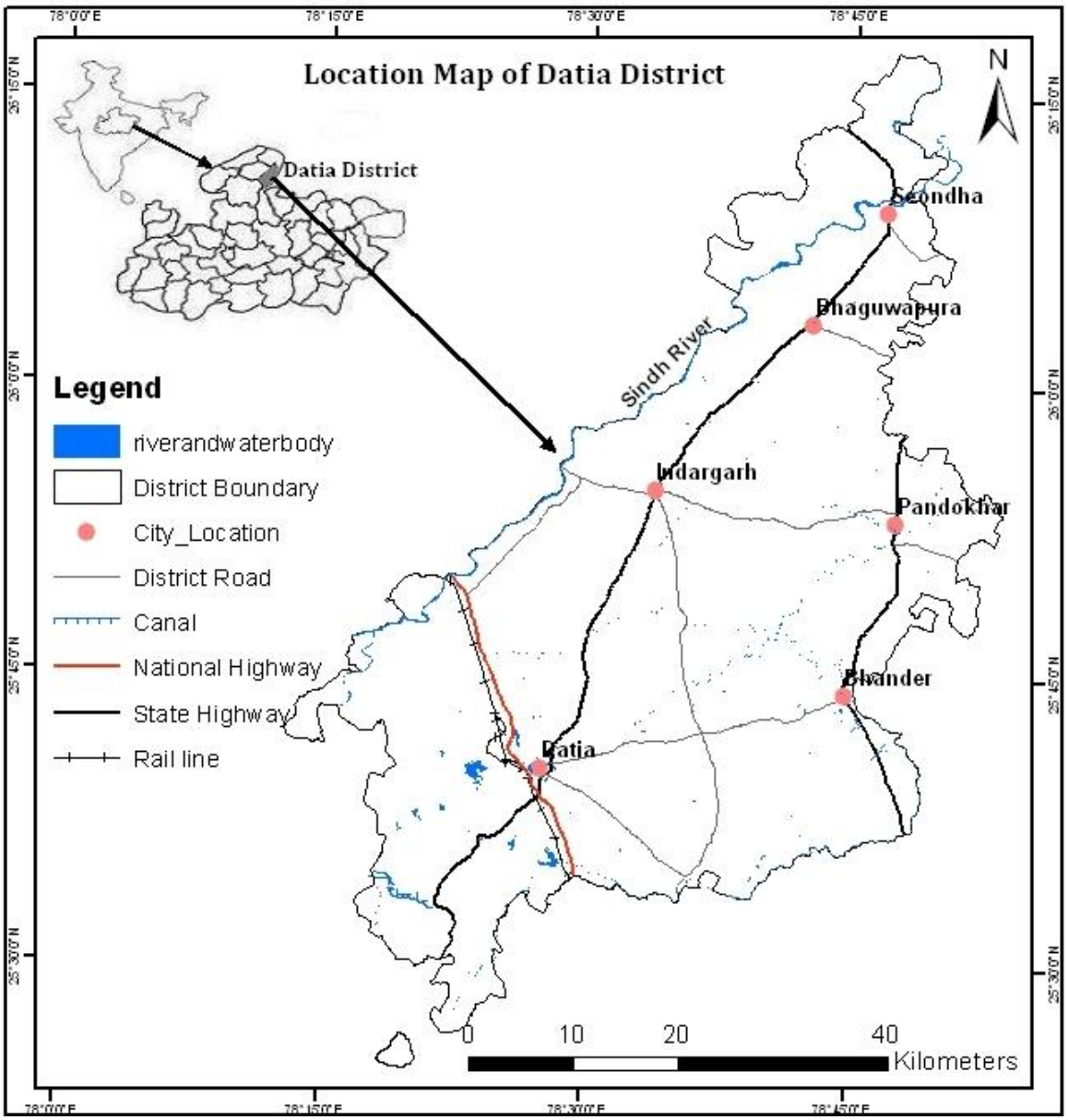

Figure 1: Location map of Datia district, M.P.

2. Materials and methodology

For the quantification of utilization of agricultural area, land use / land cover map is prepared using digitally enhanced and geo-referenced satellite imagery of Landsat ETM+ (September 2016 and February 2017). For preparation of district boundary, block boundary and location of human habitations; SOI toposheets (1:50,000) have been used. Quantification of land use/ land cover and agriculture land use for cropping in Rabi and Kharif season, visual interpretation and digital classification technique (hybrid raster classification) is used and area calculation is done using ERDAS. After the preparation of both land use/ land cover and area calculation during Rabi and Kharif seasons maps are prepared on Arc Map.

3. Results and discussion

Land use/ Land cover of Datia district is prepared using satellite data (Figure 2). Total area of Datia district is about 293000 ha and major Land use/ land cover classification area is given in table 1 and presented in figure 3. Land use/cover classification clearly shows that agricultural land cover about 75.54 % of total area of district. Forest covers 9.45 % a small part and it is characterized by scattered scanty vegetation mainly bushes and medium size trees. Built-up land is scattered in small clusters of four major towns (Datia, Bhander, Seondha and Indergarh) and villages. It covers 2.06 % area. Waste land covers 4.82 % area and water bodies 3.76 % area. Agricultural land is most precious natural resources which supports livelihood mainly of rural masses.

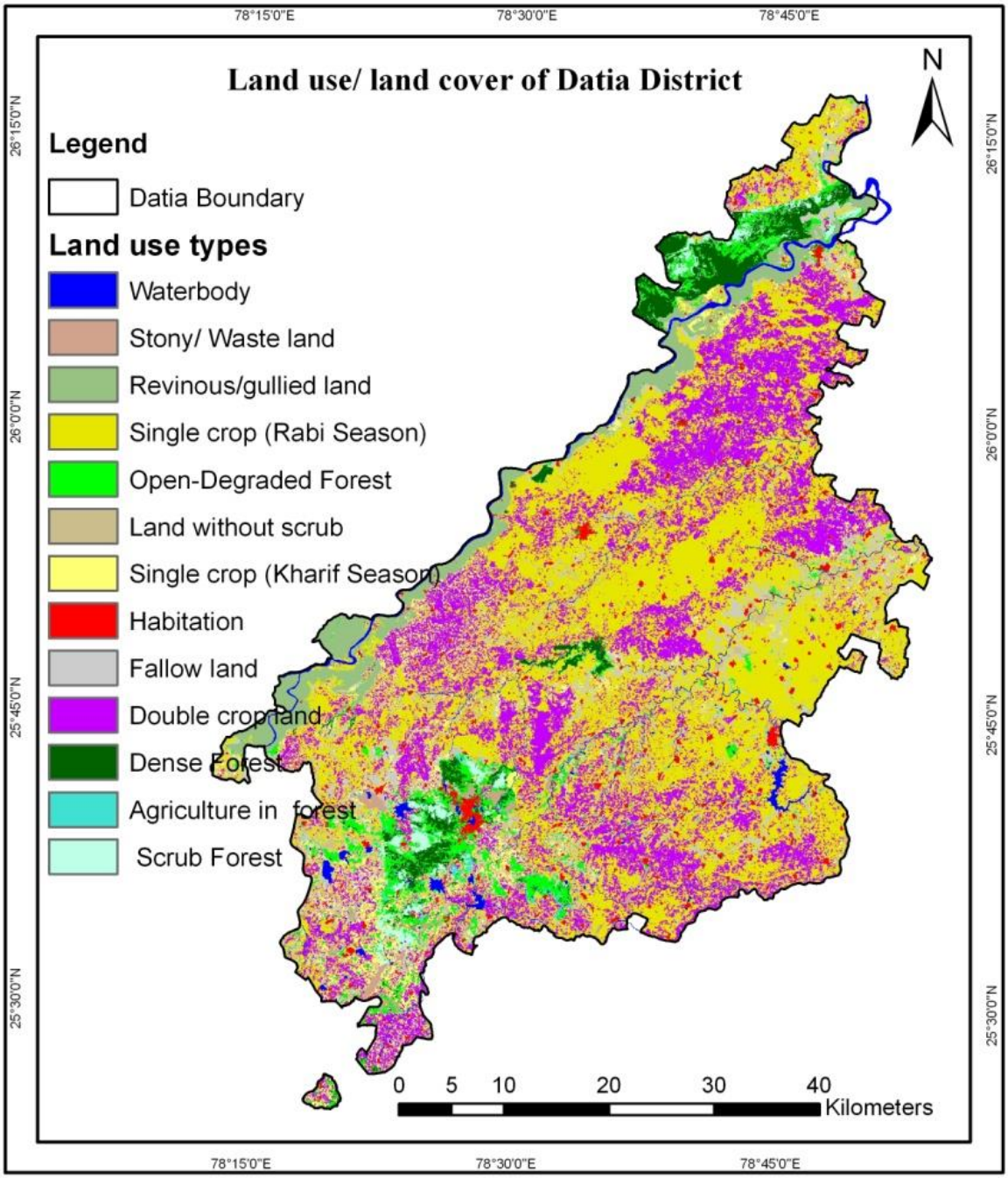

Figure 2: Land use/ land cover map of Datia district, M.P.

Table 1: Major land use classes of Datia district, M.P.

Sr No	Land use classes	Area (ha)	% Area
1	Agricultural land	220965.5	75.5
2	Land without scrub	11738.3	4.00
3	Forest	27927.52	9.5
4	Buil-up area	6039.9	2.1
5	Agriculture in forest	756.18	0.3
6	Waste land	14120.62	4.8
7	Waterbody	10984.6	3.7

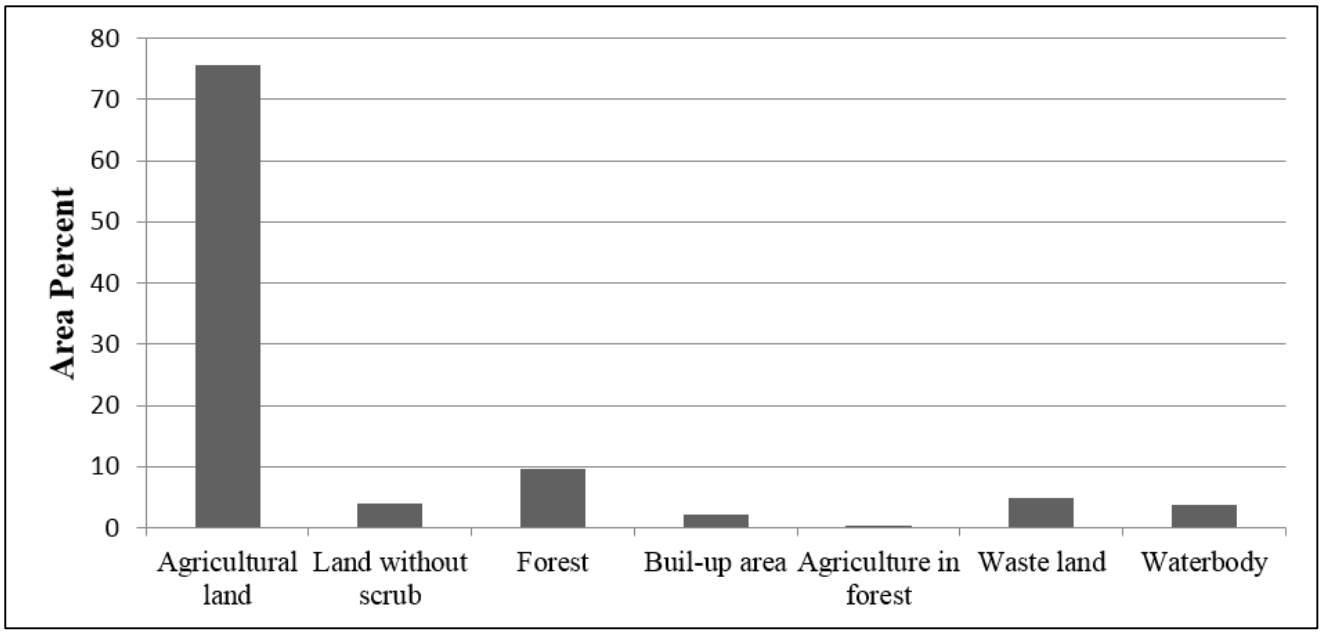

Figure 3: Land use of both seasons (Rabi & Kharif) of Datia District, M.P.

Landuse during Rabi and Kharif season and agricultural land utilization for cropping of Rabi, Kharif and double cropping is given in table 2 and presented in figure 4, 5, 6 & 7. Comparative utilization of agricultural land during Kharif and Rabi is shown in figure 8. Out of total of agricultural land, during Kharif season sown area is 39 % and fallow land is 61 % while during Rabi season is 84 % and fallow land is 16 %. This indicates that in the area during both cropping seasons agricultural land use has a big gap. Total of both season un-utilized agricultural land resource amounts to about 69 %. This is a huge amount of un-utilized land resource leading to overall lower agricultural production than expected. Land under double cropping of both cropping season is 31 % (Figure 8).

Topographically district area is drained from west to east. Western part has higher slope and rain water retention is minimum and in the east, area is almost plain with highly fertile alluvium and water is filled in agricultural fields along with erratic distribution of rain causing both drought and water logging condition causing non utilization of major percent of agricultural land. Lack of optimum use of agricultural land resource demand is proper rain water harvesting, removal of water logging problem in eastern part, sowing of selected crops & implementation of soil conservation plan in western part for maximum utilization of agricultural land resource as double cropping pattern. A proper plan of irrigation and drain network should be developed and applied to increase the production (Singh et al., 2006).

Table 2: Agriculture Land use classes of Datia district

Sl No		**Area (ha) Rabi Season**	**Area (ha) Kharif Season**	**Major Crops**
1.	Single crop	116114.00	17206.30	Black Gram, Groundnut & Sesame in Kharif
2.	Double	68341.70	68341.70	
3.	Fallow land	36509.80	135417.5	Wheat, Gram, Pea & Mustard in Rabi
4.	Total	220965.50	220965.50	

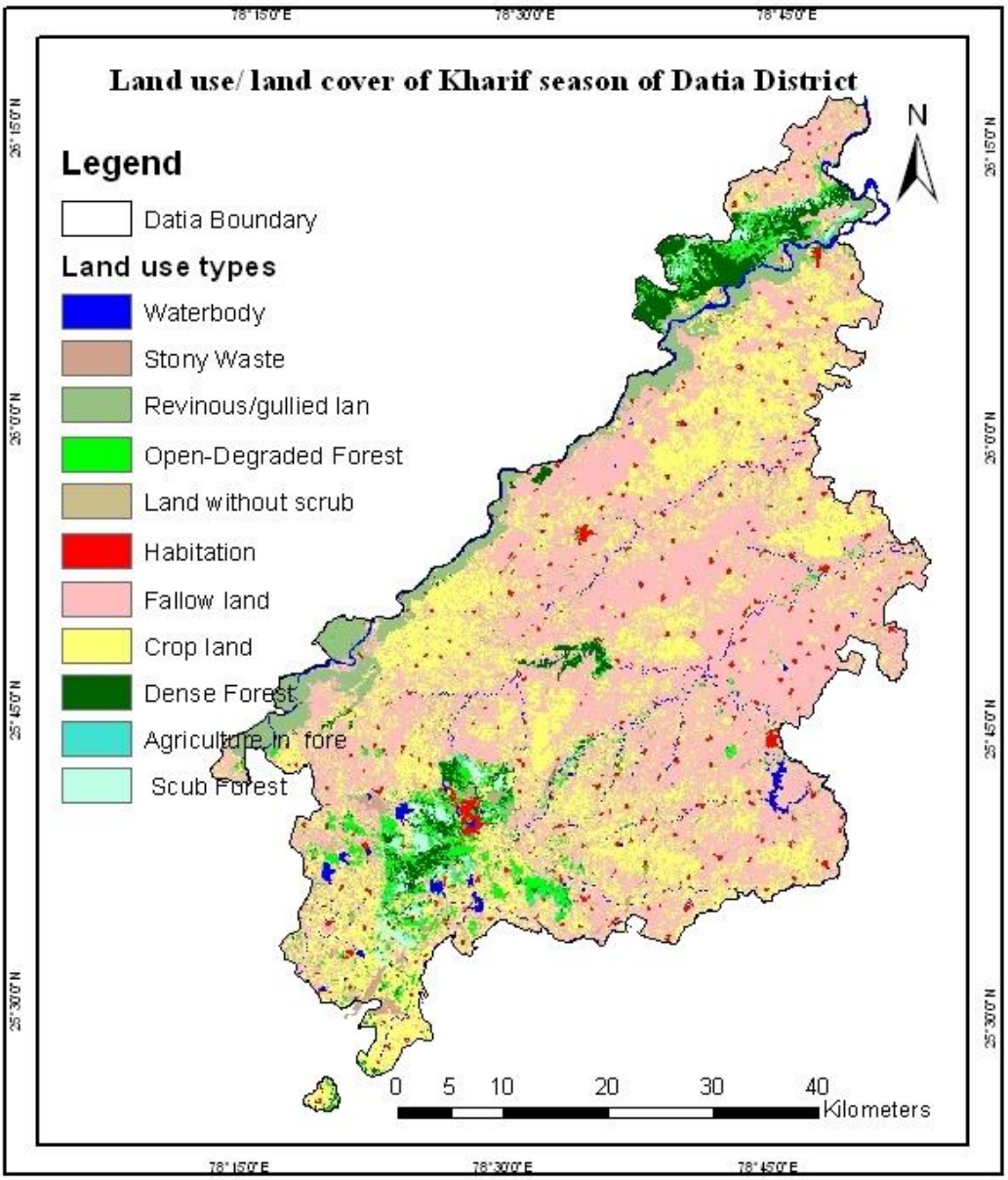

Figure 4: Land use map of Kharif season of Datia district

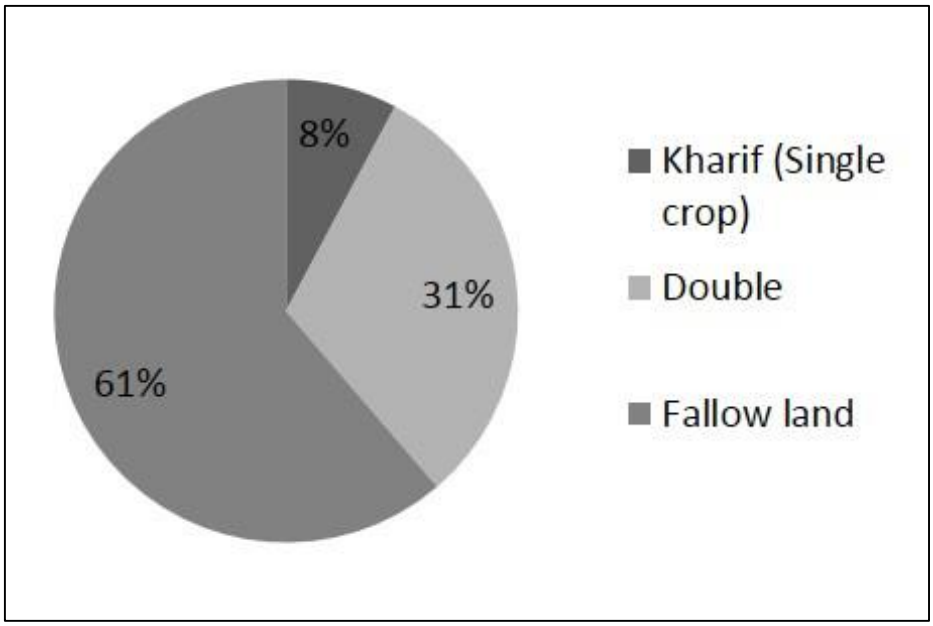

Figure 5: Crop land during Kharif season

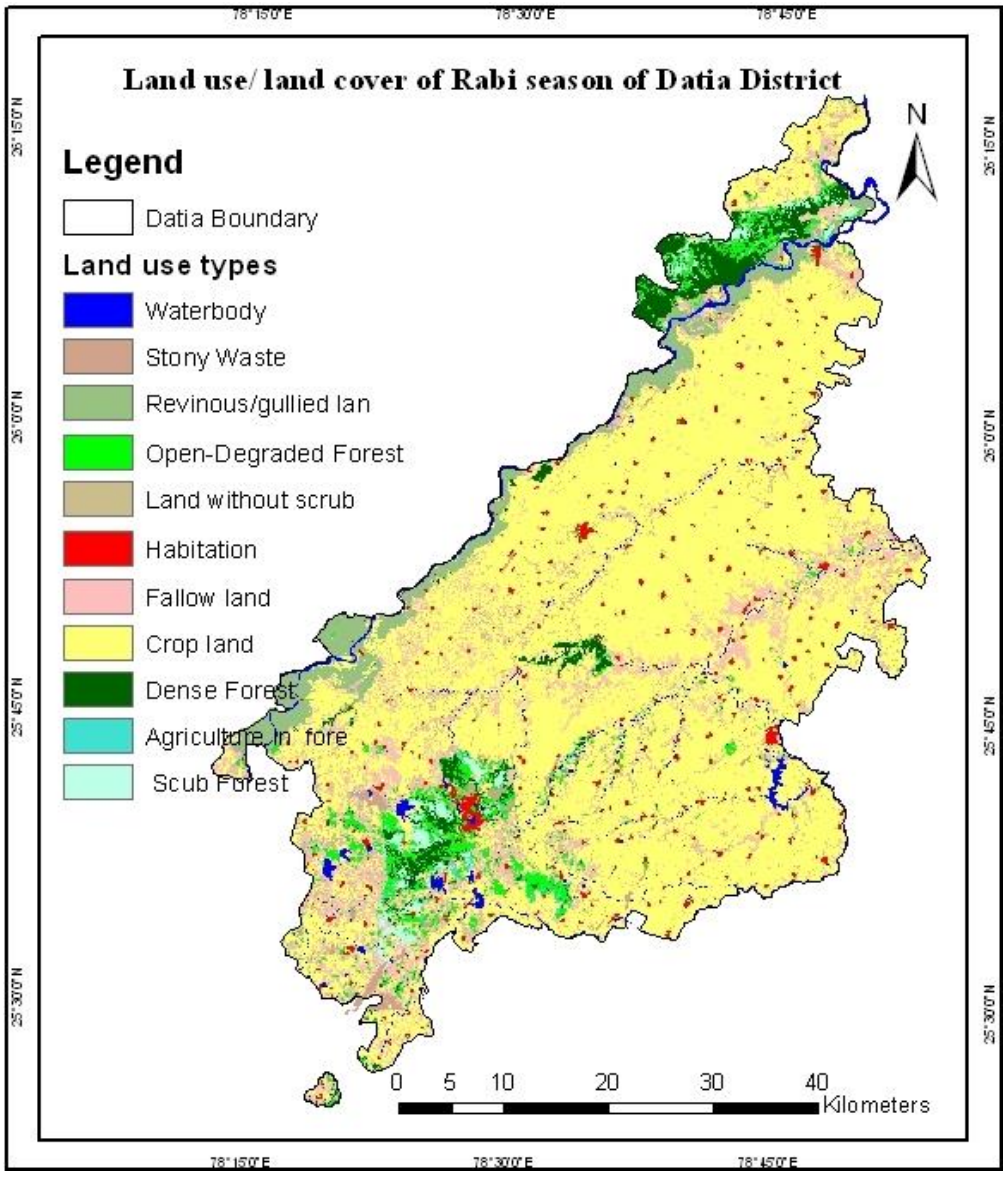

Figure 6: Land use map of Rabi season of Datia district

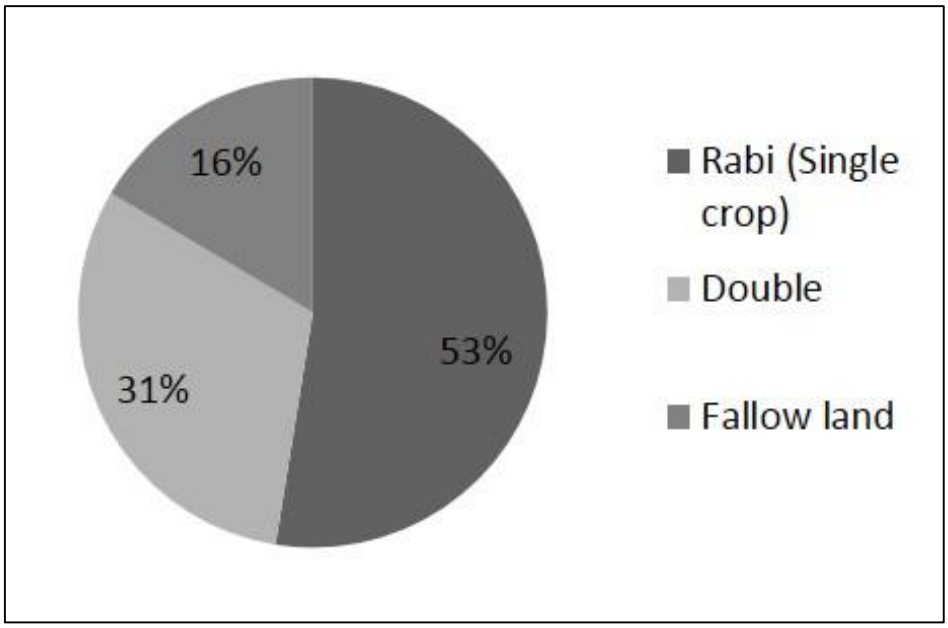

Figure 7: Crop land during Rabi season

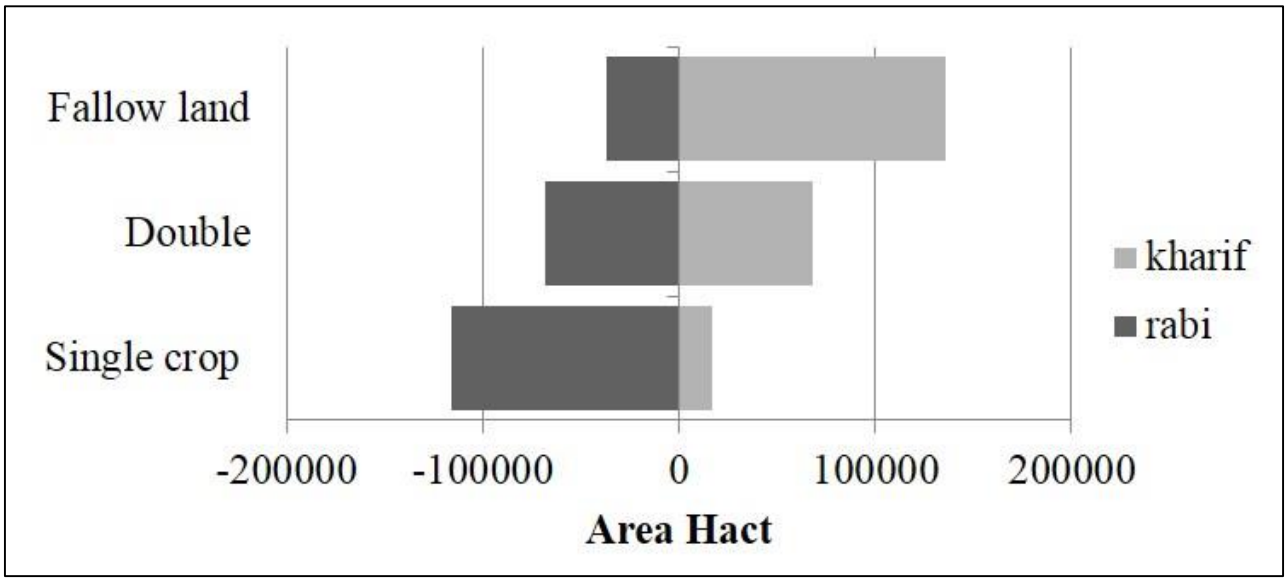

Figure 8: Pyramid of Agricultural land of Datia district, M.P.

Conclusion

Agricultural land is to be utilized to its full extent during Kharif and Rabi season. In Datia district utilization of agricultural land during Kharif season is 39 % and in Rabi about 84 %. Major part of agricultural land resource during Kharif season remains un-utilized. For maximum use of agricultural land and increased production from agricultural land during Kharif season, proper water management and modern agricultural technique plan be prepared and implemented.

References

Bhalla, G. S and G. Singh (2001). Indian agriculture: four decades of development. New Delhi: Sage Publications.

Chand, R and S. S. Raju (2009). Instability in Indian agriculture during different phases of technology and policy. Indian Journal of Agricultural Economics, 64 (2): 283-88.

Cummings, R. W and S. K. Ray (1969). The new agricultural technology: its contribution to 1967-68 production. Economic and Political Weekly, 4 (13): A7-A16.

Deshpande, R. S. (1988). Growth and instability in Maharashtra agriculture. Arthavijnana, 30 (4): 317- 39.

Hazell, P. (1982). Instability in Indian foodgrain production. Research Report 30. Washington D.C.: International Food Policy Research Institute.

Kumar., A. and P. S. Rajpoot (2013). Assessment of hydro-environmental loss as surface runoff using CN method of Pahuj River Basin Datia, India, Proceedings of the International Academy of Ecology and Environmental Sciences, 3 (4): 324-329.

Mahendradev, S. (1987). Growth and instability in foodgrains production: An Inter-State Analysis. Economic and Political Weekly, 22 (39): A82-A92.

Radhakrishna, R. (2002). Agricultural growth, employment and poverty: A Policy Perspective. Economic and Political Weekly, 37 (3).

Sawant, S. D and C. V. Achuthan (1995). Agricultural growth across crops and regions: Emerging Trends and Patterns. Economic and Political Weekly, 30 (12): A2-A13.

Seckler, D., R. Barker. and U. Amarasinghe (1999). Water scarcity in the twenty-first century. Water Resources Development, 15: 29–42.

Seraj K. (2009). District ground water information booklet of Datia district Madhya Pradesh.

Singh, P., D. Vijaya, N. T. Chinh., P. Aroon., K. S. Prasad., K. Srinivas and S. P. Wani (2006). Potential productivity and yield gap of selected crops in the rainfed regions of India, Thailand, and Vietnam, CRISAT, 2(1): 1-34.

Vaidyanathan A. (1992). Instability in agriculture: extent, causes and consequences: A review article. Indian Economic Review, 27 (2).

Vaidyanathan A. (2010). Agricultural Growth in India, Role of Technology, Incentives, and Institutions. New Delhi: Oxford University Press.

Journal of Geomatics Vol 12 No. 1 April 2018

Application of GIS technology to geospatial location of Lagos State fire stations, Nigeria

Omogunloye O. G., Otavboruo B. E., Abiodun O. E., Olunlade O. A. and Emesiani E. G.
Department of Surveying and Geoinformatics, Faculty of Engineering, University of Lagos, Lagos State, Nigeria
Email: gabolushohan@yahoo.com

(Received: Dec 08, 2017; in final form: Apr 17 2018)

Abstract: The number of lives and properties lost to fire outbreak has heightened the need for evaluating the efficiency of fire stations within Lagos State, Nigeria. In 2016, over 16 billion naira was lost to fire in the State. This research examined the application of GIS technology to geospatial location of Lagos State fire stations and their efficiencies. The aim of this research is to evaluate fire station distributions in relation to population and economic level within Lagos State using GIS technology. This evaluation provides various analyses to support efficient planning of fire services and identify areas that are less serviced within Lagos State. To accomplish this aim, graphical representation, Euclidean buffers, and network analyst, closest to facility mapping tool were used. The main data used were; Lagos State base map, XY coordinates of commercial/industrial buildings, thirty-four fire stations, (Federal, state and privately owned), and road network of Lagos State. The study revealed that within 1km coverage area, these thirty-four (34) fire stations owned by Lagos State (14 fire stations), Federal (8 fire stations) and Privately owned (18 fire stations) are insufficient for efficient service in the populated areas of Lagos state. The paper recommends need for more geospatially located fire stations in the populated areas of Lagos State for enhancing and achieving better and safe environments.

Keyword: Lives, Properties, Outbreak, Fire Station, Lagos State, GIS technology, Efficiencies,

1. Introduction

The mission of the fire service is to protect life, property, and natural resources from fire and other emergencies. With increasing demands, the fire service must utilize the best tools, techniques, and training methods to meet public expectations (ESRI, 2007 and 2012). Currently, the fire management team and information technology professionals are innovating modern and creative ways to apply this new technology to solve ever increasing fire service demands (Thomas, 2011; Ayodele, 2011 and Bukowski, 2008).

Due to increasing community's population growth, it has become necessary to upgrade, replace or relocate existing stations or build more fire stations to cope with the rise of public demands for emergency services (Conweh, 2012). With this urbanization rate and consequent heavy traffic congestion, the location of new fire stations is becoming a huge problem in urban planning and development (Stewart, 2004). The fire service requires tools to help identify the origin of any emergency, determine the shortest and quickest route to the incident and develop a more efficient approach to combat the fire via new station location. ESRI, 2012 and Badran, 1997 attributed causes of fire hazards to overcrowding in houses and work places, rapid expansion of production and commercial activities in industrial zones of newly developed areas which frequently lack adequate measures to counter fire hazards (Shikoli, 2015). Fire stations are one of the important and vital land uses in urban areas, needed to guarantee the safety of life and properties of urban residents.

The increase in urbanization has put population growth of urban areas in developing countries at the risk of imminent hazardous fire (Habibi et al 2008). According to Habibi et al (2008), the main criteria for fire station location are distance among the stations; level of fire risk in different parts of a city; accessibility; coverage area; population, and directions of city expansion. Studies like this, with existing stations must begin with an assessment of the effective response coverage area for each of those stations, usually by using time or distance limits. Most researchers chose to create the response area as a straight-line or Euclidean buffer rather than a network buffer because of computation time (Liu et al. 2006) or because the necessary network data was unavailable (Murray and Tong 2009).

2. Study area

Lagos State is a prominent place in Africa and the World, with its adjoining conurbation, having a population estimate of over twenty-one million in 2015 and it's rated the largest population/second largest city after Egypt, Cairo in Africa (National Wildlife Coordinating Group, 2014)

Lagos State, just like most urban area, is in a developing country Nigeria with a fast population growth rate. Her population according to the Lagos State Bureau of Statistics (LBS) is put at over 22,583,305 Million (Lagos State Estimate, 2014), and a population annual growth rate of 3.2 % (Annual abstract of statistics, 2012). The United Nations estimated that the city population by year 2015 will have risen to about 24.5 million at a growth rate of 6-8% per annum making Lagos State the 3rd Largest Mega city in the world (Lagos Bureau of statistics, 2016; Lagos state Fire service, 2017).

2.1 Lagos population

Within the last ten years, Lagos State Population has grown drastically. This growth is quite significant in all parts, including the suburbs (GISGeography, 2017). For instance, Epe increased from 181,000 to above 200,000, (Table 1) and figures 1 and 2 showed this increase clearly. With this population increase, it can be said that

there will be high risk of fire outbreak in these suburb areas (Burrough and McDonnell, 1998). As increase in population may give rise to imminent fire outbreak, Fire Stations facility must be increased to address any subsequent future fire outbreak (Mohammed, 2014 and Monsuru, 2015).

Figure 1 shows that Lagos State population is concentrated within the metropolis, as these areas have companies and industries (Map is prepared using UTM projection and represents Zone 31N). There is always an influx of people to a city's central business district. As a result of this, Public facilities like Fire Stations are majorly situated in this region. It can be said that economic level within the metropolis is higher than that of the suburbs.

3. Methodology

Figure 3 describe the steps and methods adopted in achieving the aim and objective of this study.

his study uses both spatial and non-spatial data, such as:

a) Lagos State population data (Table 1), acquired from Annual Abstract of Statistics, Nigeria (2012, Lagos Bureau of statistics web and National Population Commission web (2017);

b) Nigeria and Lagos State digital maps which comprises: Lagos state shapefile in Geographic coordinate system (GCS_WGS_1984: WKID: 4326 Authority: EPSG) showing local government boundaries. Source: Guinea Current Large Marine Ecosystem/Unilag Centre for Environmental Information and Decision Support Systems (EIMS).

c) Road network map shapefile of the state (GCS_WGS_1984: WKID: 4326 Authority: EPSG) Source: Open Street Map (OSM) https://www.openstreetmap.org/relation/301633.

d) XY Coordinates of Commercial/Industrial buildings, Lagos state Fire service and Federal Fire service was acquired from Google earth and Fatai and Olusegun (2016). Ground truthing was done for these sites.

Table 1: Lagos state five years interval projected population data with reference to 2006

	1991	**Census 2006**	**Projected population 2011**	**Projected population 2016**
Total	5,725,116	9,113,605	10,694,900	22,745,200
Agege	417,981	461,743	541,860	1,371,700
Ajeromi-Ifelodun	593,561	687,316	806,570	1,905,700
Alimosho	430,890	1,319,571	1,548,530	2,717,900
Amuwo-Odofin	225,823	328,975	386,060	697,000
Apapa	154,477	222,986	261,680	693,600
Badagry	119,267	237,731	278,980	316,400
Epe	101,464	181,734	213,270	241,900
Eti-Osa	157,387	283,791	333,030	1,305,900
Ibeju/Lekki	24,937	117,793	138,230	156,800
Ifako-Ijaye	233,341	427,737	501,950	988,300
Ikeja	203,383	317,614	372,720	861,300
Ikorodu	184,674	527,917	619,520	706,100
Kosofe	412,407	682,772	801,240	1,240,900
Lagos island	165,996	212,700	249,610	1,141,700
Lagos Mainland	273,079	326,700	383,390	835,800
Mushin	539,783	631,857	741,490	1,754,600
Ojo	215,837	609,173	714,870	1,250,100
Oshodi-Isolo	449,781	629,061	738,210	1,506,400
Shomolu	358,787	403,569	473,590	1,361,100
Surulere	462,261	502,865	590,120	1,692,000

Source: Lagos Bureau of statistics (2016)

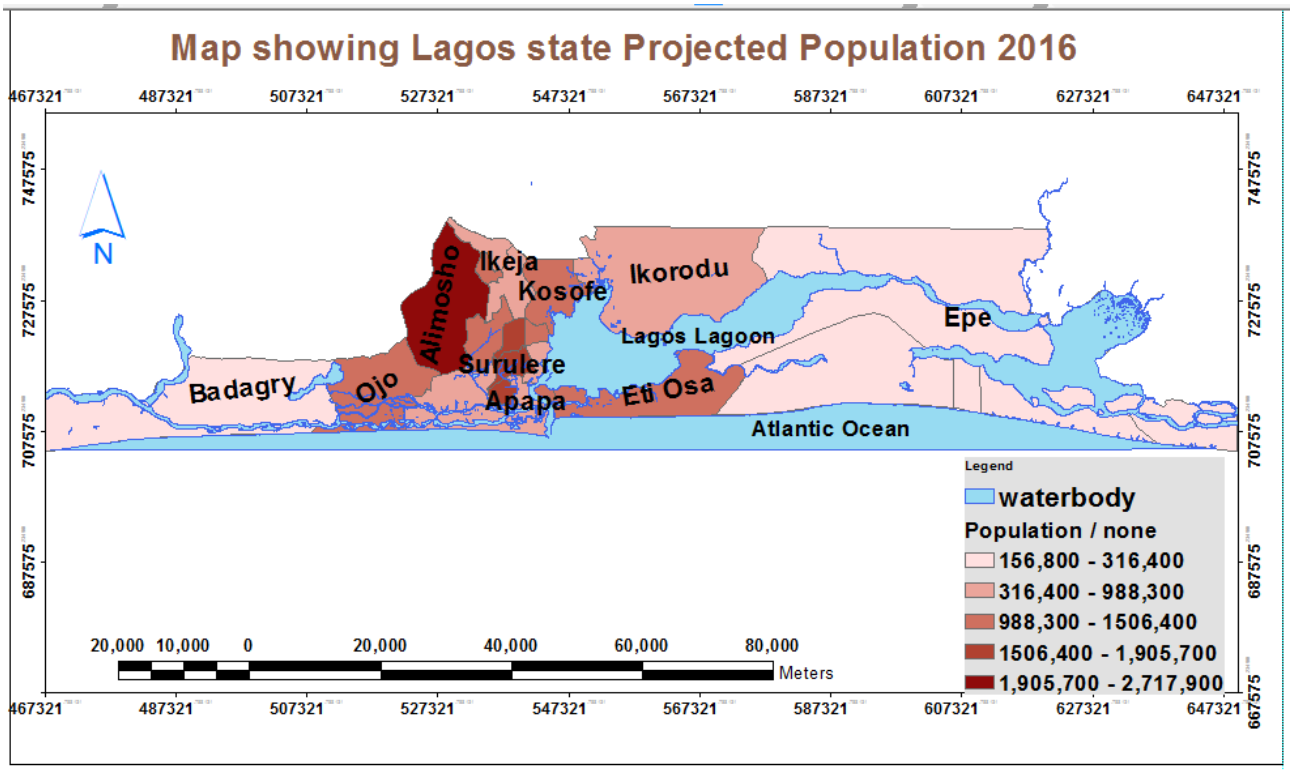

Figure 1: Map showing Lagos state projected population and water-body in 2016. (Source: Lagos Bureau of Statistics, 2016)

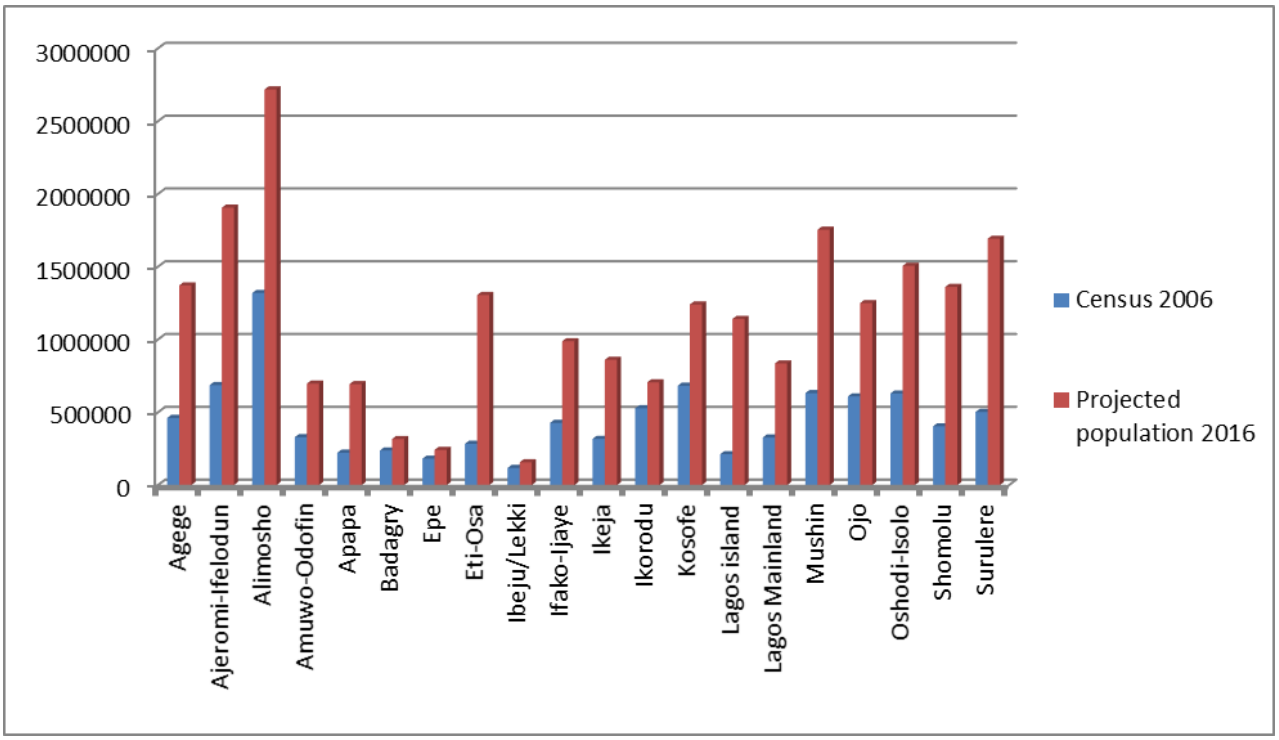

Figure 2: Graph showing Lagos population change between 2006 and 2016

4. Results

4.1 Evaluation of Fire Service in Lagos State and its population

Comparing Lagos population with number of available fire stations, it can be seen from figure 4 and table 2 that the available fire stations are concentrated within the Metropolis, while the Suburb regions like Alimosho, Ojo, Mushin, Ikorodu, and Kosofe, each, has one fire station. Therefore, area like Alimosho which have high population or increasing industries is under-served.

From the map in figure 5, and figure 6 it can be seen that both fire stations and fire hydrants are concentrated

within the metropolis, leaving the suburbs with just one fire station and no hydrants, while commercial buildings, are growing in the suburbs as seen in figure 7.

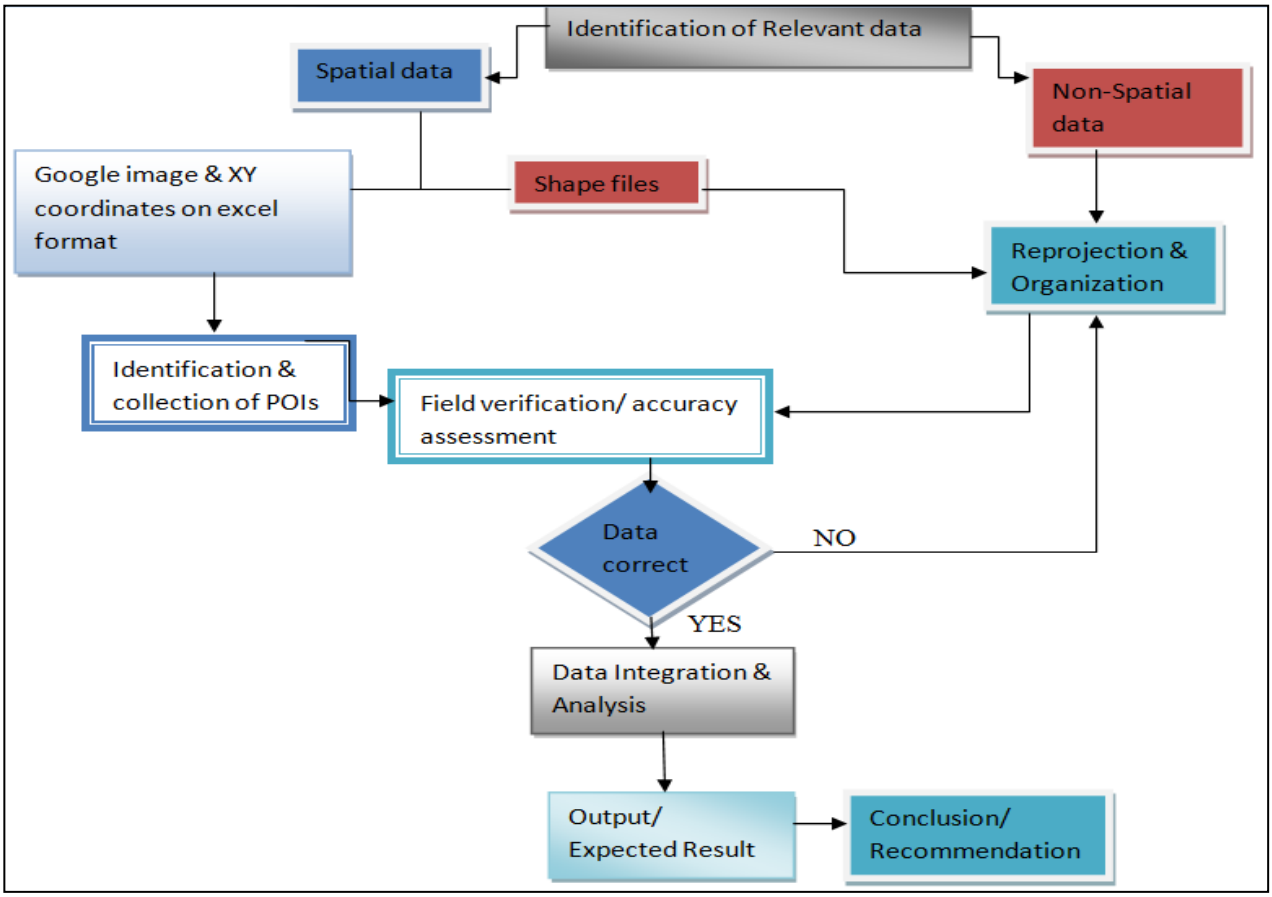

Figure 3: Flow chart of methodology

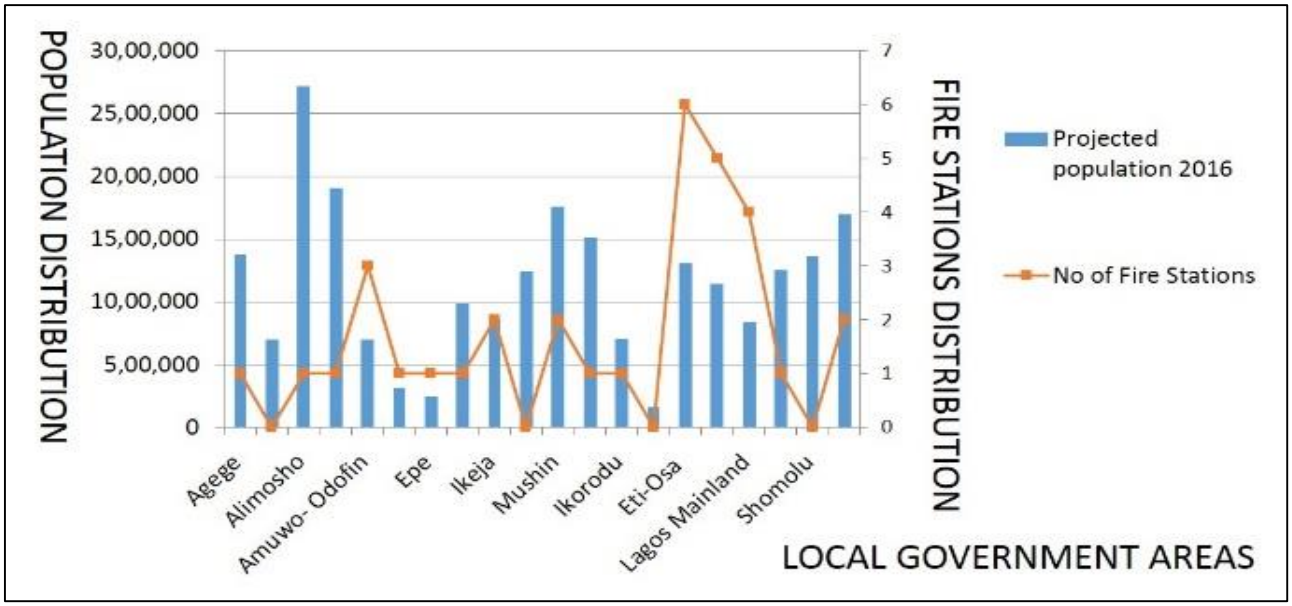

Figure 4: Graph of population distributions against number of fire stations in some Local government areas of Lagos state

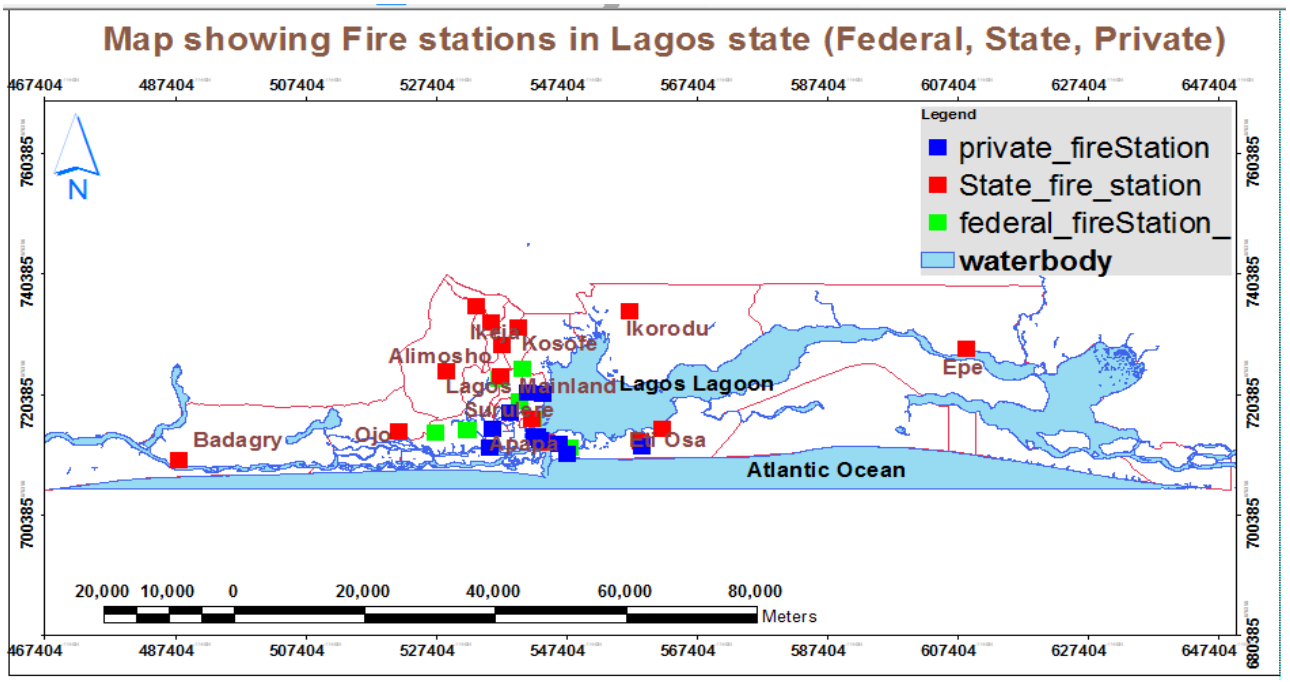

Figure 5: Federal, State and Privately owned fire stations and waterbody distributions within Local government area of Lagos state

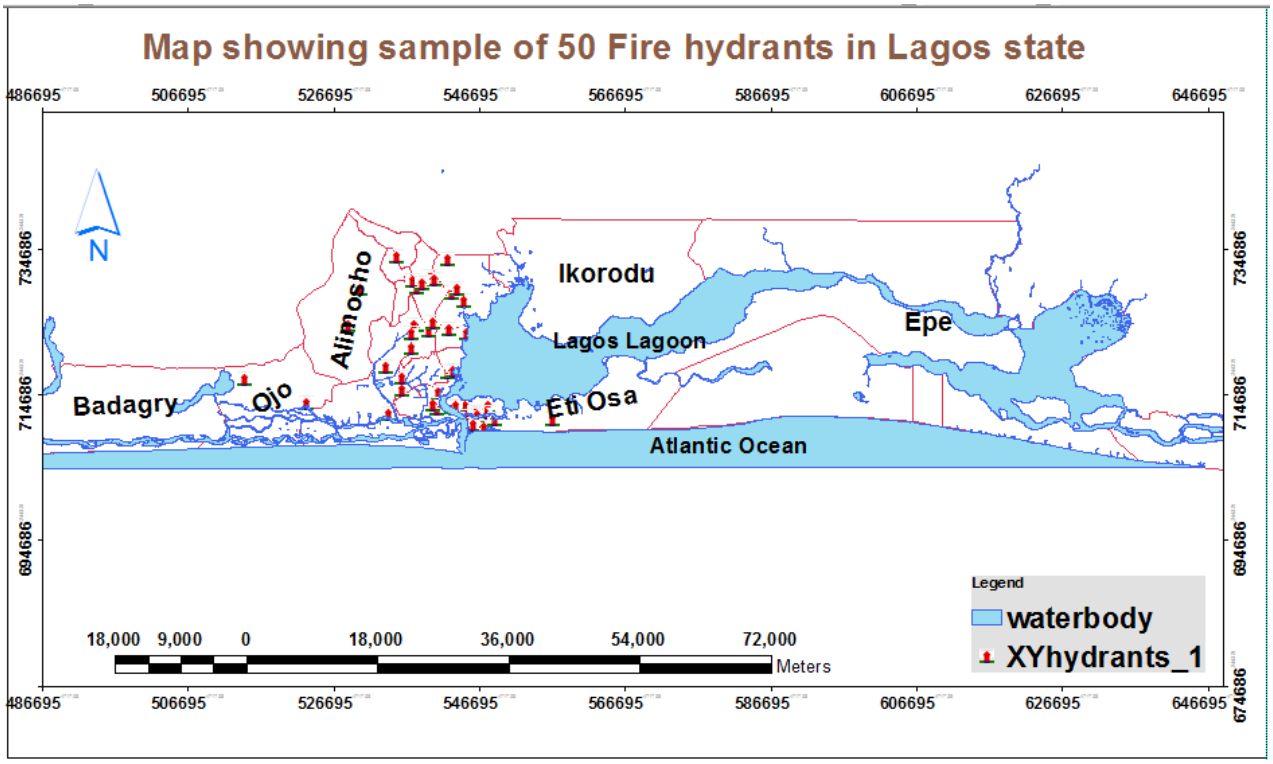

Figure 6: Map showing 50 locations of fire hydrants and water-body in Lagos state

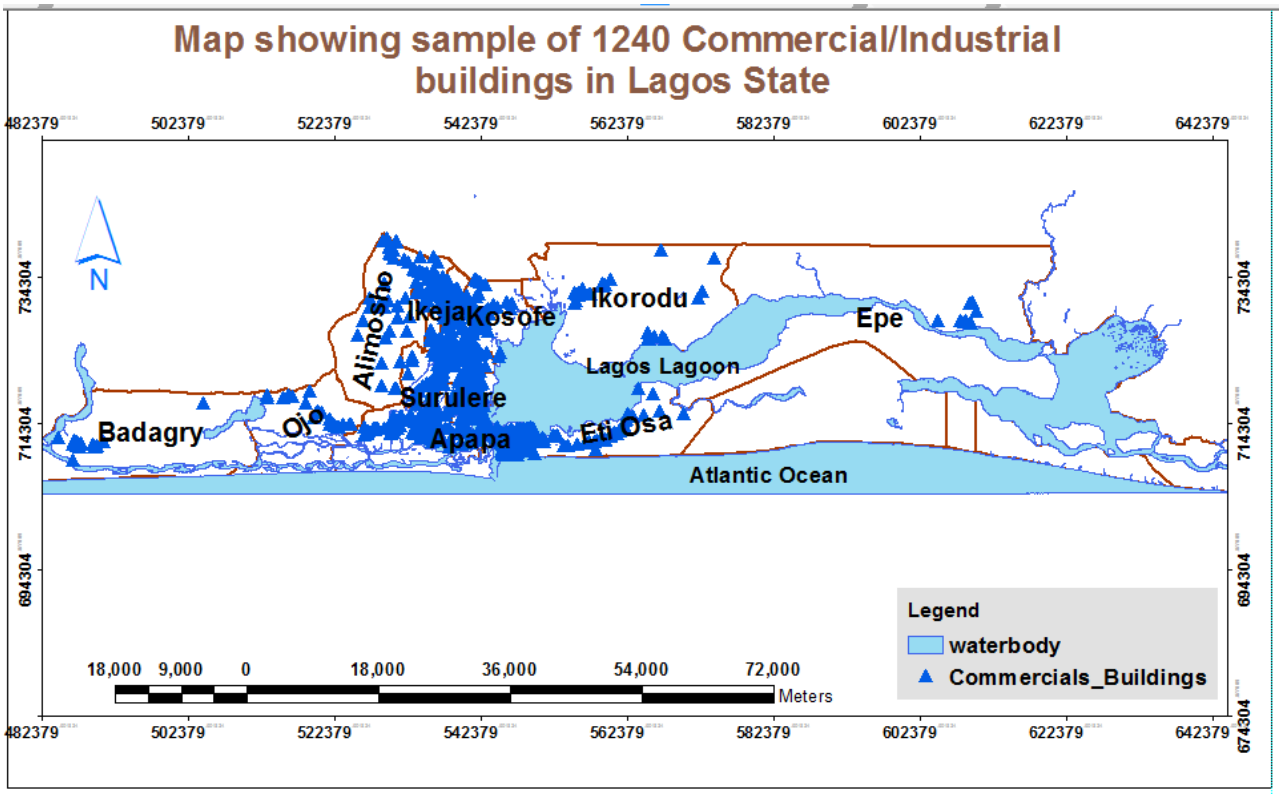

Figure 7: Map showing 1240 samples of commercials buildings distributions within Local government area of Lagos state

Table 2: Population distribution/Number of Fire stations in the twenty Local government areas of Lagos state

LGA	Population	Number of Fire Stations
Agege	461,743	1
Ajeromi-Ifelodun	687,316	1
Alimosho	1,319,571	1
Amuwo-Odofin	328,975	3
Apapa	222,986	0
Badagry	237,731	1
Epe	181,734	1
Eti-Osa	283,791	1
Ibeju/Lekki	117,793	6
Ifako-Ijaye	427,737	1
Ikeja	317,614	3
Ikorodu	527,917	2
Kosofe	682,772	0
Lagos island	212,700	5
Lagos Mainland	326,700	4
Mushin	631,857	0
Ojo	609,173	1
Oshodi-Isolo	629,061	1
Shomolu	403,569	0
Surulere	502,865	2

4.2 Closest facility mapping query

Network analyst closest to facility mapping was carried out on commercial buildings, it was used to locate the closest specific Fire station to a Commercial/Industrial building. This is seen in figure 8 and 9.

The closest facility map in figure 8 shows that closest distance of Fire Station to a shopping complex is more than 4.7 km and closest Fire Station to Ikeja secretariat is 620 meters, although other Fire Stations are 4.07 km and 4.4 km distance to the secretariat which seems quite far. As in some cases the closest Fire Station may require assistance from other Fire Station.

4.3 Euclidean distance calculation (buffer zones) The buffers zone of 1km also butress the point earlier made that demand points and historic incident points are not properly covered by any Fire station service coverage of 1 kilometer. Buffer zones are also a type of visualized coverage area, of the facility which is buffered. The map in figure 9 shows that some Commercial/Industrial buildings are left out from the 1km and 2km buffer of Fire Stations.

5. Conclusion

A major concern of any country or society is security, fire as a threat ought to be controlled at all cost. In this age of computer technology, the GIS technology has been proved to be a tool for enhancing efficiency in fire control services across the globe.

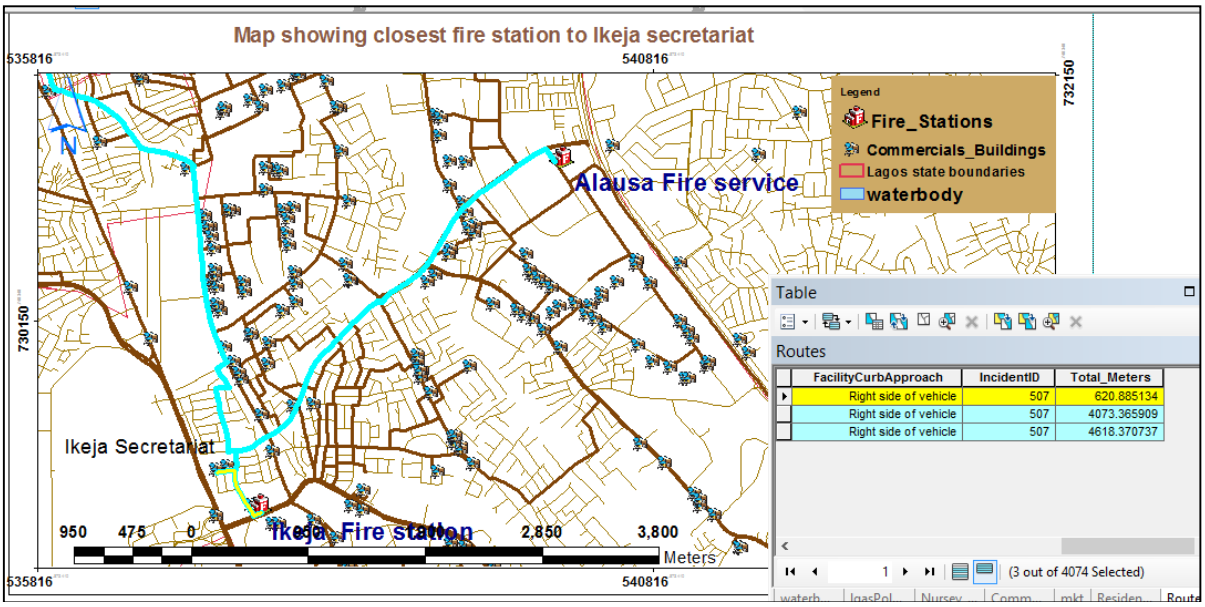

Figure 8: Closest fire station (Alausa fire station) to Ikeja secretariat

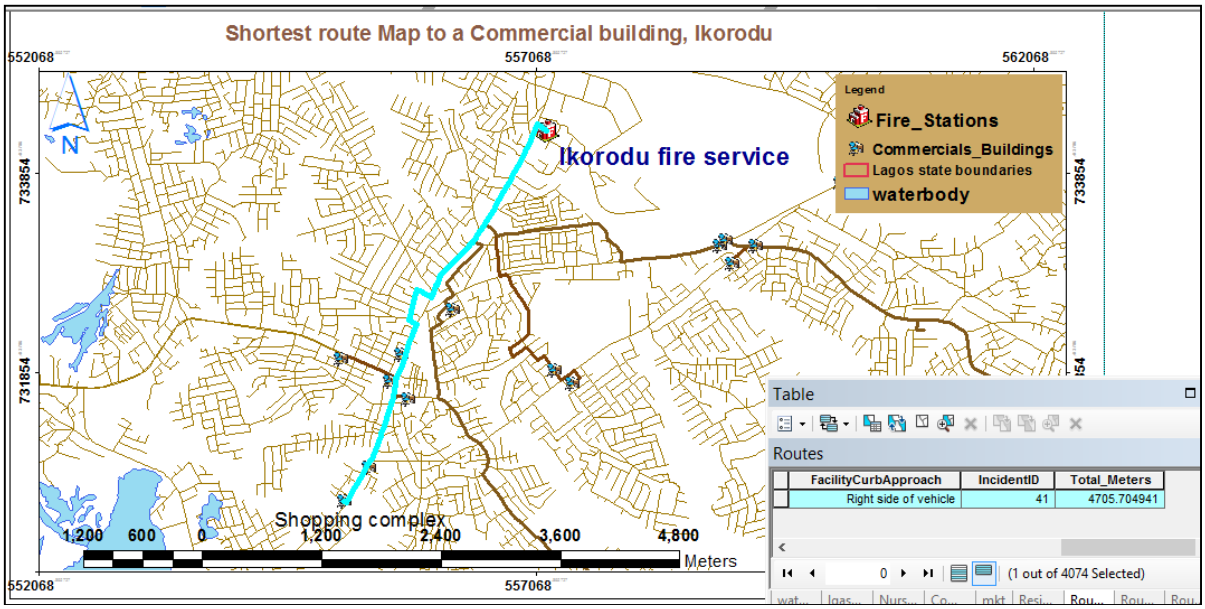

Figure 9: Map showing shortest distance from Ikorodu fire station to shopping complex

The mapping of fire facilities was achieved and the evaluation of their suitability in location as it relates to Commercial/Industrial buildings and distribution was done using Geographic Information System (GIS) technology.

The main findings from this study was that Fires service coverage area within 1km, and 2km response was concentrated more at the Lagos metropolis depriving other populated region outside the metropolis of the stipulated 1km and 2km response coverage, thus making such regions highly vulnerable to loss of lives and properties in event of a fire accident. From the result of the distribution of the number of fire stations/population of each local government of the State, it was deduced that Alimosho, Apapa, Ojo, Mushin, and Ikorodu are at risk in the event of the occurrence of any fire outbreak. This is due to the ratio of the increasing population as against the few Fire stations situated in these areas.

The need for more geospatially located Fire Stations to accommodate the present gaps shown in figure 10, between the relative buffer zones of (1-3) km. in Lagos State. This would go a long way to avert/reduce loss of lives and properties that might arise in any imminent future fire outbreak. Furthermore the study showed that distance within Fire hydrants are quite far, with a minimum distance of 820 meters apart, this is higher than the NFPA regulation of 100m apart. Also, the closest fire station to a point of interest is closer within the metropolis than in the suburbs. From the research it was revealed that everyone do not have access to fire and rescue services within five minutes of travel time. It can be concluded that the present Fire stations in Lagos State cannot serve the entire population adequately.

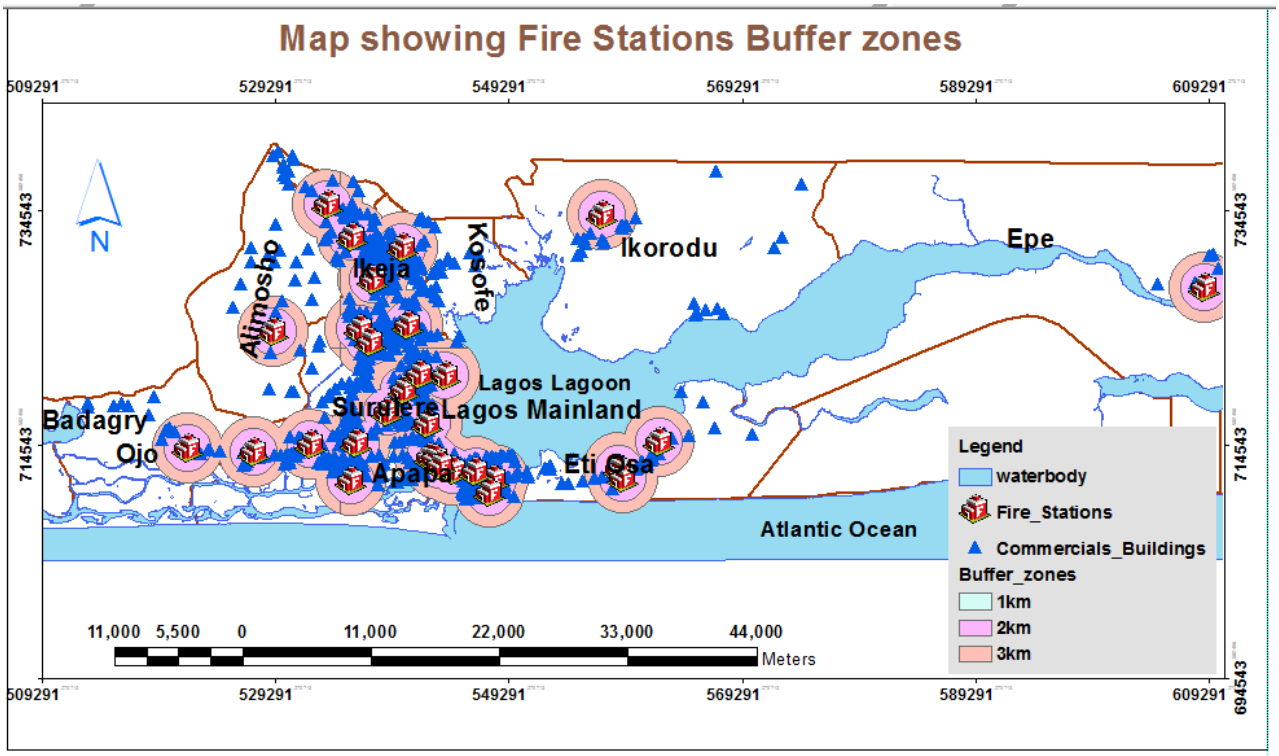

Figure 10: Fire station and Commercial/buildings buffer zones 1km-3km

6. Recommendations

New fire stations should be established using the suggested areas of short fall of fire stations. Federal government should embark on purchasing new fire trucks for federally owned stations, and Lagos state government should provide barracks to accommodate firemen officials. The present fire stations should be upgraded. Also, periodic training on safety awareness should be carried out in communities, schools, and offices regularly. State government should make it mandatory for owners of private companies and filling stations in a particular localty to jointly build fire stations as part of their "giving back to the community exercise". State government should also ensure that fire hydrants are situated within minimum distance reach in all local government areas of the state.

References

Annual Abstract of Statistics (2012). National Bureau of statistic, Federal Republic of Nigeria (PDF). www.nigerianstat.gov.ng

Ayodele S. J. (2011). Spatial distribution of petroleum filling station in Kaduna North. www.srib.com/samuel_ayodele.

Badran, (1997). Common causes of Fire Incidents, Spectron Environment and Planning Agency. https://www.facebook.com/permalink.php?id=641543305869074&story_fbid...

Bukowski, W. (2008). Performance of home smoke alarms analysis of the response of several available technologies in residential fire settings, 1455-1. USA: U.S. Government printing office.

Burrough, P.A. and R. McDonnell (1998). Principles of Geographical Information Systems, Oxford: Oxford University Press. http://www.books.google.com/Principles_of_Geographic_Information_Systems/

Conweh, C. (2012). The Use of GIS for Effective and Efficient Emergency Management: A case study of the Cardiff Fire Services in South Wales, Faculty of Advanced Technology, University of Glamorgan, Prifysgol Morgannwg. www.academia.edu/The_Use_of_GIS_for_Effective_and_Efficient_Emergency_Management/

ESRI. (2007). GIS for fire station locations and response protocol, J-9587, New York, USA.

ESRI. (2012). GIS for the fire service, J10126, New York, USA. http://www.esri.com/library/whitepaperpdfs/gis-for-fire

Fatai A.O. and O. Olusegun. (2016). Locational pattern of service in Lagos Metropolis, presented at UNILAG-ANG Annual Conference, 2016 http://www.facebook.com/permalink.php?id=641543305869074/

GISGeography (2017). Finding Service Areas Using ArcGIS Network Analyst. ahttp://gisgeography.com/finding-servic-areas-using-arcgis-network-analyst/

Habibi Y. et al. (2008). Spatial analysis of urban fire station locations byintegrating AHP model and IO logic using GIS, A case study of zone 6 of Tehran, Journal of Applied Sciences 8(19), DOI10.3923/jas.2008.3302.3315

Lagos Bureau of statistics (2016). http://mep.lagos.gov.ng/lbs-publication/

Lagos state Fire service (2017). www.fireservice.lagosstate.gov.ng/

Liu, H., et al. (2006), Radiative effect of clouds on tropospheric chemistry in a global three-dimensional chemical transport model, J. Geophys. Res., 111, D20303, doi:10.1029/2005JD006403 pdf

Mohammed, M.U. (2014). GIS-Based analysis of the location of filling stations in metropolitan Kano against the physical planning standards, American Journal of Engineering Research, 3(9), 47-158.

Monsuru, O. (2015). Lagos loses 28 lives in 552 fire incidents in five months, Vanguard July 18, 2015. http://www.vanguard.ng/lagos-loses-28lives-in-552-fire-incidents-in-five-months/

Murray, A. and D. Tong (2009). Maximizing coverage of spatial demand for service. Google Scholar, Papers in Regional Science 88:85-97.

National Wildlife Coordinating Group (2014). "Engine Types" (PDF). Retrieved January 5, 2014

Shikoli S.S. (2015). Assessment of use of GIS technology in fire control, case study: Nairobi County, Department of Geospatial and Space Technology, School of Engineering, University of Nairobi.http://erepository.uonbi.ac.ke/shikoli_Assessment_of_Use_of_Gis_Technology/

Stewart, L.A. (2004). The application of route network analysis to commercial forestry transportation. http://gis.esri.com/library/userconf/ proc05/papers/pap1309.pdf.

Thomas J. C. (2011). GIS in emergency management. http://citeseerx..psu.edu/ viewdoc/download?doi=10.1.1.134.9647&rep=rep1&type=pdf.

Journal of Geomatics Vol 12 No. 1 April 2018

Development of WebGIS based Information System: A case study of energy sector

Sagar Chhugani[1*], Shweta Mishra[2], Gaurav Jain[2], Sanket Suthar[1] and Pinal Shah[1]
[1]Chandubhai S. Patel Institute of Technology, CHARUSAT, Changa
[2]Space Applications Centre, Ahmedabad
*Email: sagarchhugani14@gmail.com

(Received: Mar 16, 2018; in final form: Apr 17, 2018)

Abstract: Geographical information is captured and stored in a huge amount nowadays. The attribute value of spatial information is deployed across many communities and websites. To store, manage and analyse this geospatial data, the common centralized system is required. Currently, information regarding energy sectors of India is not available on any centralized system and is unstructured. Accessing energy data is time-consuming and creates interoperability issues and provides irrelevant data as most of the available data may be redundant, non-geospatial or managed by various departments. The depleting conventional resources and increasing energy usage requires proper energy planning which requires an integrated and updated centralized system. The developed Information system collects the relevant data and manages it according to geographical information. This system is developed for better understanding and decision making by providing geographical information available along with energy statistics on a single platform. WebGIS open source technology is used for developing a centralized system to relate available information with geospatial data and disseminate information using maps and charts. Developed WebGIS based system is easy to understand and has a user-friendly interface. An Automated Module is developed to transform non-spatial energy data (with geographic coordinates) to spatial data to reduce manual processes. It is expected that the availability of information will support stakeholders and administrators for better decision making and will help users to understand and save energy.

Keywords: WebGIS, Open source, Energy, Geospatial, Information system

.

1. Introduction

Energy is the key factor to develop society's economic growth and improve quality of life. It plays a vital role in evolution, survival and development of all living beings. India has enough resources, better land structure and environmental conditions i.e. adequate sunshine, balanced wind speed to produce renewable energy yet nearly 20% of the total population does not have access to electricity (Indian Wind Energy, A Brief Outlook, 2017). For substantial growth, the demand of energy is increasing day by day. As the world's most populous country, development of infrastructure and better policy planning is required to fulfil ever-growing energy demands. Development of policy planning needs long-term stability and clarity of information. Most of the energy-related information is scattered, maintained by various departments, redundant or may be unavailable. Accessing this type of data is time-consuming and creates interoperability issues and provides irrelevant data as there is no common centralized system available for information storage. There are many portals developed by various ministries for individual purposes. Ministry of New and Renewable Energy (MNRE) developed a portal (www.mnre.gov.in) for matters related to new and renewable energy production and development. All available portals provide energy-related data of India but contain data only for particular resources or area and available information is non-spatial. National Renewable Energy Laboratory (NREL, U.S. Department of Energy) developed a portal (www.nrel.gov) that advances the technology to optimize energy systems. Energy Information Administration (EIA) developed a portal (www.eia.gov) for the United States. Portal contains energy-related information for U.S. and other countries. EIA is responsible for collecting, analysing and disseminating independent and impartial energy information to promote sound policymaking, efficient markets, public understanding of energy and its interaction with economy and environment in United States. Purpose of this work is to develop a prototype of a centralized web-based information system for visualisation of energy maps showing spatial and non-spatial data of electrical power generation and consumption (including renewable energy), and other energy-related infrastructure in India. Energy information system is a system for collecting, analysing and reporting of data related to energy for better energy management and resource planning. Data is collected from various sources and transformed into geospatial data format using GIS (Geographic Information System) tools. Combining GIS with web technologies provides functionality to display information using interactive maps in the browser. Web-based GIS is open source, distributed, standardized by OGC (Open Geospatial Consortium) that brings GIS technology to the general public at little or no cost (Caldeweyher et al. 2006). The WebGIS enhance decision making at the administrative, and operational levels and serves as a gateway for decision makers and general users to access the system conveniently and effectively. The hardware specifications and network architecture for this technology provides methods for publishing and accessing GIS data at high speed (Karnatak et al. 2007). It is based on client/server model. Decision makers are seeking WebGIS based solutions as they are efficient at satisfying the needs of stakeholders in terms of availability of associated collateral information. Users are not required to install any software for using WebGIS based applications. Internet /

Network connection and modern browsers are only needed by users for accessing WebGIS based systems (Sharma and Mishra, 2017). Today, Internet and Web technology has enhanced the access and dissemination of spatial data among the communities from local to Global scale (Awange, 2013). Developing a prototype of Information system for disseminating energy-related data using WebGIS technology is main goal of this work.

Visualisation of Earth observation Data and Archival System (VEDAS) is a portal to showcase scientific products from EO applications which feed into decision making system. VEDAS (https://vedas.sac.gov.in) provides access to thematic spatially enabled data repository over land and natural resource inventories generated by Space Applications Centre (SAC, ISRO) or SAC in collaboration with other participating agencies. Prototype for developing energy maps of India is taken as a case study and developed under VEDAS. Developed application facilitates users and administrators to monitor and understand energy and related parameters. It leads to better decision making and policy planning for economic development of the country.

2. Methodology

Information system development requires relevant data from one or more sources. Energy related data for development of this system is collected from various sources that are available publicly in Government portals and reports. Collected data is analysed and converted into information.

Non-spatial data is transformed into geospatial data format using developed JAVA module in which non-spatial data is combined with geometry or coordinates and then this geospatial data is stored into spatially enabled PostgreSQL database, which is a powerful, open source and relational database management system. Information is published in a WebGIS server as a web service for graphical visualization of information on an interactive map. The web application is developed to provide energy maps of India and related non-spatial data at a single portal. It is developed using open source technologies i.e. JavaScript, Angular JS and OpenLayers 3 API and deployed on Apache Tomcat server. Energy data is also disseminated using charts and tables for analysing and understanding the information. Overall methodology and flow diagram of the proposed system is shown in figure 1. Development of Information system is divided into 4 phases: Data collection, Module development for data conversion, Publishing of data in GIS server and Development of web application.

Collection of data is a crucial part of any information system. For carrying out this study and development, data related to the energy sector is used from two sources: General Review (published by Central Electricity Authority, 2014, data source: www.cea.nic.in/annualreports.html) and Energy Statistics (published by Ministry of Statistics and Programme Implementation, 2016, data source: www.mospi.nic.in/publication/energy-statistics-2016).

Data related to generation, transmission, distribution, energy loss, cost, trading and consumption of electricity by different sectors of India is used for this case study. Some of the tables used for study data for the year 2013-14 is shown in Table 1. To use GIS functionality, data must be available in the spatial format. A module is prepared in JAVA language for fetching the non-spatial data and transforming it into geospatial data, based on the geometry and stored into PostgreSQL database.

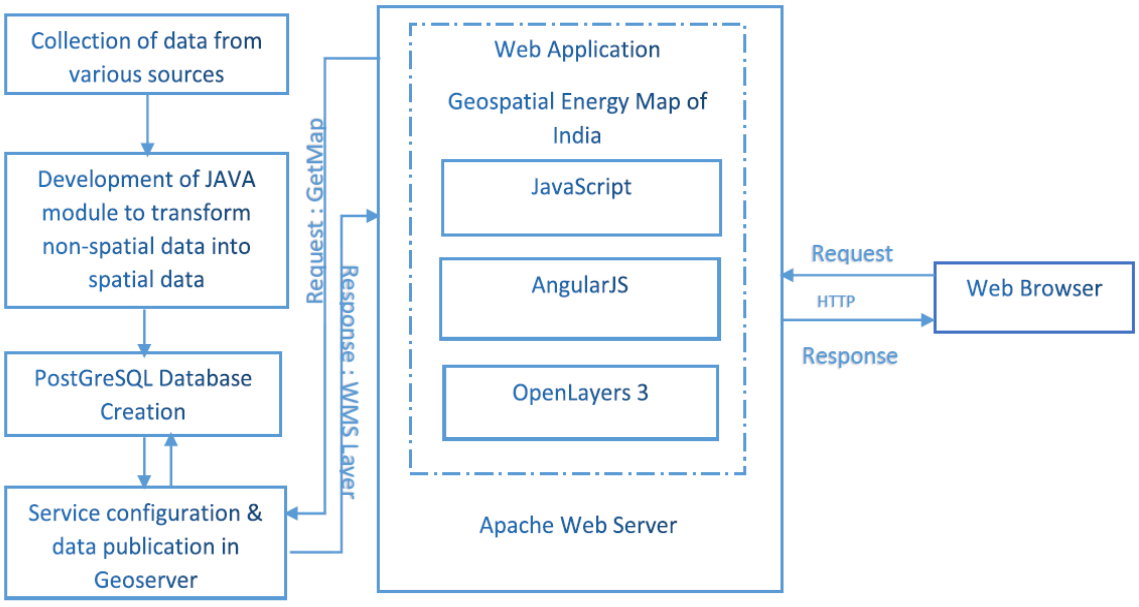

Figure 1: System flow diagram of a developed prototype

Table 1: Energy data used

No.	Data (State wise and Resource wise)
1	Installed electricity generation capacity
2	Electricity generation
3	Energy consumption
4	Peak electricity demand and supply
5	Gross electricity generation increase
6	Available power plants
	Other Data
7	Power supply and system loss
8	Transmission lines

PostGIS extension is used to add support for geographic objects in PostgreSQL. This spatially enabled PostgreSQL stores and manages non-spatial data along with its geometry or coordinates (spatial information). The WebGIS package allow to publish spatial resources and exposes them as Web services to client applications. GeoServer is JAVA based, open source WebGIS server or package which is used to share and edit geospatial data from almost all major spatial sources. It is Open Geospatial Consortium (OGC) compliant and allows flexibility in map creation and data sharing. It supports web services standards developed by OGC viz. Web Map Service (WMS), Web Feature Service (WFS), Web Coverage Service (WCS).

Web Map Service provides a simple HTTP interface for requesting map images from one or more distributed geospatial databases. It is also used to retrieve layer's metadata and server capabilities (Mishra and Sharma, 2016). Data added in PostgreSQL database is published in GeoServer as a WMS Service. As a response to the WMS request, map images are returned (i.e. JPEG, PNG, GIF) with pre-determined projection, reference and coordinate systems and with predefined associated symbols and colours. Data store is created in GeoServer to initiate a connection with PostgreSQL database. From that database, information is retrieved and published as WMS in GeoServer.

For proper planning and monitoring of energy resources, stakeholders requires an access to the energy data. To make data available and display it on a browser, WebGIS based information system is developed. It is developed using JavaScript, AngularJS and OpenLayers 3 API. JavaScript is a dynamic, open source scripting language used for building a web application. AngularJS is an open source front-end framework used for developing an application based on Model View Controller (MVC) architecture. To create maps and provide interaction with geospatial data, OpenLayers 3 API is used (Farkas, 2016). It is a lightweight JavaScript library. The developed web application contains various panels i.e. layer panel, legend panel, map panel. Layer panel displays all energy layers along with the overlay layers i.e. administrative boundary, rivers, LISS III Mosaic, RISAT Mosaic. The user can switch on or off layers using layer panel. GetMap request is sent to the server when the layer is selected. WMS service is returned as a response and displayed in a map panel. Opacity slider is added to each layer to modify the transparency of layers.

Selected layers are displayed in a map panel. The user can get feature information (i.e. energy details, layer information) by clicking on the map. GetFeatureInfo request is passed to the server with selected coordinates, which returns available information for that geometry. It provides a response in HTML format, which get displayed in a popup. Legend panel is used to provide a legend of the selected layer.

Chart, tables and tool components are developed for comparison and analysis of data. HighCharts API is used for generating user-friendly and interactive charts for a better understanding of information. For better user interaction, the toolbar is developed to provide various GIS functionalities i.e. zooming, panning, uploading/downloading files i.e. KML or GeoJSON, length/area calculator, feature drawing (point, line and polygon). The user can also save these features in KML / GeoJSON format.

3. Results and discussions

The developed application can be useful for stakeholders and users for collecting, analysing and disseminating energy information to promote sound policymaking. Better GUI and graphical representation help users to understand the information. Various electricity data layers i.e. generation, consumption, loss of electricity are available along with the overlay layers. Figure 2 shows the user interface of the web application. Layer panel containing layers related to electricity data and overlay data is shown. The user can add or remove layers using on/off checkbox. Map area displays all selected layers. Data of electricity generation by various fuels (thermal, hydro, steam, renewable) for each state is disseminated using pie chart, which can help users to analyse which mode is used most for electricity generation. i.e. Bihar, Tripura, Sikkim generate electricity mostly using renewable energy sources while other states i.e. Gujarat, Maharashtra generate electricity using thermal resources. In figure 3, various layers are stacked. The user can get feature information by clicking on a map. Feature Information of selected layers can be displayed using popup for selected location on map. The chart displayed in the figure shows a comparison of state wise energy consumption data for different years which will help in analysing the change in energy demand and supply. Based on given analysis, administrators can take measures for increasing supply or installation of power plants in the states having high energy consumption. Data of available transmission lines is also disseminated as an overlay layer in map. Figure 4 shows the data of all energy layers in tabular format, which helps in analysis of data. Legend panel shows legends for selected layers for better visual understanding of the data. Figure 5 displays layers related to solar power plants along with the opacity slider. The chart provides details of month wise installed capacity of the solar power plant.

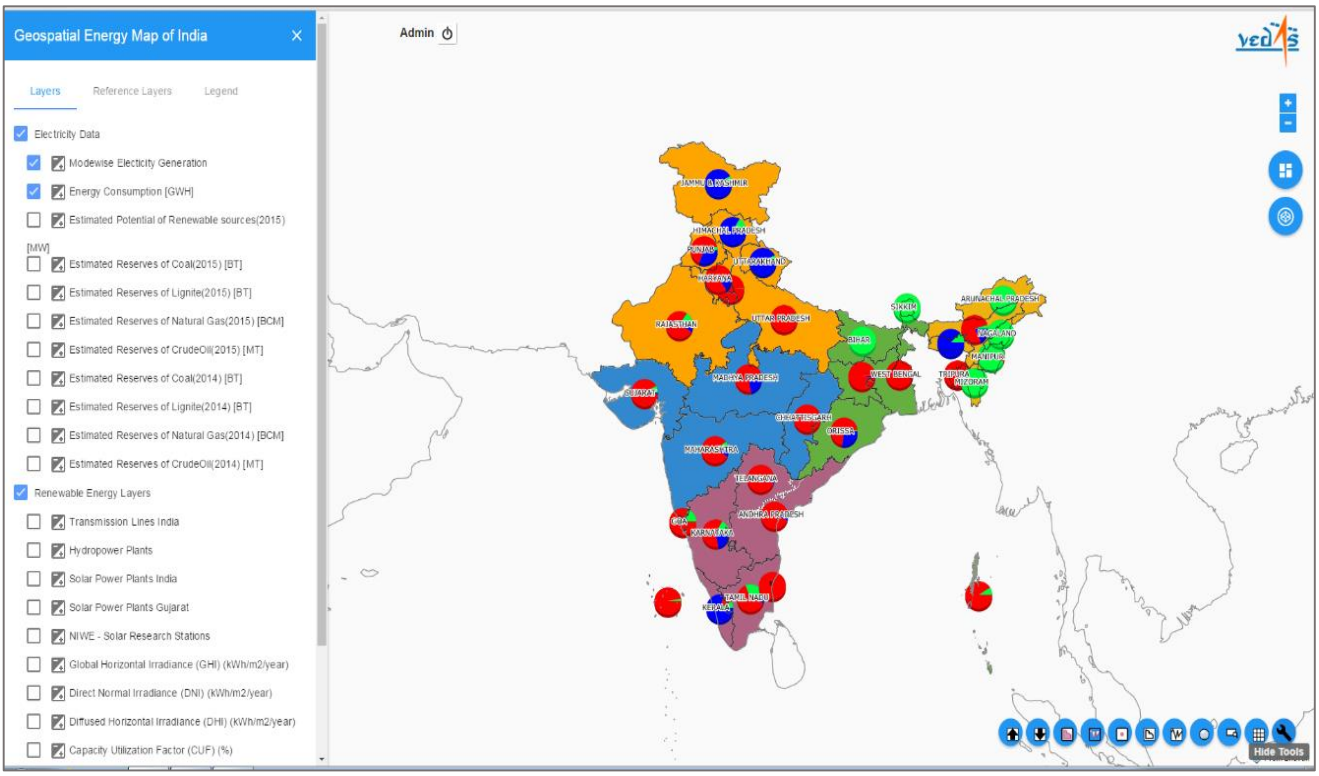

Figure 2: User interface for WebGIS based energy sector Information System

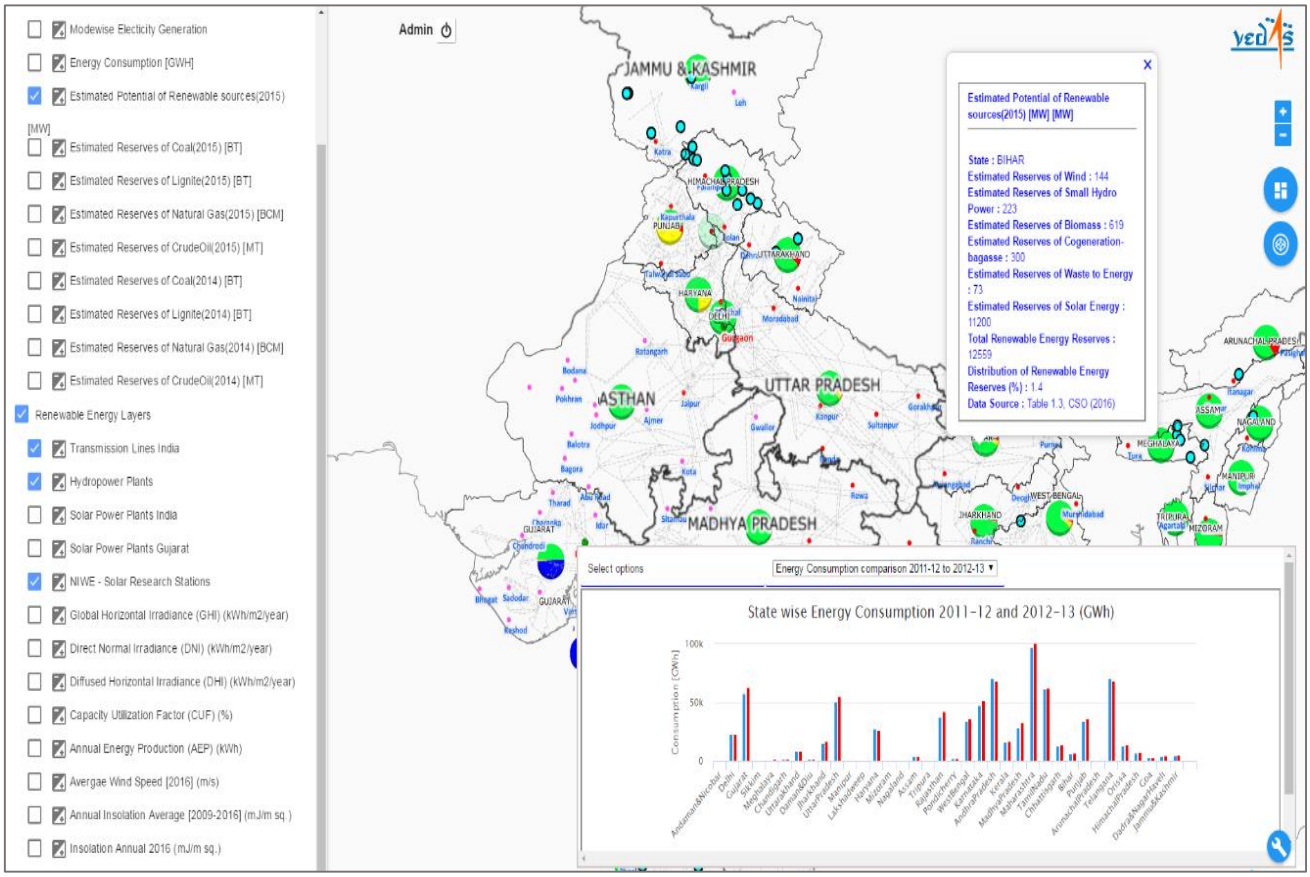

Figure 3: Layers of an estimated potential of renewable sources and transmission lines along with an energy consumption comparison chart

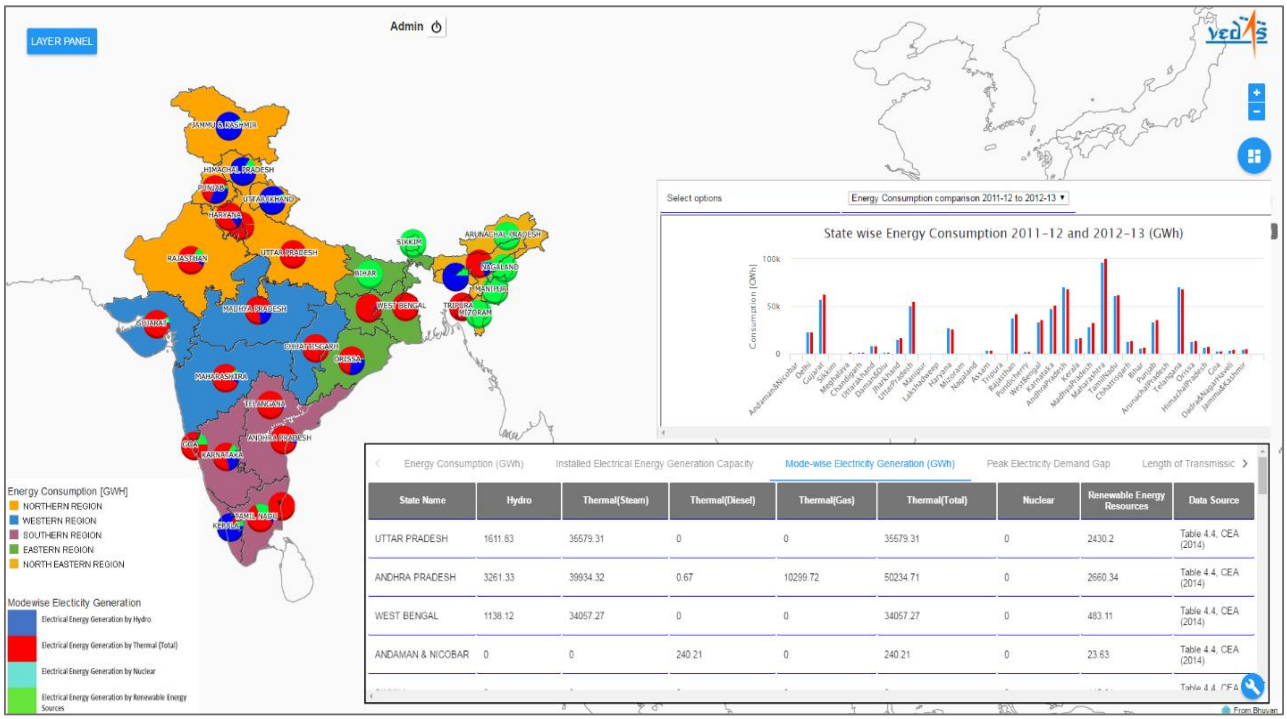

Figure 4: Layer preview along with legends and information in the chart and tabular format

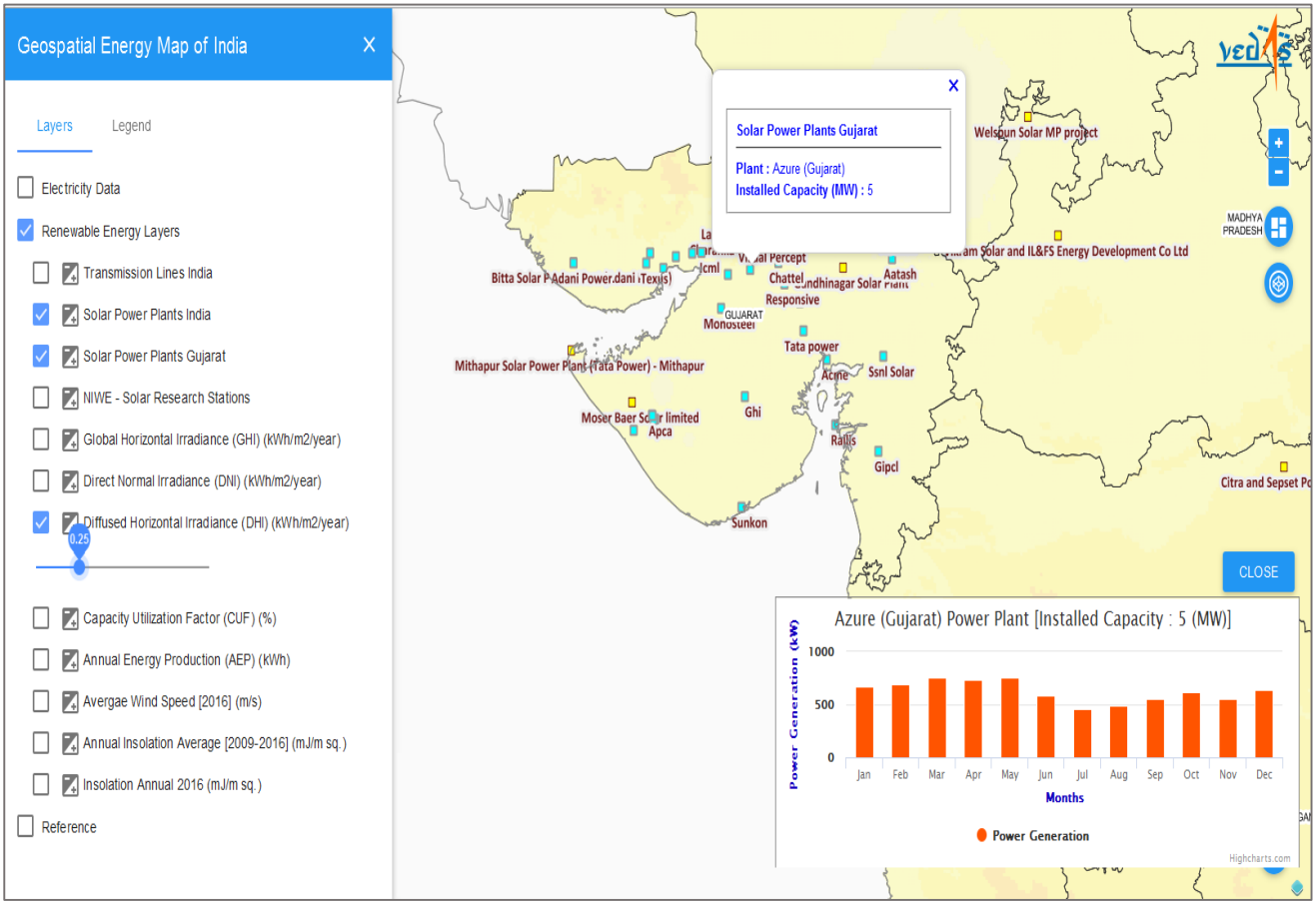

Figure 5: Chart demonstrating monthly installation capacity of the selected solar power plant

4. Conclusion

Spatially enabled PostgreSQL database creation facilitates in maintaining energy sector data centrally. Redundant data problem is solved as data has geometry as a key index. Users can visualize and analyse relevant energy data using this type of developed centralized system instead of searching from various sources. WebGIS based information system provides distributed access to the information, which removes the dependency of hardware or software to be installed at the user end. Use of open source GIS technology helps end users in retrieving information at lower or no cost. Accessing energy related data would help administrators in better decision-making and policy planning to satisfy the ever-growing energy demands. Such information can be used for development of new infrastructures of energy generation and reduce the dependency on imports of energy. As information system provides details of conventional and renewable energy resources, statistical analysis of usage of all resources will promote the utilization of green energy, which can minimize the damages done to the environment. Gathering data and making it available in graphical view can help users in providing an analytical overview of the current trends to understand and save energy.

Acknowledgements

The authors express their sincere gratitude to Shri. Tapan Mishra, Director, Space Applications Centre for their support and encouragement. The authors are also thankful to Dr Shashikant Sharma, Group Head, VRG and Dr Markand Oza, Division Head, CGDD for providing guidance and infrastructure to conduct this work.

References

Awange, Joseph & Kiema, John. (2013). Web GIS and mapping. Environmental Science and Engineering (Subseries: Environmental Science). 237-249. 10.1007/978-3-642-34085-7_18.

Caldeweyher D., J. Zhang and B. Pham (2006). OpenCIS—Open Source GIS-based web community information system. International Journal of Geographical Information Science, 20:8, 885-898.

Energy Statistics 2016. Available: www.mospi.nic.in/publication/energy-statistics-2016

Farkas G. (2016). Mastering OpenLayers 3. Packt Publishing Ltd, Birmingham, B3 2PB, UK, ISBN 978-1-78528-100-6.

General Review 2014. www.cea.nic.in/annualreports.html http://www.eia.gov

http://www.geoserver.org

http://www.mnre.gov.in

http://www.nrel.gov

http://www.openlayers.org

Indian Wind Energy, A Brief Outlook, (2017, 11 November).www.gwec.net/wp-content/uploads/vip/GWEC_IWEO_2016_LR.pdf.

Karnatak H. C., S. Saran., K. Bhatia. and P. S. Roy (2007). Multicriteria Spatial Decision Analysis in WebGIS Environment. Geoinformatica. 11:407–429, DOI 10.1007/s10707-006-0014-8

Mishra, S and Sharma, N (2016). WebGIS based Decision Support System for Disseminating Nowcast based Alerts: OpenGIS Approach. Global Journals Inc. (USA), 16(7), ISSN: 0975-4172

Sharma, N and S. Mishra (2017). Dissemination of heat wave alerts using spatial mashup technology and open source GIS. Journal of Geomatics, 11(2), 268-274.

Journal of Geomatics Vol 12 No. 1 April 2018

Comparative analysis of object based and pixel based classification for mapping of mango orchards in Sitapur district of Uttar Pradesh

Shreya Roy[2], Revati More[2], M.M. Kimothi[2], S. Mamatha[1], S.P Vyas[3] and S.S. Ray[1]*
[1]Mahalanobis National Crop Forecast Centre, DAC & FW, Pusa Campus, New Delhi, India
[2]Randstad India Pvt Ltd, Gurgaon
[3]Space Applications Centre, Indian Space Research Organisation, Ahmedabad, India
Email: *shibendu.ncfc@nic.in

(Received: Nov 07, 2017; in final form: April 18, 2018)

Abstract: Pixel based classification often fails to capture the spectral variability in high resolution images while delineating of horticulture crops, especially orchards. It tends to classify individual pixels on the assumption that individual classes contain uniform spectral behaviour but does not include contextual information like texture, shape etc. Salt and Pepper effect is very common in this type of conventional classifiers whenever there is an intra-class variation. These problems can be solved by using Object Based Image Analysis (OBIA) which combines similar neighboring pixels into meaningful geographical objects thereby preserving pixel topology. It takes into account both the spectral as well as spatial properties of the pixels while creating such objects. This study thereby attempts to evaluate the performance of per pixel classification with that of OBIA for mapping of mango orchards in Sitapur district of Uttar Pradesh (UP). High resolution imagery of IRS-Resourcesat 2 - LISS IV for the month of April, May and November have been used. Pixel based classification was performed using Supervised Maximum Likelihood Classifier (MXL) and Object based classification with Segmentation Lambda Schedule. Accuracy assessment carried out after ground truth data collection shows an accuracy of 65% and 92% respectively, which further increased to 96% after visual editing of the later. Comparison of areas obtained from remote sensing estimate and official state figures for last three years (2013-14, 2014-15 and 2015-16) shows a Relative Deviation (RD) of 22% in pixel based and -2.6% in object based, which gets reduced to negligible after post classification editing. Findings of this study concludes object based classification as the state of art for mapping of orchards with high accuracy.

Keywords: Mango Orchards; LISS IV; Classification; Object based image analysis; Accuracy

1. Introduction

Horticulture is one of the fastest growing sectors of agriculture in India and there has been a substantial increase in terms of both area and production of horticulture crops in recent years. However, to promote holistic growth there is a need of a comprehensive and updated database of the current scenario. The traditional approaches of crop estimation involved enumeration based on field surveys, which are time consuming, costly as well as labour intensive. Remote Sensing has evolved as one of the advanced tools to gather accurate information of earth's surface with its repetitive and synoptic coverage in a real time basis and thus can provide an alternative tool for monitoring and studying various aspects of horticultural crops. Studies (Rao et al., 2014) have shown use of remote sensing and geographical information systems to map the potential areas suitable under mango crop cultivation in the parts of Krishna and West Godavari districts of Andhra Pradesh using temporal data sets from AWiFS and LISS-III sensor onboard Resourcesat-1 satellite and IKONOS data. In a separate study horticultural fruit crop mapping was done in Adampur and Hisar-IInd development blocks of Hisar district using the satellite data of World View-2 for the months of March to Dec 2011 and IRS-P6-LISS-III for the month of February (Veena, 2014). The delineation of orchards using geospatial technology can provide additional information for management decision making, such as the determination of fruit yield, the quantification and scheduling of precise and proper fertilizer, irrigation needs, and the application of pesticides for pest and disease management (Panda et al., 2010). Johansen et al., (2009) showed the utility of high resolution data for delineation of banana plantations. However, studies (Whiteside and Ahmad, 2005, Wang et al., 2010, Aggarwal et al., 2013, Hebbar et al., 2014, Yadav et al., 2015, Aggarwal et al., 2016) have shown that conventional per pixel classifiers fails to capture the spectral heterogeneity and contextual information associated with high resolution images and thus results in poor accuracy in delineation of horticulture crops. Object Based Image Analysis (OBIA) on the other hand seeks to create "meaningful" objects by segmenting an image into groups of pixels with similar characteristics based on spectral and spatial properties (Benz et al., 2004). In a study (Basayigit and Ersan, 2015) carried out in Isparta-Turkey for separation of crop pattern using high resolution data of Quickbird-2, object-based classification method was found to give the highest accuracy in higher plants and perennial crops that consist of a mixture of soil and vegetation where elimination of the soil reflection was an essential factor. The accuracy of separation was believed to increase by combining the vegetation index with the object-based classification method. For homogenous patterns such as bare soil, vegetables and feed crops, the supervised classification method was found to be more successful than the object-based method.

In India, the CHAMAN (Coordinated Horticulture Assessment and MAnagement using geoiNformatics) project was initiated with the primary goal of providing area assessment and production forecast of major

horticultural crops in selected districts of major states (Ray et al., 2016). This project was launched by Ministry of Agriculture & Farmers' Welfare, under the Mission for Integrated Development of Horticulture (MIDH) and is being coordinated by Mahalanobis National Crop Forecast Centre (MNCFC). Mango is one of the crops identified under CHAMAN project for orchard mapping and area estimation.

Uttar Pradesh (UP) is the leading producer of mango in India and Sitapur district is one of the major mango belts in the state. Very few works have been carried out in mango orchard mapping in this state, using remote sensing data. This study thereby attempts to find the best technique for accurately mapping of mango orchards by comparing the performance of traditional pixel based classifier with that of OBIA in Sitapur district of Uttar Pradesh (UP) as a part of the CHAMAN programme.

2. Materials and methods

2.1 Study area

The Sitapur district of Uttar Pradesh is situated in central plane between 27°.54'- 27°.60' N and 80°.18- 81°.24' E above 100-150m mean sea level (Figure 1). Major horticultural fruit crops cultivated in Sitapur are mango, banana, papaya and guava. The total area under mango in Sitapur district is 15.5 thousand hectares. Other crops include wheat, paddy, urad, sugarcane, mustard, mentha etc.

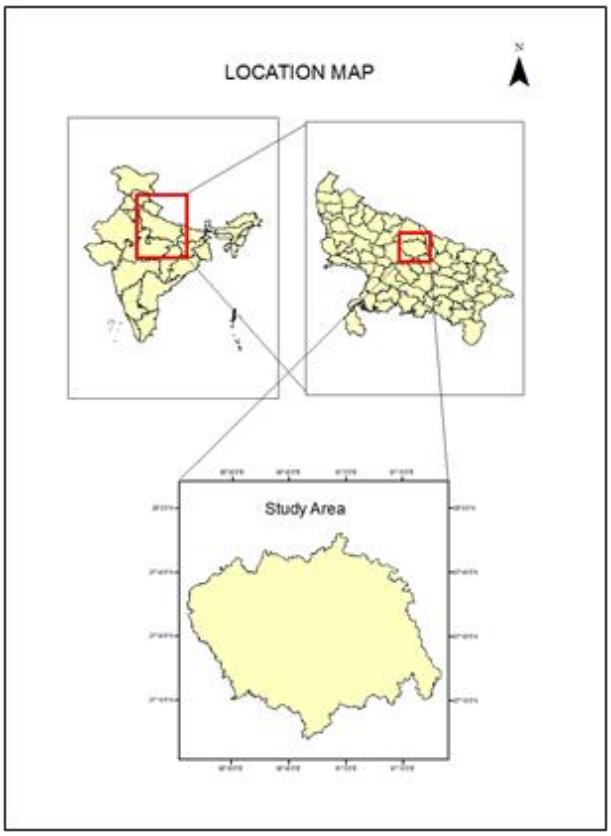

Figure 1: Study Area

2.2 Data

Dataset used, comprised of both spatial and non-spatial nature as discussed below.

Remote sensing data

High resolution ortho-rectified LISS (Linear Self Imaging and Scanning) IV data (with 5.8 m spatial resolution) have been used for this study. The details of satellite datasets are given in table 1.

Months of April, May and November are best suitable for mapping of orchard crops as crop cover is minimal during those time period (Singh et.al., 2016). Also orchards are perennial in nature so that duration of two three years will not make any great difference.

Field data:

Ground truth (GT) survey was carried out in the month of May on the basis of varying spectral signatures as discernible on the satellite image as well as those marked in google earth to identify the competing in the study area. GT was done using CHAMAN App in Android phone for recording the geographic coordinates of orchards or fields, developed by National Remote Sensing Centre. Other ancillary information such as orchard area, row spacing, orchard age, and variety etc. were also recorded during field survey. In total 41 GT points were collected.

Collateral data:

Land Use Land Cover (LULC) map at 1:50k scale, was collected from Uttar Pradesh State Remote Sensing Centre, Lucknow.

Orchard statistics data:

Last 10 years (2006-07 to 2015-16) district level statistical data of mango orchards were collected from the Uttar Pradesh State Horticulture Mission Report and online HAPIS (Horticulture Area Production Information System) portal.

Table 1: Satellite data used

Satellite Data	Sensor	Bands	Path/Row	Date
Resourcesat-2	LISS IV	1,2,3 (Green, Red, NIR)	99-52B	15th April 2013, 12th Nov 2014
			100-52A	15th April 2014,4th May 2015
			100-52C	15th April 2014,4th May 2015

2.3 Satellite data pre-processing

All the scenes of LISS IV were subjected to the following pre-processing steps, viz. geometric correction, conversion of Digital Number (DN) to radiance and radiance to top of atmosphere (TOA) reflectance, before being used for analysis as per the methodology elucidated in Baba Shaeb et al. (2013).

2.4 Normalized Differential Vegetation Index (NDVI) generation

NDVI (Rouse et al., 1974) images were generated from the reflectance images using the equation given below:

$$NDVI = (\rho_{NIR} - \rho_{Red}) / (\rho_{NIR+} \rho_{Red}) \quad \ldots\ldots \quad (1)$$

where ρ is reflectance.

2.5 Pixel based classification

Methodology for pixel based classification has been shown in Figure 2.

Building the vegetation mask

NDVI index is a direct indicator of green cover hence could be used to mask out the urban settlements, water bodies and other non-vegetation classes. The NDVI values ranges from -1 to +1. It is generally below 0 equal for water and non-vegetation classes and shows a positive values for normal to healthy vegetation. Here, the NDVI value of 0. 3 was selected as a threshold and the theme classes having value below the threshold were masked out and a binary vegetation mask was thereby generated.

Use of LULC to delineate forest/natural vegetation class

In this study the target object to be delineated was orchards, hence the possibility of mixing of orchard and forest/ natural vegetation classes could not be overlooked as the near similar spectral signatures and tone/ texture of these two classes may lead to miss classification. The LULC map was used to address this issue and major forest classes were removed.

Image classification

Training samples were generated using ground truth data as well as taking reference from google earth and supervised classification using Maximum Likelihood Classifier (MXL) technique was performed over the masked images. MXL classifier assumes that the population from which training samples are drawn are multivariate normal in their distribution (Navalgund et.al., 2007).

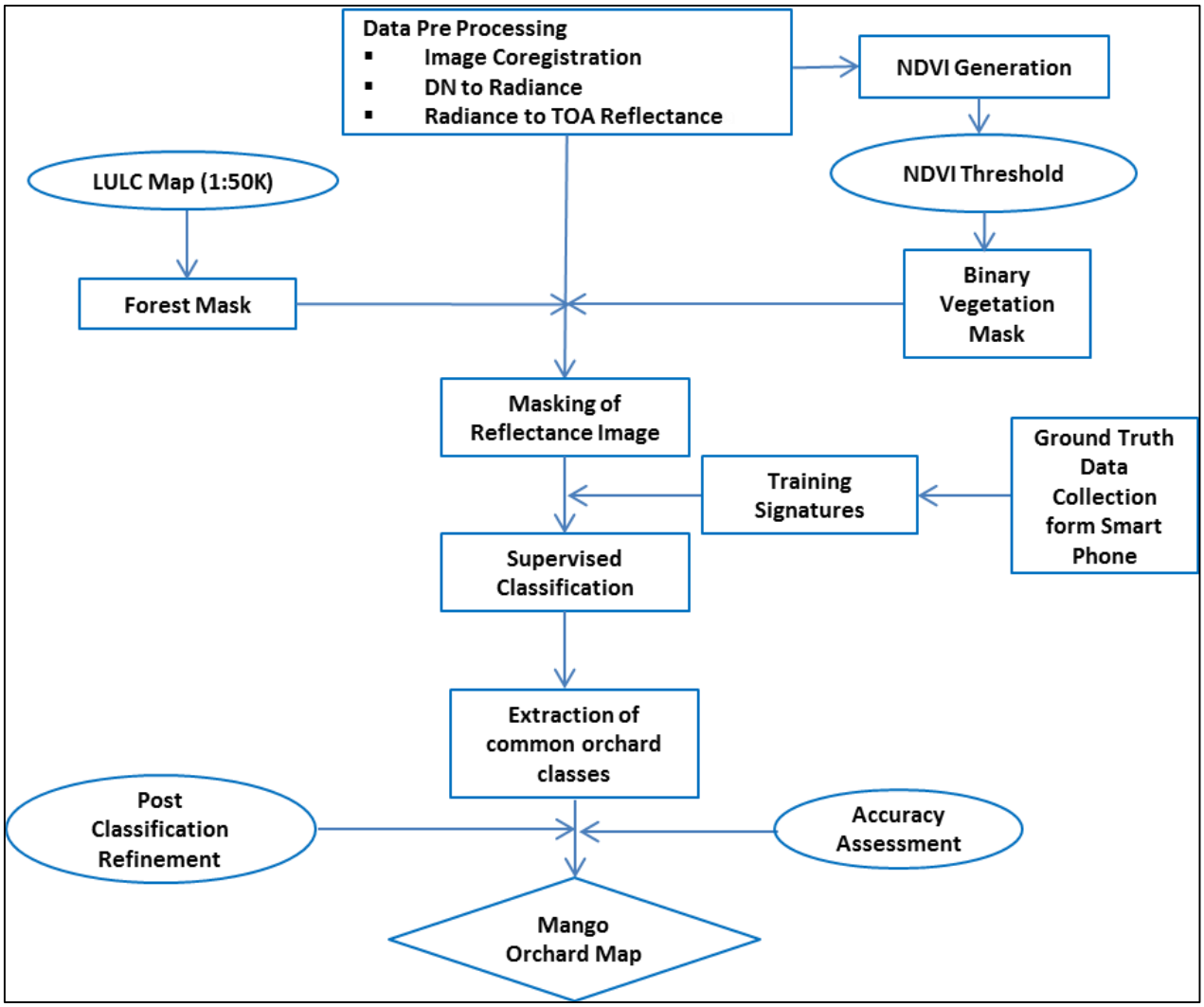

Figure 2: Methodology for Pixel Based Classification

Extraction of common orchard classes
All the scenes were classified separately and the common orchard area found in them were combined to extract the common orchard area. Orchards are perennial in nature and show similar spectral signatures in all the scenes unlike field crops which have peak spectral values at the time of maximum vegetative stage and weak spectral values at the time of harvest.

Post classification refinement
Post classification refinement of the derived area was performed to remove the redundant/misclassified small clusters by re-verifying with google earth images and visual comparison of tone and texture. The final mango orchard map was derived.

Accuracy assessment
Accuracy assessment is an important step in the process of verifying and validating the analysed remote sensing data. The most common way to express classification accuracy is the preparation of error matrix also known as confusion matrix or contingency matrix (Stehman, 1997). Such matrices show the cross tabulation of the classified land cover and the actual land cover reported by ground truth and calculation of overall accuracy of classification.

2.6 Object based classification
Image segmentation is the first step in object-based image analysis (Castilla and Hay, 2008). This process separates the image into segments that are arranged according to the classification of spectral, geometric, textural and other characteristics of the objects (Veljanovski et al., 2011). There are many techniques to perform image segmentation and those techniques can be categorized into three classes: thresholding/ clustering, region based and edge based (Fu and Mui., 1981, Haralick and Shapiro, 1985).

In this study object based classification of orchard areas is based on Segmentation Lambda Schedule algorithm (Govedarica et al., 2015) which is available as part of Objective Erdas Imagine software 2015.

Raster pixel processor
First step is the processing of pixels with Single Feature Probability (SFP) function. It computes a probability metric (between 0 to 1) to each pixel of the input image based on its pixel values and training samples (orchards). Pixels with values similar to those that represent the orchard class, will have a higher probability value. Lower probability value is assigned to pixels that differ significantly from the pixels that represent an orchard class.

Raster object creator
The resultant probability pixel layer is then grouped into meaningful objects based on Segmentation Lambda Schedule (FLS) algorithm. Unlike normal segmentation parameter it considers spectral as well as texture, size and shape while grouping of homogenous pixels depending upon the weights assigned while grouping (Imagine Objective User Guide, 2015). Segment size also depends upon pixel: segment ratio. In this case the average size of the segment is set to 250.

The spectral information was given a higher weightage as compared to texture (Measured as mean of DN values to segment) since the base data is multispectral LISS IV. Segmentation parameters used in this study has been shown in table 2.

Table 2: Segmentation Parameters

Spectral	Texture	Shape	Size
0.7	0.5	0.3	0.3

Raster object operator
In order to improve the results of the segmentation, probability filter was used. This operator removes all raster objects whose zonal probability mean is less than the specified Minimum Probability. In this case, two probability filters were chosen one at 0.3 (P1) and another at 0.1 (P2) as shown in Figure 3. In P1(0.3) The number of orchard pixels captured were less owing to its higher threshold value than in P2. However, lowering the threshold led to inclusion of some non-orchard pixels also which has to be refined by manual editing later on.

Raster to vector conversion
Raster Objects created in previous step were then converted to the vector objects using polygon trace.

Vector object operator
Smooth filter was then applied to smoothen the boundaries of orchard polygons. Smoothening factor of 0.5 was chosen which was found to be optimum.

Vector object processor
This step performs operation on vector layer. Area and Eccentricity factors were considered to clean up the vector objects. Higher values of Eccentricity (0.9) helps to eliminate linear features. In this case row plantations mixing with mango orchard classes were removed.

Vector clean up operator
Cleaning of vector layers was done in Arc GIS by onscreen visual interpretation and applying the non-vegetation mask to remove scrub land/ wetlands and erroneous vector object if any. The final mango orchard map was prepared by combining the orchard areas of all the overlapping/two date scenes.

Accuracy assessment
Mapping accuracy (Hebbar et al., 2014) was carried out with the ground truth points.

$$MA = \frac{No\ of\ correctly\ classified\ GT\ points}{Total\ number\ of\ GT\ points} \quad \text{.....(2)}$$

Figure 4 shows the methodology.

.

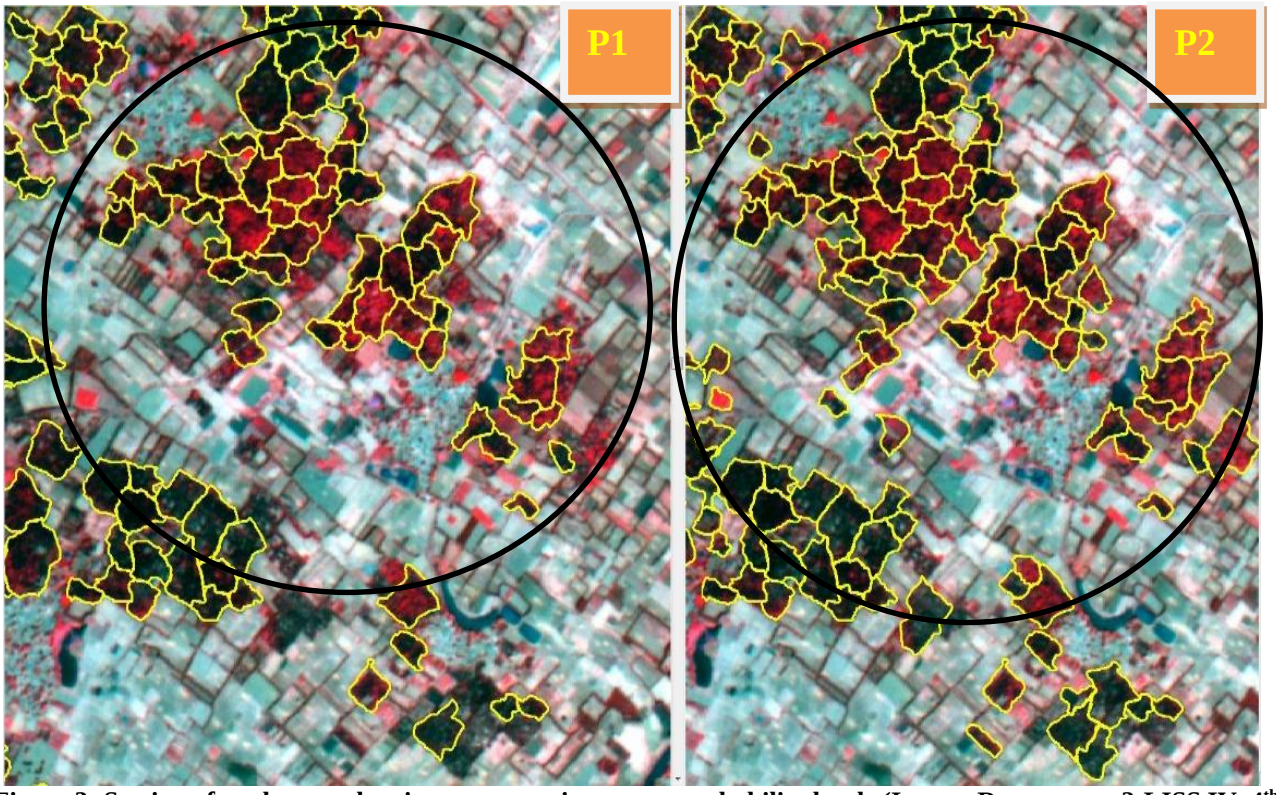

Figure 3: Section of study area showing segmentation at two probability levels (Image: Resourcesat 2-LISS IV, 4th May, 2015)

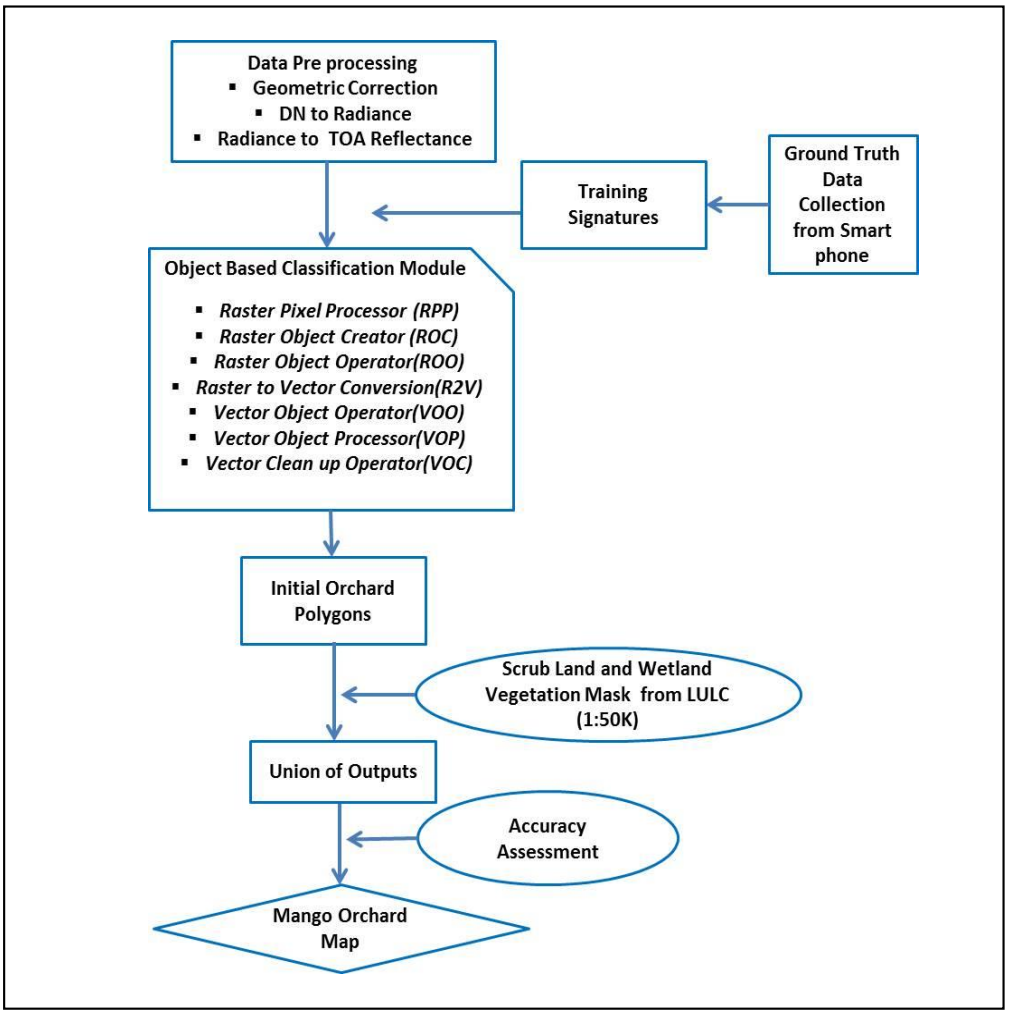

Figure 4: Methodology for Object Based Classification

4 Results and discussions

3.1 Comparison between pixel based and OBIA

Orchard plantations have a characteristic row and column pattern of planting with wide spaces in between two trees which gives soil exposure or weak NDVI values. In pixel based approach pixels are grouped in a class based only on its spectral characteristics, hence those spaces are treated as different class resulting in non-uniform class or gaps in final classified output which led to area under estimation as shown in Figure 5. It also fails to include the boundary and edge pixels. Young orchards exhibiting weak spectral signature and texture almost similar to agricultural field or fallow are also misclassified. On the other hand, OBIA considers group of pixels within an orchard as meaningful objects based on spectral, tonal, textural, size and shape characteristic and thus captures within orchard variability and heterogeneity. The final output shows well demarcated orchard boundaries distinctly different from field and fallow classes as shown in Figure 5. Thus the area estimation is quite reliable in OBIA. Manual digitization on high resolution google earth images gives even more clarity which is however good for a small part of the study area but is a crude and time consuming method for making district level orchard maps. OBIA is semi-automatic in nature and the output can also be overlayed on high resolution images for further refinement if needed.

3.2 Accuracy assessment

Accuracy assessment carried out after ground truth (GT) data collection shows an accuracy of 65% in pixel based and 92% in object based, which upon further refinement increased to 96%. Table 3. shows comparison of area obtained from both the approaches with the average statistics for three years obtained from HAPIS (Horticulture Area and Production Information System) online portal shows a Relative Deviation (RD) of 22% in pixel based and -2.6% in object based approach has been observed. After post classification editing in the latter case the RD got reduced to minimal.

Table 3: Comparison of final Area (Hectares) estimates through different classifiers

Pixel Based Estimate	Object Based Estimate	Horticulture Statistics Average of 3 years (2013-14 to 2015-16)
12117	15435	15379

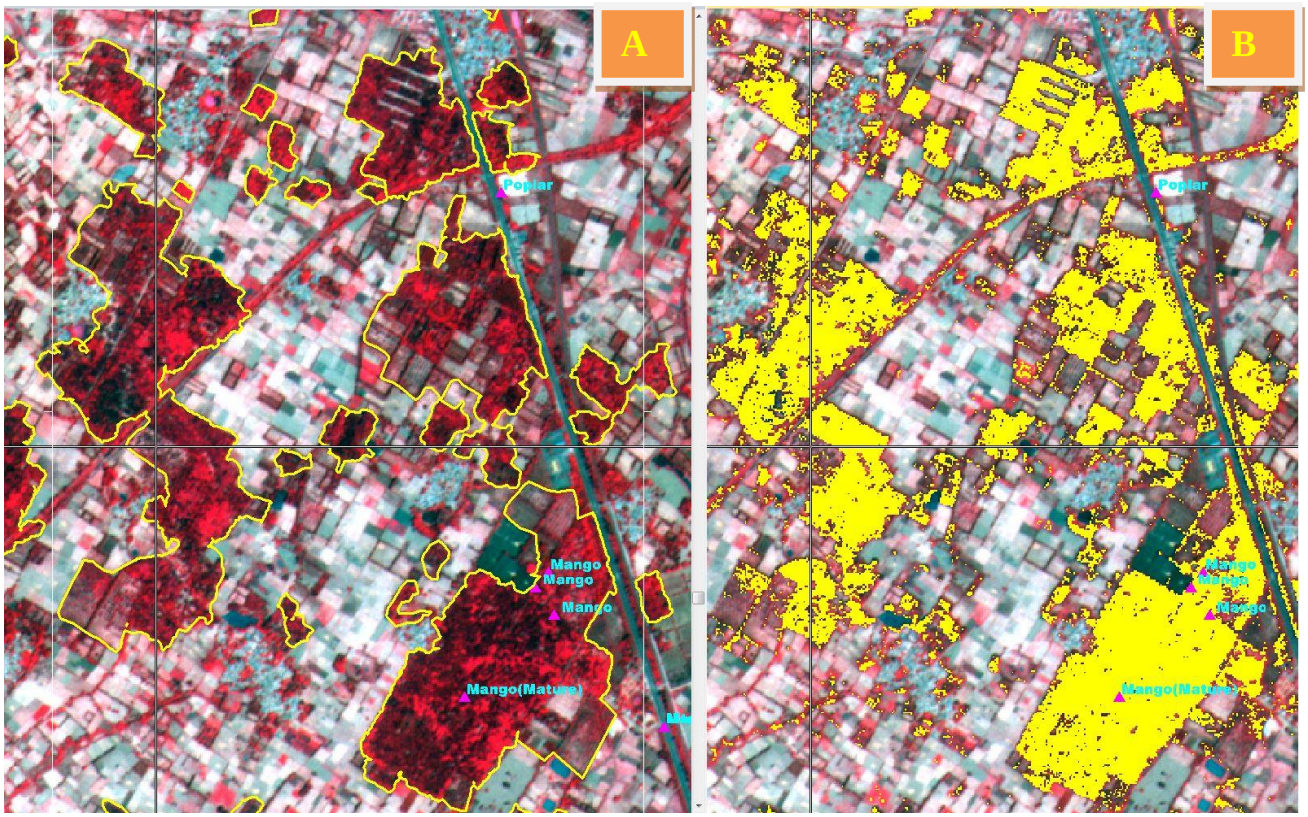

Figure 5: Part of study area showing comparison between two approaches A: Object Based Classification and B: Pixel Based Classification (Image: Resourcesat 2-LISS IV; Date: 4th May, 2015)

Conclusion

The current study shows the comparison of traditional pixel based classifier with that of Object Based Classification (OBIA) for mango orchard mapping in Sitapur. It was observed that conventional per pixel classifiers though convenient to use in homogenous areas, fails to capture the heterogeneity and intra-class variability with the increase of spatial resolution. The property of class uniformity breaks in former case leading to less accuracy, chances of mixed pixels, salt and pepper effects. It often fails to capture the differential canopy reflectance owing to different age groups of trees in an orchard as well as intercropping, soil exposure etc. On the other hand, in OBIA similar pixels are converted into objects, based on texture, spectral and spatial parameters like size, shape, eccentricity, compactness and proves far more superior in terms of capturing orchard heterogeneity. It also reduces the chance of occurrence or redundant and mixed pixels. It can be concluded that OBIA is the state of art in orchard mapping as compare to pixel based classification. The current study is however limited to use of high resolution multispectral data of LISS IV. Further research work is needed to differentiate between different competing orchards viz. mango and litchi by inclusion of very high resolution satellite data of sub meter level spatial resolution where individual tree crowns can be detected.

Acknowledgment

The above study was carried under the CHAMAN project of Department of Agriculture, Cooperation and Farmer's Welfare, Ministry of Agriculture and Farmers' Welfare. Authors wish to thank State Horticulture Department and Uttar Pradesh Remote Sensing Applications Centre (RSAC-UP) for their cooperation and logistic support for carrying out ground truth in Sitapur district. Authors are thankful to Dr Pradeep Kumar, Assistant Director, MNCFC for critically reviewing the paper.

References

Aggarwal, N., M. Srivastava and M. Dutta (2016). Comparative analysis of pixel-based and object-based classification of high resolution remote sensing images – A Review, International Journal of Engineering Trends and Technology, 38(1), 5-11.

Aggarwal, S., L.S. Vailshery, M. Jaganmohan, H. Nagendra (2013). Mapping urban tree species using very high resolution satellite imagery: Comparing pixel-based and object-based approaches, ISPRS International Journal of Geoinformation, 2, 220-236.

Baba Shaeb, K. Hareef, A.K. Joshi and S.V. Moharil, (2013). Surface reflectance retrieval from the high resolution multispectral satellite image using 6S radiative transfer model, International Journal of Remote Sensing and GIS, 2(3), 130-137.

Basayigit, L. and R. Ersan (2015). Comparison of pixel-based and object-based classification methods for separation of crop patterns, Scientific Papers. Series E. Land Reclamation, Earth Observation & Surveying, Environmental Engineering, IV,148-153.

Benz, U., P. Hofmann, G. Willhauck, I. Lingenfelder and M. Heynen (2004). Multi-resolution, object-oriented fuzzy analysis of remote sensing data for GIS-ready information. ISPRS Journal of Photogrammetry and Remote Sensing, 58, 239-258.

Castilla, G. and Hay, G.J. (2008). Image objects and geographic objects. Object-Based Image Analysis – Spatial concepts for knowledge driven remote sensing applications (Thomas Blaschke, Stefan Lang, Geoffrey J. Hay: Editors), 91-110.

Erdas Imagine Objective User Guide (2015).

Fu, S.K. and J.K. Mui (1981). A Survey on Image Segmentation Pattern Recognition, 13, 3–16.

Govedarica, M., A. Ristic, D. Jovanovic, M. Herbei, M. and F. Sala (2015). Object oriented image analysis in remote sensing of forest and vineyard areas, Bulletin UASVM Horticulture, 72(2).

Haralick, R.M. and L.G. Shapiro (1985). Image segmentation techniques, Computer Vision Graphics and Image Processing, 29 (1),100-132.

Hebbar, R., H.M. Ravishankar, S. Trivedi, S.R. Subramoniam, U. Raj and V.K. Dadhwal (2014). Object oriented classification of high resolution data for inventory of horticultural crops. The International Archives of the Photogrammetry, Remote Sensing and Spatial Information Sciences, XL-8, ISPRS Technical Commission VIII Symposium, Hyderabad, India, December 09-12, 2014.

Imagine Objective User Guide (2015).

Johansen, K., S. Phinn, C. Witte, S. Philip, and L. Newton (2009). Mapping banana plantations from object-oriented classification of SPOT-5 Imagery. PE & RS, 75(9),1069–1081.

Navalgund, R.R., V. Jayaraman and P.S. Roy (2007). Remote sensing applications: An overview, Current Science, 93(12).

Panda, S.S., G.J.P. Hoogenboom and O.P. Joel (2010). Remote sensing and geospatial technological applications for site-specific management of fruit and nut crops: A review, Remote Sensing, 2, 1973-1997.

Rao, K.P.V., P.V. Ramana, M.V.R. Seshashai, (2014). Identification of potential areas for horticulture expansion using remote sensing and GIS techniques, Journal of Space Science and Technology, 3(1), 1-8.

Ray S. S., S. Mamatha S, K.R Manjunath., Uday Raj, M.V.R. Seshasai, K.K. Singh, M.M. Kimothi, J.S. Parihar and M.Saxena (2016). CHAMAN: A National Level Programme for Horticultural Assessment & Development. NNRMS Bulletin (40), 1-6.

Rouse, J.W., R.H. Haas, J.A. Scheel and D.W. Deering (1974). Monitoring vegetation systems in the Great Plains with ERTS. Proceedings, 3rd Earth Resource Technology Satellite (ERTS) Symposium, (1), 48-62.

Singh, N., K.N. Chaudhari and K.R. Manjunath (2016). Comparison of citrus orchard inventory using LISS-III and LISS-IV data. Proceedings of the SPIE, Volume 9880, Multispectral, Hyperspectral and Ultra spectral Remote Sensing Technology, Techniques and Applications, *VI,98802E*

Stehman, S. (1997). Estimating standard errors of accuracy assessment statistic under cluster, Remote Sensing of Environment, 62 (1),77–89.

Veena (2014). Horticulture fruit crops mapping of Adampur and Hisar-IInd Blocks of Hisar District using geoinformatics techniques. International Journal of Science and Research (IJSR), 3 (8),1855-1859.

Veljanovski, T., U. Kanjir and K. Ostir (2011). Object based image analyses of remote sensing data, Geodetski vestnik,, 55 (4),665-688.

Wang, K., E.S. Franklin, X. Guo and M. Cattet, (2010). Remote sensing of ecology, biodiversity and conservation: A review from the perspective of remote sensing specialists, Sensors,10, 9647–9667.

Whiteside, T. and W. Ahmad (2005). A comparison of object-oriented and pixel-based classification methods for mapping land cover in Northern Australia. Proceedings of SSC2005 Spatial intelligence, innovation and praxis: The national biennial Conference of the Spatial Sciences Institute, Melbourne: Spatial Sciences Institute.

Yadav, S., I. Rizvi and Kadam, S. (2015). Comparative study of object based image analysis on high resolution satellite images for urban development, International Journal of Technical Research and Applications, 31, 105-110.

Journal of Geomatics Vol 12 No. 1 April 2018

Geospatial assessment on the occurrences of erosion and pattern of channel migration of river Brahmaputra along the Majuli Island of Assam

Jonali Goswami[1], Dibyajyoti Chutia[1], Stuti Singhania[2], Monidip Chutia[3], Vikas Sharma[1], Chirag Gupta[1] and PLN Raju[1]
[1]North Eastern Space Applications Centre, Department of Space, Shillong, Meghalaya, India
(jonali.goswami@gmail.com, d.chutia@nesac.gov.in)
[2]Kumaun University, Nainital, Uttarakhand, India (stuti@gmail.com)
[3]Department of Soil Conservation, Jorhat Division, Assam, India (monidip@gmail.com)

(Received: Jan 24, 2018; in final form: Apr 18, 2018)

Abstract: Majuli Island of Assam has been suffering heavy erosion through ages, whether it is bankline or surface soil erosion. The Brahmaputra and Subansiri rivers are the main cause of the depletion of this island since they change their course after every flood event since the plains of the Assam suffer from heavy rains during monsoon. The river also erodes the surface picking up a lot of sediment from the area. So, the process of erosion and deposition continues every year. Geospatial technology combined with unmanned aerial vehicle (UAV) remote Sensing (UAV-RS) has been effectively used to assess the changing scenario and channel migration pattern of Brahmaputra along the island over a span of 40 years from 1976 to 2017. A part of Majuli breached by the river during flood was mapped and studied. Deposition is prominent at the right bank from the right side, but gradual erosion hinders the middle part. Therefore, the river was found widening at the middle part. This has in turn reduced the land surface of the island due to which Majuli has been shrinking and sinking over the years and it has been estimated that it will disappear in 10-15 years if such circumstances continue to prevail and no preventive measures are taken.

Keywords: Erosion, Geospatial technology, UAV, Brahmaputra

1. Introduction

Majuli is the largest river island in the world in the Brahmaputra river, Assam, India and also the first Island district of the country. The island had a total area of 1,250 sq km at the beginning of the 20th century (Sharma and Acharjee, 2012), but having lost significantly to erosion, an area of only 352 sq km in 2014 has been estimated (Lahiri and Sinha, 2014). Majuli has shrunk as the river surrounding it has grown (http://majulilandscape.gov.in/geography.php). The island (Figure 1) was formed by the Brahmaputra river in the South and the Kherkutia Xuti, a branch of the Brahmaputra, joined by the Subansiri river in the North (http://en.wikipedia.org/wiki/Majuli). It was simply a landform formed out of continuous depositions of sand due to the changing course of rivers viz. The Brahmaputra flows to the north of Majuli and one of its tributaries- the Dihing, flowing south of Majuli which received the Dikhow, Jhanji, Bhogdoi, Dhansiri rivers and some other small tributaries to meet the Brahmaputra at Lakhu. Physiographically, Majuli has an undulating land form. The river Brahmaputra and its tributaries were shifting southward, eastward and westward as part of the change of course in the river. As the main course of river Brahmaputra (Lohit) was much wider than the course of river Dihing, the northwestern part of Majuli was majorly affected by annual flooding. This resulted in the constant deposition of sand and the introduction of new plant species on the land. Majuli has been suffering huge erosion problems, whether it is bankline erosion or surface soil erosion, caused mainly due to the annual floods during the monsoon season when the Brahmaputra river swells up. Brahmaputra Board in 1997 prepared a report where the area of the island is mentioned to be 925 km^2 in 1971 (http://www.brahmaputraboard.gov.in/NER/Archive/Archive.html).

1.1 Geospatial technologies for soil erosion study

Geospatial technology has proven to be a significant tool for erosion studies on a large scale since field studies for prediction and assessment of soil erosion are expensive, time-consuming and need to be collected over many years. Though providing a detailed understanding of the erosion processes, field studies have limitations because of complexity of interactions and the difficulty of generalizing from the results (Saha et al., 1992). Space Application Centre (SAC) and Brahmaputra Board (1996) jointly studied the river erosion problem of Majuli Island and identified the areas of the island which have undergone changes along the bankline due to erratic behaviour of the river (Gogoi and Borpujari, 2014). Mani et al., 2003 studied the erosion affect around Kaniajan village in south Majuli using temporal satellite data to estimate land lost due to erosion. Temporal data from satellite imageries also play as an important tool to identify the channel migration pattern of river banklines over the years. Sarma and Phukan (2004) gave a comprehensive account of the origin and geomorphological changes, including erosion and deposition in Majuli Island (Sarma and Phukan, 2004). Kotoky et al., 2004 studied the erosion and deposition of the island from 1914 to 1998 and revealed that the extent of erosion and deposition was not same for the period 1914–75 and 1975–98 (Kotoky et al., 2004).

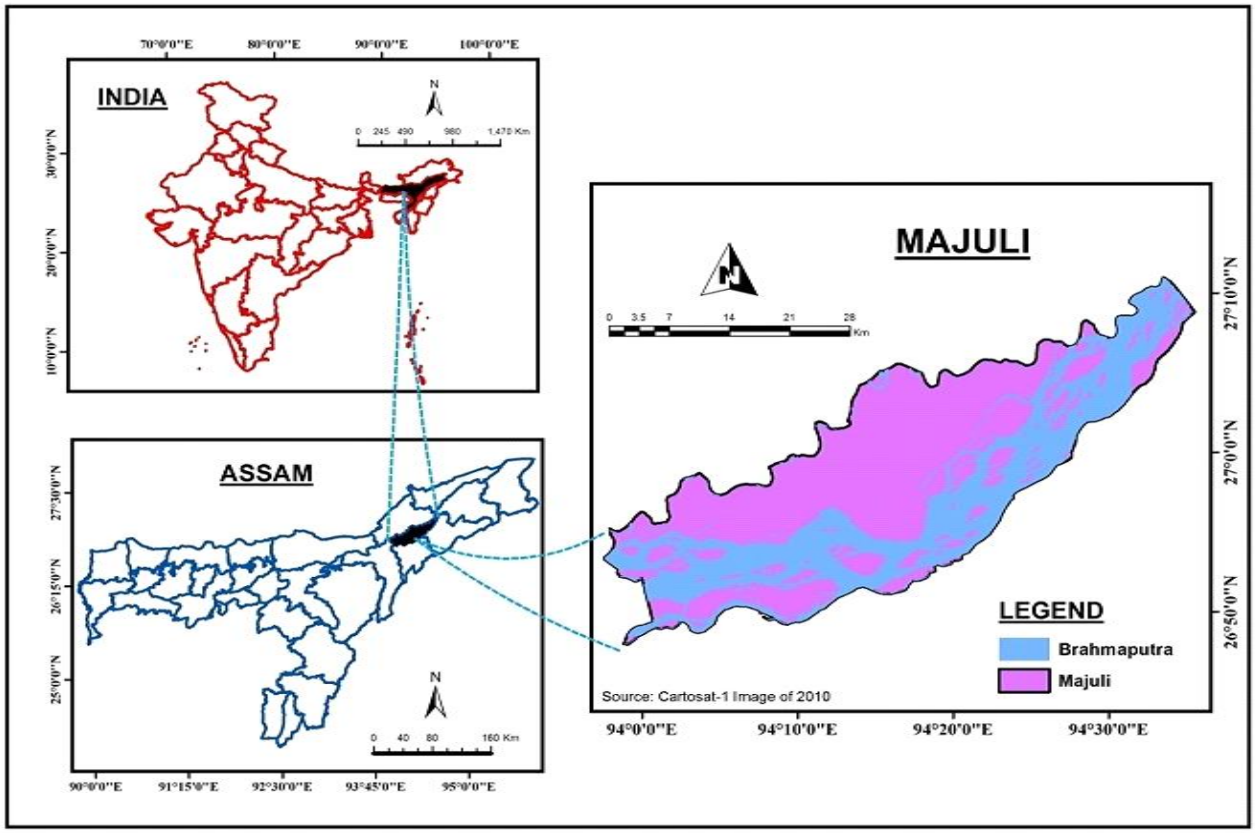

Figure 1: Geographical location of Majuli Island of river Brahmaputra

1.2 Scope and objective

Water erosion is the most widespread form of land degradation and occurs widely in all agro-climatic zones. The displacement of soil material by water can result in either loss of topsoil or terrain deformation or both. This category includes processes such as splash erosion, sheet erosion, rill or gully erosion. The result is more loss of fertile topsoil and plant nutrients. In some cases where subsoil has kankars, lime nodules, etc will get exposed on the top thereby altering the pH regime of the surface soil and subsequent nutrient holding capacity and their availability to plants. Majuli has been suffering huge erosion problems.

The main objective of this work is to assess the occurrences of erosion and pattern of channel migration of river Brahmaputra along the Island over a span of 40 years from 1976 to 2017.

2. Geospatial data and methodology

Satellite images of last 40 years from 1976 to 2017 (1976, 1989, 1999, 2009 and 2017) of Landsat Multispectral Scanner (MSS) of Landsat-1, Landsat-2, Landsat-4 and Landsat-5 with 60 m spatial resolution, 0.5-1.1 µm spectral range, Landsat Thematic Mapper (TM) of Landsat 4 and Landsat 5 with 30 m spatial resolution with 0.45-0.90 µm spectral range and Operational Land Imager (OLI) of Landsat 8 with 30 m spatial resolution with 0.45-0.90 µm spectral range have been utilized to study the fluvial geomorphology of the Brahmaputra river around Majuli Island. Geospatial technology supported by the sophisticated UAV for acquiring high resolution satellite imagery was effectively used for estimation damage caused by the floods on a real time basis. The ground pixel resolution of the UAV image was 5 cm which was flown at a 100 m height from msl in a breaching location in Majuli Island, Assam.

Bankline digitization is done for each year and then these banklines are overlaid approximately at 10 years of interval i.e. 1976-1989, 1989-1999, 1999-2009 and 2009-2017 and then an overall from 1976 to 2017 to analyze the changes. Bankline migration was measured taking 17 cross-sections using the recent channel pattern for each interval to observe the areas being continuously eroded. Bankline migration of the river along with location of 17 cross-sections during time frame 1976 to 1989, 1989 to 1999, 1999 to 2009 and 2009 to 2017 are shown in figure 2, figure 3, figure 4 and figure 5 respectively. The rate of erosion and fill were calculated for the part of Brahmaputra River, which falls within the study area.

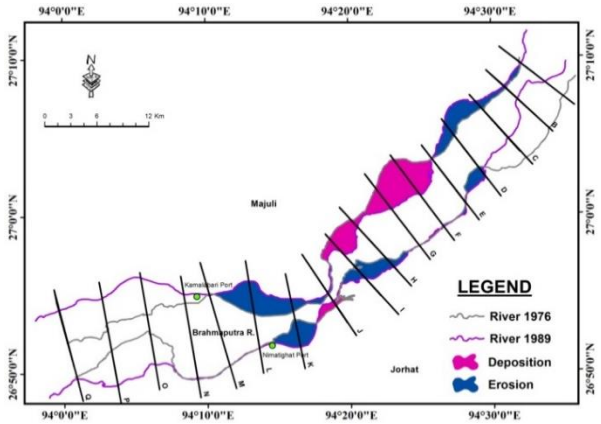

Figure 2: Bankline migration from 1976 to 1989

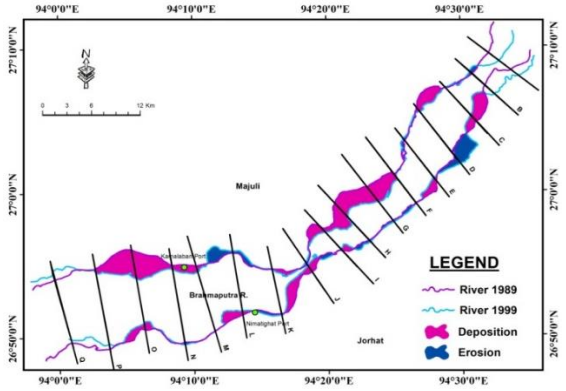

Figure 3: Bankline migration from 1989 to 1999

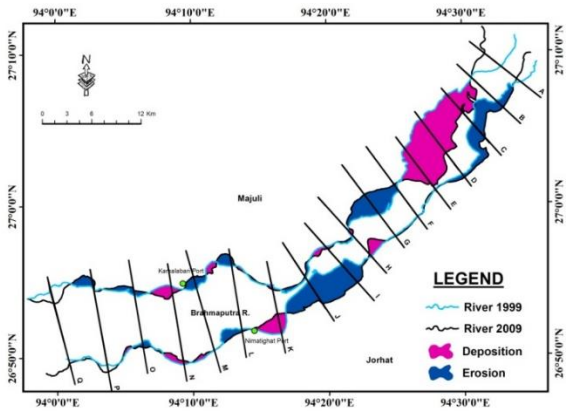

Figure 4: Bankline migration from 1999 to 2009

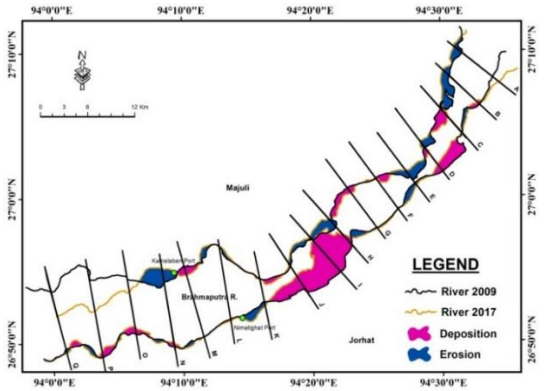

Figure 5: Bankline migration from 2009 to 2017

3. Results and discussion

The river Brahmaputra is flowing from north to south from the high Himalayas of Tibet through Arunachal Pradesh to the plains of Assam, the shifting of the river means shifting the bankline towards the eastern or western side. It was observed that Brahmaputra River below Majuli has been changing patterns continuously over the years.

Except the sections A and B, deposition is more dominant along the both banks of the river which indicates shifting of the channel towards eastern side and narrowing of the river except the sections K to O where the river is widening over the time (Figure 5). Since 1976, the river at the right bank has been continuously eroding the land at the cross sections J (1089.87 m) and L (5572.87 m). Along the left bank (Figure 7), the land being eroded continuously since 1976 is at the section G (423.01 m). The braided channel of the river strikes the bank directly and undermines the silty bank causing overhanging blocks to be carried away easily by the river current. Minus sign (-) in the figure 6 and 7 indicates shifting of the river due to erosion and plus sign (+) indicates shifting due to deposition. Approximately 85.23 sq. km area has been eroded and 135.38 sq. km area deposited since 1976 on both the banks.

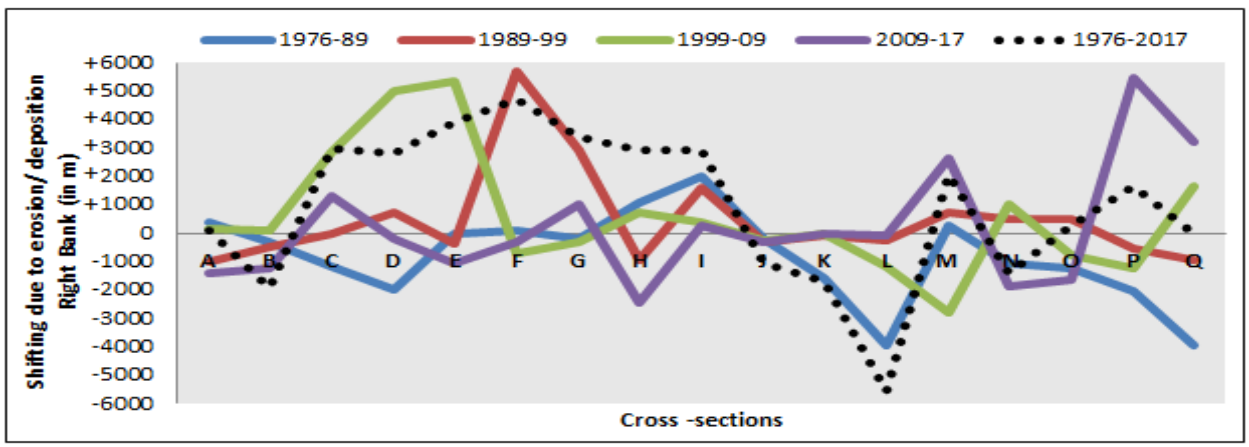

Figure 6: Shifting of the right bank of the Brahmaputra river from 1976-2017 due to Erosion and Deposition

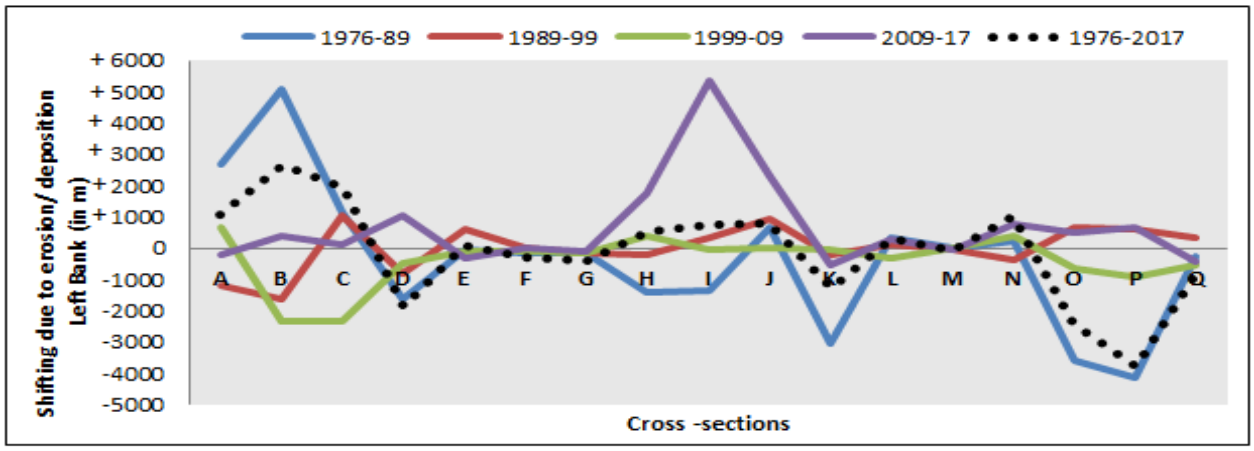

Figure 7: Shifting of the left bank of Brahmaputra river from 1976-2017 due to Erosion and Deposition

Erosion mostly affected the agricultural area and grazing land. The study also helps in understanding the probable erosion affected villages in Majuli. Approximately around 19 villages have been affected to a large extent due to erosion problem and they are under the threat of being completely eroded in coming years (Table 1). A number of important Satras (Satras are treasure troves of cultural artifacts) like AuniatiSatra and Kamalabari etc. are severely affected (Nath, 2012). The main river ports, i.e. Nimatighat and Kamalabari ports were seen shifting from their original location over the years. Nimatighat port has shifted about 0.56 km South and Kamalabari port about 0.65 km North. An example of the image captured by UAV from 100m height is depicted in the figure 8.

Table 1. Erosion Affected Villages

Feature	Village	Feature	Village
0	Bhogpur Satra	10	Borboka Pathar
1	Sekuli Pathar	11	Atoi Chuk
2	Kamjan Alengi	12	Katoni Gaon Na-Satra
3	Lahalial	13	Dakhinpat Satra
4	Potia Gaon	14	Bessa Mara
5	Bhogpur Pathar	15	Sumoi Mari
6	Pohardia	16	Auniati Lekhraj
7	Kamalabari Satra	17	Goroi Mari
8	Radha Chapari	18	Burha Kalita
9	Phutuka Pathar		

Figure 8: UAV image captured from 100m height

The image was acquired with a ground pixel resolution of 5 cm taken in a breaching location in Majuli Island, Assam. The scene shows that the embankment which was breached due to the flood during August 2016. This was also the major road in the villages in and around Samaria. A new path was constructed for the villagers. It was reported that water levels are now receding; however, significant challenges remain to be overcome. The late floods destroyed all agricultural crops and they have also hindered the planting season. Large scale classified image of the UAV data showing breaching location is shown in the figure 9. Geospatial technology supported by the sophisticated UAV for acquiring high resolution satellite imagery can be effectively used for estimation damage caused by the floods on a real time basis.

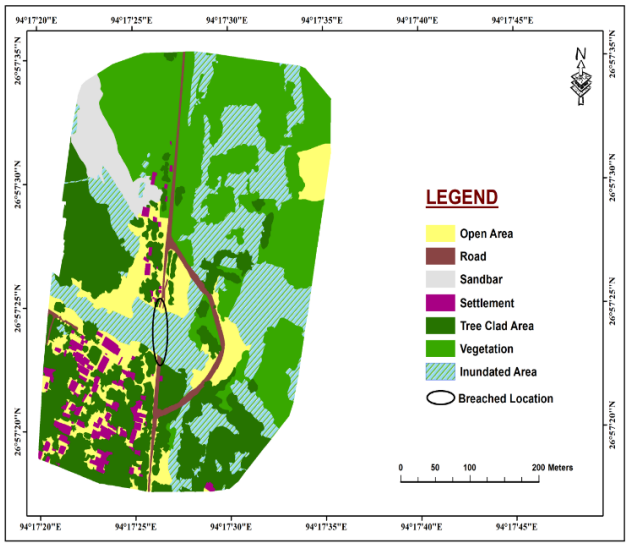

Figure 9: Large scale classified map showing breaching location

4. Conclusion

Majuli is getting eroded continuously due to the erosive nature of the surrounding rivers i.e. Brahmaputra and Subansiri rivers. Among them Brahmaputra is highly destructive, creating a lot of commotion around Majuli. In this paper, bankline migration of the Brahmaputra and its effects around Majuli has been examined. From 1976 to 2017, the bankline of the river changed significantly. Deposition is prominent at the right bank from the right side, but gradual erosion hinders the middle part. Therefore, the river is found to be widening at the middle part. This has in turn reduced the land surface of the island due to which Majuli has been shrinking and sinking over the years and it has been anticipated that a major part of Majuli will disappear within 5-10 years if this process continues to prevail for long without taking up preventive measures in a planned and scientific manner.

Acknowledgement

The authors acknowledge the Department of Soil Conservation, Jorhat Division, Assam and North Eastern Space Applications Centre (NESAC), Umiam, Meghalaya for providing necessary support and guidance during the study.

References

Gogoi. L and C. Borpujari (2014). Problems of river erosion in Majuli, Assam, India: A geo-environmental analysis. International Journal of Research in Applied, 2(11), 35-42.

http://en.wikipedia.org/wiki/Majuli

http://majulilandscape.gov.in/geography.php

http://www.brahmaputraboard.gov.in/NER/Archive/Archive.html

Kotoky, P., D. Bezbaruah., J. Baruah, and J. N. Sarma (2004). Nature of bank erosion along the Brahmaputra river channel, Assam, India. Current Science, 88(4), 634-640.

Lahiri, S. K., and R. Sinha (2014). Morphotectonic evolution of the Majuli Island in the Brahmaputra valley of Assam, India inferred from geomorphic and geophysical analysis, Geomorphology, 227, 101–111.

Mani, P., R. Kumar, and C. Chatterjee. (2003). Erosion study of a part of majuli river-island using remote sensing data, Journal of the Indian Society of Remote Sensing, 31(1), 12-18.

Nath, S.N. (2012). Satra Society and Culture, Pitambardeva Goswami and History of Garamur Satra, DVS Publisher, ISBN 978-81-86307-56-4.

Saha, S.K., Kudarat and M Bhan (1992). Erosion soil loss prediction using digital satellite data and Universal soil loss equation – soil loss mapping in Siwalik hills in India. In book on. “Application of Remote Sensing in Asia and Oceanic- Environmental change monitoring ” (Ed.Shunji Murai) ; Pub. Asian Association on Remote Sensing, 369-372.

Sarma, J. N and M. K. Phukan (2004). Origin and some geomorphological changes of Majuli Island of the Brahmaputra river in Assam, India, Geomorphology, 60 (1–2): 1–19. doi:10.1016/j.geomorph.2003.07.013

Sharma, J. N., and S. Acharjee. (2012). A GIS based study on bank erosion by the river Brahmaputra around Kaziranga National Park, Assam, India. Earth Syst. Dynam. Discuss., 3, 1085-1106. https://doi.org/10.5194/esdd-3-1085-2012.

Journal of Geomatics Vol 12 No. 1 April 2018

Accuracy assessment of free web-based online GPS Processing services and relative GPS solution software

Khaled Mahmoud Abdel Aziz
Department of Surveying Engineering, Shoubra Faculty of Engineering, Benha University, Benha, Egypt
Email: Khaled.Mahmoud@feng.bu.edu.eg

(Received on Jan 31, 2018; in final form: Apr 20, 2018)

Abstract: Recently many organizations give a free automatic processing web based online services for processing the GPS observations for any place in the world whether relative GPS Processing solution or Precise Point Positioning (PPP) technique. In this research, baseline lengths of GPS network in Egypt are obtained by using the free automatic processing web based online services and compared with the baseline lengths computed by relative solution using the Trimble Baseness Center (TBC) commercial software at different observation times 1,2,3 and 4 hours. The automatic processing web based online services used in this research are with relative GPS solutions (AUSPOS and Trimble CenterPoint RTX post-processing) and with PPP technique (CSRS-PPP). The network baseline lengths at different observation times 1,2,3 and 4 hours are compared with the baseline lengths computed by a total time of observations by using the above different approaches. The maximum vector length errors obtained by using TBC, Trimble RTX, AUSPOS and CSRS-PPP at 1 hour are 0.015 m, 0.093 m 0.235 m and 0.075 m respectively, at 2 hours are 0.009 m, 0.066 m, 0.033 m and 0.061 m respectively, at 3 hours are 0.008 m, 0.017 m, 0.033 m and 0.016 m respectively and at 4 hours are 0.005 m, 0.019 m, 0.014 m and 0.021 m respectively. The relative GPS solution software (TBC) are observed to give better result at all observation times.

Keywords: Trimble Center Point RTX post-processing, AUSPOS, CSRS-PPP, TEQC (Translation, Editing, and Quality Checking), Precise Ephemeris and Trimble Baseness Center (TBC) software

1. Introduction

Traditionally, most of the professional GPS users have used relative (differential) positioning technique to provide high accuracy. However, this technique has some limitations. Minimum two or more GPS receivers should be used and the true coordinates of the reference stations should be known. Addition to this, increase of the distance between the reference station (base) and rover station has reduced the position accuracy. For instance, while in differential GNSS (DGNSS) technique where single-frequency code (pseudo range) observations are used, decimeter level positioning accuracy can be achieved, in real time kinematic (RTK) techniques where dual/multi-frequency carrier phase observations are used, centimeter level positioning accuracy can be derived. To obtain more accurate positioning, GPS observations should be collected in relative static surveying mode, and then computed with different post-processing scientific or commercial software (Ocalan, 2016). However, the usage of such software is also quite difficult because they generally require deep knowledge of the GNSS and experience in the processing. Furthermore, they mostly need a licensing fee. Regarding the improvements in information technology and GNSS data processing methodology, many new opportunities have been offered to the users. In this respect, several institutions, research centers or organizations have developed web-based online GNSS processing services and they have started to become a strong alternative to the conventional data processing method. The only requirement for using these services which are generally provided free of charge with limitless usage, is a computer having an Internet connection and web browser. These services are designed to be as simple as possible for the user and with minimal input. Users of such systems have to perform uploading/sending of their collected RINEX data by using the web site of these services, e-mail or ftp sites to the system and selecting a few options such as static/kinematic modes, datum, antenna etc. With these services, when the data is received to the service, processing starts and the results (together with the coordinates, process reports along with other necessary information for analyzing the results) are sent to the user in a short amount time. Some of these services process not only the GPS but also the data of other systems, particularly those of GLONASS, and provide resilience and a higher accurate positioning service in certain cases to their users. As of today, there are several web-based online GNSS processing services, in which some of them calculate the coordinates with a relative solution approach (e.g. Trimble RTX, AUSPOS, OPUS,); or with the PPP technique (e.g. CSRS-PPP, magicGNSS, APPS) (Alkan et al.,2016).

2. Study area and data sources

The major aim of this research is to assess the automatic processing web based online services Trimble CenterPoint RTX post-processing, AUSPOS and CSRS-PPP with relative GPS processing solution software (TBC) by using a network of stations in Egypt see figure 1.

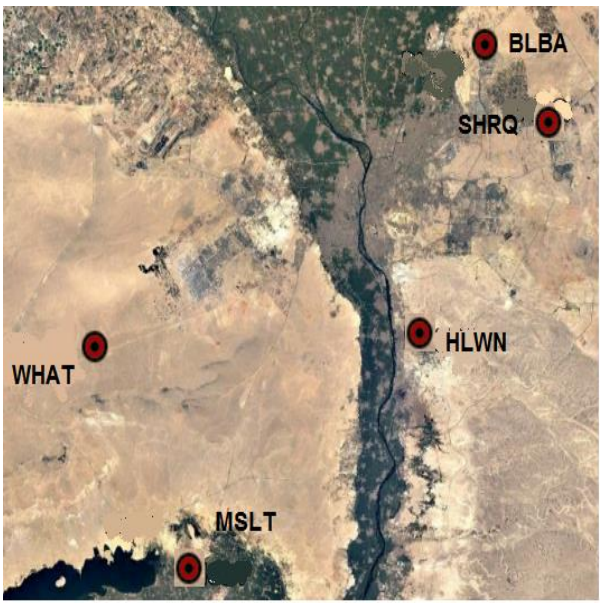

Figure 1: Study area, a network of stations in Egypt

The data used for this test are stated in the following items:

1- The rinex files of data observations for BLBA, MZLT and WHAT stations. The time of observation is approximately 48 hours.
2- The rinex files of data observations for SHRQ and HLWN stations. The time of observation is approximately 24 hours.
3- Using the TEQC (Translation, Editing, and Quality Checking) software (UNAVCO, 2017) to divide the observation files into numbers of observation files with different time of observations (1, 2, 3 and 4 hours).
4- Using the Trimble Baseness Center (TBC) commercial software to process the network stations ion Egypt by relative solution.
5- Precise satellite ephemerides (final orbits) for GPS observations on days 4-3-2013 and 5-3-2013.

3. Automatic GNSS processing web based online services

GNSS users prefer the relative positioning method in surveying applications if high accuracy is needed. All GNSS methods depending on the relative positioning principle require simultaneous observations occupied at least one reference station whose coordinates are well known. The primary factors for point positioning accuracy are the baseline length between two receivers and the observation duration. Relative positioning determines the point coordinates by using double differencing on phase measurements (Ocalan et al., 2016). However, in recent years, a method, namely PPP, has become an alternative technique to relative and differential techniques to provide high precision positioning. GPS PPP technique, which is a developed type of absolute positioning has been implemented effectively by users (Ocalan, 2016).

In this research, the relative solution using the Trimble Baseness Center (TBC) commercial software in addition to some web-based online GNSS processing services are used. The following paragraph illustrates the web-based online GNSS processing services used to compute the positions in this study by using a relative solution approach (e.g. Trimble RTX, AUSPOS) and PPP technique (e.g. CSRS-PPP).

3.1 Relative solution approaches

3.1.1 AUSPOS online GPS processing service

AUSPOS is a free online GPS data processing service provided by Geoscience Australia. AUSPOS takes advantage of both the IGS Stations Network and the IGS product range, and works with data collected anywhere on earth; users submit their dual frequency geodetic quality GPS RINEX data observed in a static mode to your GPS data processing system. The service aims to assist a variety of users from the private and public sector who require GDA94 and ITRF coordinates. This includes people undertaking surveys such as:

- DGPS reference station positioning
- Remote GPS station positioning
- Ultra-long GPS baseline positioning
- GPS connections to IGS and ARGN stations
- High accuracy vertical GPS positioning
- GPS network quality control

Finally, this service does not process real time, kinematic, or single frequency GPS data (Geoscience Australia. AUSPOS - Introduction, 2017).

AUSPOS uses the Bernese GNSS Software for processing baselines, IGS orbits and IGS network stations. Solutions are available for anywhere on the earth (gpsworld.com, 2013).

3.1.2 Trimble centerpoint RTX post-processing

Trimble RTX is a global GNSS technology that provides centimeter-level positioning, worldwide, at any time. This application allows you to upload GNSS observation data to the CenterPoint RTX post-processing service and receive positioning calculations. The positioning calculations are performed in ITRF2008 current epoch. Transformation can be performed by selecting a different coordinate system and tectonic plate (trimblertx.com, 2017).

The Trimble RTX technology utilizes real-time data from a Trimble owned global reference station infrastructure to compute and relay satellite orbit, satellite clock, and other system adjustments to the receiver. This results in centimeter level positions that deliver repeatable high accuracy positions worldwide. These adjustments are transmitted to the receiver via satellite, Internet Protocol (IP or Cellular), while post-processed results are sent to the user via email or a client interface.

The achievable accuracy is very closely correlated to the length of the observation file. It is recommended to use data sets that are a minimum of 1-hour in length to achieve

2 cm horizontal accuracy. Data sets less than 1-hour will result in less accurate position results. Data sets longer than 1-hour will yield even greater accuracy and can approach 1 cm. The CenterPoint RTX post-processing service does not accept observation files that are longer than 24 hours in length (Trimble CenterPoint RTX post-processing FAQS, 2016).

3.2 Precise Point Positioning (PPP) technique

According to the developments on satellite geodesy, precise satellite ephemerides and clock products are obtained by organizations such as IGS, Jet Propulsion Laboratory (JPL), Natural Resources Canada (NRCan) etc., and these are presented to the users. Due to this development, PPP technique becomes the most effective on GPS positioning. PPP is an absolute positioning technique, which provides cm or dm level point accuracy in static or kinematic mode depending on observation duration with a dual-frequency receiver (Ocalan et al., 2013).

The Canadian Spatial Reference System (CSRS) PPP service provides post-processed position estimates over the internet from GPS observation files submitted by the user. Precise position estimates are referred to the CSRS standard North American Datum of 1983 (NAD83) as well as the International Terrestrial Reference Frame (ITRF). Single station position estimates are computed for users operating in static or kinematic modes using precise GPS orbits and clocks. The online PPP positioning service is designed to minimize user interaction while providing the best possible solution for a given observation availability. Currently, users need only to specify the mode of processing (static or kinematic) and the reference frame for position output (NAD83 (CSRS) or ITRF). CSRS PPP service is processing both single and dual frequency observations from GPS and GLONASS (Farah, 2016).

4. Methodology

GPS observation data were collected from 13:00 Hrs. on day 4-3-2013 to 01:00 Hrs. on day 5-3-2013 for a period of 12 Hrs. for all the five stations. The data were split using TEQC (Translation, Editing, and Quality Checking) software into different observation time interval of 1, 2, 3 and 4 hours. The GPS observations data of all the five stations HLWN, BLBA, SHRQ, MZLT and WHAT were processed using Trimble CenterPoint RTX post-processing (trimblertx.com, 2017), AUSPOS (Geoscience Australia, 2017) and (CSRS) PPP (Natural Resources Canada, 2017) web based online processing services. Since the BLBA station data were collected for a period of 48 hrs instead of 12 hrs. the station is identified as base station for the estimation of the co-ordinate of other stations. Above mentioned web based online services were used to process observation files having 1 hour, 2 hour, 3 hour and 4 hour observation periods. GPS data was also processed using the Trimble Business Centre (TBC) commercial software for all the 5 stations.

5. Results and analysis

The estimated co-ordinates using TBC software are provided in the WGS-84 co-ordinate system, while the web based online services computed co-ordinates are provided in ITRF-2008 co-ordinate system. This discrepancy in co-ordinates leads to small difference between the coordinates of a position in ITRF and the WGS-84 (Trimble CenterPoint RTX post-processing FAQS, 2016). It may be noted that the difference in coordinate systems in this research between the automatic processing web based online services and the results obtained by TBC software do not have any effect on the results, since the analysis has been performed to compare baseline lengths between stations instead of the absolute co-ordinates.

The Vector Length Error (VLE) obtained by using TBC processing software gave the best results for all baseline lengths and all time of observation sessions. The figures 2 to 5 illustrate the Vector Length Errors (VLE) computed from subtracting the baseline lengths obtained by using the total time of observations and baseline lengths obtained by using observation time at each 1 hour on time periods 1 PM on 4-3-2013 to 1 AM on 5-3-2013 using the four processing approaches.

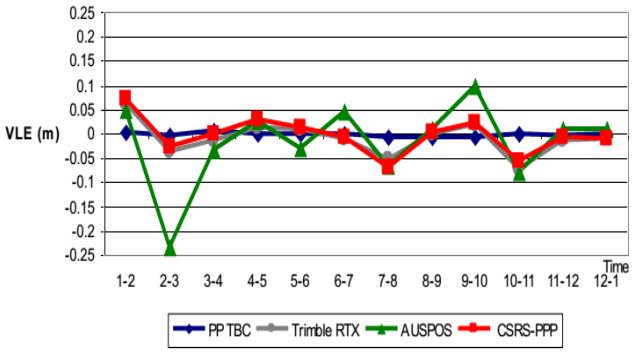

Figure 2: Vector Length Errors (VLE) for base line BLBA - SHRQ by using the four processing approaches at (1h) and base line whose length is 17.52

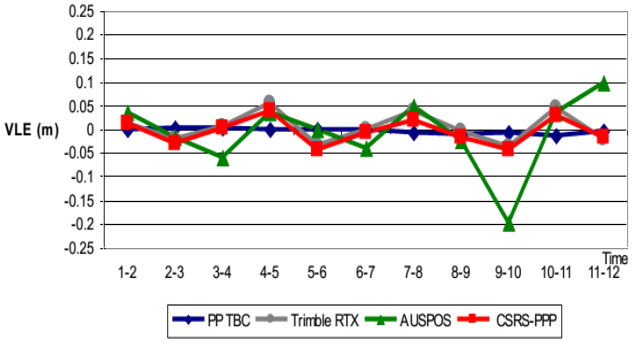

Figure 3: Vector Length Errors (VLE) for base line BLBA - HLWN by using the four processing approaches at (1h) and base line whose length is 48.793 km.

Table 1 summarizes the minimum and maximum values of VLEs at all baseline lengths processed by the four approaches. Through these figures and table note that, the vector length errors at 1h for different baselines obtained by TBC processing software gave a better result compared to the all free automatic processing web based online services. Where the maximum VLE obtained by TBC software is 0.015 m and the results obtained by using automatic processing web based online services approved that, the VLE of CSRS-PPP and Trimble RTX are better than AUSPOS.

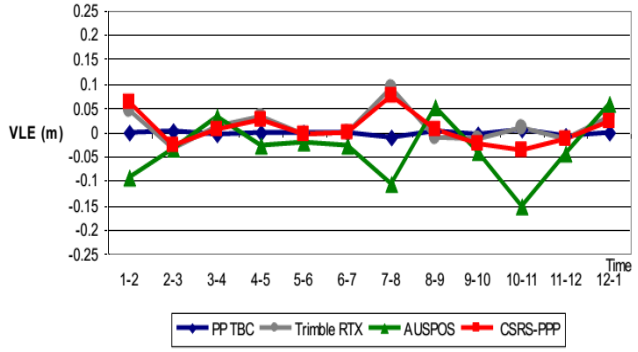

Figure 4: Vector Length Errors (VLE) for base line BLBA - WHAT by using the four processing approaches at (1h) and base line whose length is 91.279 km

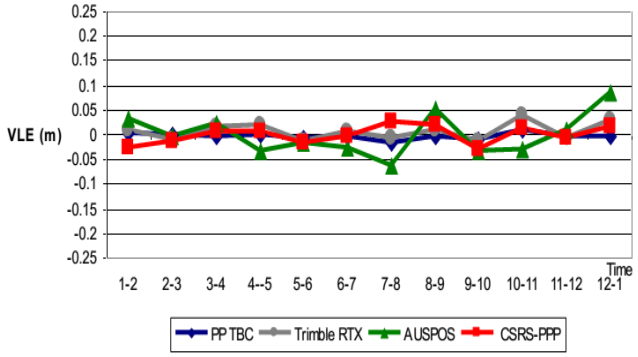

Figure 5: Vector Length Errors (VLE) for base line BLBA - MZLT by using the four processing approaches at (1h) and base line whose length is 102.777 km

Table 1: The Maximum and Minimum Vector Length Errors (VLE) for Different Baseline Lengths at 1h by Using the Four Processing Approaches

Processing Approaches								Baselines
CSRS-PPP		AUSPOS		Trimble RTX		PP TBC		
Max VLE (m)	Min VLE (m)	Max VLE (m)	Min VLE (m)	Max VLE (m)	Min VLE (m)	Max VLE (m)	Min VLE (m)	
0.073	-0.0005	-0.235	0.009	-0.072	-0.0002	0.008	-1E-06	BLBA - SHRQ
-0.043	0.002	-0.197	-0.001	0.057	0.0003	-0.012	-5E-05	BLBA - HLWN
0.075	0.001	-0.150	-0.020	0.093	0.0001	-0.011	0.0004	BLBA - WHAT
-0.031	-0.004	0.086	-0.003	0.039	-0.005	-0.015	-0.0002	BLBA - MZLT

From figure 6 to 9 and table 2 it is clear that, the use of TBC processing software at two hours of observation over the 12 hours is better than the automatic processing web based online services. In addition to the improvement in accuracy results obtained from the increased observational time from one hour into two hours, made VLE obtained by TBC software to be 0.009 m and VLEs obtained by processing web based online are improved with 2 hours of observation time.

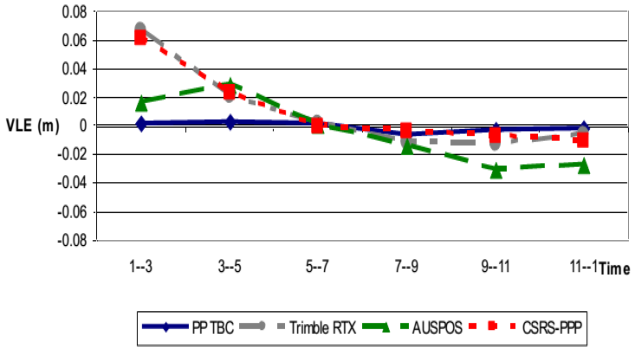

Figure 6: Vector Length Errors (VLE) for base line BLBA - SHRQ by using the four processing approaches at (2h) and base line whose Length is 17.523 km

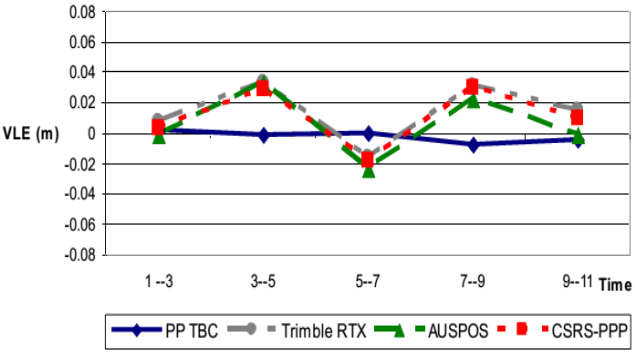

Figure 7: Vector Length Errors (VLE) for base line BLBA-HLWN by using the four processing approaches at (2h) and base line whose length is 48.793 km

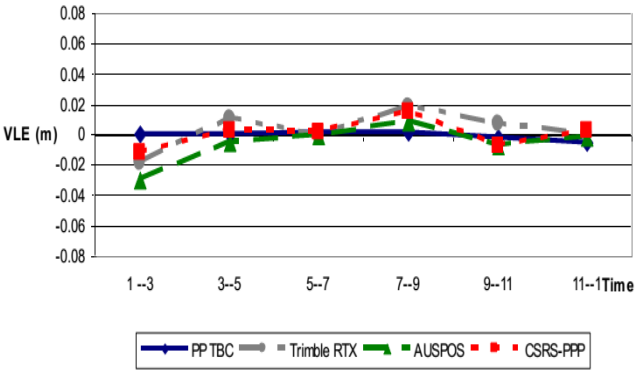

Figure 8: Vector Length Errors (VLE) for Base Line BLBA - WHAT by Using the Four processing approaches at (2h) and Base Line Whose Length is 91.279 km

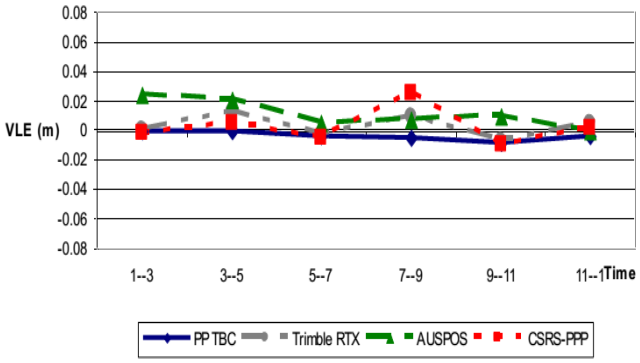

Figure 9: Vector Length Errors (VLE) for base line BLBA-MZLT by using the four processing approaches at (2h) and base line whose length is 102.777 km

Table 2: The Maximum and Minimum Vector Length Errors (VLE) for Different Baseline Lengths at 2h by Using the Four Processing Approaches

Processing Approaches								Baselines
CSRS-PPP		AUSPOS		Trimble RTX		PP TBC		
Max VLE (m)	Min VLE (m)	Max VLE (m)	Min VLE (m)	Max VLE (m)	Min VLE (m)	Max VLE (m)	Min VLE (m)	
0.061	-0.0001	-0.031	0.0006	0.066	0.002	-0.006	0.001	BLBA - SHRQ
0.0293	0.0033	0.033	-0.0007	0.0333	0.0078	-0.008	-2E-04	BLBA - HLWN
0.0155	0.00132	-0.030	-0.0008	0.0187	0.0002	-0.006	3E-04	BLBA - WHAT
0.0251	0.00156	0.0240	-0.0008	0.0126	0.001	-0.009	-1E-04	BLBA - MZLT

The figures 10 to 13 and table 3 shows that most results obtained by Trimble RTX are better than CSRS-PPP and CSRS-PPP is better than AUSPOS at 3h time of observations.

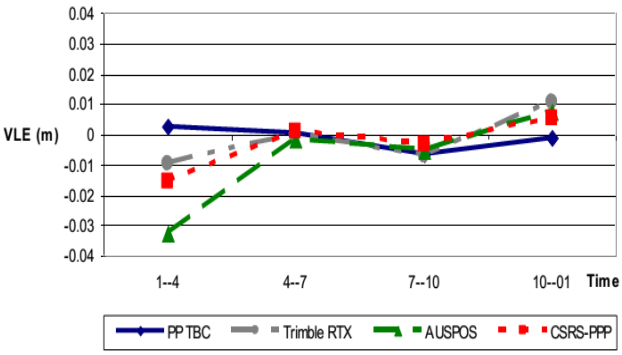

Figure 10: Vector Length Errors (VLE) for base line BLBA- SHRQ by using the four processing approaches at (3h) and base line whose length is 17.523 km

At 4h of observation time illustrated in figures (14) to (17) and table (4) the VLEs computed by AUSPOS is better than Trimble RTX and CSRS-PPP. To obtain the VLE less than 1 cm for baseline lengths less than 110 km the TBC processing software at 2h time of observations can be used.

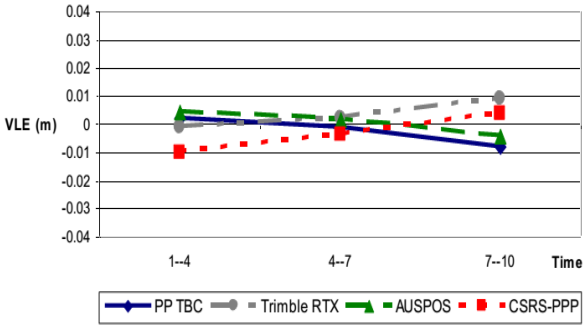

Figure 11: Vector Length Errors (VLE) for base line BLBA-HLWN by using the four processing approaches at (3h) and base line whose length is 48.793 km

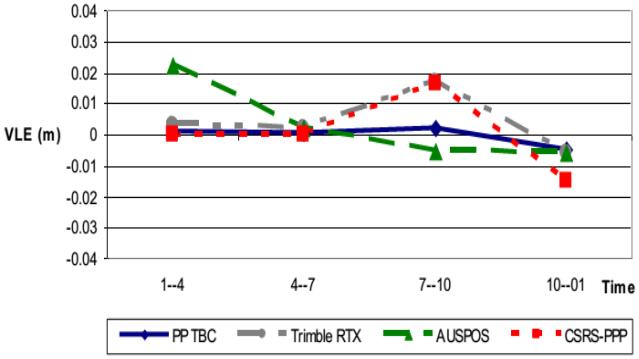

Figure 12: Vector Length Errors (VLE) for base line BLBA-WHAT by using the four processing approaches at (3h) and base line whose length is 91.279 km

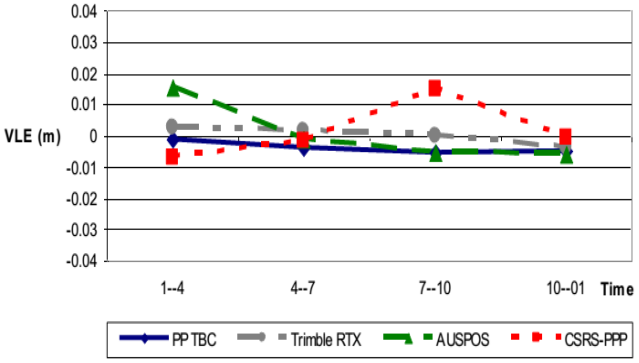

Figure 13: Vector Length Errors (VLE) for base line BLBA-MZLT by using the four processing approaches at (3h) and base line whose length is 102.777 km

Table 3: The Maximum and Minimum Vector Length Errors (VLE) for different baseline lengths at 3h by using the four processing approaches

Processing Approaches								Baselines
CSRS-PPP		AUSPOS		Trimble RTX		PP TBC		
Max VLE (m)	Min VLE (m)	Max VLE (m)	Min VLE (m)	Max VLE (m)	Min VLE (m)	Max VLE (m)	Min VLE (m)	
-0.016	0.0012	-0.033	-0.0018	0.0104	-8E-05	-0.006	7E-04	BLBA - SHRQ
-0.001	0.0037	0.0040	0.0013	0.0089	-0.001	-0.008	-0.001	BLBA - HLWN
0.016	9.2E-05	0.0222	0.0021	0.0173	0.0021	-0.005	7E-04	BLBA - WHAT
0.015	-0.0004	0.0153	-0.0011	-0.0035	-0.0002	-0.005	-9E-04	BLBA - MZLT

The automatic processing web based online services gives the VLE within 2 cm at the 4h time of observations with the baseline lengths less than 110 km. The classical relative solution using GPS software's is better than the automatic processing web based online services with relative GPS solutions (AUSPOS and Trimble CenterPoint RTX post-processing) and with PPP technique (CSRS-PPP).

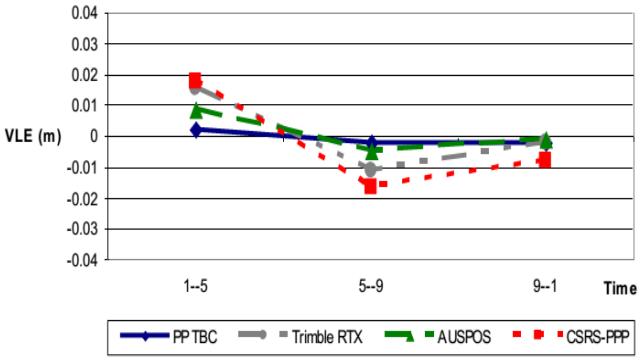

Figure 14: Vector Length Errors (VLE) for base line BLBA- SHRQ by using the four processing approaches at (4h) and base line whose length is 17.523 km

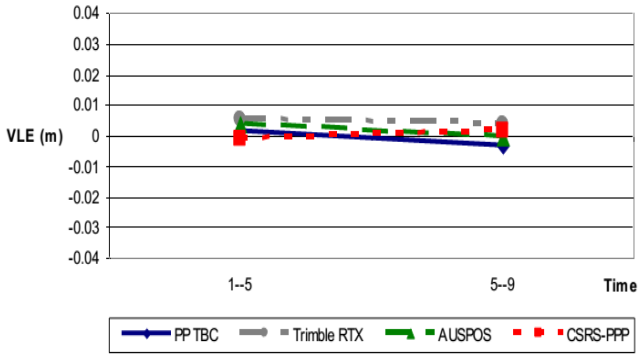

Figure 15: Vector Length Errors (VLE) for base line BLBA-HLWN by using the four processing approaches at (4h) and base line whose length is 48.793 km

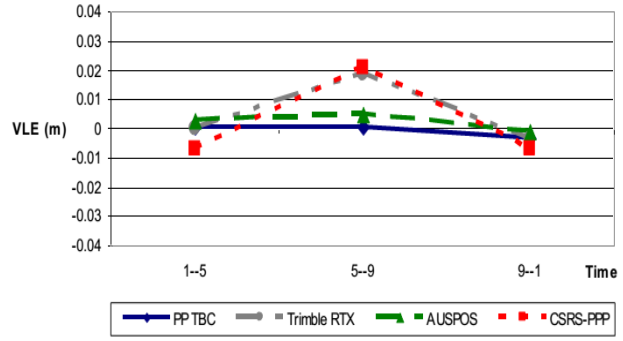

Figure 16: Vector Length Errors (VLE) for base line BLBA-WHAT by using the four processing approaches at (4h) and base line whose length is 91.279 km

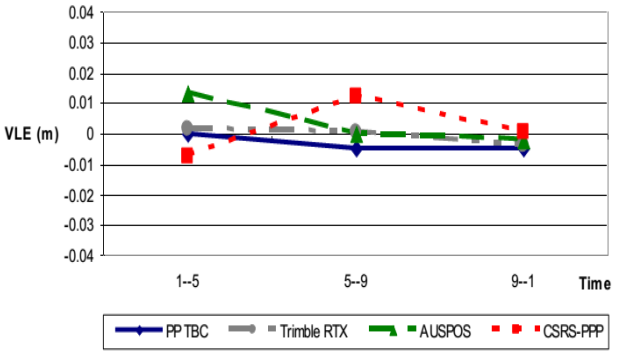

Figure 17: Vector Length Errors (VLE) for base line BLBA - MZLT by using the four processing approaches at (4h) and base line whose length is 102.777 km

Table 4: The Maximum and Minimum Vector Length Errors (VLE) for different baseline lengths at 4h by using the four processing approaches

Processing Approaches								Baselines
CSRS-PPP		AUSPOS		Trimble RTX		PP TBC		
Max VLE (m)	Min VLE (m)	Max VLE (m)	Min VLE (m)	Max VLE (m)	Min VLE (m)	Max VLE (m)	Min VLE (m)	
0.0177	-0.009	0.009	-0.0011	0.0154	-0.0023	0.002	0.002	BLBA - SHRQ
0.002	-0.001	0.004	-0.0004	0.0053	0.004	-0.003	0.002	BLBA - HLWN
0.021	-0.007	0.005	-0.0001	0.019	-0.0001	-0.003	8E-04	BLBA - WHAT
0.0120	0.0007	0.014	-2.3E-05	-0.004	0.0005	-0.005	-1E-04	BLBA - MZLT

6. Conclusions

The relative GPS solution software (TBC) are observed to give better result at all observation times. The maximum vector length errors obtained by using TBC, Trimble RTX, AUSPOS and CSRS-PPP at 1 hour are 0.015 m, 0.093 m 0.235 m and 0.075 m respectively, at 2 hours are 0.009 m, 0.066 m, 0.033 m and 0.061 m respectively, at 3 hours are 0.008 m, 0.017 m, 0.033 m and 0.016 m respectively and at 4 hours are 0.005 m, 0.019 m, 0.014 m and 0.021 m respectively.

It is suggested to carry out further work by using long baseline lengths and use GPS data of different seasons to study the effect of the atmosphere.

Acknowledgements

I would like to express my deep gratitude to the staff of the National Research Institute of Astronomy and Geophysics (NRIAG) in Egypt for providing me the data of GPS stations.

References

Alkan, R., İlçi, V and Ozulu,I. (2016). Web-based GNSS data processing services as an alternative to conventional processing technique. FIG Working Week 2016, Recovery from Disaster, Christchurch, New Zealand.

Farah, A. (2016). Accuracy evaluation for online Precise Point Positioning services. Journal of Geomatics, 10(1), 12-18.

Geoscience Australia. AUSPOS - Introduction (2017). web page, http://www.ga.gov.au .

http://gpsworld.com/a-comparison-of-free-gps-online-post-processing-services/.

Natural Resources Canada (2017). web page, https://webapp.geod.nrcan.gc.ca/geod/tools-outils/ppp.php

Ocalan, T. (2016). Accuracy assessment of GPS Precise Point Positioning (PPP) technique using different web-based online services in a forest environment. Šumarski list, 7–8, CXXXX (2016), 357–368.

Ocalan, T., Erdogan, B and Tunalioglu, N. (2013). Analysis of web-based online services for GPS relative and precise point positioning techniques. Bol. Ciênc. Geod., sec. Artigos, Curitiba, v. 19, no 2, p.191-207, abr-jun, 2013.

Ocalan,T., Erdogan,B., Tunalioglu,N and Durdag,U. (2016). Accuracy investigation of PPP method versus relative positioning using different satellite ephemerides products near/under forest environment. Earth Science Research Journal, 20(4), D1 - D9.

Trimble CenterPoint RTX Post-Processing (2017). web page, http://www.trimblertx.com/UploadForm.aspx

Trimble CenterPoint RTX post-processing FAQS (2016). web page, http://trl.trimble.com/docushare/dsweb/Get/Document-792295/TAP201606-0017-FAQ%20-%20Frequently%20Asked%20Questions%20-%20Trimble%20CenterPoint%20RTX%20Post-Processing.pdf (last accessed29-03-2017).

UNAVCO (2017). web page, https://www.unavco.org/software/data-processing/teqc/teqc.html

INDIAN SOCIETY OF GEOMATICS: AWARDS

National Geomatics Award for Excellence

This award has been instituted to recognize outstanding and conspicuously important contribution in promoting geomatics technology and applications at the country level. The contributions should have made major impact on the use of this technology for national development.
Areas of contribution considered for the award are:

1. Geographical Information System
2. Global Positioning System
3. Photogrammetry
4. Digital Cartography
5. Applications of Geomatics

The award shall consist of Rs. 50,000/- in cash, a medal and citation.

Eligibility

Any citizen of India, engaged in activities related to geomatics technology and its applications is eligible for this award. The prize is awarded on the basis of work primarily done in India.

The age limit for awardees is 45 years or above as on June 30 of the year of award.

Selection

A duly constituted Award Committee will evaluate all nominations received. The committee shall consist of eminent experts in the field of geo-spatial technology, to be identified by the Executive Council, ISG. The committee shall forward selected name/s to ISG – EC for approval and announcement. Apart from those persons, whose nominations have been received, the Committee may consider any person or persons who, in their opinion, have made outstanding contributions to development of geo-spatial technology and applications.

The award can be withheld in any year if, in the opinion of the committee, no candidate is found suitable in that particular year.

Presentation of the Award

The award shall be presented during the Annual Convention of ISG. Local Hospitality shall be taken care by ISG & Air fare (low cost) may be reimbursed if awardees request for it.

How to make Nomination

The nominations can be proposed by Head of a major research institute/ centre; Vice-Chancellor of a university; Secretary of Government Scientific Departments; President of a National Academy, President, Indian Society of Geomatics / Indian Society of Remote Sensing / Indian National Cartographic Association / ISG fellow or two life members of the society with more than 10 year old membership.

A candidate once nominated would be considered for a total period of two years. Nomination should be sent in the prescribed format to Secretary, ISG.

The last date for receiving nominations shall be September 30 or otherwise extended.

Format for nomination of Geomatics Award for Excellence

1. Name of the Nominee
2. Postal Address
3. Academic Background (Bachelor degree onwards)
4. Field of Specialisation
5. Important positions held (in chronological order)
6. Professional Experience including foreign assignments.
7. Important Awards / Honours
8. Important Publications/Patents: (A set of ten most important publications to be enclosed with this form)
9. Contributions of Nominee based on which the nomination is sent (in 1000 words, also provide a statement
   in 50 words which may be used for citation.):
10. Other Relevant Information:

Proposer:

Signature
Name
Address
Phone/ Fax
E-mail
Life Membership No. (in case of ISG Member):

Place & Date

Endorsed by (in case nomination is by 2 ISG Life members)

Signature
Name
Address
Phone/ Fax
E-mail
Life Membership No. (in case of ISG Member):

Place & Date
(The proposer should give a brief citation of the nominee's work)

National Geomatics Award

National Geomatics Award to be given each year: a) for original and significant contribution in Geomatics technology, b) for innovative applications in the field of Geomatics. Each award comprises a medal, a citation and a sum of Rs 25,000/- The guidelines for these awards are available on ISG website.

ISG Chapter Award for Best Performance

The best chapter award will be given to an active chapter of Indian Society of Geomatics, which has made significant contribution to further the mandate and goal of the society. The award consists of a citation and medal

President's Appreciation Medal for Contribution to the ISG

This award will be given to a member of the society, who has made noteworthy contribution to the growth of the ISG (its main body or any chapter). The Award consists of a Medal and a Citation.

Prof. Kakani Nageswara Rao Endowment Young Achiever Award

Indian Society of Geomatics instituted a new award from year 2013 named "Prof. Kakani Nageswara Rao Endowment Young Achiever Award", to encourage young researchers/scientists/academicians pursuing research in the field of geospatial technology/applications. The award carries a cash prize of Rs. 10,000/- along with a citation.

NATIONAL GEOMATICS AWARD

Indian Society of Geomatics has instituted two National Geomatics Awards to be given each year for (a) Original and significant contribution in Geomatics technology, (b) Innovative application(s) in the field of Geomatics. Each award comprises a medal, a citation and a sum of Rs. 25,000/-.

The guidelines for the award are as under

Areas of contribution considered for the award (both technology and applications)

1. Geographical Information System
2. Global Positioning System
3. Photogrammetry
4. Digital Cartography
5. Remote Sensing

Eligibility

Any citizen of India engaged in scientific work in any of the above-mentioned areas of research is eligible for the award.

The awards are to be given for the work largely carried out in India.

- First award will be given for original contribution in the field of Geomatics technology supported by publications in a refereed journal of repute.
- Second award will be given for carrying out innovative application(s). Supported by publications in rear reviewed Journals of repute.
- The contribution for the first award should have been accepted by peers through citation of the work.
- Work based on the applications of existing technologies will not be considered for the first award.
- The work should have made impact on the overall development of Geomatics.

How to Send Nomination

Nominations should be sent in the prescribed format, completed in all aspects to the Secretary, Indian Society of Geomatics, Space Applications Centre Campus, Ahmedabad 380 015 by August 31, 2017.

Selection Process

An expert committee, consisting of at least three members, constituted by the Executive Council of the Indian Society of Geomatics, will scrutinize the nominations and recommend the awardees' names to the Executive Council. The Council will decide on the award based on the recommendations.

FORMAT FOR AWARD NOMINATION

1. Name of the Candidate:
2. Present Position:
3. Positions held earlier (chronological order):
4. Academic qualifications (Bachelor's degree onwards):
5. Names of at least three Indian Scientists/Technologist in the area as possible referees *:
6. Brief write up on the work (500 words) for which award is claimed:
7. Publication(s) on the above work (reprint(s) to be enclosed):
8. List of other publications of the candidate:
9. Citation of the work for which award is claimed:
10. Impact of the work (for which award is claimed) on the development in the field of Geomatics (500 words):
11. Whether the work has already won any award? If so, give details:

The Applications in the above format (five copies) should be submitted (by Registered Post or Speed Post) to

The Secretary, Indian Society of Geomatics,
Space Applications Centre Campus,
Ahmedabad-380015

so as to reach by September 30, 2018

*ISG is, however, not bound to accept these names and can refer the nomination to other experts/peers

INDIAN SOCIETY OF GEOMATICS: FELLOWS

Shri Pramod P. Kale, Pune
Dr George Joseph, Ahmedabad
Dr A.K.S. Gopalan, Hyderabad
Dr Prithvish Nag, Varanasi
Dr Baldev Sahai, Ahmedabad
Shri A.R. Dasgupta, Ahmedabad
Dr R.R. Navalgund, Bengaluru
Shri Rajesh Mathur, New Delhi
Dr Ajai, Ahmedabad
Prof P. Venkatachalam, Mumbai
Dr Shailesh Nayak
Prof I.V. Murli Krishna
Prof SM Ramasamy, Tiruchirapalli
Dr Ashok Kaushal, Pune
Shri A.S. Kiran Kumar, Bengaluru
Prof. P.K. Verma, Bhopal
Maj. Gen. Siva Kumar, Hyderabad

INDIAN SOCIETY OF GEOMATICS: PATRON MEMBERS

P-1 Director, Space Applications Centre (ISRO), Jodhpur Tekra Satellite Road, Ahmedabad - 380 015
P-2 Settlement Commissioner, The Settlement Commissioner & Director of Land Records-Gujarat, Block No. 13, Floor 2, Old Sachivalay, Sector-10, Gandhinagar – 382 010
P-3 Commissioner, Mumbai Metropolitan Region Development Authority, Bandra-Kurla Complex, Bandra East, Mumbai - 400 051
P-4 Commissioner, land Records & Settlements Office, MP, Gwalior - 474 007
P-5 Director General, Centre for Development of Advanced Computing (C-DAC), Pune University Campus, Ganesh Khind, Pune - 411 007
P-6 Chairman, Indian Space Research Organization (ISRO), ISRO H.Q., Antariksha Bhavan, New BEL Road, Bengaluru 560 231
P-7 Director General, Forest Survey of India, Kaulagarh Road, P.O. I.P.E., Dehra Dun – 248 195
P-8 Commissioner, Vadodara Municipal Corporation, M.S. University, Vadodara - 390 002
P-9 Director, Centre for Environmental Planning and Technology (CEPT), Navarangpura, Ahmedabad - 380 009
P-10 Managing Director, ESRI INDIA, NIIT GIS Ltd., 8, Balaji Estate, Sudarshan Munjal Marg, Kalkaji, New Delhi - 110 019
P-11 Director, Gujarat Water Supply and Sewerage Board (GWSSB), Jalseva Bhavan, Sector – 10A, Gandhinagar - 382 010
P-12 Director, National Atlas & Thematic Mapping Organization (NATMO), Salt Lake, Kolkata - 700 064
P-13 Director of Operations, GIS Services, Genesys International Corporation Ltd., 73-A, SDF-III, SEEPZ, Andheri (E), Mumbai - 400 096
P-14 Managing Director, Speck Systems Limited, B-49, Electronics Complex, Kushiaguda, Hyderabad - 500 062
P-15 Director, Institute of Remote Sensing (IRS), Anna University, Sardar Patel Road, Chennai - 600 025
P-16 Managing Director, Tri-Geo Image Systems Ltd., 813 Nagarjuna Hills, PunjaGutta, Hyderabad - 500 082
P-17 Managing Director, Scanpoint Graphics Ltd., B/h Town Hall, Ashram Road, Ahmedabad - 380 006
P-18 Secretary General, Institute for Sustainable Development Research Studies (ISDRS), 7, Manav Ashram Colony, Goplapura Mod, Tonk Road, Jaipur - 302 018
P-19 Commandant, Defense institute for GeoSpatial Information & Training (DIGIT), Nr. Army HQs Camp, Rao Tula Ram Marg, Cantt., New Delhi - 110 010
P-20 Vice President, New Rolta India Ltd., Rolta Bhavan, 22nd Street, MIDC-Marol, Andheri East, Mumbai - 400 093
P-21 Director, National Remote Sensing Centre (NRSC), Deptt. of Space, Govt. of India, Balanagar, Hyderabad - 500 037
P-22 Managing Director, ERDAS India Ltd., Plot No. 7, Type-I, IE Kukatpalli, Hyderabad - 500 072
P-23 Senior Manager, Larsen & Toubro Limited, Library and Documentation Centre ECC Constr. Gp., P.B. No. 979, Mount Poonamallee Road, Manapakkam, Chennai - 600 089.
P-24 Director, North Eastern Space Applications Centre (NE-SAC), Department of Space, Umiam, Meghalaya 793 103
P-25 Progamme Coordinator, GSDG, Centre for Development of Advanced Computing (C-DAC), Pune University Campus, Pune – 411 007
P-26 Chief Executive, Jishnu Ocean Technologies, PL-6A, Bldg. No. 6/15, Sector – 1, Khanda Colony, New Panvel (W), Navi Mumbai – 410 206
P-27 Director General, A.P. State Remote Sensing Applications Centre (APSRAC), 8th Floor, "B" Block, Swarnajayanthi Complex, Ameerpet, Hyderabad- 500 038
P-28 Director, Advanced Data Processing Res. Institute (ADRIN), 203, Akbar Road, Tarbund, Manovikas Nagar P.O., Secunderabad –500 009
P-29 Managing Director, LEICA Geosystems Geospatial Imaging Pvt. (I) Ltd., 3, Enkay Square, 448a Udyog Vihar, Phase-5, Gurgoan- 122 016
P-30 Director, Defense Terrain Research Limited (DTRL), Ministry of Defense, Govt. of India, Defense Research & Development Organisation, Metacafe House, New Delhi – 110 054
P-31 Chairman, OGC India Forum, E/701, Gokul Residency, Thakur Village, Kandivali (E), Mumbai – 400 101
P-32 Managing Director, ML Infomap Pvt. Ltd., 124-A, Katwaria Sarai, New Delhi – 110 016
P-33 Director, Rolta India Limited, Rolta Tower, "A", Rolta Technology Park, MIDC, Andheri (E), Mumbai – 400 093
P-34 Director, State Remote Sensing Applications Centre, Aizawl – 796 012, Mizoram

Instructions for Authors

The journal covers all aspects of Geomatics – geodata acquisition, pre-processing, processing, analysis and publishing. Broadly this implies inclusion of areas like GIS, GPS, Photogrammetry, Cartography, Remote Sensing, Surveying, Spatial Data Infrastructure and Technology including hardware, software, algorithm, model and applications. It endeavors to provide an international forum for rapid publication of developments in the field – both in technology and applications.

A manuscript for publication must be based on original research work done by the author(s). It should not have been published in part or full in any type of publication nor should it be under consideration for publication in any periodical. Unsolicited review papers will not be published.

The Editorial Board or the Indian Society of Geomatics is not responsible for the opinions expressed by the authors.

Language

The language of the Journal will be English (Indian). However, manuscripts in English (US) and English (British) are also acceptable from authors from countries located outside India.

Manuscript Format

Each paper should have a title, name(s) of author(s), and affiliation of each of the authors with complete mailing address, e-mail address, an abstract, four to six keywords, and the text. The text should include introduction/background, research method, results, discussion, followed by acknowledgements and references. The main text should be divided in sections. Section headings should be concise and numbered in sequence, using a decimal system for subsections. Figures, images and their captions should be inserted at appropriate points of the text. Figures, images and tables should fit in two column format of the journal. If absolutely necessary, figures, images and tables can spread across the two columns. Figures and images, however, should not exceed half a page in height. A title should be provided for each Table, Image and Figure. All figures and images should be in 600 dpi resolution and sized as per column/margin width. Authors must ensure that diagrams/figures should not lose easy readability upon reduction to column size. The SI (metric) units and international quantities should be used throughout the paper. In case measurements are given in any other system, equivalent measurements in SI (metric) units should be indicated in brackets.

Use MS Word with English (UK/US) or English (Indian) dictionary. The page size should be A4 paper, with 2 cm margin on all sides. Title, authors and affiliation should be centred. Abstract should be justified across margins. The manuscript text should be in two columns of 8.2 cm each with a gutter of 6mm between them. Use only Times New Roman fonts. Title should be 12 points bold. Authors and affiliation should be 9 points. All other text including headings should be 10 points. Heading numbering scheme should be decimal e.g. 1, 1.1, 1.2.3, etc. Headings should be in bold.

Normally length of a published paper should be about 6-10 pages in A4 size including figures. Use of illustrations in colour should be restricted and resorted to only where it is absolutely necessary and not for enhancing the look of the paper. If the number of colour illustrations exceeds five, authors' institution may be asked to reimburse the extra cost involved, which at current rates is about Rs. 2500 per coloured figure/diagram/plate/illustration.

Submission of Manuscript

Submissions should be in electronic form via email. The manuscript may be sent by email to drajai1953@gmail.com. In exceptional cases hard copy submission in camera ready form may be allowed with the prior permission of the Chief Editor. Submission in any other form will be returned to the author. To speed up the review process, authors are advised to provide a list of three probable reviewers with their institutional address and e-mail IDs.

Guidelines for Citing References

Names of all cited publications should be given in full. No abbreviations should be used. Following procedure is to be adopted.

Journal Publications

Bahuguna, I.M. and A.V. Kulkarni (2005). Application of digital elevation model and orthoimages derived from IRS-1C Pan stereo data in monitoring variations in glacial dimensions, Journal of the Indian Society of Remote Sensing, 33(1), 107- 112. (to be referred to in the text as Bahuguna and Kulkarni (2005) or if more than two sets of authors are to be referred to, as (Bahuguna and Kulkarni, 2005; Jain et al., 1994)) When more than two authors are to be referred to, use Jain et al. (1994). However, in References, all authors are to be mentioned.

Publication in a Book

Misra, V.N. (1984). Climate, a factor in the rise and fall of the Indus Civilization – Evidence from Rajasthan and Beyond in Frontiers of the Indus Civilization (B.B. Lal and S.P. Gupta: Chief Editors) Books and Books, New Delhi, pp. 461-489

Papers Published in Seminar/ Symposium Proceedings

Jain, A., A.R. Shirish, M. Das, K. Das, M.C. Porwal, and P.S. Roy (1994). Remote Sensing and Geographic Information System – An approach for the assessment of biotic interference in the forest ecosystem. Proceedings. 15th Asian Conference on Remote Sensing, Bangalore, November 17-23, 1994, pp. 65-72.

Books

Possehl, Gregory L. (1999). Indus Age: The beginnings. Oxford and IBH Publishing Corporation, New Delhi.

Reviewing

Each paper will be reviewed by three peers. Papers forwarded by members of the Editorial or Advisory Boards along with their comments would get processed faster and may be reviewed by two referees only.

Sample format for Authors is available in downloadable form at ISG website: www.isgindia.org/JOG/Sample_format.doc

Copyright

The copyright of the paper selected for publication will rest with the Indian Society of Geomatics. Corresponding author shall be required to sign a copyright assignment form, on behalf of all authors, once the paper is selected for publication. Authors are, however, at liberty to use this material elsewhere after obtaining permission from the Indian Society of Geomatics.

If the authors have used any copyright material in their manuscript, it is understood that they have obtained permission from the owner of the copyright material and they should convey the same along with the manuscript to the Chief Editor.

Certificate of Original Work

The authors will also provide a certificate that the paper is an original work, not published or being considered for publication elsewhere.

In the event the certificate turns out to be false, the Journal shall ban the author(s) from publishing in the Journal for a period of five years and inform the same to all other related publications.

Reprints

Authors will be allowed to download the (PDF) of their paper from ISG Website www.isgindia.org, No hard copy reprints will be provided.

Journal of Geomatics

Advertisement Rates

	1 Issue	4 Issues
Back Cover Page in colour	**Rs. 25,000**	**Rs. 80,000**
Inside Cover Page in colour	**Rs. 20,000**	**Rs. 64,000**
Full Page inside in colour	**Rs. 15,000**	**Rs. 48,000**
Full Page inside in B/W	**Rs. 10,000**	**Rs. 32,000**

Advertisement Details

Mechanical Details
Double Spread/Center Spread (42 x 29.7) cm
Full page bleed (21 x 29.7) cm
Full page non-bleed (19 x 27.7) cm

Art Requirements

Negatives: Art must be right reading, emulsion, down. Film must be supplied in one piece per color, each identified by color. Camera-ready art is accepted for black & White adds; however, film is preferred. Electronic Files are also accepted.

Electronic File Requirements: All material must be received before ad close dates.

Software: Adobe illustrator 9.0 (saved as EPS). Adobe Photoshop CS (saved as EPS or TIFF). Please convert higher versions down. If you can only supply an IBM format, the file must be in viewable EPS or TIFF format with fonts embedded as that format.

Colour Ads: Colour separations must be provided, right reading, emulsion down. Please note that files using RGB or Pantone colours (PMS) must be converted to CMYK before we receive files.

To,
The Secretary, Indian Society of Geomatics
6202, Space Applications Centre (ISRO)
AHMEDABAD – 380 015. INDIA

Sir,

I want to become a Member/ Life Member/ Sustaining Member/ Patron Member/ Foreign Member/ Student Member of the Indian Society of Geomatics, Ahmedabad for the year _____. Membership fee of Rs. _____ /- is being sent to you by Cash/ DD/ Cheque. (In case of DD/ Cheque No._____dated_____drawn on Bank
_____ . I **agree to abide by the Constitution of the Society.**

Date:

Place: **Signature**

- Name: Mr/Ms/Mrs/Dr_____
- Address: _____

_____PIN: _____

Phone: _____ Fax: _____Email:

_____ • Date of Birth

_____

•Qualifications_____

- Specialisation: _____
- Designation: _____ Organisation. _____
- Membership in other Societies: _____
- Mailing Address: _____

_____PIN: _____

Proposed by:
(Member's Name and No)
Signature of Proposer

For Office Use: A/P/L Member No.		Receipt No.		Date:	

Indian Society of Geomatics (ISG), Room No. 6202 Space Applications Centre (ISRO), Ahmedabad-380015, Gujarat. Url: www.isgindia.org Phone: +91-79 26916202
Email: secretary@isgindia.org or sasharma@sac.isro.gov.in Fax +91-79-26916287

MEMBERSHIP FEES

Sr. No.	Membership Category	Life/Patron Membership fees ₹ Indian	Life/Patron Membership fees US $ Foreign	Annual Subscription ₹ Indian
1.	Annual Member	10	---	300
2.	Life Member a) Admitted below 45 years of age	2500	250	
	b) Admitted after 45 years of age	2000	200	
3.	Sustaining Member	---	---	2000
4.	Patron Member	50000	3000	---
5.	Student Member	10	---	100

MEMBERSHIP GUIDELINES

- Subscription for Life Membership is also accepted in two equal instalments payable within duration of three months, if so desired by the applicant. In such a case, please specify that payment will be in instalments and also the probable date for the second instalment (within three months of the first instalment).
- A Member of the Society should countersign application of membership as proposer.
- Subscription in DD or Cheque should be made out in the name of **'Indian Society of Geomatics'** and payable at Ahmedabad.
- Direct deposit in ISG A/Cs must include bank fee RS. 25/- for cash payment.
- Financial year of the Society is from April 1 to March 31.
- For further details, contact Secretary, Indian Society of Geomatics at the address given above.
- ISG has chapters already established at the following places. Ahmedabad, Ajmer, Bhagalpur, Bhopal, Chennai, Dehradun, Delhi, Hissar, Hyderabad, Jaipur, Ludhiana, Mangalore, Mumbai, Mysore, Pune, Shillong, Trichi, Srinagar, Vadodara, Vallabh Vidya Nagar, Visakhapatnam and Trivandrum. Applicants for membership have the option to contact Secretary/Chairman of the local chapter for enrolment. Details can be found at the website of the Society: www.isgindia.org.
- Journal of the Society will be sent to Life Members by softcopy only.

Indian Society of Geomatics (ISG), Room No. 6202 Space Applications Centre (ISRO), Ahmedabad-380015, Gujarat. Url: www.isgindia.org Phone: +91-79 26916202
Email: secretary@isgindia.org or sasharma@sac.isro.gov.in Fax +91-79-26916287

Geomatics Revealed

IGiS

Integrated GIS & IP Software

VERSION 2.0

MAKE IN INDIA

National Awards on Technology
By The Former President of India,
Dr. A. P. J. Abdul Kalam

Launch of IGiS Version 2.0
By Padam Shri AS Kiran Kumar, Chairman, ISRO and
Shri Tapan Mishra, DIRECTOR, SAC, ISRO.

What's new in IGiS

IGiS Version 2.0 is full of enhancements which you'll appreciate every day. New advanced GIS/IP and SAR modules are vital now a days. New COM Based Architecture makes you even more productive. The more you do with IGiS Version 2.0, the more you'll wonder how you ever did without it.

Enhancements in IGiS Version 2.0

- Advanced GIS / Image Processing
- Microwave SAR Analysis
- Meteorological Analysis
- COM Based Scalable Architecture
- New Ribbon Bar GUI
- Python Customization
- OGC Standards

Product Development Partner

इसरो isro
Government of India | Department of Space
Indian Space Research Organisation - (ISRO)

SGL Scanpoint Geomatics Ltd.
www.scanpointgeomatics.com

Scanpoint Geomatics Ltd.
Corporate Office : 12, Abhishree Corporate Park, Iskcon - Ambli Road, Ahmedabad - 380 058. Gujrat (India)
[P] +91 2717 297096-98 [F] +91 2717 297039 [E] info@scanpointgeomatics.com [W] www.scanpointgeomatics.com

INDIAN SPACE RESEARCH ORGANISATION
GOVERNMENT OF INDIA

A Smart Destination For Geospatial Solutions

National Remote Sensing Centre
Hyderabad, India
www.nrsc.gov.in
www.bhuvan.nrsc.gov.in
data@nrsc.gov.in

nrsc

इसरो isro

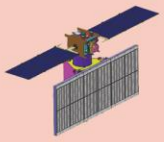

Only Organization in the Country to Acquire & Supply Satellite Data to Users

Aerial Acquisition for Specific User Demands & Disaster Management Support

Open Data & Value Added Products Dissemination Through Bhuvan

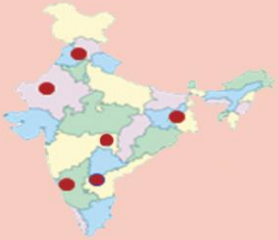

Region Specific Solutions

Capacity Building in Remote Sensing Applications